Toughening Thermosetting Resins with Modified Graphene Oxide

A Dissertation

SUBMITTED TO THE FACULTY OF THE

UNIVERSITY OF MINNESOTA

By

Siyao He

IN PARTIAL FULFILLMENT OF THE REQUIREMENTS

FOR THE DEGREE OF

DOCTOR OF PHILOSOPHY

Advisor: Andreas Stein

October 2018

Acknowledgements

There are many great minds that enlightened me during my five years of study in the University of Minnesota. Among them, I would like to give my thanks to Prof. Andreas Stein and Prof. Chris Macosko first. Andreas is an excellent advisor who not only gives me valuable instructions and suggestions that help me develop scientific methods for research but also takes good care of the well-being of his students. As a scientist, he pushes for more rigorous research, better results, and deeper understanding; as an advisor, he is always trying his best to communicate with his advisees and offer help if they are facing difficulties. Chris is also an excellent advisor who taught me so much about plastics engineering and rheology. Chris introduces me to many experts in my field, so I can consult with them for my research; and he also nominated me many times for important conferences, so I can expand my horizon. His precious help prepared me well for working as a polymer composite engineer after graduation.

Secondly, I want to thank Prof. Lee Penn and Prof. William Smyrl for allowing me to use their equipment, which significantly facilitate my research. I also thank all my smart and diligent coauthors: Dr. Yuqiang Qian, Mr. Kunwei Liu, Dr. Nicole Petkovich, Dr. Lian Bai, Dr. Tuoqi Li, Dr. Saibom Park, Dr. Benjamin Wilson, Prof. Bohejin Tang, Dr. Qi An. We have worked together to solve countless problems and made contribution to the scientific community. I give my thanks to Kunwei Liu for testing all my composite samples, and he also did the fiber-reinforced composites synthesis, testing, and data analysis work in Chapter 6. Saibom should also be credited to the PE composite synthesis, rheological

study, and conductivity measurement in Chapter 7. I give my thanks to John Ryder and Huikang Fu who shared much of my lab work to allow me to better focus on data analysis and design of experiment. I thank Dr. Frank Thibodeau, Dr. Robert Ferris, and Dr. Gregory Moriarty, who provided very important inputs when we discussed my project.

Finally, I would like to thank all my friends in the lab: Dr. Stephen Rudisill, Dr. Camille May, Dr. Jinbo Hu, Dr. LiangLiang Gu, Dr. David Giles, Nam Tran, Yangming Kou, Zhao Wang, Wenyang Zhao, and Brian Spindler for teaching me various lab techniques and providing me creative suggestions to solve my research problems.

This thesis is dedicated to:

My beloved parents, Shuzhen Zou and Zhifu He

Abstract

Thermosetting resins are highly crosslinked polymers that exhibit good chemical resistance, high thermal stability, and high modulus after curing. While these properties render thermosetting resins useful as structural, coatings, adhesives, and insulating materials, their high crosslink density causes thermosets to be inherently brittle and prone to cracking. Thus, both the academia and industry have made enormous efforts to toughen thermosetting resins. To date, liquid rubbers, core-shell rubbers, and block copolymers are commercially available as toughening additives for these resins. However, adding polymeric tougheners either significantly decreases the resin modulus and glass transition temperature (T_g) or requires a high loading level, which complicates the processing due to increased viscosity. Researchers have shown that rigid nanoparticles can toughen a resin with minimal reduction, or sometimes even an increase, of modulus and T_g. To harness the strength of inorganic tougheners, we studied the toughening effects of graphene derivatives, which have drawn much attention recently due to their high aspect ratios and outstanding mechanical properties. In addition, graphene-based toughener can toughen resin at extremely low loading levels, which means it is economically viable for price-driven unsaturated polyester (UP) and vinyl ester (VE) resins market. The objective of this thesis the to understand the toughening effect of graphene derivatives in resins.

To achieve this goal, several surface modifications of graphene oxide were developed to help disperse GO into the resins. The best performing modified GO (mGO) investigated in this work can be homogeneously dispersed into a resin with merely mechanic mixing. To simplify the materials handling and further improve the toughener dispersion, a styrene

masterbatch route was developed to avoid the freeze-drying step in the mGO synthesis. The functionalization of GO was characterized by FTIR, XRD, TGA, and XPS. The morphology of mGO aggregates was characterized by TEM, AFM, SEM, and VLM. The toughening effect of pristine and modified graphene oxide was tested in both unsaturated polyester and vinyl ester resins. The result indicated that GO and its derivatives can toughen UP and VE resins at a loading lower than 0.04 wt.%.

Although, these toughening are highly efficient in terms of required loading, we found that the toughness improvement obtained by adding mGO is insensitive to changes in particle-matrix interfacial strength and toughener loading. To better understand this behavior, we studied the inorganic filler interference to mGO toughening, and also how the toughening effect brought by adding mGO is affected by the physical dimensions of GO sheet size and mGO aggregate size. The sizes of various fillers and mGO samples were analyzed using SEM. More sophisticated data analysis involving computerized particle analysis were also carried out to better characterized the size differences between samples. The results show that the toughening effect of mGO is identical to that of other inorganic fillers, and this toughening effect is independent of filler mechanical properties.

Finally, the toughening performance of mGO was tested in glass fiber reinforced composites, which is the target product for UP and VE resins. Both the interlaminar fracture toughness test and Izod impact test showed no improvement in composite toughness after adding mGO. A detailed fractography analysis of failed composite samples indicate that the failure happens between the resin and the glass fiber, which means increasing the fracture toughness of the resin matrix will not likely show any effect on the composite fracture toughness.

Table of Contents

List of Abbreviations

AFM	Atomic Force Microscopy	ILSS	Interlaminar Shear Strength
ATBN	Amine-Terminated Butadiene Acrylonitrile	IR	Infrared Spectroscopy
ATRP	Atom Transfer Radical Polymerization	LLDPE	Linear Low-Density PE
BCP	Block Copolymer	mGO	Modified Graphene Oxide
CFRP	Carbon Fiber-Reinforced Plastic	NS	Non-Sonicated
CNT	Carbon Nanotube	OD	Oven-Dried
CSM	Random Chopped Strand Mat	OPE	Oxidized PE
CSR	Core-Shell Rubber	PCC	Precipitated Calcium Carbonate
CT	Compact Tension	PDMS	Polydimethylsiloxane
CTBN	Carboxyl-Terminated Butadiene Acrylonitrile	PE	Polyethylene
DCB	Dual Cantilever Beam	RAFT	Reversible Addition− Fragmentation Chain Transfer
DCM	Dichloromethane	RMB	Resin Masterbatch
DDA	Dodecylamine	SA	AEROSIL PDMS-Treated Fumed Silica
DHA	Dihexylamine	SAED	Selected Area Electron Diffraction
DI	Deionized	SC	CAB-O-SIL Untreated Fumed Silica
DMA	Dynamic Mechanical Analysis	SEM	Scanning Electron Microscopy
DMF	*N*,*N*-Dimethylformamide	SMB	Styrene Masterbatch
DSC	Differential Scanning Calorimetry	TDI	2,4-Toluene diisocyanate
EMI	Electromagnetic Interference	TEM	Transmission Electron Microscopy
ESD	Electrostatic Discharge	TGA	Thermogravimetric Analysis
FD	Freeze-Dried	TMI	3-Isopropenyl-α,α-dimethylbenzylisocyanate
FGO	Functionalized GO	TRG	Thermally Reduced GO
FRP	Fiber Reinforced Plastic	UP	Unsaturated Polyester
FTIR	Fourier-Transform IR	UPR	Unsaturated Polyester Resin
GCC	Ground Calcium Carbonate	VE	Vinyl Ester
GFRP	Glass Fiber Reinforced Plastic	VER	Vinyl Ester Resin
GNP	Graphite Nano-Platelet	VLM	Visible Light Microscopy
GO	Graphene Oxide	XPS	X-Ray Photoelectron Spectroscopy
GPC	Gel Permeation Chromatography	XRD	X-Ray Diffraction

List of Tables

List of Figures

Chapter 1

Introduction

1.1 Background of research

Synthetic polymers are of key importance in modern society. Ranging from chewing gum to spacecrafts, polymers have diverse applications such as structural materials, barrier coatings, insulators, adhesives, electrical or optical materials, and so on. But for many applications, polymers are not used in their pure forms. Adding a secondary phase to a polymer can be advantageous, because it can introduce useful new properties to the final product.[1] For instance, adding another polymer (polymer blends) may change the mechanical properties such as modulus,[2] impact strength,[3] or elongation at break[4] of a matrix polymer; adding inorganic fillers can reduce the thermal expansion,[5] change the rheological properties,[6, 7] or improve the thermal/electrical conductivity;[8, 9] incorporating air produces polymer foams, which are light-weight insulating materials.[10] The technique of adding a secondary phase to create polymer composites allows people to design polymer products with tunable characteristics that can meet the needs for a plethora of scenarios in different industries.

In recent years, polymer scientists and engineers discovered that polymer nanocomposites, which contain nano-sized secondary phases, manifest enhanced property changes at a much lower filler loading level than conventional composites, owing to a drastically increased interfacial area between the filler and the matrix polymer. This is because the behavior of the polymer chains can be perturbed by the presence of a different material. The perturbed volume is usually of a few nanometers in thickness around the

secondary phase. Winey and Vaia calculated that by decreasing the spherical particle size from 20 nm to 2 nm, the volume percentage of filler-affected polymer increases from 1.2 vol.% to about 63 vol.%, assuming a 6-nm thick interface for both cases.[1] In addition, decreasing the particle size at a constant filler loading level also significantly decreases the particle-particle distance in composites, which links to a lowered percolation threshold in polymer nanocomposites.[11] This is especially useful in situations in which a high volume fraction of a secondary phase undermines other properties such as density, or elongation at break.[12]

Graphene, a two-dimensional layer of sp^2 carbon atoms in a honeycomb array, has attracted much attention in the past decade because of its superior electrical and thermal conductivity, barrier property, as well as high modulus and strength. Due to its small thickness of one carbon atom, graphene has a very high theoretical surface area of 2600 m^2/g.[13] The union between excellent physical properties and high surface area hints that graphene could be a promising nanofiller in polymers. However, achieving good dispersion of graphene in a polymer matrix is difficult because graphene has very strong van der Waals interactions between multiple graphene layers and very poor compatibility with many polymers.[14] Surface incompatibility limits the application of graphene-based materials in polymer composites.

In this research, the main objective is to utilize graphene-based materials for toughening thermosetting resins. The scope of the thesis includes researching suitable chemical modifications for compatibilizing graphene with thermosetting resins, developing scalable processing techniques to disperse modified nanofillers into resins, studying the factors that may impact the toughening effect, and evaluating the nanofiller

toughening effect in fiber-reinforced plastic composite. Aside from that, a conductive polymer composite made with reduced graphene oxide is also included as a special topic. Various characterization techniques are employed to study the chemical modifications, resin composite mechanical properties, and possible mechanisms for fracture toughness improvement.

1.2 Graphene polymer nanocomposites

1.2.1 Synthesis of graphene

Despite the great mechanical, electrical, and barrier properties discovered for graphene, obtaining these single sheets remains one of the greatest challenges for large scale applications. Though direct synthesis of graphene by chemical vaper deposition[15-18] or unzipping carbon nanotubes and fibers[19, 20] has been reported, graphite exfoliation is by far the most promising method of producing graphene for polymer composite applications due to high process cost and low yield of more direct syntheses. According to the nature of the transformation, exfoliation of graphite can be done physically or chemically.

Physical exfoliation methods include micromechanical exfoliation,[21] surfactant intercalation-exfoliation,[22-25] and sonication.[26-28] Micromechanical exfoliation, or the "Scotch tape method", uses clear tape to peel off graphene layers from a graphite crystal, and the process is repeated until single layer graphene is obtained. This method produces high quality graphene monolayers with few defects and very good electrical performance, but it has minimal yield and is hard to scale-up. Surfactant-assisted exfoliation utilizes a high-speed shear mixer to cleave graphite, and the exfoliated few-layer graphene sheets are simultaneously stabilized by surfactant molecules. It is possible to scale up this process

since large industrial shear mixers are available, but the material produced by this method is predominantly multilayered and contains large amounts of solvent and surfactant,[25] which is not favorable for subsequent surface modification. Although prolonged sonication (460 h) of graphite in *N*-methylpyrrolidone (the best solvent for graphene) can yield a 1 mg/mL dispersion,[27] both sonication and the centrifugation steps required to remove unexfoliated graphite demand high investment and operating cost,[28] thus the sonication exfoliation process is impractical for large-scale synthesis.

While physical exfoliation relies on strong external forces to overcome the interaction between graphene layers, chemical exfoliation aims at reducing the interlayer van der Waals and π-π stacking interactions by creating sp^3 carbon defects and changing the local conformation of the carbon networks. This will inevitably disrupt the delocalized π orbitals on the graphene plane and thus decrease the conductivity, but, since most of the carbon network remains intact, the mechanical properties of graphene are to a large extend preserved. Chemical exfoliation also introduces copious heteroatom-containing functional groups that can be further modified, and it shows a good potential for scale-up.[29] Also, the weakened interlayer attraction renders the chemically treated graphite easy to exfoliate in common organic solvents, which benefits the solvent processing method for preparing polymer composite.

It has been reported that graphene can be simultaneously exfoliated and chemically modified using alkali metal intercalation[30-31] or electrochemical exfoliation.[32] NaK alloy intercalated graphite can be used as a reactive intermediate that can react with diazonium salts or alkyliodide to covalently attach aryl or alkyl groups to the graphene surface. However, this route involves using highly reactive and moisture sensitive NaK alloys;

therefore, the scalability and possible modifications are limited. Electrochemical exfoliation is usually slow and oxidative, which means it has little advantage over bulk oxidation methods.[32]

The most promising method so far to mass producing graphene derivatives is to functionalize and/or reduce graphene oxide. Graphene oxide (GO) is exfoliated graphite oxide, which is generally prepared by oxidizing graphite in a strong acidic environment and then exfoliating the layers. Three major methods to oxidize graphite flakes are the Brodie's method, the Staudenmaier's method, and the Hummers' method.[33] Brodie first discovered graphite oxide by oxidizing graphite flakes with potassium perchlorate in fuming nitric acid. Staudenmaier changed Brodie's procedure by adding potassium perchlorate in aliquots over time in a nitric-sulfuric acid mixture. In 1958, Hummers reported a much safer and faster graphite oxide synthesis using potassium permanganate and sodium nitrate to replace potassium perchlorate and nitric acid.[34] Since then, Hummers' method has been widely used for synthesizing graphite oxide. Recently, Tour et al. modified Hummers' method by carrying out the reaction in a sulfuric acid-phosphoric acid mixture, which gives highly oxidized graphite with much less emission of toxic gas.[35] The structure of graphene oxide can be well described by the Klinowski model.[36, 37] As shown in Figure 1.1, graphene oxide sheets contains hydroxyl and epoxy groups on the basal plane and carboxylic acid and ketone groups on the periphery. These oxygen-containing functionalities on GO not only stabilize exfoliated GO sheets in various polar solvents, but also provide active sites for further covalent chemical modifications.

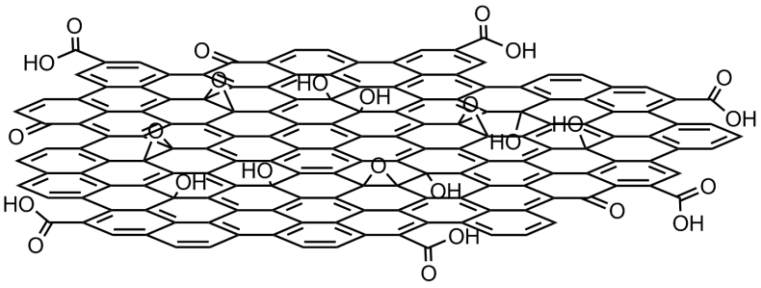

Figure 1.1. Structure of graphene oxide. Hydroxyl and epoxy groups are located on the basal plane. Carbonyl and carboxyl groups are located at the edge of the GO sheets.

As mentioned earlier, it is crucial to compatibilize graphene or GO with a polymer matrix to achieve good dispersion of graphene based nanofiller throughout the composite. Poorly dispersed graphene not only means an increase in nanomaterials loading in order to achieve a desired property, but graphene aggregates could also undermine the structural integrity of a composite. The scientific community has expended tremendous efforts to developing various surface functionalization methods of graphene/GO. Given the focus of this work, only major bulk modifications of graphene or GO are reviewed. However, one should not underestimate the importance of surface deposited graphene and its derivatives because they have good potential to be utilized in sensors, transistors, and other electronic devices.

1.2.2 Functionalization of graphene and graphene oxide

Due to the stable structure, direct covalent functionalization of graphene is difficult. However, several successful attempts were reported. Aside from the Na-K alloy intercalation method discussed above, there are two other classes of covalent reactions that can be done on graphene: free radical reaction and dienophile addition.[38] The diazonium reaction is the most important free radical reaction for functionalizing graphene. Aryl and

substituted aryl groups can be covalently bonded to graphene sheets via aryl diazonium salt treatment of chemically converted graphene.[39-40] Upon heating, diazonium salt loses nitrogen and forms aryl free radicals. Then, the reactive free radicals attack the carbon-carbon double bonds in graphene and attach aromatic functional groups to it. If the attached aryl groups have additional functionalities, they can be further modified through an atom transfer radical polymerization (ATRP) reaction to introduce polymer chains[41] or by click chemistry (Figure 1.2) to attach different end groups.[42] It should be noted that diazonium salts can also be used for modifying GO. Researchers have demonstrated that GO treated with diazonium salt has high electrical conductivity after reduction.[43] Also, the reaction can be done in GO aqueous dispersion, which generates less hazardous waste. This reaction provides a good way of attaching poly-aromatic or other complicated organic moieties to GO.[44, 45]

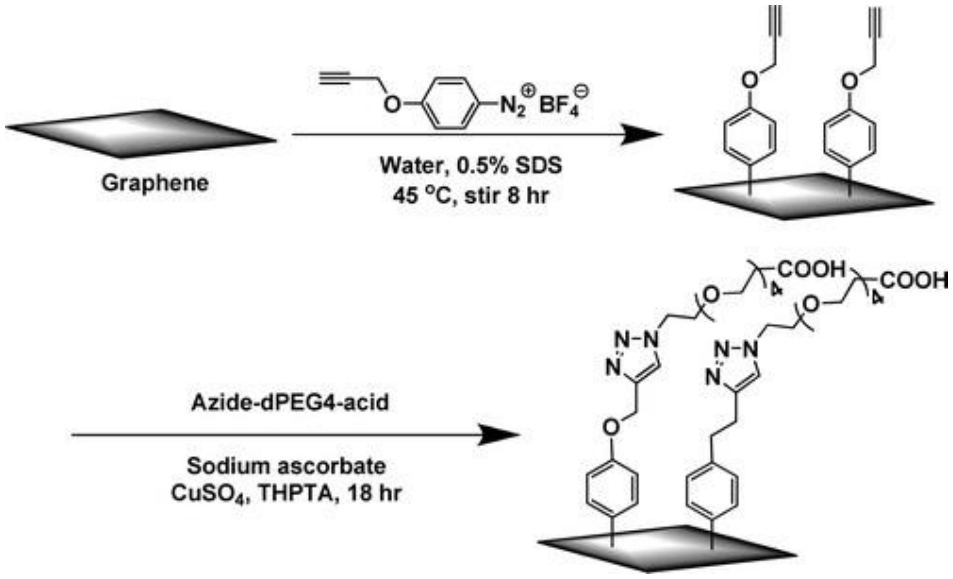

Figure 1.2. Diazonium salt functionalization of graphene and subsequent click reaction. Figure reprinted from ref. 42 with permission. Copyright © 2011, American Chemical Society.

Dienophiles can also react with graphene by addition. Azomethine ylide forms pyrrolidine rings on the graphene surface by 1,3 dipolar cycloaddition to adjacent unsaturated carbon pairs.[46] Similar reactions can also happen via nitrene addition by using azide compounds[47] or aryne addition by reacting graphene with a benzyne intermediate.[48] These modifications usually give products that can be well dispersed in organic solvents while maintaining a good electrical conductivity. However, the rate of reaction is typically very slow and inefficient. Considering the difficulties to obtain well dispersed monolayered graphene as the starting material, dienophile routes are not economic for producing graphene polymer composites.

Noncovalent functionalization provides other ways to circumvent the chemical inertness of graphene. Due to the strong π-π interactions between graphene and macrocyclic/polycyclic compounds, derivatives of pyrene, porphyrin, and phthalocyanine are capable of stabilizing graphene sheets in various organic solvents and even water.[39, 49] Pyrene based compounds show a good balance between strong affinity towards graphene and versatility for design at molecular level.[50, 51] These small molecule modifiers could be potentially useful for preparing functionalized graphene for optoelectronic, catalytic, and sensing applications. The density of functional groups on directly functionalized graphene depends on the degree of exfoliation; thus, all direct surface modifications benefit from method improvement of physical exfoliation processes.

Unlike graphene, graphene oxide contains ample hydroxyl, epoxy and carboxylic acid groups on its surfaces, and the rich chemistry of these oxygen-containing moieties enables a wide range of modifications to give modified GO tunable physical, chemical, and biological properties. Considering that graphite oxide is easier to exfoliate than graphite,

GO is therefore a much more versatile starting material for graphene derivatives. In addition to the opportunity to introduce new chemically reactive surface groups, GO modification often provides a repeatable and flexible way to tune the surface compatibility of modified GO in various solvents or polymer matrices. Later, the functionalized GO can be reduced to regain some thermal stability and electric conductivity. In the following sections, three well established routes for covalent GO functionalization, namely esterification/amidation, isocyanate functionalization and silanization, together with particle modification, polymer modification, and asymmetrical functionalization strategy, will be reviewed briefly.

Esterification and amidation

Esterification and amidation of GO can be actualized by reacting hydroxyl or amine group-bearing molecules directly with GO or the acyl chloride derivatives of the molecules (Figure 1.3). The targets of functionalization are the carboxyl groups at the edges and the epoxy groups at the graphene plane (amidation only). Using this method, researchers linked amine terminated thiophene oligomers to GO under the catalysis of *N*,*N*'-diisopropylcarbodiimide.[52] An esterification functionalization equivalent can be done by reacting hydroxyl terminated oligothiophene with $SOCl_2$ treated GO.[53] Similarly, polymers like poly(ethylene glycol),[54] and hydroxyl/amine group containing chromophores, for instance porphyrin, fullerene[55] and azobenzene,[56] can also be attached to GO.

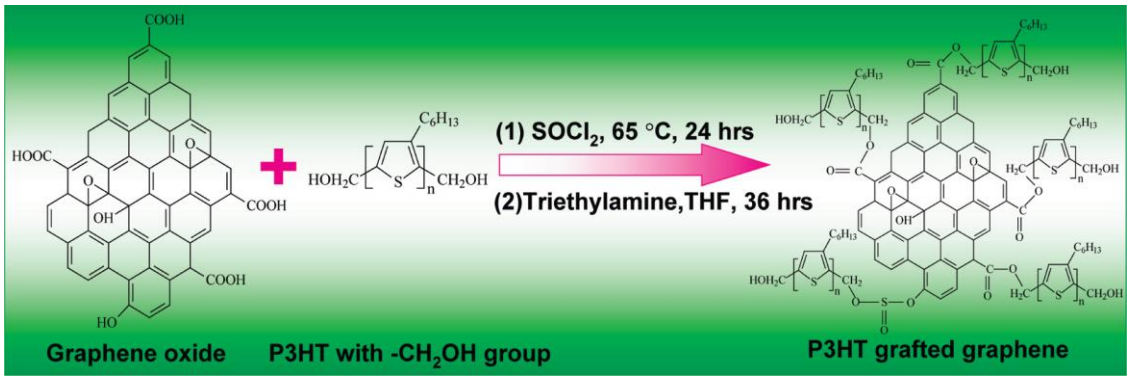

Figure 1.3. Synthesis of P3HT-grafted graphene. Image reprinted from ref. 53 with permission. Copyright © 2010, American Chemical Society.

In addition to coupling complex molecules with GO, amidation with alkylamines stabilizes GO sheets in nonpolar solvents by introducing long aliphatic chains (10 to 18 carbon atoms).[57-59] Further research indicated that alkylamine functionalized GO also disperses well in a polystyrene matrix, with a loading as high as 10 wt%.[59] A good dispersibility of modified GO in a nonpolar environment is desirable for toughening thermosetting polymers, since the curing process reduces matrix polarity.

Isocyanate functionalization

Due to the extreme hydrophilic nature of graphite oxide, it exfoliates poorly in organic solvents that lack hydrogen bonding.[60] These aprotic solvents, unfortunately, are oftentimes required for grafting additional moieties. However, isocyanate functionalization provides a possibility to exfoliate graphite oxide in polar aprotic solvents.[60] It was proposed that, hydroxyl groups and carboxyl groups, which contribute to the interlayer hydrogen bonding in graphite oxide and lead to good exfoliation in protic solvents,[61] can react with the isocyanate to form urethane and amide linkages during the functionalization (Figure 1.4). Thus, the weakening of interlayer interactions and the decrease in surface polarity

ensure a good exfoliation of isocyanate treated graphite oxide in organic solvents.[60] Research also showed that aryl isocyanate functionalization can improve the π-π stacking interactions between GO and polythiophene,[62] which could be advantageous in making dye-sensitized solar cells. But diisocyanates, at low concentrations, could link GO sheets to produce a 3D network rather than facilitate exfoliation.[63]

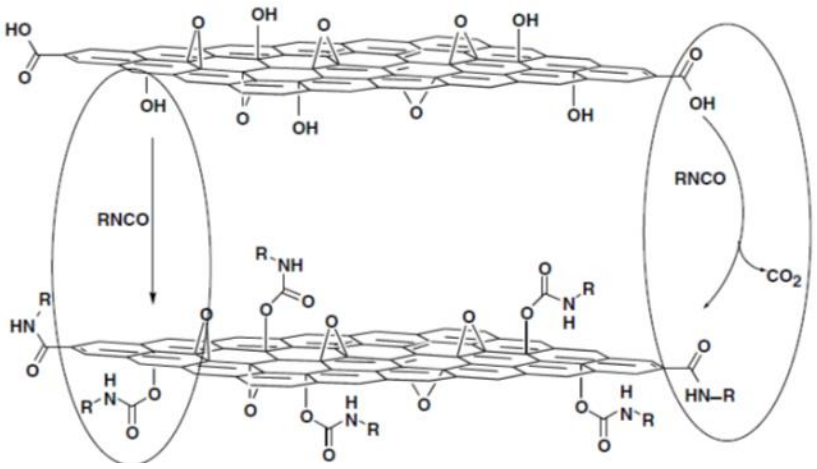

Figure 1.4. Proposed reaction scheme of isocyanate treatment of GO. Figure reprinted from ref. 60 with permission. Copyright © 2006, Elsevier.

Silanization

Silanization of GO also provides the possibility of attaching various functional groups. The most frequently reported precursors for GO silanization are substituted trimethoxysilanes[64-67] and triethoxysilanes.[68, 69] A proposed reaction scheme depicts that the hydroxyl oxygen attacks the partially positive silicon atom, and the alkoxy group on silicon dissociates to form the final product (Figure 1.5). According to literature, these silicon alkoxide derivatives are capable of introducing reactive functionalities such as amino groups,[68, 69] vinyl groups[64] and methacrylate groups[65, 66] to the GO surfaces. These

functionalities can then bond to thermosetting resins, and consequently improve the particle-matrix adhesion. Another advantage of silanization is the relatively low cost of the reactants. As a prevailing class of surface modifiers, numerous silicon alkoxides are produced in large quantity, which helps control the cost of functionalized GO.

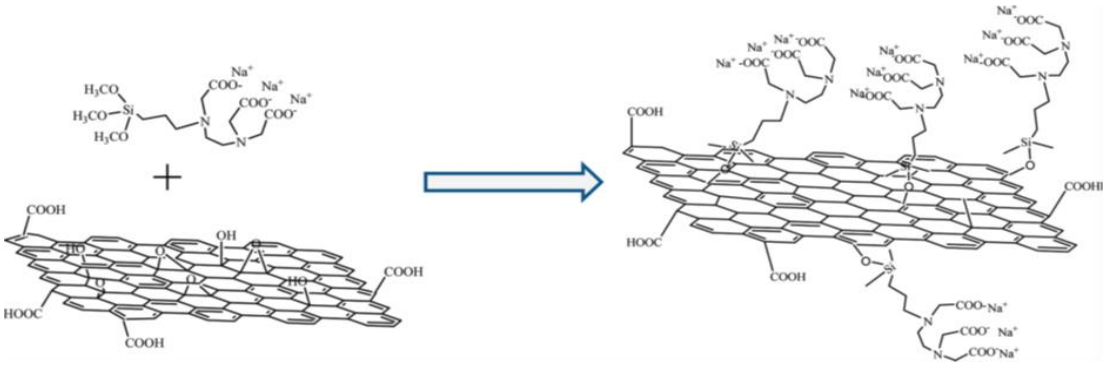

Figure 1.5. GO silanization by *N*-(trimethoxysilylpropyl) ethylenediamine triacetic acid. Figure obtained from ref. 66 with permission. Copyright © 2010 American Chemical Society.

Polymer modification

Polymer modification of GO receives special attention because it significantly increases particle-polymer matrix affinity and forms compact interfaces that facilitate stress transfer.[70] To attach polymer chains to the GO surfaces, there are two strategies: grafting end-functionalized polymer or in-situ polymerization on GO surfaces. In the former case, polymers with acid anhydride,[71] amine,[72] or hydroxyl[73] end groups can react directly with GO. Alternatively, small molecule surface modifications can add new anchoring groups such as amine,[74] or alkyne[75, 42] to GO, so coupling reactions can be used.

In-situ synthesized polymer can also be covalently attached by controlled radical polymerization. For ATRP reactions, alkyl halide moieties can be attached to the

carboxylic acid groups on the edges;[76] Chain transfer agents can be introduced for reversible addition− fragmentation chain transfer (RAFT) polymerization;[77] modifying GO with TEMPO derivatives enables nitroxide-mediated radical polymerization.[78] All these reactions can generate a covalently attached polymer layer on graphene, which stabilizes modified GO in matrix polymer.

Particle modification

Recently, researchers started to investigate the application of GO modified with inorganic particles in polymer composites. It is well known that graphene derivatives modified with metal particles have good catalytic activities and can also be used for supercapacitor materials,[79] but the properties of the composites made with inorganic particles/GO hybrids deserve further study. Titania and silica modified GO has been used as an additive for anticorrosion coatings,[80-82] dielectric media,[83] and thermomechanical strength enhancer.[84] Layered double hydroxide modified GO can be used as flame retardance agent in polymer composites.[85] Inorganic nanoparticles can be either physically attached to GO[84] or chemically bonded by silane.[82] Nanoparticle decorated GO shows better dispersion in epoxy resin, possibly due to the decreased van der Waals interactions between GO sheets.[80, 81]

Asymmetric surface functionalization

In the past few years, asymmetrically modified GO or Janus GO has become a hot topic. Due to its unique asymmetric structure, Janus GO can be designed to show hydrophilicity on one side and hydrophobicity on the other. This amphiphilic feature endows the Janus GO with very high adsorption energy at some polar-nonpolar interfaces. Wu et al. reported a potentially scalable synthesis of Janus GO by locating and fixing GO sheets at wax-in-

water Pickering emulsion interfaces.[86] Akbari et al. used this method to prepare Janus GO with one-side dodecylamine functionalization and made polymer composite films with this material. Their result shows the filtration film with Janus GO manifests a significant increase in pure water flux compared to the control made with homogeneously modified GO.[87] Given its unique interface affinity, Janus GO may bring new properties to some of the well-researched graphene polymer nanocomposite systems.

1.2.3 Properties and applications of graphene polymer nanocomposites

Structural materials

Graphene-based additive are capable of improving the mechanical properties of a polymer matrix. Tensile and flexural moduli, for instance, are known to be affected by adding inorganic fillers; therefore, it is not surprising to see an increase in modulus in graphene polymer composites.[88-90] However, graphene-based filler also improves elongation at break and ultimate strength in some of the studies, as graphene particles with large aspect ratios can facilitate continuous plastic deformation.[90] Fracture toughness is another important property of polymeric materials that can be improved by graphene. Since this topic is the main research focus of the thesis, it will be discussed in detail later in the introduction.

Aside from the mechanical properties, dimensional stability, thermal stability, and glass transition temperature (T_g) are also important for using graphene composites as structure materials. When polymers are to be used at elevated temperatures, thermal stability and T_g need to be high so that a structural part can retain its mechanical strength. Graphene composites provide a solution because they usually show increased thermal

stability[91-93] and T_g,[94] which is because graphene with strong particle-matrix interfaces restricts the polymer chain movement or increases polymer crystallinity. Dimensional stability is related to thermal expansion behavior of a polymer, and this becomes important when the structural materials are to be cycled in a wide temperature range, for example, when used as electronic packaging materials. The thermal expansion coefficient of a polymer decreases when graphene oxide is incorporated due to the negative thermal expansion coefficient of GO.[95, 96]

Electrostatic discharge (ESD) and electromagnetic interference (EMI) shielding materials

ESD materials are conductors, so the charge on a surface of these materials will not accumulate. EMI shielding materials are also conductive, so the incident electromagnetic wave can induce electrostatic displacement of charge or eddy currents to cancel the incident EM fields. Compared to conventional metal-based materials, conductive polymer composites have several advantages, such as low weight, flexibility, corrosion resistance, and easy processing. Graphene or reduced graphene oxide has a good conductivity and a high aspect ratio, thus graphene in polymer composites can reach a percolation threshold and become conductive at a relatively lower loading level, compared to conventional conductive fillers such as carbon black.[92, 97, 98] Usually, the required conductivity for ESD materials is between 10^{12} and 10^5 Ω per square, and EMI shielding materials have a resistivity lower than 10^5 Ω per square,[99] which is within the range of graphene polymer composites. Many papers have been published in recent years that investigated the performance of graphene polymer composites made with polystyrene, polyurethane, polyetherimide, polyvinylidene fluoride, and so on. The results indicate that graphene-

based materials can achieve good EMI shielding of about 20 dB radiation attenuation.[100-105] Also, graphene additives can function as reinforcing fillers and improve the thermal or mechanical performance of a polymer foam or fabric,[101] or the composite can be engineered to show superhydrophobicity and self-cleaning characteristics.[102] Versatile graphene polymer composites are, therefore, suitable for multifunctional applications.

Flame retardance additives

Graphene based materials have been demonstrated as good flame retardance additives in polymers. Although it seems counterintuitive that these combustible carbon materials can reduce the flammability of a polymer, researchers find that both the peak heat release rate and total heat release during combustion of a polymeric material are decreased when a few weight percent of graphene or modified graphene oxide are incorporated.[106-111] This phenomenon is due to the fact that layered graphene slows down the release of a flammable gas from the overheated polymer, facilitating the formation of a char layer on the surface of the composite to reduce the heat transfer.[106] The char layer also restricts the "dripping" of the flammable liquid degradation product from a burning composite.[107] Because of the high surface area and abundant functional groups on the surface, GO can be modified with other flame retardants to achieve better performance. For instance, organophosphorus flame retardant 9,10-dihydro-9-oxa-10-phosphaphenanthrene-10-oxide can be grafted onto GO with poly(glycidyl methacrylate) as the linker;[108] GO with synthetic clay particles on the surface also shows improved flame retardance;[85] GO flame retardant functionalized with metal oxide particles reduces toxic gas release.[110] The reinforcing effect and thermal/electrical conductivity of some graphene derivatives can also be utilized in this

flame retardance scenario to create polymer-based coatings, thermal interface materials, or EMI shielding packaging with a reduce fire hazard.

Antibacterial

Graphene oxide is known for its antibacterial effects. Although, it is still unclear why GO prohibits the growth of bacteria, there are a number of hypotheses regarding the antimicrobial mechanisms.[112-115] These include membrane stress, oxidative stress, electron transfer, and wrapping. The size-dependent activity of GO suggests that wrapping is the preferred mechanism for large sheet size GO, and membrane stress and oxidative stress are the major mechanisms for small sized GO particles.[114, 115] The most interesting application of GO as an antibacterial agent is its use in polymer composites as antibiofouling membranes and antibacterial wound dressing. Various studies have shown that GO sheets in many polymer matrices have strong antibacterial effects,[116-119] which are useful for modifying functional polymeric membranes for water purification, desalination, and gas separation.[112] Recent publications also suggest that GO-containing hydrogels promote wound healing,[120, 121] thus these mechanically robust hydrogels could be promising wound dressing materials.

Gas barrier membranes

Defect-free graphene sheets are impermeable to all gas molecules and can, therefore, be used in polymer composites to produce flexible and lightweight gas barriers. Ideally, graphene sheets in the composites should be single-layered, have high aspect ratios, and should be aligned perpendicular to the gas partial pressure gradient. In such a case, the tortuosity of the diffusion pathway and the barrier properties are maximized. However, mass production of graphene sheets for barrier materials is still challenging; therefore, in

most cases, well exfoliated graphene oxide is used instead.[122, 123] Although GO has many gas permeable defects on its basal plane, GO is much easier to exfoliate and well dispersed in polymer matrices. Considering that GO can be functionalized to improve matrix compatibility, which also increases path length for gas diffusion, the overall performance of GO-based composite gas barriers is comparable to that of composites made with graphene.[124] The methods for preparing gas barrier composites include solvent casting,[124-126] in situ polymerization,[127] and layer-by-layer self-assembly.[128] The layer-by-layer method gives the lowest gas permeability among all three methods, possibly due to high GO loading and good alignment of the GO sheets.

Other applications

There are many other applications of graphene polymer composites that cannot be reviewed here due to the limitation of space. These include polymer gas sensors,[129] fuel cell membranes,[130] anticorrosion coatings,[131, 132] desalination membranes,[133] and so on. The ever-growing scope of applications for graphene composites manifests the unique characteristics of graphene, which leads to our researching of graphene-based thermosetting polymer toughening agents.

1.3 Toughening of thermosetting resins

1.3.1 Thermosetting resins are brittle materials

Thermosetting resins, or thermosets, are highly crosslinked polymer networks that are unmeltable and insoluble after curing (Figure 1.6). Common thermosets include epoxy, unsaturated polyester, vinyl ester, cyanate ester, polyurethane, phenol-formaldehyde, and so on. Thermosets are widely utilized as structural materials, adhesives, coatings or

insulating materials in the automotive, aviation, electronic, construction and packaging industries.[134, 135] Due to a high crosslink density, thermosetting resins are thermally stable, chemically inert, and mechanically stiff. But, despite these advantages, thermosets are brittle and prone to mechanical failure. This is because high-density crosslinks lock the polymer chains in well-defined positions, so that the polymer network cannot deform elastically or plastically except at a very low strain. Once the stress passes a critical value, the covalent bonds inside a resin will break and rearrange, leading to brittle fracture. Consequently, a part made with a thermosetting resin will lose its structural integrity quickly once the stress concentrated by a small structural defect passes a critical value. This limits the application of thermosetting resins in some areas where anti-fracture and anti-fatigue properties are vitally important.[134]

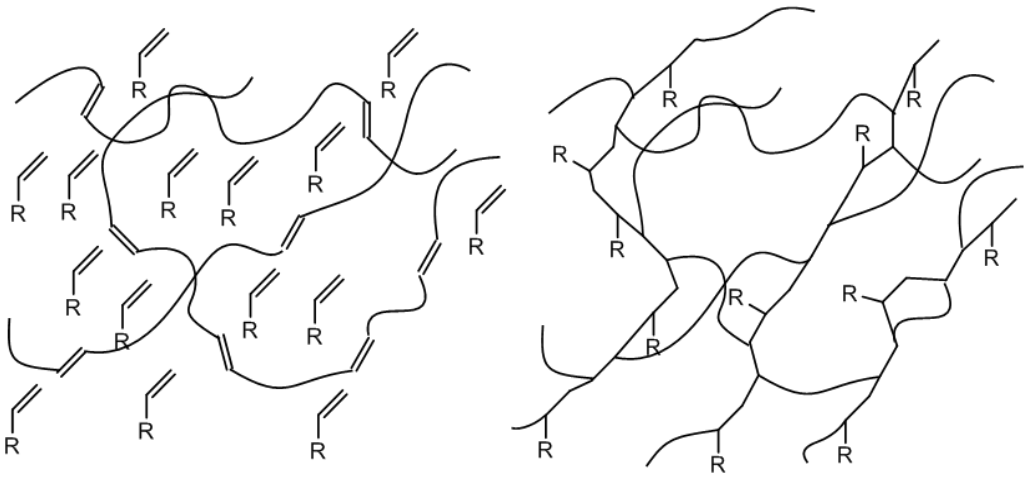

Figure 1.6. A schematic of thermosets before (left) and after (right) free radical polymerization crosslinking.

Unsaturated polyester (UP) is a thermosetting resin of advantageous chemical resistance and low cost, which requires only mild curing conditions.[136, 137] Commercially

available UP resins are usually sold as reactive diluent (double bond containing solvent molecules, e.g., styrene, that can be copolymerized with the resin backbone) solutions of polyester prepolymers. The UP prepolymers, or the resin "backbones", are synthesized through a condensation reaction between diacid components and diol components. Once an initiator is added, the free radical chain-growth copolymerization between the solvent and the unsaturated moieties in the polymer backbones will link the linear polymer chains together to form a 3-D network (Figure 1.7).

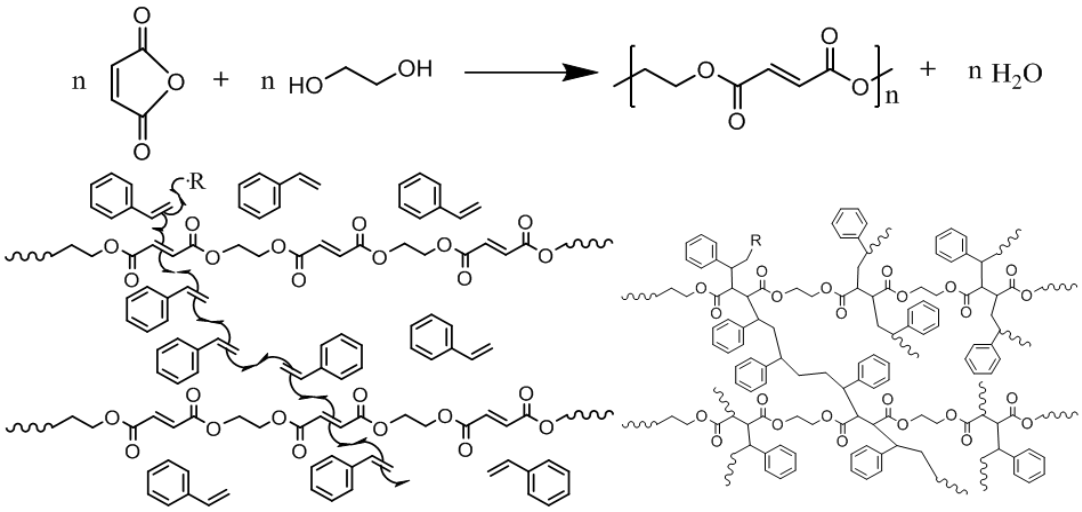

Figure 1.7. Schematic reactions of forming UP backbone (top), crosslinking initiation (bottom left), and cured resin (bottom right).

Vinyl ester (VE) resin is similar to UP resin in that it is also based on an unsaturated prepolymer. But in VE resins the prepolymer has an epoxy “core” and unsaturated acrylate or methacrylate end groups. Figure 1.8 shows the structure of a common VE prepolymer based on bisphenol A diglycidyl ether epoxy. Later, the crosslinking happens when styrene copolymerizes with the unsaturated end groups. Compared to UP resins, VE resins offer better toughness and corrosion resistance at a slightly higher cost.[134] VE resins are therefore

more commonly applied in the chemical industry, where the mechanical properties and chemical resistance of UP resins are inadequate.

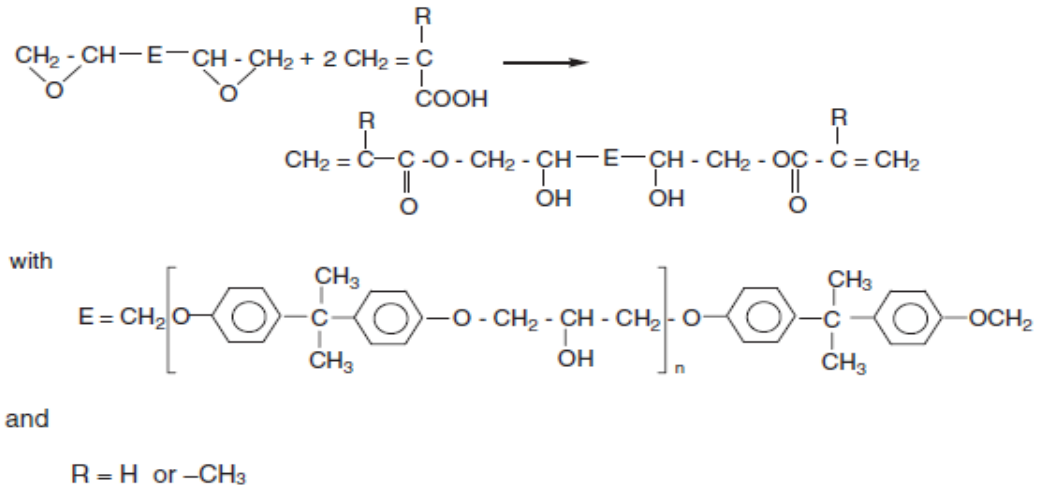

Figure 1.8. Formation of VE resin prepolymer with bisphenol A diglycidyl ether oligomer and (meth)acrylic acid.

UP and VE resins are commonly used resins for making fiber reinforced composite parts via sheet molding compounds, bulk molding compounds, and laminates. However, like any other thermosets, these resins are severely affected by a poor resistance to crack propagation, which limits their use in applications where applied stress is relatively static. Since their invention,[138] much effort has been made to address the problem of low fracture toughness of UP and VE resins.

1.3.2 Methods of UP and VE resin toughening

Due to their brittleness, neat UP and VE resins have minimal industrial applications. However, the corresponding fiber composites of these resins have good mechanical properties, so they are commonly used in industry. Fiber reinforced plastics, or FRPs, are

comprised of strong fibers (glass fibers, synthetic wools, etc.) and a resin matrix that binds the fibers together. The resin transfers stress to fibers, and the fibers are firmly fixed in the resin matrix so that such a composite can withstand the applied load. Common mechanical properties, such as tensile strength and modulus, of a FRP are usually dominated by the fiber component because of the high fiber content. Thus, FRPs can have high mechanical strength that is comparable to metal alloys with a much better corrosion resistance. In addition, the invention of sheet molding compounds and bulk molding compounds greatly simplifies the building of FRP parts,[139] which also benefits the application. Recent research on FRP has focused on the substitution or supplement glass fibers with stronger and lighter carbon fibers[140-142] or natural fibers.[143-149] However, stacking fibers with sub-millimeter diameters results in a wide distribution of vacancy sizes. Thus, although fiber reinforcement significantly enhances the toughness of a resin matrix, the resin rich regions inside a FRP are nonetheless prone to craze and cracking, which may lead to structural failure.[149] This unevenness inside the resin matrix demands a secondary reinforcement to toughen the low fiber density areas of the composite. The published toughening methods can be put into three major categories, namely rubber toughening, block copolymer (BCP) toughening, and inorganic nanofiller toughening.

In order to quantify the effect of toughening, a unified standard must be established. In materials science, critical stress intensity factor and critical strain energy release rate are two major criteria for characterizing the fracture toughness of a common material. The critical stress intensity factor corresponds to the minimum stress intensity at the crack front to propagate an existing crack. The critical strain energy release rate corresponds to the energy needed to develop a unit area of crack surface. There are three modes of fracture in

solid materials, namely opening, in-plane shearing and out-of-plane shearing. The opening fracture mode, or the fracture mode-I, which has a tensile stress normal to the plane of a crack, is commonly used to study the fracture behavior. In our work, mode-I critical stress intensity factor (K_{IC}) and the mode-I critical strain energy release rate (G_{IC}) are chosen to quantify fracture toughness.

Addition of liquid rubber or core-shell rubber

The rubber toughening of epoxy resins has been intensively studied, and the toughening mechanism is well understood.[150-153] Typically, the rubber component is blended into the epoxy resin to create a homogeneous polymer mixture before the addition of the amine component. The increasing crosslink density, as well as the decreasing matrix polarity, due to the step-growth polymerization of epoxy components and amine components, forces the previously miscible rubber molecules to phase-separate and form a rubbery secondary phase (Figure 1.9). The well distributed micron-sized rubbery phase absorbs mechanical energy of impact and crack propagation.[152, 153] However, unlike epoxy, liquid rubber has poor solubility in UP resins, which affects the toughening.[154] To overcome this challenge, two rubber modification strategies are generally adopted.

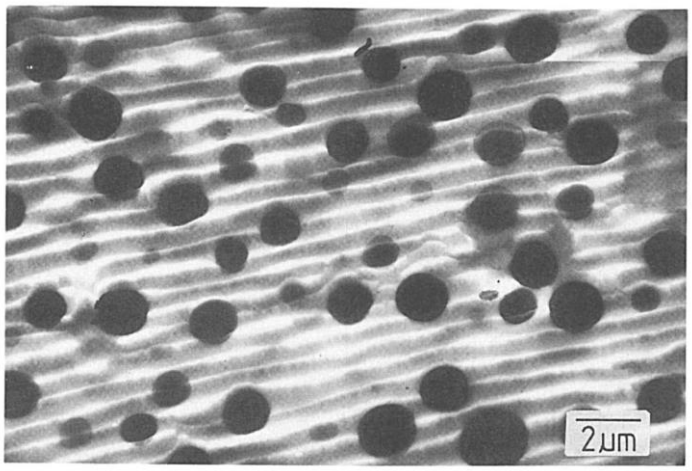

Figure 1.9. TEM image of rubber toughened epoxy sectioning, stained with osmium tetroxide. The micro-sized rubber domains appear darker in the image. Image reprinted from ref. 150 with permission. Copyright © 1993, American Chemical Society.

Some research has been done to modify the terminal group of liquid rubber molecules. Such a method requires the introduction of polar end groups such as diacid anhydride,[154] diacid imide,[155] and isocyanate groups.[156] These polar and reactive terminal groups help the rubber disperse well in the uncured resin and also are able to bond to the UP polymer chains for better particle-matrix adhesion. A significant increase of fracture toughness (100% increase in K_{IC}) was observed as well as a small decrease in modulus (8–10%)[155]. However, because the polymerization-induced phase separation of the rubbery component depends heavily on reaction kinetics, the reproducibility of rubber toughening is problematic.[157] A similar strategy can be applied to VE resins, and liquid rubber toughened VE resins also show decreased modulus and strength.[158-160]

Another approach to incorporate rubber in a UP matrix involves the synthesis of core-shell structured rubber (CSR). CSRs are synthesized through emulsion polymerization. Usually, the reaction happens in the dispersion of core particles, and the polymer generated

in the reaction directly coats the cores. By changing the concentration of monomer, reaction temperature, and agitation speed, the thickness of the polymer layer can be tuned. The resulting CSR has a layered structure with either rubbery core/glassy shell or glassy core/rubbery interlayer/glassy layer configuration.[160-162] The rubbery center or interlayer serves as a fracture energy absorber, and the glassy layer stabilizes the CSR particles in the UP resin. Since the structure of the synthesized CSR is well controlled, the toughening effect remains the same under various curing conditions. The cured resin composite showed a better fracture toughness with an increase in K_{IC} as high as 60% at the cost of a small modulus decrease (4%).[161]

Incorporation of block copolymer

Block copolymer (BCP) toughening has attracted intense interest because it improves the optical transparency of the toughened resin, which could be desirable for polymer coatings.[163] Compared to rubber, BCP tends to form self-assembled nano-sized domains (Figure 1.10) during polymerization-induced phase separation,[166] which yields a better transparency.

Though successful works on BCP toughening of epoxy have been widely reported, publications on BCP modified UP resin are quite scarce. Recent work demonstrated that poly[(ethylene oxide)-*b*-(propylene oxide)-*b*-(ethylene oxide)] block copolymer, or PEO-*b*-PPO-*b*-PEO, enhances the fracture toughness of the UP (40% increase in K_{IC}), but the 50% reduction in modulus severely limited its application.[163] The morphological study on PEO-*b*-PPO-*b*-PEO modified UP resin showed a micro-phase separation of this BCP with PEO blocks anchoring in resin rich domains and PPO blocks separated as the secondary phase.[164] Subsequent research showed that the poor modulus of PEO-*b*-PPO-*b*-PEO

toughened resin can be improved by incorporating cellulose microfibers,[165] or changing the PEO to PPO ratio.[167]

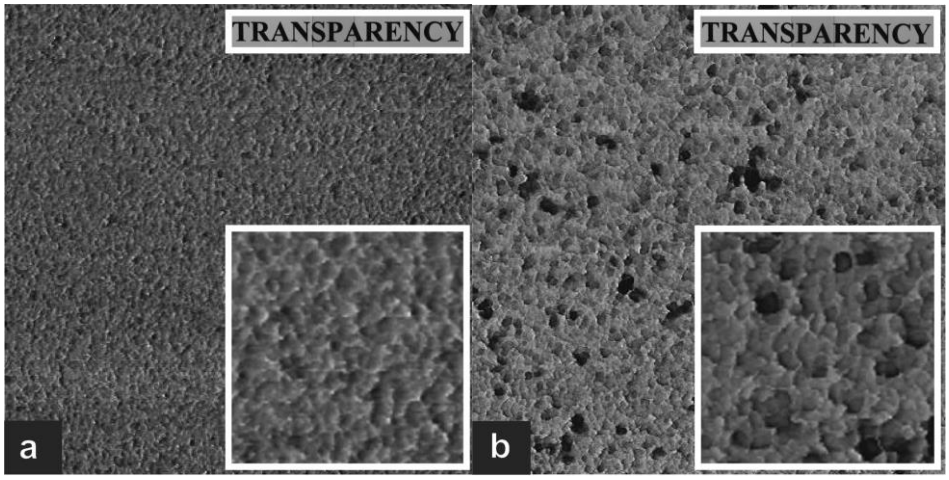

Figure 1.10. AFM phase images (1 μm × 1 μm) of cured neat resin (a) and UP resin containing 5% PEO-*b*-PPO-*b*-PEO BCP (b). The top insets show digital images of 1 mm thickness resin sheets. The bottom insets correspond to 200 nm × 200 nm AFM images. The dark regions show the rubbery domains. Image obtained from ref. 163 with permission. Copyright © 2013, American Chemical Society.

Inorganic nanofiller toughening

UP resin reinforced with inorganic nanofiller shows a better chemical resistance, modulus and impact resistance than resin incorporated with rubber or BCP.[168] Experiments indicated that K_{IC} of UP resin increases by 60% with 1 vol % loading of 37 nm TiO_2 nanoparticles.[169] To facilitate dispersion, functionalization of TiO_2 nanoparticles with 3-(methacryloxy) propyl trimethoxysilane was also studied.[170] Similar work using surface-modified Al_2O_3 nanoparticle reinforcement demonstrated that organosilane treatment not only facilitates dispersion, but the enhanced interfacial adhesion by forming covalent

bonding improves the fracture toughness of the filled UP composite.[171] The toughening mechanism of rigid nanoparticle reinforcement involves crack pinning, crack bifurcation and deflection, and micro cracking.[172-174] The crack pinning effect, which is unique to resin filled with rigid particles,[175] can be explained as follows: the particles beyond the crack front transfer the built up stress deep into the matrix, so the effective stress intensity at the crack front decreases. A higher applied load is needed to propagate such a crack as if the crack front is pinned by particles. Large particles also force the crack to split into two smaller cracks (bifurcation) or change its direction (deflection), which create additional crack surfaces and lower the stress intensity. Since the nanofiller itself concentrates stress inside the composite, small cracks could initiate at one particle-matrix interface and terminate at another. This internal cracking, or craze, absorbs energy and prevents the composite from catastrophic failure.

1.3.3 Graphene material as a promising toughener in unsaturated polyester systems

Compared to other materials, graphene has ultra-high strength and large aspect ratios, which ensures that the toughening effect is significant even at very low loading levels.[176, 177] Ideally, a minimal amount of single-layered graphene additive should be transparent to visible light, rendering graphene a good candidate for resin tougheners. Few-layered graphene, or graphite nano-platelets (GNPs), and graphene oxide materials have shown great toughening effects in epoxy systems,[176-186] with a K_{IC} improvement up to 120% at 0.489 vol % loading.[183] A dramatic increase in anti-fatigue properties (measured in the number of cycles of stretch and release towards failure under certain stress loading) of glass fiber reinforced epoxy resin with graphene oxide nanofiller has also been reported.[182, 185] The increase in glass transition temperature, T_g, shows good bonding between the graphene

sheets and the epoxy matrix, which is also manifested by the enhanced ultimate tensile strength and Young's modulus. A fracture mechanism study indicated that 54% area of a composite fracture surface shows stress whitening (light scattering from the structural defects inside the material), which can be attributed to plastic deformation induced by graphene sheets.[177] This occurs as the graphene sheets deflect and split the crack front, so that more yielding of the resin matrix happens around filler particles. In other literature, the toughening effect was attributed to microcrack initiation[178] and the increased fracture surface area from crack deflection and pinning.[181] Previous results[187] showed that graphene-based materials can toughen a UP resin. The structural similarity between VE and UP resin and the widely accepted toughening mechanisms suggest that graphene-based material could be a universal toughener for improving mechanical properties of UP and VE resins. However, the large aspect ratio of graphene also means it is energetically favorable for the graphene sheets dispersed in a solvent to reaggregate, if there is a surface energy mismatch between graphene and the solvent. Unfortunately, this is the case in graphene/UP resin dispersions since the surface energy of graphene is close to 40 $dyn \cdot cm^{-1}$, which is far above that of styrene (30.7 $dyn \cdot cm^{-1}$).[188] The aggregation of graphene toughener creates resin rich zones, where the crack can propagate freely. To address such difficulties, graphene surface modification should be adopted so that new functional groups can encourage a stronger interface to a resin matrix to counteract the interlayer π-π stacking and van der Waals interactions.

1.4 Thesis outline

This thesis focuses on utilizing GO and its derivatives to toughen thermosetting polymers. The effect of different surface modifications, processing methods, particle-

particle interactions, and fiber composite toughening were studied in detail. The thesis also includes a study of an rGO/polyolefin conductive composite.

Chapters 2 describes GO covalent modifications and mGO characterization. GO treated by unsaturated isocyanate and dodecylamine shows significant toughening effect in a unsaturated polyester resin (UPR) with very low loadings. The detailed mechanical analysis of the mGO resin composites shows mGO toughener can toughen resin without introducing T_g or modulus reduction.

Chapter 3 focuses on the development of a styrene masterbatch process to help disperse mGO into a resin. This masterbatch route significantly reduces mGO aggregation, and it also allows easy dispersion of mGO without sonication treatment. Although fracture toughness of the final products shows only a small dependence of dispersion quality, flexural strength of the composites is better preserved with well dispersed mGO particles.

Chapter 4 is about how the presence of inorganic filler particle would influence the toughening effect brought by incorporating mGO. Common thermosetting resin fillers were studied, and the result suggest that the interference of toughening effect depends on the size of the filler particle aggregates. The conclusion in this chapter shed light on the origin of the mGO toughening effect.

Chapter 5 illustrates how the toughening effect of mGO can be altered by changing the mGO aggregate size. The result from this chapter indicates that the particle-matrix interfacial strength does not affect resin toughening in mGO/UPR system. The maximum achievable toughness improvement in an unsaturated polyester resin is independent of mGO surface chemistry and loading level.

Chapter 6 shows a study about the mGO toughening effect in glass fiber reinforced composites (GFRP). The incorporation of mGO does not improve the interlaminar fracture toughness of the fiber composites due to poor resin-fiber adhesion in all UPR GFRP samples. The interlaminar fracture toughness of UPR GFRP is found to be related to resin ductility, rather than the fracture toughness of unreinforced mGO/resin composites.

Chapter 7 discusses conductive composite made of reduced functionalized GO and polyethylene. The result from this chapter shows the advantage and disadvantage of optimizing the dispersion of graphene sheets in PE by covalent surface modification.

Chapter 2*

Unsaturated Polyester Resin Toughening with Very Low Loadings of GO Derivatives

2.1 Introduction

Thermosets are widely utilized as structural materials, adhesives, coatings or insulating materials in the automotive, aviation, electronics, construction, and packaging industries.[134, 151] Due to the high crosslink density, thermosetting resins are thermally stable, chemically inert, and mechanically stiff. However, despite these advantageous properties, thermosets are brittle and prone to mechanical failure. This limits the application of thermosetting resins in uses where material fracture toughness and anti-fatigue properties are vitally important.[134] Much effort has been put into researching and developing tougheners that can improve the fracture toughness of thermosets, in particular epoxy resins. But for unsaturated polyester resin (UPR), which is a low-cost thermosetting resin with advantageous chemical resistance that requires only mild curing conditions,[136, 163] the toughening results are still far from satisfactory.

It has been reported that elastomeric tougheners (rubber,[154-156] core-shell rubber,[157, 161, 189] block copolymer[190, 164-167]) are capable of toughening UPR. Generally, they function by creating a rubbery secondary phase evenly distributed throughout the resin phase. As the crack propagates, these rubbery particles can absorb extra energy by deforming, debonding,

* This chapter was reproduced from *Polymer* **2017**, *110*, 149 with permission. © Copyright 2017, Elsevier. Mechanical data used in this chapter were collected and processed by Kunwei Liu.

cavitating and deflecting cracks. Although they can significantly increase the fracture toughness of UPR, there are still a few critical drawbacks. Rubber tougheners tend to increase the resin viscosity and therefore make processing more difficult. They also decrease the resin modulus, as well as the glass transition temperature.[154-157, 161, 164-166, 189, 190] Block copolymer (BCP) tougheners are able to partially address deficiencies,[167] but their high loading level and cost make them less economical.

Another category of tougheners is based on rigid particles. UPR reinforced with inorganic nanofillers show better chemical resistance, modulus, and impact resistance than resin modified with rubber or BCP.[191] It has been reported that nanoparticles of TiO_2 and Al_2O_3 can serve as good tougheners in UPR,[169-171] and introducing particle matrix bonding can further improve toughening.[170] Compared to conventional 3D nanoparticles, graphene, a 2D one-atom-thick nanomaterial, has a greater potential to be a good toughener, not only because its high aspect ratio renders it effective at extremely low loading level, but graphene itself possesses excellent mechanical properties. Many studies involving epoxy resins have indicated that graphene/graphite nanoplatelets can improve the fracture toughness with loading levels less than 1%.[176-186, 192] A few publications also show similar phenomena in UPR systems.[187] Although other techniques of graphite exfoliation have been reported, such as direct bulk functionalization,[30] mechanical cleaving,[21] and surfactant-assisted high speed shearing,[23, 25, 193, 194] oxidative exfoliation to obtain graphene oxide (GO) remains one of the most useful ways to obtain single layer GO/reduced-GO derivatives.[29] The chemical reactivity of GO due to oxygen-containing moieties on its surface provides facile functionalization opportunities.

In our research, different methods of GO functionalization were investigated to demonstrate how these can improve the fracture toughness of a UPR. With the knowledge built up in our previous research on epoxy composites,[192] we focused our attention on the particle-matrix bonding and surface compatibility of the GO particles with a UP resin. The study of UPR-based nanocomposites with extremely low loadings of modified GO (0.04 wt.%) showed a significant increase in fracture toughness compared to the neat resin. The dispersibility of modified GO inside the resin was characterized by transmission electron microscopy (TEM) and visible light microscopy (VLM). Without proper surface treatment, GO platelets can form major agglomerates inside the resin, which deteriorates the homogeneity of the composite and induces structural failure. To address this problem, 3-isopropenyl-α,α-dimethylbenzylisocyanate (TMI) and dodecylamine (DDA) modifications were adopted. The TMI modification introduces the possibility of particle/matrix covalent bonding, and the DDA functionalization improves surface compatibility with the resin. Combining both modifiers yielded a product that can be easily dispersed in resin without sonication and gives an even better toughening result. Low cost, due to remarkably low loading levels, combined with better processability, make the GO derivative toughener economically viable. Fractography analysis, using scanning electron microscopy (SEM), unveiled that crack pinning is the major contributing mechanism of resin toughening in these materials.

2.2 Experimental section

Sodium nitrate (ACS grade), potassium permanganate (ACS grade), hydrogen peroxide (30% solution in water, ACS grade), toluene (HPLC grade), triethylamine (99%), and potassium bromide (IR grade) were obtained from Fisher Scientific. *N*, *N*'-

dimethylformamide (99.8%, anhydrous), 3-isopropenyl-α,α-dimethylbenzylisocyanate (TMI isocyanate, 95%), 1,4-diazabicyclo[2.2.2] octane (99%), styrene (99%), cobalt(II) 2-ethylhexanoate solution (65 wt.% in mineral spirits), 4-*tert*-butylcatechol (98%), and 2-butanone peroxide (Luperox DDM-9, 35 wt.% in 2,2,4-trimethyl-1,3-pentanediol diisobutyrate) were purchased from Sigma-Aldrich. Dodecylamine (DDA, 98%) was obtained from Alfa-Aesar, ammonium hydroxide (28–30% in water, ACS grade) and tert-butanol (99%) from Macron, sulfuric acid (98%, ACS grade) and hydrochloric acid (37%, ACS grade) from BDH, and graphite flakes (SP1) from Bay Carbon. Deionized (DI) water with a resistivity of 18 $M\Omega \cdot cm^{-2}$ was produced onsite using a Barnstead purification system. The AROPOL 8422 unsaturated polyester resin was provided by Ashland.

2.2.1 Synthesis of functionalized GO

Synthesis of GO

The method of GO synthesis was adapted from Hummers and Offeman's paper[40] with small modifications. In a typical synthesis, 2.5 g $NaNO_3$ was dissolved in 115 mL concentrated sulfuric acid in an ice bath, and 5 g of graphite was then added to the solution. Under moderate stirring, 5 g $KMnO_4$ was added every 10 min for a total of 15 g. The ice bath was then replaced by a water bath at room temperature to raise the reaction temperature and later absorb excess heat, and the mixture was allowed to react at 35 °C for 1 h. Later, the water bath was removed, and 230 mL of DI water was added under rapid mixing. After stirring for 15 min, the mixture was further diluted to 1 L. The reaction was quenched by adding 30% hydrogen peroxide drop-wise until the effervescence stopped, and the mixture turned light brown. After overnight sedimentation, the supernatant was decanted, and the crude graphite oxide slurry was collected for purification. GO was

washed with 0.1 M hydrochloric acid a few times, followed by 5 days of dialysis (Fisher, 21-152-5 dialysis tubing) against DI water. Purified GO was diluted in DI water, and the pH was adjusted to 9 with ammonium hydroxide. The basic GO dispersion was then sonicated for 1h in a bath sonicator (Branson 3510). The resulting dispersion was centrifuged at 1500 rpm for 10 min to remove poorly oxidized particles before freeze-drying (Freezemobile, SP Scientific).

Synthesis of TMI-functionalized and TMI/dodecylamine-functionalized GO

To synthesize TMI functionalized GO, 300 mg of the dried GO was dispersed in 75 mL anhydrous *N*,*N*-dimethylformamide (DMF) and then bath sonicated for 1 h. The resulting homogenous dispersion was transferred into a 150 mL two-necked round bottom flask and purged under nitrogen flow for 2 h with 300 rpm stirring. After that, 3 mL TMI isocyanate was injected, and the mixture was allowed to react at 40 °C for 24 h under nitrogen. The reaction was quenched by adding 225 mL dry toluene, and the resulting mixture was then centrifuged at 3000 rpm for 15 min. The precipitate obtained after centrifugation was washed 3 times with toluene and twice with *tert*-butanol, followed by freeze-drying to obtain the final product (TMI-GO).

For the TMI/dodecylamine functionalization, GO was first treated with a larger amount of TMI (2 mL per 100 mg GO) at 60 °C with 1,4-diazabicyclo[2.2.2]octane (5 mg per 100 mg GO) added as the catalyst. The resulting purified and freeze-dried TMI-functionalized GO was redispersed in DMF in the same way as described before (2 mg/mL). The dodecylamine was then added (4 mg per 1 mg TMI-GO), and the reaction was kept at 70 °C for 24 h while stirring at 300 rpm. The reaction was terminated by pouring the mixture into DI water, at which point the functionalized GO flocculated immediately. The crude product

was collected by centrifugation and purified by 4 washes in dry ethanol and 2 washes in DI water. The purified product (TMI-DDA-GO) was freeze dried to obtain it in powder form.

2.2.2 Preparation of resin samples

The stock AROPOL 8422 UPR was first diluted to 55 wt.% by adding styrene monomer. Then, 40 mg 4-*tert*-butylcatechol (inhibitor) and 100 mg cobalt(II) 2-ethylhexanoate solution (promoter) were added per 100 g of resin. To prepare the non-sonicated (NS) composite sample, a certain amount of TMI-DDA-GO was added to AROPOL 8422 UP resin, and the mixture was stirred with a magnetic stir bar at the maximum speed of the stir plate for 3 h to generate a homogenous dispersion. Non-sonicated GO and TMI-GO resin dispersions were also prepared, but no composite sample was made due to their poor dispersion stability. For the other samples, 2 h of probe sonication (Misonix S-4000, 4 s pulse, 2 s pause, 35% amplitude) together with mechanical stirring was used to generate the dispersion. The resin dispersions were initiated with 1.25 g 2-butanone peroxide (Luperox DDM-9) per 100 g and allowed to react for 10 min with mechanical stirring at a moderate speed, followed by 10 min vacuum de-gasing. After the resin was poured into the mold, it was left at room temperature for 24 h to allow it to gel before placing it into an oven for curing. The curing procedure required heating the fully gelled resin plaque at 70 °C for 3 h and at 120 °C for an additional 3 h. The resin plaques were then cut into specimens for mechanical tests (Figure 2.1).

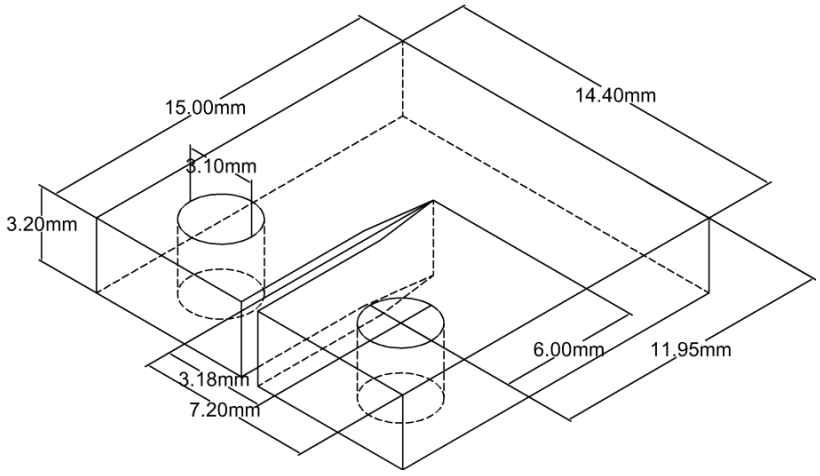

Figure 2.1. The dimensions of the compact tension (CT) specimen.

2.2.3 Characterization

Infrared (IR) spectroscopy was performed on a Magna-FTIR 760 spectrometer (Nicolet) using KBr pellets of GO and modified GO samples. Powder X-ray diffraction (XRD) experiments were performed with a PANalytical X'Pert Pro diffractometer. This instrument utilized a Co anode (Kα radiation, 1.79 Å) and X'celerator detector, and it was operated at 45 kV accelerating voltage with a 40 mA emission current. Thermogravimetric analysis (TGA) was carried out under a nitrogen atmosphere using a Netzsch STA 409 Simultaneous TGA-DSC with ~2.5 mg of sample loaded in an alumina crucible. The ramp rate was 10 °C/min, and the heating range was 25 °C to 600 °C. A JEOL 6700 field emission scanning electron microscope (SEM) mounted with a tungsten filament source was used for imaging. SEM images were taken using an acceleration voltage of 5 kV. All SEM samples were coated with 50 Å Pt prior to imaging. A FEI Tecnai T12 transmission electron microscope (TEM) with a LaB_6 source operating at an acceleration voltage of 120 kV was used to obtain TEM micrographs. GO and modified GO samples were first dispersed in ethanol and then dip coated onto lacey carbon grids (Ted Pella lnc.). The resin

composite TEM specimens were made using a Leica EM UC6 Ultramicrotome. The visible light microscopy (VLM) images were taken on a Nikon Eclipse Ti-e Optical Microscope, using 1.5 mm thick fully cured resin plates as specimens.

Flexural modulus and ultimate flexural strength were determined using an RSA-G2 solids analyzer (TA Instruments) according to ASTM D790-10.[195] The three-point bend experiment was performed with a span-to-thickness ratio of 16:1 and a crosshead rate of 1 $mm \cdot min^{-1}$ (0.01 min^{-1} strain rate). The fracture toughness test was performed using a compact tension (CT) method on an Instron 1011 single column system equipped with a 5 kN load cell per ASTM D5045-99.[196] After having been pre-cracked by fresh razor blade tapping, all specimens were pulled at 10 $mm \cdot min^{-1}$ until complete failure. In a typical test, five three-point bend and at least ten CT specimens were tested, and the average was reported along with the standard deviation.

The critical stress intensity factor (K_{IC}) was calculated using equation 2.1, and the critical strain energy release rate (G_{IC}) was calculated via equation 2.2.[196]

$$K_{IC} = \frac{P_C}{B\sqrt{W}} \times \frac{\left(2+\frac{a}{W}\right)\left[0.886+4.64\frac{a}{W}-13.22\left(\frac{a}{W}\right)^2+14.72\left(\frac{a}{W}\right)^3-5.6\left(\frac{a}{W}\right)^4\right]}{\left(1-\frac{a}{W}\right)^{\frac{3}{2}}} \tag{2.1}$$

$$G_{IC} = K_{IC}^2\left(\frac{1-\upsilon^2}{E}\right) \tag{2.2}$$

Here, P_C is the critical applied load, B is the specimen thickness, W is the specimen width; a is the crack length, E is the flexural modulus, and υ is the Poisson's ratio of UPR, which is taken to be 0.39.

2.3 Results and discussion

2.3.1 Chemical modifications of GO

The successful functionalization of GO with isocyanate/alkylamine was confirmed by infrared spectroscopy (Figure 2.2). The spectrum of GO shows a broad band around 3400 cm^{-1} corresponding to O–H stretching vibrations of hydrogen-bonded surface hydroxyl groups, and other peaks corresponding to the carboxylate C=O stretch at 1721 cm^{-1}, surface adsorbed water and a graphitic skeleton stretch at 1623 cm^{-1},[197] a C–OH bending absorption at 1399 cm^{-1}, and a C–O stretch at 1072 cm^{-1}.[198] After TMI functionalization, new absorption peaks appear at 2920 and 2850 cm^{-1}, which correspond to antisymmetric and symmetric C–H stretching vibrations and originate from the three methyl groups in the TMI molecule. Also, the urethane C=O stretch peak at 1649 cm^{-1} indicates that TMI is bonded to hydroxyl groups on the GO plane. The modification by dodecylamine introduces absorption peaks from strong methylene stretches at 2922 and 2850 cm^{-1}, which are typical for long alkyl chains. The peaks at 1466 and 723 cm^{-1} can be assigned as methylene scissoring and rocking bands, respectively. The amide N–H stretching peak at 1583 cm^{-1} together with the absence of a carboxylate peak indicates successful bonding of amine to GO.[199]

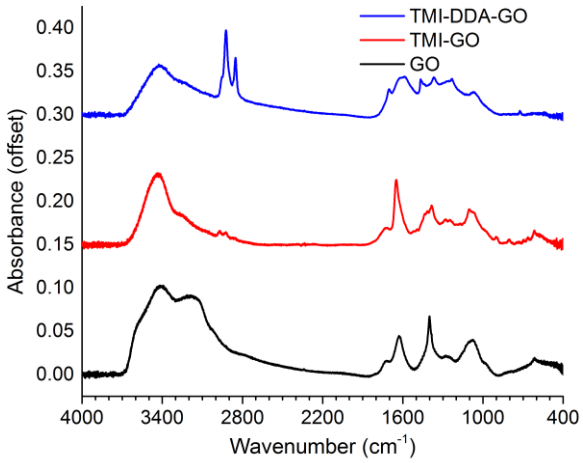

Figure 2.2. Infrared spectra of pristine and modified GO samples.

The interlayer distance between two GO sheets correlates with the readiness for exfoliation inside the resin. Thus, a key goal of this research is to increase the interlayer distance and reduce the interlayer attraction. Figure 2.3 shows powder X-ray diffraction patterns of modified GO materials. It is evident that all functionalization methods increase the layer-to-layer distance of GO, which is 8.1 Å. TMI modification increases the *d*-spacing between GO layers only slightly to 9.0 Å, possibly due to the low reactivity of TMI towards the GO surface. A significant interlayer expansion (15 Å) was observed in dodecylamine-treated TMI-GO, which can be attributed to the bulky nature of dodecyl group as well as a strong affinity between amine and GO.[200] The broad peak around 23.2° 2θ in the XRD pattern of TMI-DDA-GO corresponds to an interlayer distance of 4.5 Å, which is the commonly observed most intense peak in the pattern of chemically reduced graphene oxide. This result indicates that minor reduction of GO also occurs during the reaction, consistent with an observed color change of mGO from brown to black after this modification step.[200]

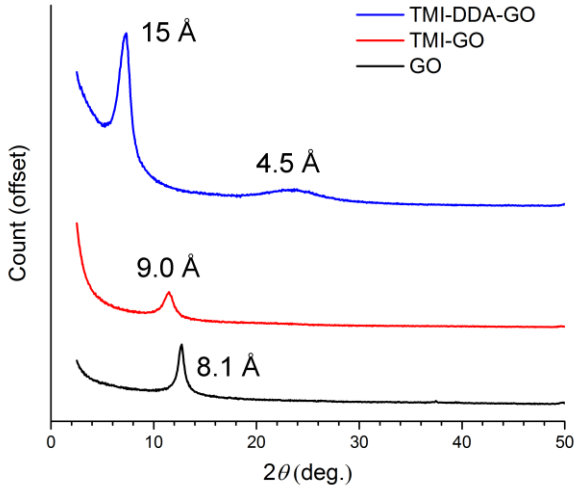

Figure 2.3. X-ray diffraction patterns of pristine and modified GO (Co Kα source).

To estimate the density of functional groups on GO, X-ray photoelectron spectroscopy (XPS) was used to analyze the elemental composition of pristine and modified GO (Figure 2.4). We assumed that the N in GO was present as an ammonium salt that could be removed during isocyanate functionalization. Consequently, the N detected in TMI-GO was assumed to originate solely from TMI moieties. Thus, per 100 mol of non-hydrogen atoms in TMI-GO, there are 1.12 mol of TMI moieties, which contribute 14.6 mol C and 1.12 mol O; the remaining 57.2 mol C and 25.6 mol O are attributed to the GO backbone. The C:O ratio of GO in TMI-GO was calculated to be 2.23, which is the same as the C:O ratio measured in pristine GO (2.23). Assuming GO is completely exfoliated, and it has defect-free graphene sheets, we obtained a TMI function-group density of 1 per 25.5 C6 rings. To estimate the density of dodecyl groups, we assumed that TMI-GO loses neither C nor N during the dodecylamine (DDA) modification. This gives a composition of TMI-DDA-GO (per 100 mol non-hydrogen atoms, sulfur atoms ignored in calculation) as follows: GO: (38.2 mol C, 17.1 mol O), TMI: (9.72 mol C, 0.748 mol O, 0.748 mol N), and DDA: (34.7

mol C, 2.89 mol N). The sum of all elements yields 82.6 mol C, 3.64 mol N, and 17.8 mol O. The fact that less O was observed by XPS (13.71 atom%) can be explained as a consequence of the reduction of GO during dodecylamine functionalization, which is consistent with the XRD results (Figure 2.3) and the observed color change from brown to black. Therefore, we estimated the density of dodecyl moieties to be 1 per 6.60 C6 rings.

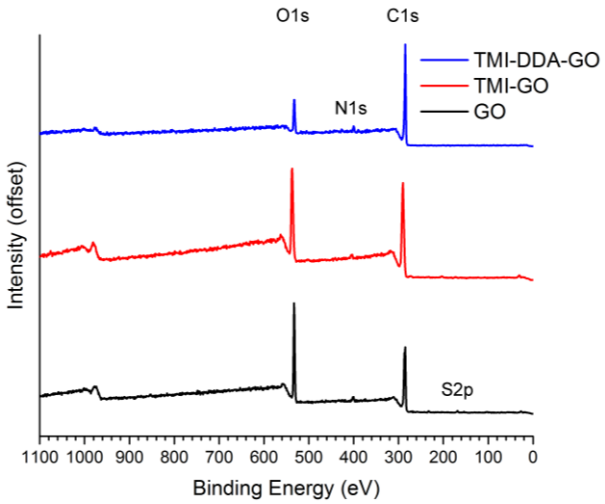

	GO	TMI-GO	TMI-DDA-GO
C	66.62	71.74	82.65
O	29.82	26.70	13.71
N	2.72	1.12	3.64
S	0.84	0.44	<0.1

Figure 2.4 XPS data of pristine and modified GO (top), and corresponding elemental compositions in atom% (excluding H atoms) from the XPS analyses (bottom).

One concern of using GO-based nanofillers is their thermal stability. Due to the thermodynamically unstable nature of GO, the rapid decomposition, even explosion, of

GO can occur when it experiences temperatures above 200 °C.[201] Figure 2.5 shows the TGA data of GO and modified GO samples. The weight loss before 120 °C is caused mainly by losing surface-adsorbed water,[201] thus all TGA data were normalized to show the weight change beyond this point. The data indicate that TMI modification introduces only a limited quantity of functional groups on the GO surface. The rapid mass loss around 210 °C for TMI-GO corresponds to decomposition of unreacted functionalities on GO. Upon treatment with dodecylamine, more oxygen containing groups are converted so the mass loss of TMI-DDA-GO appears to be more gradual between 200 °C and 500 °C. The lower residual mass also suggests a high density of DDA functional groups in TMI-DDA-GO.

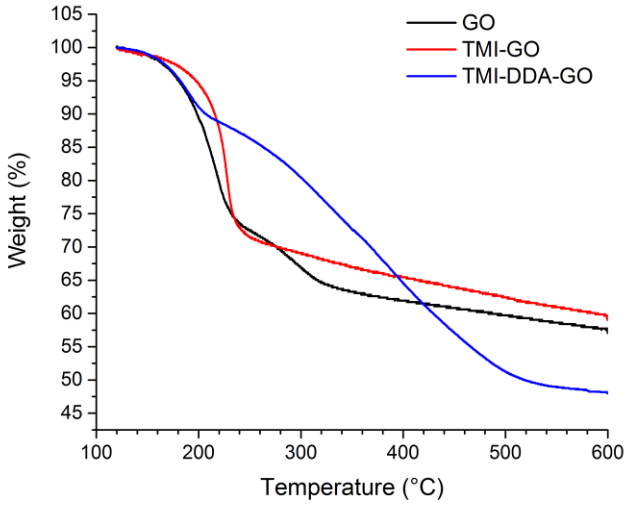

Figure 2.5. Thermogravimetric analysis of modified GO. Weight normalized to 100% at 120 °C.

The TEM and VLM images (Figure 2.6) reveal that the modified GO samples are predominately multilayered. Depending on the surface compatibility towards UPR, these

GO-based tougheners are present as less-stacked aggregates (dark lines or flakes embedded in brighter resin matrix), which are observed in a TMI-DDA-GO resin composite (Figure 2.6b), or many-layered aggregates (large, high contrast, and irregular dark agglomerates), like what is shown in GO (Figure 2.6h) or TMI-GO loaded UPR (Figure 2.6e). According to TEM micrographs, these GO aggregates are typically oblong; they are several hundred nanometers to a few micrometers long and a few hundred nanometers thick. The macroscopic dispersibility of the GO-based materials can be better discerned by optical microscopy (Figure 2.6 c, f, i) because well dispersed monolayers or few-layer graphene particles give minimal contrast in such circumstances. As shown in Figure 2.6, TMI-DDA-GO forms small, loose clusters (gray spots) inside the resin; in contrast, TMI-GO appears as dark spots with irregular shapes and various sizes, which means TMI-GO has a higher tendency to aggregate than TMI-DDA-GO. GO, however, does not exfoliate well in UPR, and its macroscopic stacks are present as large particles with distinct boundaries. This difference has significance in composite processing since greater effort is required for dispersing the nanoparticles into the polymer, and poor dispersion results in reduced mechanical properties.

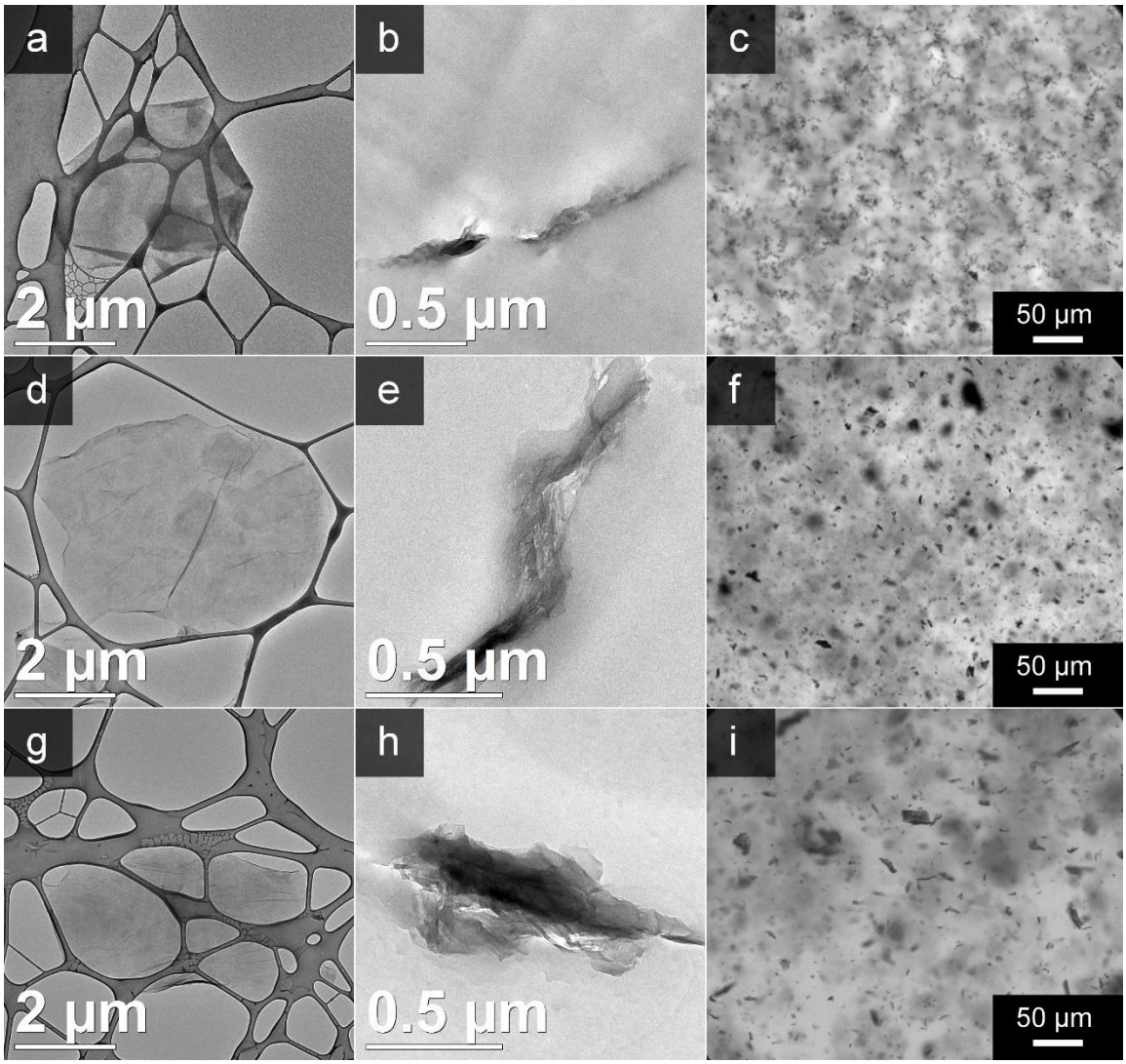

Figure 2.6 TEM and VLM micrographs of TMI-DDA-GO (a,b,c), TMI-GO (d,e,f), and GO (g,h,i) in ethanol dispersion (a,d,g) and in the resin composite (TEM: b,e,h; VLM: c,f,i).

2.3.2 Mechanical Properties of Graphene-toughened UPR

To evaluate the toughening effect of GO-based nanoparticles at very low loading levels, fracture toughness of corresponding UPR composites was tested. In this work, values of the mode-I critical stress intensity factor (K_{IC}) were measured on compact tension specimens, and the critical strain energy release rate (G_{IC}) was calculated using K_{IC} and the flexural modulus determined in a three-point bending test (eq. 2). Figure 2.7a, b shows the

comparison of K_{IC} and G_{IC} for the neat resin and the resin loaded with different modified GO toughenners. The successful toughening of the UPR is well illustrated by a 12–25% increase in K_{IC} and an 18–55% improvement in G_{IC} with only 0.02–0.08 wt.% mGO. Except for pristine GO, the other GO toughenners have an optimal loading level of 0.04 wt.% based on K_{IC}. The rather small increase in K_{IC} in GO-loaded resin suggests that at such low loading levels, good dispersion is of key importance. Comparisons of the toughening effect between TMI-GO/GO and TMI-DDA-GO/TMI-GO indicate that better particle-matrix bonding and surface affinity also help to boost the toughening effect by stabilizing particles and preventing macroscopic aggregation. Better dispersion means an increased number of GO platelets inside the resin, so the amount of large aggregates decreases (Figure 2.6 c, f, i) and the roughness of crack surface increases (Figure 2.9 c, e, g) in the order GO, TMI-GO and TMI-DDA-GO. The non-sonicated TMI-DDA-GO sample shows an even higher toughening effect, which means that the advantage of TMI/dodecylamine functionalization lies not only in the ease of composite processing, but also in the performance of the final product. Sonication better homogenizes the dispersion, but it also decreases the size of GO aggregates (Figure 2.6b, c). A minor reduction in ultimate strength was observed at the loading levels studied, which can be explained as nanoparticles acting as stress concentrators and structural defects that facilitate the initiation of cracks. This effect becomes more obvious in samples with poorly dispersed particles (eg. pristine GO, Figure 2.7d) than in more uniform composites. Some fluctuation in flexural modulus can be attributed to the counteracting factors of the ability of graphene to inhibit crosslinking, which decreases the modulus, and to act as a rigid filler, which can increase the modulus.

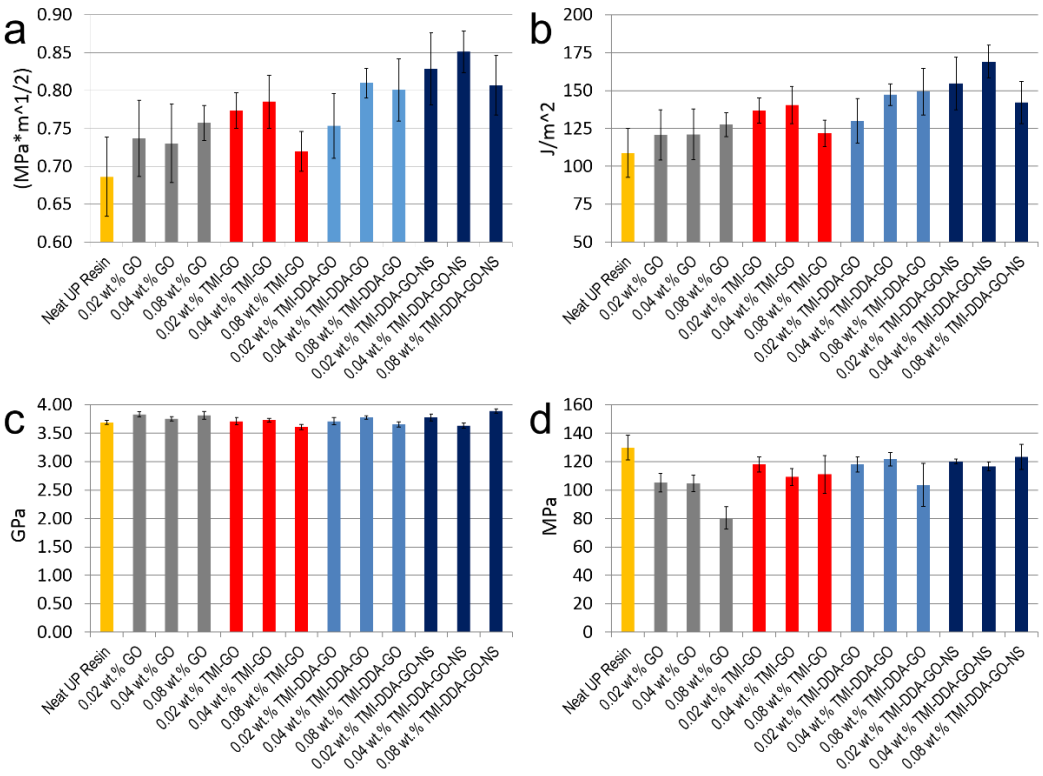

Figure 2.7 Mechanical properties of UPR loaded with pristine and modified GO. "NS" denotes non-sonciated samples. (a) K_{IC}, (b) G_{IC}, (c) flexural modulus, and (d) flexural strength.

2.3.3 Fractography Analysis

According to the speed of crack propagation, the fracture surface of a failed compact tension specimen can be divided into two regions: a near precrack region and a fast propagation region (Figure 2.8). The near precrack region has a slow propagation rate due to the gradual stress build-up behind the precrack (re-initiation). Neat resin shows some plastic deformation as thin resin pieces hanging on the “cliffs” (Figure 2.9a), but beyond this region, all different crack surfaces quickly join the main crack plane (Figure 2.9b). In the modified GO filled resin, a rougher surface with many protrusions and pits is typically

observed as well as a larger area of slow propagation. This can be explained as a result of rigid GO particles pin the crack front and stopping the crack from growing.[153, 202-204] Also, a comparison between near precrack regions of different samples suggests that composites with better dispersed GO show rougher near-precrack regions. Pristine GO composite sample also shows some pulled-out GO platelets on its fracture surface (Figure 2.9c, d), which suggests a weak particle-matrix interaction.

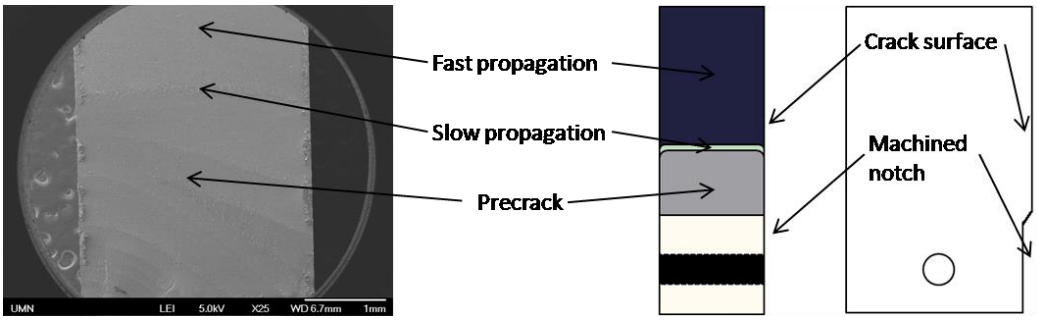

Figure 2.8. Definition of different regions on the crack surface. (a) Low magnification SEM image of a failed CT specimen; (b) a schematic of the crack surface.

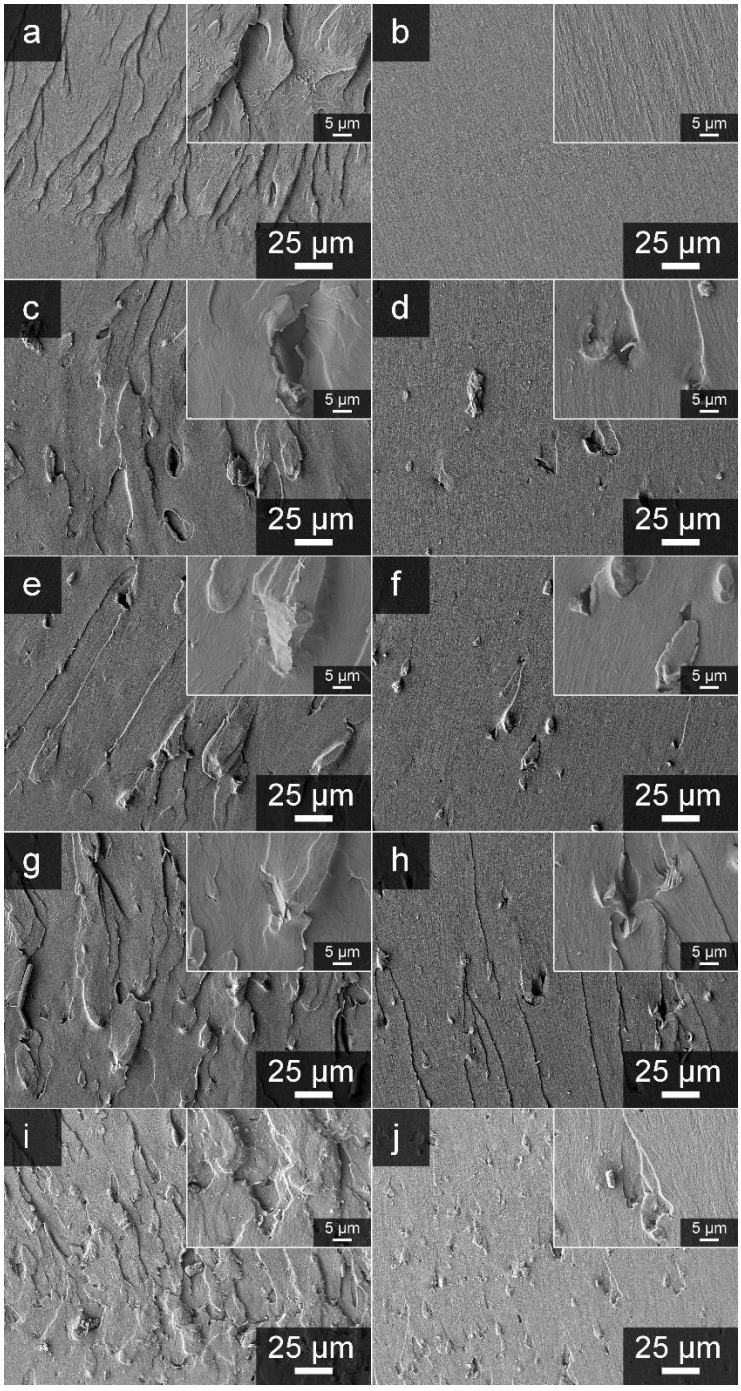

Figure 2.9 SEM fractographs of failed compact tension samples. Near precrack (a, c, e, g. i) and far beyond precrack (b, d, f, h, j) images taken from neat UPR (a, b), GO/UPR (c, d), TMI-GO/UPR (e, f), TMI-DDA-GO/UPR (g, h), and non-sonicated TMI-DDA-GO/UPR (i, j). All samples except the neat resin have 0.04 wt.% GO loading. Insets show higher magnification images of sample specimens. The nominal propagation direction for all fracture surfaces is from the bottom to the top.

In the region immediately after the near-precrack zone, a relatively even main crack plane forms. The dynamic cracking process is unstoppable in such a brittle matrix, leaving a more regular fracture surface with tadpole shaped features on it. The "heads" of these features are the places where the GO aggregates were located.[203] As the crack propagates, GO particles retard the crack, forcing it to go around the particle and rejoin the main plane afterwards. This perturbation causes the split crack planes to travel at an angle with each other, so an edge forms after the pinning point. Due to this edge effect, these events can be identified as white lines parallel to the crack propagation direction in the SEM images. Also, the crack may change its direction when it meets a GO sheet but is unable to penetrate it. The deflected crack then leaves some irregular crack edges around the GO particles, which can be seen as the irregular curves in the SEM images (Figure 2.9). These events create additional crack surfaces, which in turn increases the energy required to propagate the crack. Like the slow propagation regions, the fast propagation regions show more events and rougher surface with better dispersed particles.

Fractography analysis indicates that the main toughening mechanisms of modified GO in UPR are crack pining and crack deflection, which is consistent with the previous research on the rigid particle filled resin systems.[169, 170] The size difference between GO sheets (Figure 2.6) and the surface features (Figure 2.9) indicates GO particles interact with the crack in the form of small aggregates. The crack surface changes with varying GO content (Figure 2.10). Estimated from the fast propagation region, the number of toughening events increases with increasing GO loading. But significant coalescence of these events can be observed in the slow propagation region at higher GO content. The coalescence of toughening events produces less plastic fracture (judging from the plastic

deformation lines between pinning points), thus decreases the toughening effect at 0.08 wt.% GO loading.

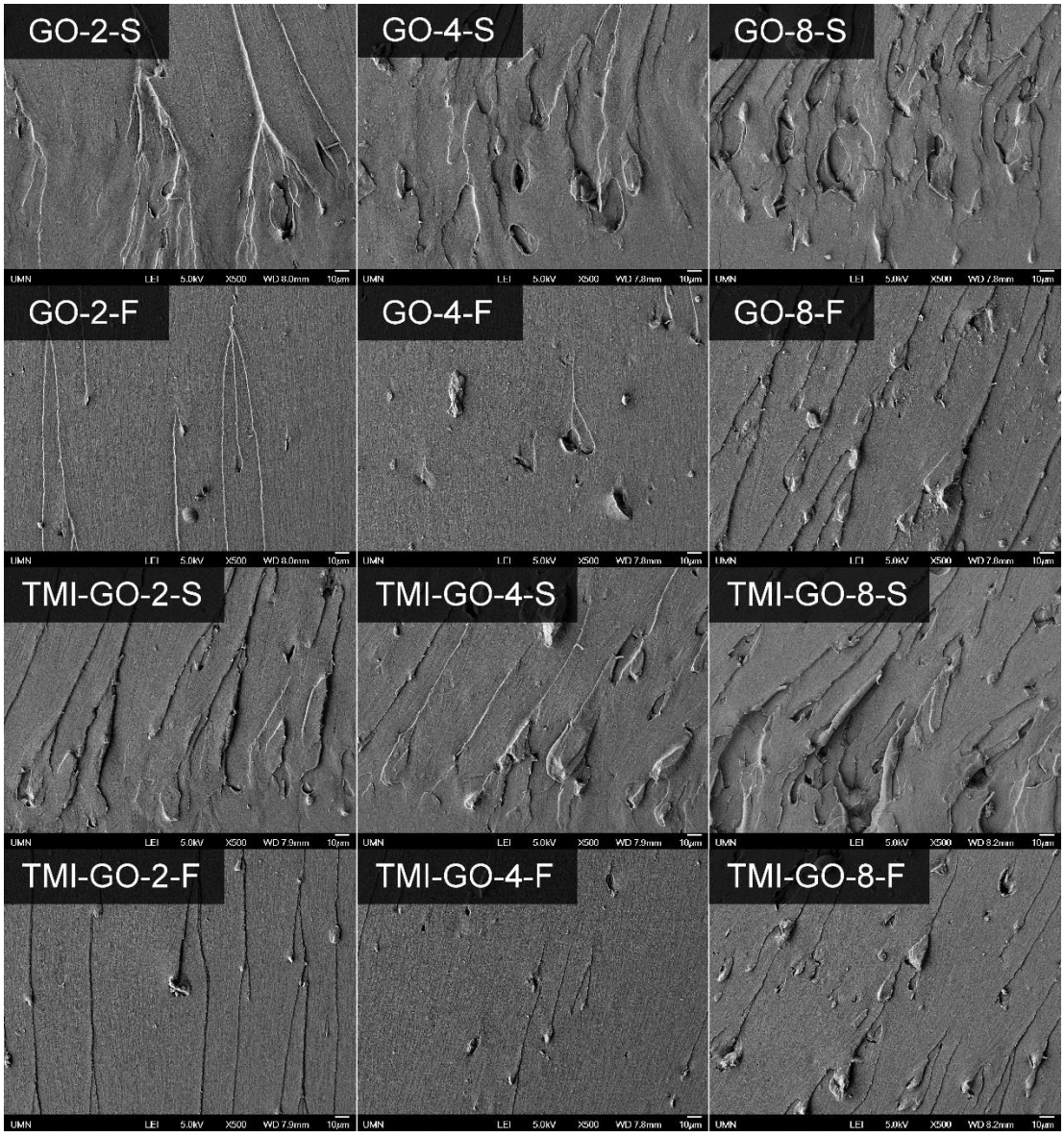

Figure 2.10. Additional fractographs of resin/GO or resin/mGO composites with different particle loading levels and in different regions of the crack surface. All samples are labeled as "**Toughener**-0.0**X** wt.%-**S**low propagation/**F**ast propagation." "NS" refers to non-sonicated samples.

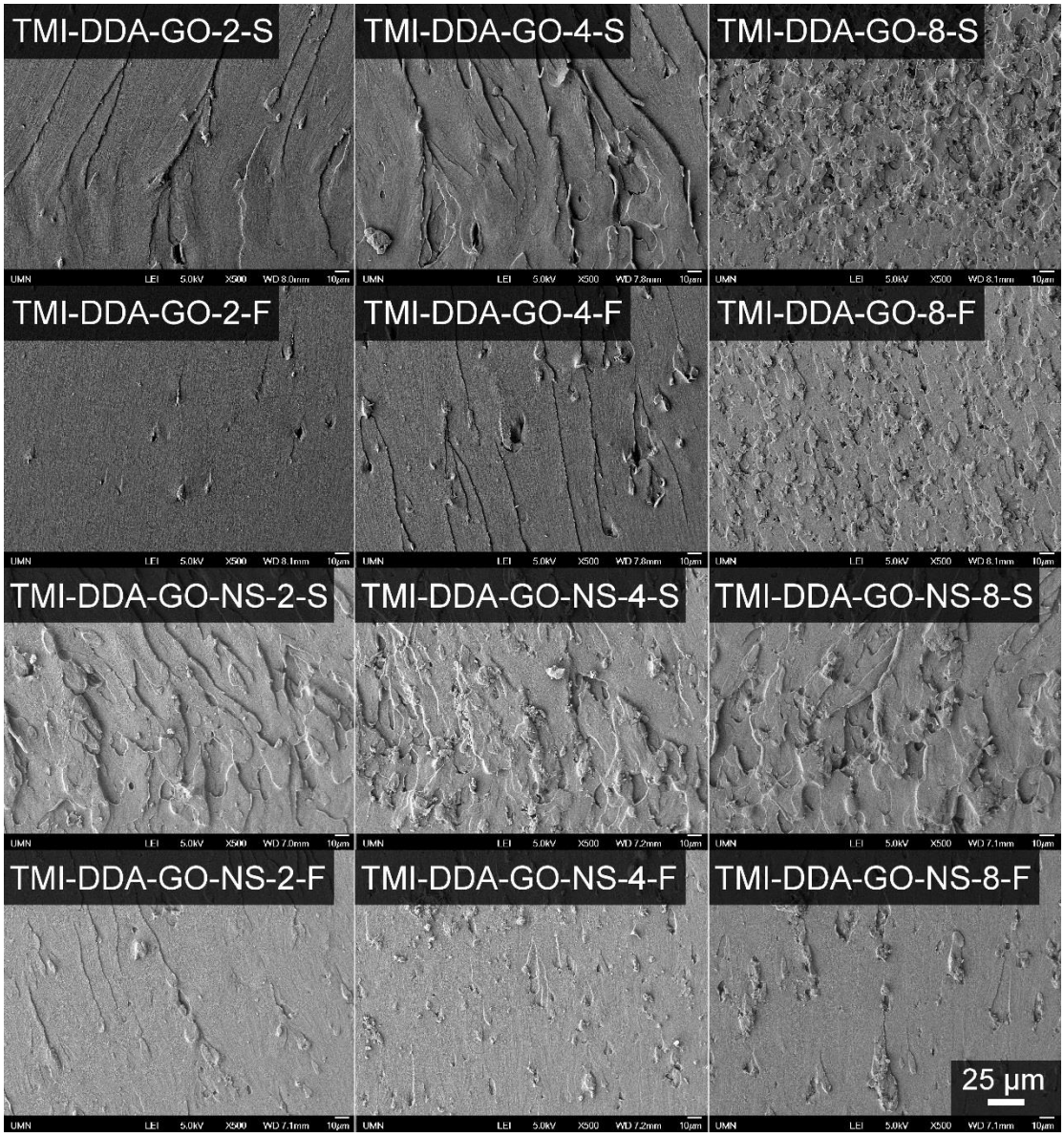

Figure 2.10. Continued.

2.4 Conclusion

Our research demonstrates that GO and its appropriately functionalized derivatives are promising materials for toughening of unsaturated polyesters. This type of nano-toughener is able to toughen UPR (55% increase in G_{1C}) at a very low loading level around 0.04 wt.%, which makes it economically viable in the cost-sensitive UPR market. Chemical modifications studied in this work improve the toughening effect by enhancing particle-

matrix bonding and surface compatibility. More importantly, the TMI/dodecylamine functionalization enables easy dispersion of GO into the resin with simple mechanical mixing that helps overcome the common processing difficulties of incorporating 2-D nanomaterials.

The study of the toughening mechanism indicates that the GO-based tougheners, in the form of small aggregates, work mainly by pinning the crack. Reducing the size of the aggregates by probe sonication results in fewer effective toughening events. On the other hand, if particles are too highly aggregated, this causes a deterioration of the composite properties as it introduces large structural defects. The optimal loading level is around 0.04 wt.%, and a small reduction of the toughening effect (K_{IC}) is observed by increasing the loading beyond the optimum. This phenomenon can be explained as resulting from the coalescence of toughening events, which facilitates the crack propagation.

Chapter 3*

Modified-Graphene-Oxide-Containing Styrene Masterbatches for Thermosets

3.1 Introduction

Synthetic polymers are some of the most extensively used materials in modern society due to their unparalleled combination of light weight, low cost, and relative ease of processing. However, it is very hard to produce polymers that have high strength, modulus, and toughness at the same time. Thus, a nanoscale, secondary phase is often introduced to reinforce the polymer matrix.[205, 206] The resulting material is referred to as a polymer nanocomposite. Among different types of composites, graphene–polymer composites have attracted enormous attention among researchers because they can possess good thermal and electrical conductivity,[207] gas barrier properties,[207] and thermomechanical properties.[13, 122] However, the performance of graphene nanocomposites is highly dependent on the homogeneity of the dispersion.[205] Poorly dispersed nanomaterials can have adverse effects on the strength of the composite because the nanomaterials can function as structural defects.[208-210] If the dispersibility of nanomaterials is poor, a higher loading of graphene nanomaterials may be needed to achieve certain desired physical properties, which can increase the production costs.

* This chapter was reproduced from *Ind. Eng. Chem. Res.* ***2017****, 56, 11443 with permission*. © Copyright 2017, American Chemical Society. Mechanical data used in this chapter were collected and processed by Kunwei Liu.

A good dispersion of nanomaterials in polymer matrices is difficult to obtain. On one hand, nanomaterials tend to agglomerate due to their high surface energy.[205, 211] On the other hand, unlike protic solvents, polymer matrices lack the ability to stabilize nanoparticles via repulsive electric forces between particles.[212] This is particularly problematic for graphene-based materials because of their high aspect ratios. To overcome this difficulty, researchers have explored a wide range of covalent and noncovalent surface modification techniques.[40, 41, 49, 68, 213]

In spite of these challenges, there are a few methods suitable to produce graphene or graphene oxide (GO) polymer nanocomposites with good dispersion quality. For thermoplastics, solvent casting and melt mixing methods both produce composites with very evenly distributed nanofiller.[214-218] However, these methods are not applicable for thermosets because they either leave residual solvent that could be detrimental to the mechanical properties of the final product,[207] or cause irreversible hardening (curing) of the polymer matrix. In-situ polymerization methods can also produce high quality composites. For thermosetting resins, in-situ polymerization is the only viable option. This method requires dispersing graphene or its derivatives into resin before curing.

Typically, when graphene nanosheets are added to a low-viscosity resin prepolymer, the low viscosity does not provide high enough shear stress during simple mechanical mixing to break down graphene aggregates. Better dispersion of nanofillers in thermosets is possible by sonication[206] or three-roll milling.[219] However, sonicating nanomaterials in polymers is difficult and expensive to conduct on a large scale. Three-roll milling provides strong shear forces and a good dissipation of heat, but it causes a rapid loss of volatiles, which could be problematic. Strong interactions between graphene or GO sheets are a

reason that even with powerful dispersing techniques it remains difficult to exfoliate dry products in a resin.

Previous research indicates that graphene oxide derivatives can toughen thermosets at very low loading levels.[192, 220-225] For example, 0.04 wt.% isocyanate/dodecylamine modified GO raised the fracture energy of UP resin by 55%;[220] however, freeze-drying and probe sonication were used to achieve a good dispersion. These two techniques are costly and energy consuming, unfavorable for processing materials at a very large volume. Thus, it is imperative to develop new processes that avoid freeze-drying during GO preparation and probe sonication during resin formulation while keeping the GO sheets well dispersed in a resin phase.

In this research, we have created a scalable method to prepare styrene monomer masterbatches of modified graphene oxide for the fabrication of unsaturated polyester (UP) resin and vinyl ester (VE) resin composites. The method features a few simple solvent-exchange steps with centrifugation at moderate speed for separation. The resulting styrene masterbatch contains about 1 wt.% modified GO, and it can be readily incorporated into UP or VE resins with simple mechanical mixing. The masterbatch concentration is chosen to be around 1% to keep the viscosity low enough for the masterbatch to be pourable. Optical microscopy and mechanical properties of resin nanocomposites are the main criteria for assessing the quality of dispersions obtained by different processing methods. The study shows that composites made with a masterbatch containing modified GO in styrene exhibit similar fracture toughness improvements and better flexural strength, compared to composites made with freeze-dried or oven-dried powders of modified GO.

3.2 Experimental Procedures

Materials. Styrene (99%), cobalt(II) 2-ethylhexanoate solution (65 wt.% in mineral spirits), 4-*tert*-butylcatechol (98%), and 2-butanone peroxide (Luperox DDM-9, 35 wt.% in 2,2,4-trimethyl-1,3-pentanediol diisobutyrate) were purchased from Sigma-Aldrich. Dodecylamine (98%) was obtained from Alfa-Aesar, *tert*-butanol (99%) from Macron, and graphene oxide (GO) slurry (2.88 wt.% in water, C:O = 2.4 by XPS as reported by Graphenea) from Graphenea. Deionized (DI) water with a resistivity of 18 $M\Omega \cdot cm^{-2}$ was produced onsite using a Barnstead purification system. The AROPOL 8422 unsaturated polyester resin and Hetron 922L-25 vinyl ester resin were produced by Ashland Inc.

3.2.1 Synthesis and workup of modified GO

GO slurry was diluted to 4 mg/mL with DI water, and the pH of the dispersion was adjusted to 9 using 4% aqueous sodium hydroxide solution. After mechanical mixing for 15 min, the aqueous GO dispersion was sonicated in a bath sonicator (Branson 3800) for 30 min. One part by volume of the resulting GO dispersion was then rapidly mixed with two parts by volume of a solution containing 6 g/L dodecylamine in ethanol. The mixture was heated to 70 ˚C and allowed to react for 24 h under stirring. The reaction mixture was then centrifuged at 3000 rpm for 15 min to collect the sediment. The crude product was washed four times with ethanol and three times with styrene by mixing and centrifugation to obtain the final product. Purified dodecyl-GO was redispersed in styrene at approximately 1 wt.% by sonicating for 30 min in a bath sonicator to prepare the styrene masterbatch (SMB). For comparison, purified dodecyl-GO was also oven-dried at 70 ˚C (OD) or freeze-dried at room temperature after washing with *tert*-butanol (FD) to obtain

the corresponding dry form.

3.2.2 Preparation of resin composite

AROPOL 8422 UP resin containing 45% styrene was prepared by diluting stock resin with styrene. To 100 g diluted resin, 40 mg of 4-*tert*-butylcatechol inhibitor and 100 mg of 65% cobalt(II) 2-ethylhexanoate promoter in a solution of mineral spirits were added. Hetron 922L-25 VE resin was purchased with promotor and inhibitor already added. For OD and FD samples, the desired amount of dry product was directly added to the formulated resin. For SMB samples, the amount of styrene added for resin dilution was adjusted accordingly to account for the extra styrene present in the masterbatch. All resin samples were shear mixed (Eurostar power-b, IKA) in 75 g-batches with a 1" Cowles blade at 2000 rpm for 15 min to obtain the dispersions. For comparison, a sample of SMB resin dispersion was also probe sonicated (Misonix S-4000, 4 s pulse, 2 s pause, 35% amplitude) for 1 h, which is denoted as SMB-S. Due to the extremely low loading levels of mGO, all UP resin dispersions have very similar viscosity values around 0.13 Pa·s. All resin dispersions (including VE dispersions) were subsequently initiated with 1.25 g 2-butanone peroxide (Luperox DDM-9) initiator per 100 g resin and allowed to react for 10 min with magnetic stirring at a moderate speed, followed by 10 min de-gasing in vacuum. The degassed, initiated resin was poured into a mold made from two 10 mm thick, 200 × 200 mm glass plates separated by a 3 mm thick rubber spacer. A 1.5 mm spacer was used to prepare samples for the three-point bending test and optical microscopy. The molded resin was cured at room temperature for 24 h before post-curing. The post-curing procedure included 3 h of heating at 70 °C and 3 h of heating at 120 °C. The fully cured resin plaques were milled into specimens according to ASTM D790-10 and ASTM D5045-99. A

summary of the different processes and corresponding sample designations can be found in Figure 3.1.

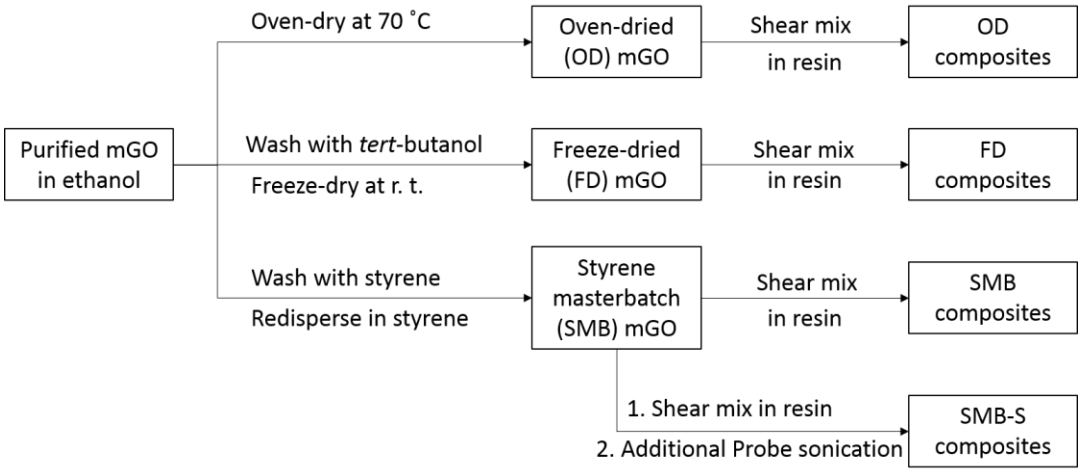

Figure 3.1. Schematic of post-synthesis processes and sample designations (r.t. = room temperature, mGO = dodecylamine modified graphene oxide).

3.2.3 Characterization

Infrared (IR) spectroscopy was performed on a Magna-FTIR 760 spectrometer (Nicolet) using KBr pellets of GO and modified GO samples. Powder X-ray diffraction (XRD) experiments were performed with a PANalytical X'Pert Pro diffractometer. This instrument utilized a Co anode (Kα radiation, 1.79 Å) and X'celerator detector, and it was operated at 45 kV accelerating voltage with a 40 mA emission current. Thermogravimetric analysis (TGA) was carried out under a nitrogen atmosphere using a Netzsch STA 409 simultaneous TGA-DSC with ~2.5 mg of sample loaded in an alumina crucible. The ramp rate was 10 °C/min, and the temperature range was 25 °C to 600 °C. A JEOL 6700 field emission scanning electron microscope (SEM) with a tungsten filament source was used for imaging. SEM images were taken using an acceleration voltage of 5 kV. All fracture surface SEM

samples were coated with 50 Å Pt prior to imaging. Visible light microscopy (VLM) images were taken on a Nikon Eclipse Ti-e Optical Microscope in transmission mode, using 1.5 mm thick, fully cured resin plates as specimens.

Flexural modulus and ultimate flexural strength were determined using an RSA-G2 solids analyzer (TA Instruments) according to ASTM D790-10. The three-point bending experiment was performed with a span-to-thickness ratio of 16:1 and a crosshead rate of 1 mm·min^{-1} (0.01 min^{-1} strain rate). The fracture toughness test was performed using a compact tension (CT) method on an Instron 5966 dual-column system equipped with a 500 N load cell per ASTM D5045-99. After having been pre-cracked by tapping with a fresh razor blade, all specimens were pulled at 10 mm·min^{-1} until complete failure. In a typical test, five three-point bend and at least ten CT specimens were tested, and the average was reported along with the standard deviation.

The critical stress intensity factor (K_{IC}) was calculated using equation 3.1, and the critical strain energy release rate (G_{IC}) was calculated via equation 3.2 (ASTM D5045-99).

$$K_{IC} = \frac{P_C}{B\sqrt{W}} \times \frac{\left(2+\frac{a}{W}\right)\left[0.886+4.64\frac{a}{W}-13.22\left(\frac{a}{W}\right)^2+14.72\left(\frac{a}{W}\right)^3-5.6\left(\frac{a}{W}\right)^4\right]}{\left(1-\frac{a}{W}\right)^{\frac{3}{2}}} \qquad (3.1)$$

$$G_{IC} = K_{IC}^2\left(\frac{1-\upsilon^2}{E}\right) \qquad (3.2)$$

Here, P_C is the critical applied load, B is the specimen thickness, W is the specimen width; a is the precrack length, E is the flexural modulus, and υ is the Poisson's ratio of UPR, which is taken to be 0.39. The precrack was created by tapping a razor blade in the machined notch, see Figure 2.8 in Chapter 2.

3.3 Results and Discussion

3.3.1 Chemical modification and post-modification work-up of GO

The chemical modification of GO with dodecyl groups was carried out to enhance surface interactions between the modified GO sheets and the polymer matrix and to increase the separation between GO sheets so that mGO would exfoliate more readily upon mixing. The dodecylamine modification of GO was confirmed by infrared spectroscopy (Figure 3.2). A broad absorption band centered at 3420 cm^{-1} in both spectra corresponds to the O–H stretching vibrations of hydrogen-bonded surface hydroxyl groups.[197] Other absorption peaks corresponding to the carboxylate C=O stretch at 1722 cm^{-1}, a graphitic skeleton stretch at 1576 cm^{-1}, a C–O–C stretch at 1220 cm^{-1}, and a C–O stretch at 1050 cm^{-1} in the spectrum of GO can also be found in that of mGO.[198] After dodecylamine functionalization, new absorption peaks associated with antisymmetric and symmetric C–H stretching vibrations appear at 2921 cm^{-1} and 2849 cm^{-1}, which is commonly observed for long-chain alkyl groups. The peaks that can be assigned as methylene scissoring and rocking absorption bands also appear at 1456 cm^{-1} and 769 cm^{-1} respectively.[199] The decrease in the intensity of the peak associated with the carboxylate C=O stretch and an increase in intensity of the amide N–H bending absorption band around 1640 cm^{-1} indicate the formation of an amide bond between GO and dodecylamine. The decrease in the intensity of the epoxide stretch absorption, together with a new peak at 1358 cm^{-1} corresponding to the amine C–N stretch,[199] implies that the ring opening reaction between amine and epoxy group also occurred.

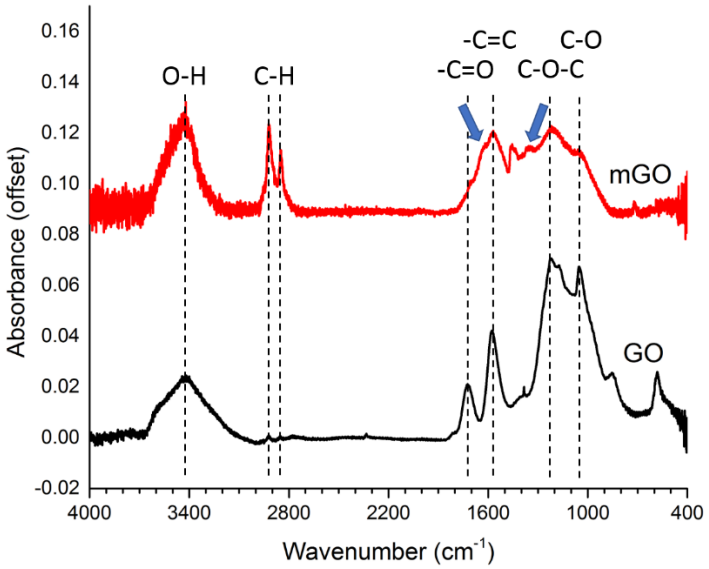

Figure 3.2. Infrared spectra of pristine GO and dodecylamine-modified GO (mGO). Arrows mark the 1640 and 1358 cm^{-1} peak positions discussed in the text.

Figure 3.3 shows the powder X-ray diffraction patterns of GO and mGO. A significant interlayer expansion from 7.7 Å to 14 Å can be observed after functionalization of the GO particles. This increase in interlayer distance is attributed to the bulky nature of the dodecyl groups and a good coverage of dodecyl groups on the GO sheet surface. The broad peak around 24° 2θ in the XRD pattern of mGO, corresponding to an interlayer distance of 4.4 Å, is the commonly observed most intense peak in the pattern of chemically reduced graphene oxide.[200] Its presence in the pattern of mGO indicates that reduction of GO occurred during the modification and that some reduced graphene layers are closely stacked. As a result of partial reduction, the sample color changed from brown for GO to black for mGO.

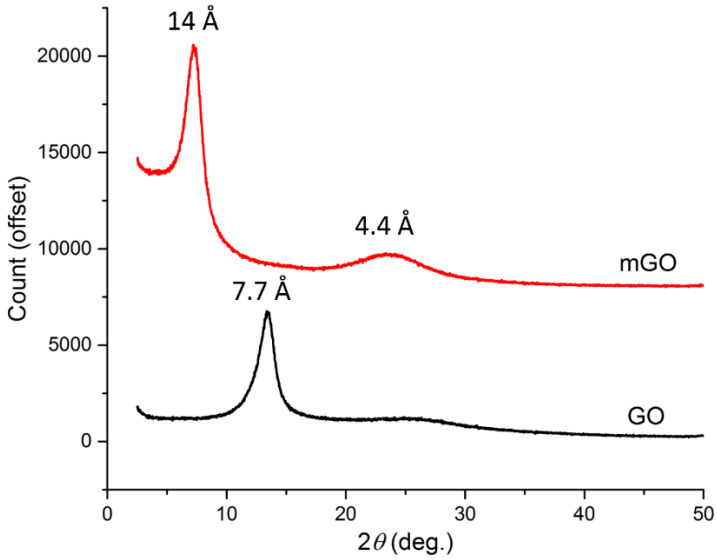

Figure 3.3. X-ray diffraction patterns of pristine GO and modified GO (Co Kα source).

Dodecylamine modification significantly improves the thermal stability of GO. Figure 3.4 shows the TGA data of GO and mGO samples. Mass loss before 120 °C is caused mainly by removal of surface-adsorbed water; therefore, all TGA data were normalized to show the mass change beyond this point. The mass loss around 160–200 °C in both samples corresponds to decomposition of unreacted oxygen-containing groups on GO; the relatively small mass loss observed for mGO in this region suggests that a large fraction of these groups were converted during the modification process. The mass loss between 200 °C and 500 °C can be explained as the gradual loss of physisorbed, weakly bonded (epoxy-amine reaction), and strongly bonded (amide formation) dodecylamine. A mass loss of more than 40% in this range suggests a high density of dodecyl functional groups in mGO, although a fraction of this mass loss may be associated with loss of oxygen and carbon from GO during heating.[220]

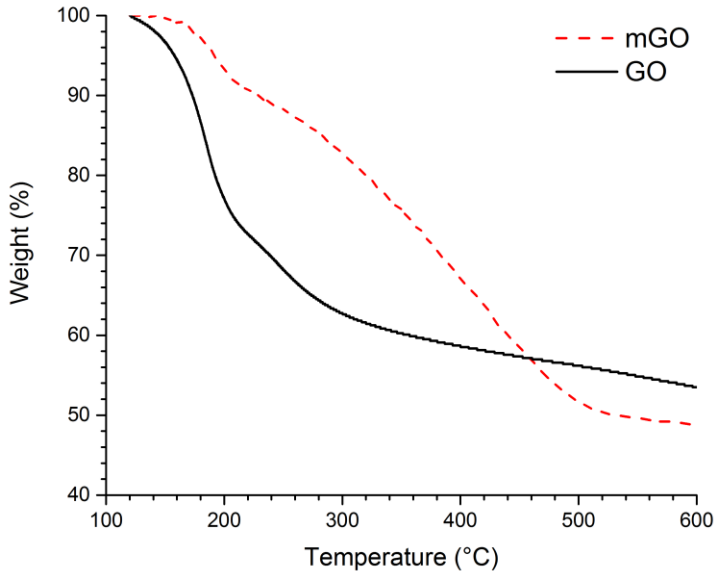

Figure 3.4. Thermogravimetric analysis of GO and mGO materials. The residual mass was normalized to 100% at 120 °C.

Figure 3.5 shows the XPS data of pristine and modified GO. The difference in nitrogen content between mGO and GO was used to estimate the fraction of dodecylamine in mGO. On the basis of the nitrogen content of mGO, the dodecylamine functional group accounts for about 27% of the total mass of mGO, which is lower than the value of 40% weight loss determined by TGA. The latter weight loss may include some loss of oxygen and carbon from GO during heating. Comparing the X-ray photoelectron spectroscopy results of GO and mGO, GO was reduced during modification. The C:O ratio changed from 2.38:1 to 5.27:1 (carbon from dodecylamine subtracted) after dodecylamine modification, which explains the reduction peak in the XRD pattern of mGO at 24° 2θ that is typically associated with chemically reduced GO.

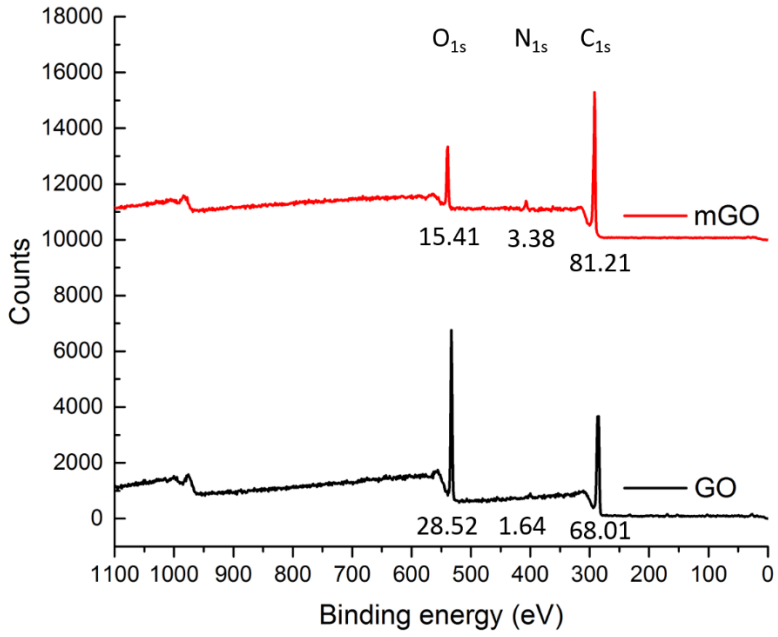

Figure 3.5. X-ray photoelectron spectroscopy data of pristine GO and modified GO. The number under each peak represents the abundance in atom percent of the corresponding element in the sample.

The different post-synthesis processing methods of mGO have relatively little impact on the chemical composition of mGO, as differently processed mGO samples exhibit only small differences in their IR spectra and XRD patterns (Figure 3.6). The OD-mGO sample gives a slightly broader low-angle peak, which may indicate that the rapid drying process causes more disorder inside the aggregates. The additional IR absorption peak at 1159 cm^{-1} of the FD-mGO sample corresponds to the C–OH stretching vibration, which originates from the hydroxyl groups on the GO surface that cannot be removed by room temperature freeze drying.

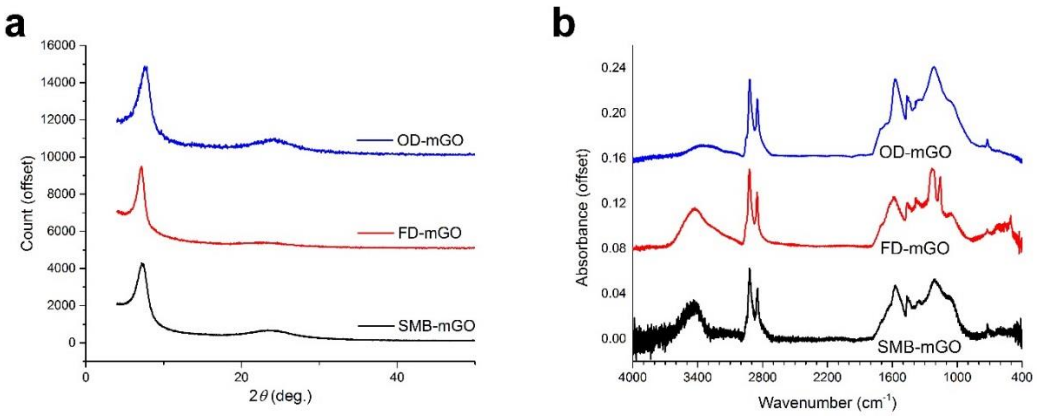

Figure 3.6. (a) XRD patterns and (b) IR spectra of differently processed mGO.

However, processing conditions have a significant effect on how mGO sheets re-stack. To study this effect, all mGO samples were dispersed in dichloromethane with magnetic stirring. The resulting particle suspensions were subsequently drop cast onto a silicon wafer and dried under dichloromethane atmosphere. The SEM micrographs of the resulting mGO samples are shown in Figure 3.7. Compared to SMB-mGO (Figure 3.7c), the FD-mGO sample (Figure 3.7a) has a much larger aggregate size and more stacking. Aggregates in the OD-mGO sample (Figure 3.7b) are even larger, and the presence of bright lines due to edge effects also means that stacking is significantly more pronounced. It should be noted that the aggregated mGO particles can break down by sonication in styrene (Figure 3.7d), but some large aggregates remain unchanged.

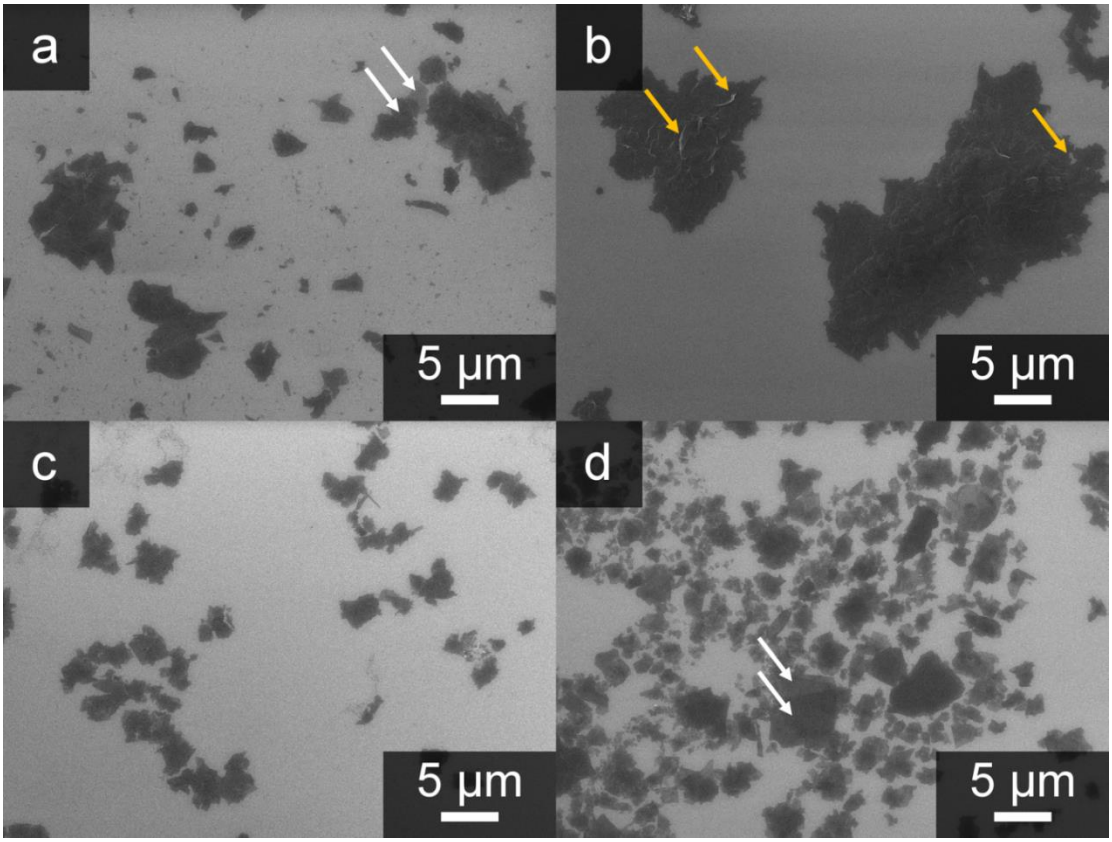

Figure 3.7. SEM micrographs of differently processed mGO. (a) FD-mGO, (b) OD-mGO, (c) SMB-mGO, (d) FD-mGO sonicated for 30 minutes in styrene. Note the contrast within the aggregates (white arrows), which indicates restacking of mGO sheets. Bright lines caused by edge effects (yellow arrows) indicate significant aggregation, because in these cases, the edges of thick mGO stacks point away from the silicon wafer surface.

3.3.2 Characterization of dispersion quality and mechanical properties of the composites

The composite samples were prepared as described in the experimental section. A summary of the different nanocomposite processing steps is presented in Figure 3.1. Freeze-dried and oven-dried composite samples were synthesized to evaluate the effectiveness of freeze-drying to prevent the formation of large aggregates in the resin. A comparison between composites made with dried mGO and those made with an mGO/styrene masterbatch shows how the drying process affects mGO dispersibility. Additional sonication treatment of the mGO masterbatch/resin dispersion was also studied to investigate whether sonication can further improve the quality of dispersion by breaking down mGO aggregates from the masterbatch.

Photographs of the nanocomposite resin plaques are shown in Figure 3.8. The appearance of the plaques differs significantly, depending on the processing method. The OD sample shows the least discoloration, but large aggregates of mGO are apparent even to the eye. The FD sample is darker and more uniform; however, aggregates can still be seen. Both samples prepared from the mGO/styrene masterbatch (SMB and SMB-S) are homogenous and uniformly darkened by the nanoparticles.

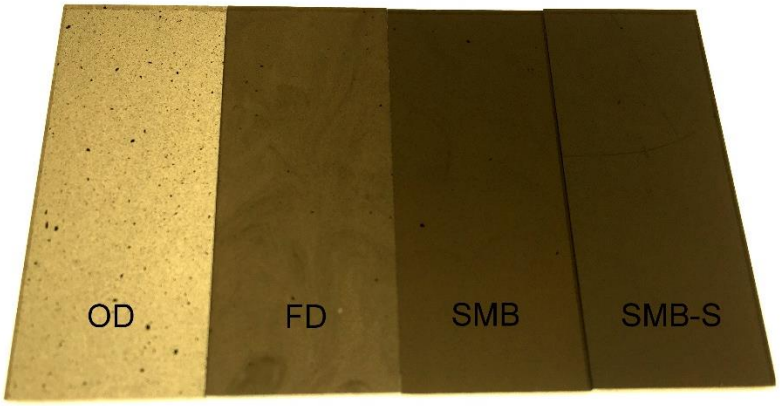

Figure 3.8. Photograph of 1.5 mm UP resin plaques containing 0.04 wt% mGO and prepared by the four different processes outlined in Figure 1.

The quality of mGO/resin dispersions can be characterized more quantitatively by visible light microscopy (VLM). Figure 3.9 shows a comparison of differently processed mGO in UP resin. When made into a composite, the oven-dried mGO (Figure 3.9a) formed the largest aggregates, some of which were a few tens of micrometers in diameter. A freeze-drying process reduced the aggregation of mGO, thus the FD sample (Figure 3.9b) shows a more uniform distribution of mGO particles with fewer large aggregates. The styrene masterbatch process produced a much better dispersion of mGO in the resin, and the size of mGO aggregates was further reduced. As indicated by the particle count on the images at the same loading level, the number of particles in a composite made with SMB mGO (Figure 3.9c) increased significantly compared to that of the OD and FD composites. Additional 1 h probe sonication of the SMB mGO/UP dispersion did not further improve the quality of the dispersion, as Figure 3.9d looks similar to Figure 3.9c.

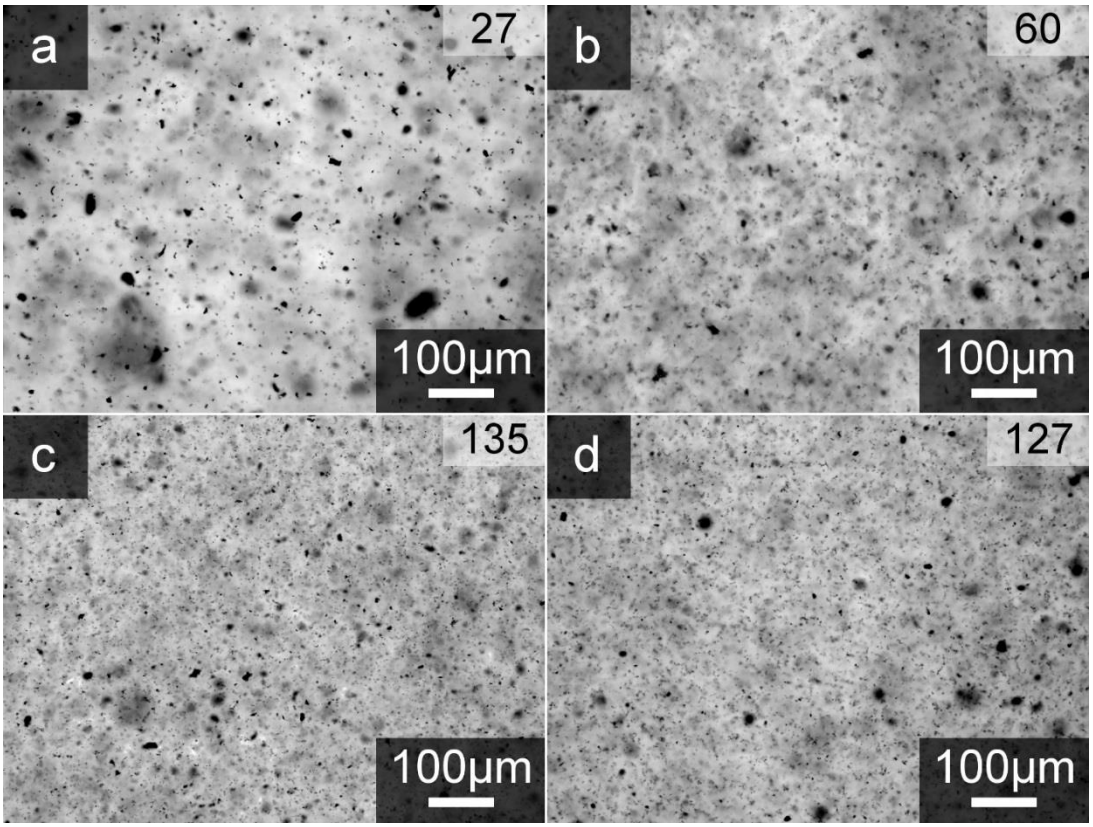

Figure 3.9. VLM micrographs of UP resin composites with differently processed mGO: (a) oven-dried mGO (OD); (b) freeze-dried mGO (FD); (c) styrene masterbatch (SMB); (d) styrene masterbatch with additional probe sonication (SMB-S). Particle count in particles/10^4 µm^2 is given on each image. All samples are 1.5 mm thick and have an identical loading of 0.02 wt.% mGO.

A plot of size distributions of mGO aggregates in all samples can be found in Figure 3.10. It should be noted that well dispersed mGO sheets or aggregates that are smaller than 0.3 µm cannot be detected by VLM due to the Rayleigh limit. If the primary intent of a dispersion process is to reduce macroscopic aggregation, any drying step should be avoided when mGO is transferred into a resin matrix. The masterbatch process showed the advantage of transferring wet graphene nanosheets to the designated resin without any

drying step. Also, additional probe sonication is unfavorable, since it adds additional cost to the process without further reducing the average size of aggregates to a significant extent.

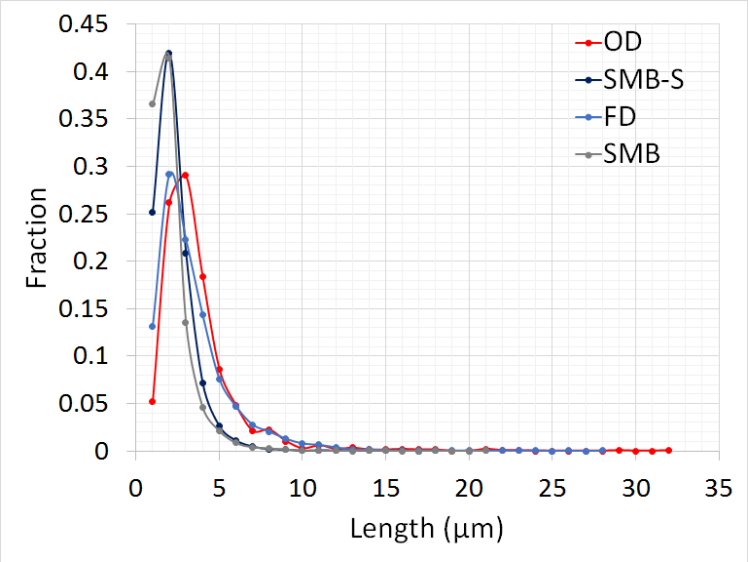

Figure 3.10. Particle size distributions of mGO aggregates in differently processed mGO/resin composites. Trendlines are used only to guide the reader's eyes. The total sampling area for each sample is 0.574 mm^2. Total counts are 1564, 3425, 7734, and 7291 for the OD, FD, SMB, and SMB-S samples, respectively.

While the masterbatch process is potentially applicable to other systems that require good dispersion of modified graphene oxide, the focus of this research is to study how the quality of dispersion affects the mechanical properties of UP resin composites. A previous study indicated that addition of graphene oxide derivatives to UP resin at very low loading levels can toughen the matrix significantly,[220] so it is important to know how different dispersing processes will influence the performance of the final product. To be specific, the mode-I critical stress intensity factor (K_{IC}), critical strain energy release rate (G_{IC}), flexural modulus (E), and flexural strength (σ) are properties of interest. As shown in Figure 3.11a and b, OD and FD mGO composites have slightly higher fracture toughness

(K_{IC}) and fracture energy (G_{IC}) than the SMB and SMB-S composites, which suggests that the formation of large aggregates may be beneficial for toughening UP composites.[226] Due to the very low loading levels, the flexural modulus values (Figure 3.11c) for all composite samples are very close to one another. The flexural strength, however, shows a strong dependence on aggregation size. The OD and FD samples exhibit a larger reduction of ultimate strength, compared to the SMB and SMB-S samples. This is because aggregates can function as structural defects and concentrate stress for crack initiation.[208-210] The mechanical properties of SMB and SMB-S composites are very similar, and the same is true for the OD and FD samples. Furthermore, additional probe sonication does not improve the mechanical performance of composites any further, consistent with what was observed by VLM. Because sonication is difficult and expensive for industrial scale operations, the masterbatch process is advantageous for replacing sonication processes during resin formulation without lowering the quality of dispersion.

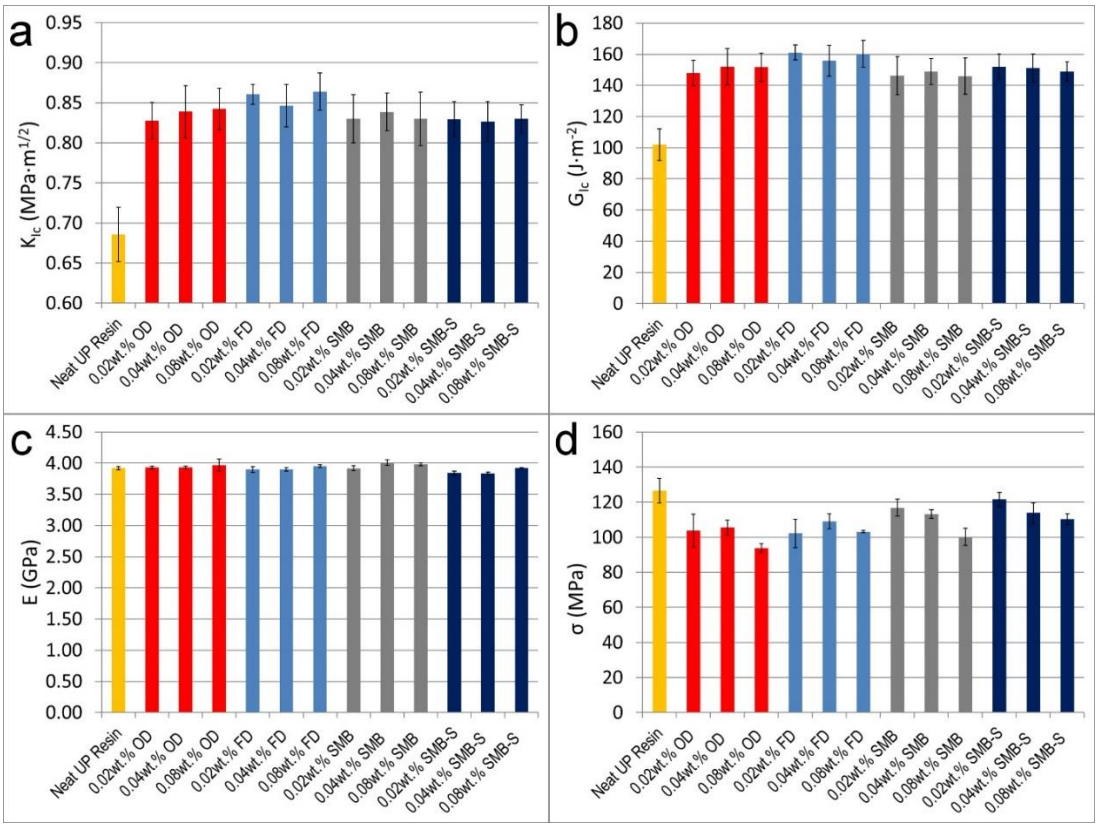

Figure 3.11. Mechanical properties of UP resin composites with differently processed mGO. (a) K_{IC}, (b) G_{IC}, (c) flexural modulus, and (d) flexural strength.

When a styrene masterbatch is prepared from freeze-dried mGO (SMB-FD), aggregation of mGO sheets is partially reduced, as shown in Figure 3.7, but the overall mechanical properties of corresponding UP resin composites are very similar to those of samples made with FD mGO (Figure 3.12). This implies that any drying step in processing modified GO materials should be avoided to prevent further particle aggregation and to retain better composite strength.

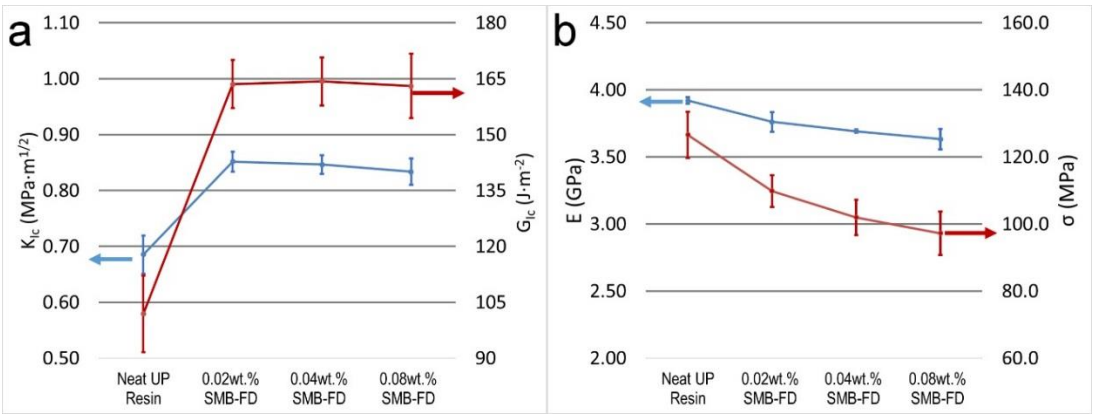

Figure 3.12. Mechanical properties of SMB-FD mGO/UP resin composites. (a) K_{IC} and G_{IC}, (b) flexural modulus and flexural strength.

3.3.3 Fractography Analysis

Fractography analysis can provide useful information about the dispersion of particles inside the matrix and how these particles affect the mechanical performance of composites. The fracture surface resulting from mode-I cracking can be divided into two regions: a near-precrack region and a fast propagation region (Figure 2.8 in Chapter 2). The near-precrack region has a slow propagation rate due to the gradual stress build-up behind the precrack (re-initiation), and the features in this region show how a matrix filled with particles responds to the slowly increasing applied stress.[174, 227] In general, the contributing toughening events in GO toughened resins are crack pinning and crack deflection, which appear as tadpole-shaped features and irregular edges in SEM fractographs, respectively. Distinctive aggregates and river-like "bright tails" following those aggregates can be observed for the OD and FD samples in Figure 3.13a and c, respectively. In contrast, patches of surfaces at different heights separated by irregular edges are visible for the SMB and SMB-S samples in Figure 3.13e and g, respectively, which implies a change in the

toughening mechanism. Although the crack pinning mechanism is predominant in OD and FD samples and the crack deflection mechanism predominant in SMB and SMB-S samples, all composite fracture surfaces have roughness near the precrack regions (Figure 3.13a, c, e, g), which explains the similar K_{IC} values obtained for these samples. Catastrophic failure of test specimens happens in the fast propagation region (Figure 3.13b, d, f, h), where the growth of cracks can no longer be stopped. This brittle fracture leaves a smooth surface with small features of pulled out particles, which is useful for visualizing the particle distribution inside a resin matrix. By counting the events on the SEM micrographs in Figure 3.13, the particle aggregate densities in terms of counts per 10,000 μm^2 were estimated to be: 10 for the OD sample, 19 for the FD sample, 29 for the SMB sample, and 32 for the SMB-S sample. Compared to FD, SMB, and SMB-S samples the OD sample shows a significantly lower particle density, which suggests more severe aggregation of mGO inside its composite. The trend is similar to that observed by optical microscopy in Figure 3.9 where the particle density is about 3~4 times that observed by SEM on the fracture surfaces. The size of aggregates is also smaller in SMB/SMB-S samples than in OD/FD samples, judging from the high magnification SEM micrographs of the fracture surfaces.

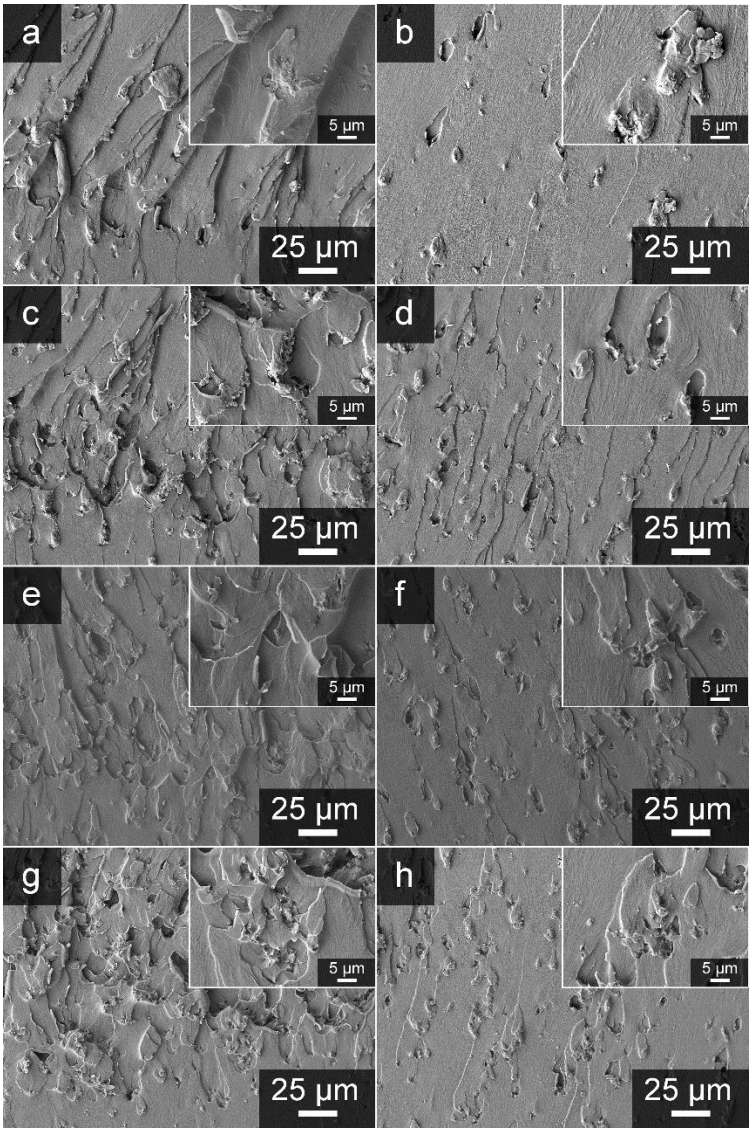

Figure 3.13. SEM fractographs of compact tension samples after testing: OD (a, b), FD (c, d), SMB (e, f), and SMB-S (g, h). Positions in the specimens: near precrack (a, c, e, g), and fast propagation region (b, d, e, h). A definition of the different regions on the fracture surface is presented in Fig. S9. All samples contain 0.04 wt.% mGO in UP. Crack propagation direction: from bottom to top. A corresponding image of the neat resin can be found in Figure 2.9 in Chapter 2.

3.3.4 Toughening Vinyl Ester (VE) Resin

Like what was observed in the UP resin, mGO masterbatch can also toughen VE resin. The masterbatch prepared in this chapter can be easily mixed into VE resin and achieve good dispersion. Figure 3.14 shows an optical micrograph of mGO-VE resin composite, which is similar to UP resin composites in terms of dispersion and aggregate size.

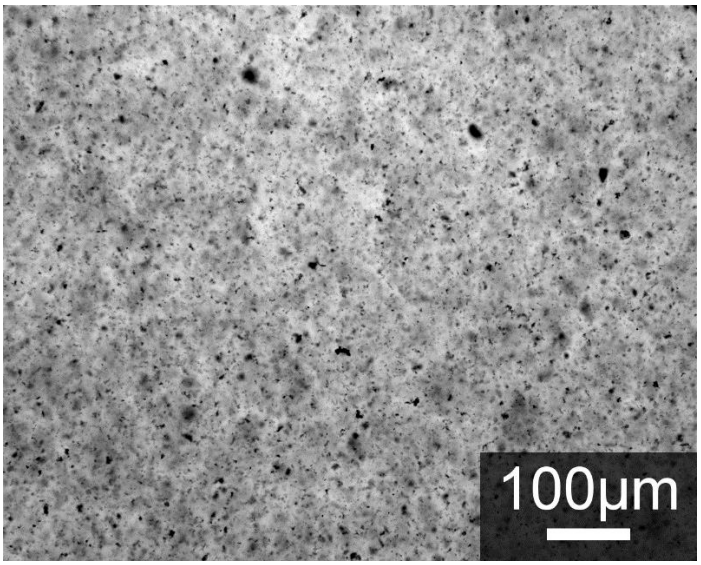

Figure 3.14. VLM micrograph of VE resin with 0.04 wt.% SMB mGO.

Similar increases in fracture toughness were also observed when mGO was incorporated in VE composites (Figure 3.15), with peaks in K_{IC} and G_{IC} at an even lower loading of 0.02 wt.%.

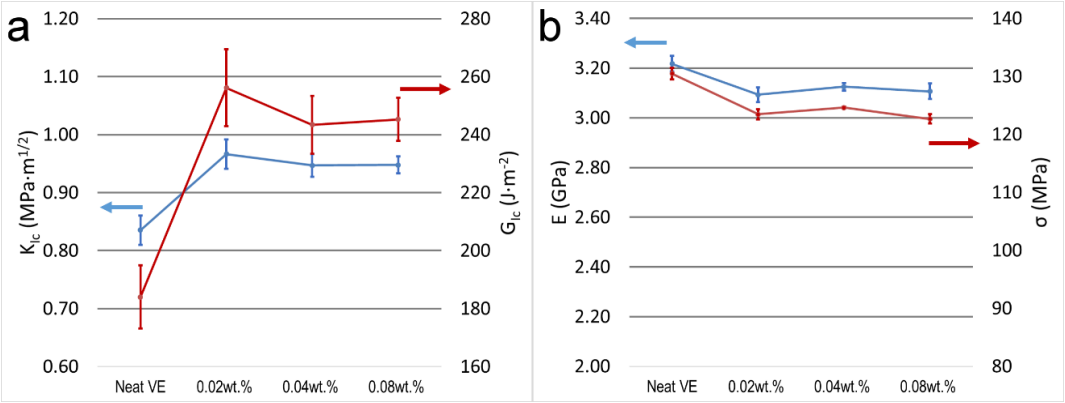

Figure 3.15. Mechanical properties of mGO/VE resin SMB composites. (a) K_{IC} and G_{IC}, (b) flexural modulus and flexural strength.

The features on the fracture surfaces of VE composites made with SMB mGO are similar to those observed in UP composites, as shown in Figure 3.16.

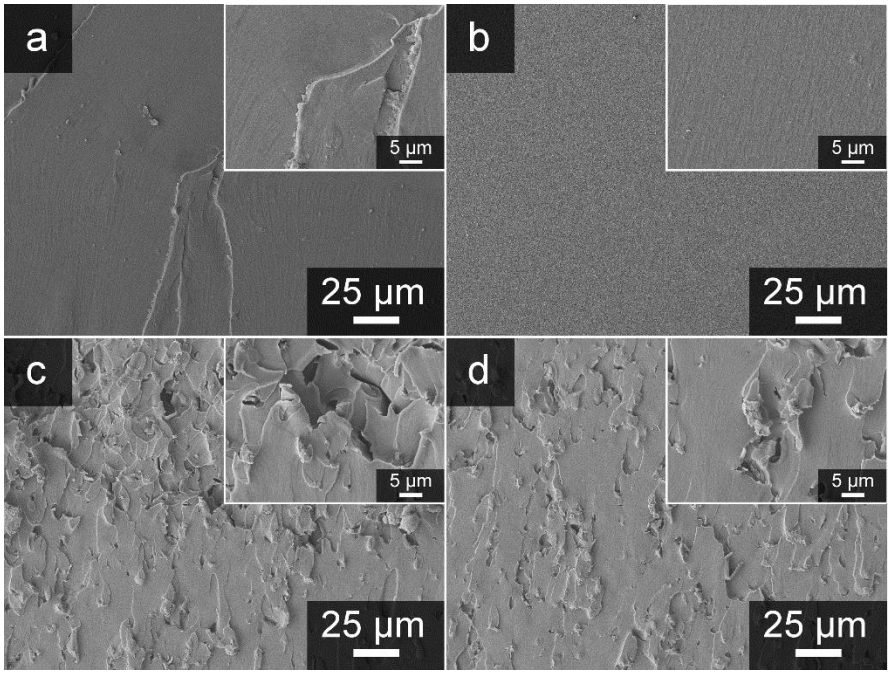

Figure 3.16. SEM fractographs of failed compact tension samples: neat VE resin (a, b), VE resin with 0.04 wt% mGO prepared by the SMB process (c, d). Positions in the specimens: near precrack (a, c), and fast propagation region (b, d). Crack propagation direction: from bottom to top.

3.4 Conclusion

A simple dodecylamine functionalization of GO was utilized to synthesize mGO compatible with UP and VE resins. The GO modification was confirmed by FTIR, XRD, and TGA. This research demonstrates that mGO in the form of a styrene masterbatch can be readily incorporated into UP resin by mechanical mixing. Although the preparation of the masterbatch itself requires bath sonication, no sonication step is needed for resin formulation by the end user. It should be noted that the volume of the masterbatch required for processing is significantly less than the volume of resin. VLM images and SEM of fracture surfaces show that the size of aggregates is much smaller in masterbatch-derived samples than in oven-dried or freeze-dried samples, and no significant difference in aggregation was observed before (SMB) and after (SMB-S) additional sonication. This is advantageous because sonication treatment is expensive and difficult to carry out for processing large volumes of resin dispersions. Although better dispersion does not guarantee better fracture toughness, a UP composite with less aggregated mGO shows better retention of flexural strength in mechanical tests. Another advantage of incorporating mGO directly in a masterbatch is that the dispersed graphene oxide is safer to ship and easier to handle during mixing than the dry powder. Freeze-dried mGO offers a slightly better toughening effect than SMB mGO, but it is overall not favorable, considering its processing cost and the observed flexural strength reduction. Processing is simplest for oven-dried mGO albeit at the expense of significant strength reduction, which renders this route competitive only when the ultimate strength of the composite is not a concern. The study shows the significant effects that different methods used to concentrate and disperse

nanoparticles have on resulting properties. This is relevant to many other types of nanoparticles.

Chapter 4*

Effects of Inorganic Fillers on Toughening of Vinyl Ester Resins by Modified Graphene Oxide

4.1 Introduction

For thermosetting resins, fracture toughness is a vitally important property.[228] Thermosets are inherently brittle due to their highly crosslinked structure, which means that a small crack can lead to catastrophic failure of a resin part. However, increasing the resin fracture toughness by reducing the crosslink density is impractical, because this would also reduce the stiffness and heat distortion temperature of the resin.[229] Thus, a toughening agent is often used to increase the fracture toughness of a thermosetting resin. Despite the great success of polymeric toughgeners, such as reactive liquid rubbers, core-shell rubbers, and block copolymers, researchers have suggested that inorganic nanoparticles could better serve as resin toughgeners because they can toughen the matrix without reducing its modulus or glass transition temperature (T_g).[169, 170, 191, 230] Among inorganic toughgeners, graphene-based nanomaterials have received special attention in recent years, because they are effective at extremely low loading levels (0.04 wt % or lower).[192, 220, 221] At such low levels, adding a graphene-based toughener does not increase the base resin viscosity, and also keeps modulus and T_g relatively constant.[220] These characteristics render graphene-based toughgeners competitive in cost-driven resin markets.

* This chapter was reproduced from *Ind. Eng. Chem. Res.* **2018**, *57*, 4592 with permission. © Copyright 2018, American Chemical Society. Mechanical data used in this chapter were collected and processed by Kunwei Liu.

Unsaturated polyester (UP) resins and vinyl ester (VE) resins are extensively used as composite resins for building structural parts in automobiles, marine construction, storage tanks, pipelines, and home-building industries.[231] They are the most common types of thermosetting resins to be used for manufacturing fiber-reinforced plastics, because they are inexpensive, easy to process, and exhibit good mechanical stiffness and moderate chemical resistance.[134] Compared to UP resins, VE resins offer better toughness and corrosion resistance at a slightly higher cost.[134] Application of VE resins is therefore more common in the chemical industry, where the mechanical properties and chemical resistance of UP resins are inadequate. Both resins are used mainly for fiber-reinforced structural parts; therefore, fracture toughness is of great importance. In addition, whereas some price tolerance is associated with high performance engineering plastics, UP or VE resin industries tend to place more emphasis on cost control. At low loadings, graphene-based toughening are potentially cost-effective for toughening these resins.

A few publications have indicated that polymeric toughening can toughen particle-filled resins,[145, 232] but, to the authors' knowledge, most research on resin toughening with rigid inorganic nanoparticles was done in neat resins. Although removing fillers from a resin formulation simplifies the system, fillers can influence the mechanical properties of the resin, because these particles can both act as reinforcements and introduce defect sites. Thus, it is important to learn how inorganic nanoparticle toughening, such as graphene-based toughening, interact with filler particles in a resin. In addition, fillers are commonly found in UP and VE formulations, because they can be used to reduce cost, control shrinkage, and adjust viscosity. Therefore, it is particularly worthwhile to investigate the interactions between common fillers and graphene toughening agents in UP and VE resins.

In this work, the mechanical properties of a VE resin with different fillers were studied with and without the presence of modified graphene oxide (mGO) toughener. The results indicate that fillers may or may not impact the toughening effect of graphene, depending on the size of the fillers or particle aggregates relative to that of mGO particles.

4.2 Experimental

Materials

Styrene (99%), 2-butanone peroxide (Luperox DDM-9, 35 wt % in 2,2,4-trimethyl-1,3-pentanediol diisobutyrate), and kaolin clay were purchased from Sigma-Aldrich. Dodecylamine (DDA, 98%) was obtained from Alfa-Aesar. Untreated fumed silica (CAB-O-SIL M-5) and PDMS-treated silica (AEROSIL R 202) were obtained from Cabot Corp. and Evonik Corp., respectively. Calcium carbonate samples of different sizes (Ultra-Pflex A-16-083-11, precipitated calcium carbonate 70 nm average particle size; Super-Pflex 100 A-2-201-22, precipitated calcium carbonate 700 nm average particle size; Vicron 15-15 A-16-042-11, 3.5 μm) were obtained from Specialty Minerals Inc. Deionized (DI) water with a resistivity of 18 MΩ·cm was produced onsite using a Barnstead purification system. The Hetron 922L-25 vinyl ester resin was supplied by Ashland Inc. GO in water slurry was purchased from Graphenea.

Synthesis of modified GO

A detailed procedure for the synthesis of modified GO can be found elsewhere.[233] Briefly, one part by volume of an aqueous dispersion of GO (4 mg/mL) prepared by sonication was rapidly mixed with two parts by volume of a solution of 6 g/L dodecylamine in ethanol. The mixture was then heated to 70 ˚C and allowed to react for 24 h under stirring.

The crude product was washed 4 times with ethanol and 3 times with styrene by mixing and centrifugation to obtain the final product. Purified dodecylamine-modified GO (mGO) was redispersed in styrene at approximately 1 wt % with 30 min sonication to prepare the styrene masterbatch.

Preparation of resin composite

Generally, a small amount of styrene was removed from the as-received VE resin by vacuum distillation, and various quantities of styrene were then added back to account for the extra styrene from the mGO masterbatch. Dry fillers were added to the VE resin afterwards. All resin dispersion samples were shear mixed with a 1" Cowles blade at 2000 rpm for 15 min (Eurostar power-b, IKA) to obtain a uniform dispersion. Filled resin dispersions were subsequently initiated with 1.25 g 2-butanone peroxide initiator per 100 g resin and allowed to react for 10 min with magnetic stirring at moderate speed, followed by 10 min degasing in vacuum. For fumed silica samples, an extra degasing step was added prior to initiation. Resin was poured between two 3/16-inch-thick borosilicate glass plates clamped over a 3-mm (1.5-mm for flexural modulus/strength testing specimens) diameter high temperature silicon rubber cord. Samples were cured at room temperature for 24 h before 4 h of post-curing at 90 °C. For mechanical testing, the fully cured resin plaques were cut into test specimens according to ASTM D790-10 and ASTM D5045-99. A detailed description of specimen dimensions can be found in our previous publication.[7]

Characterization

A JEOL 6700 field emission scanning electron microscope (SEM) with a tungsten filament source was used for imaging. SEM images were taken using an acceleration

voltage of 5 kV. For SEM all samples except mGO, were coated with 5 nm Pt prior to imaging. A FEI Tecnai T12 transmission electron microscope (TEM) with a LaB_6 filament operating at an acceleration voltage of 120 kV was used to obtain TEM micrographs. The resin composite TEM specimens were made using a Leica EM UC6 ultramicrotome. To image mGO by SEM, samples were taken from the masterbatch, dispersed in dichloromethane and then dip coated onto a silicon wafer (Ted Pella lnc.). Rheology measurements were carried out on a AR-G2 rheometer (TA Instruments) with a parallel plate geometry. Samples were sheared between a 40-mm diameter stainless steel upper disk and a temperature-controlled Peltier plate. All rheology tests were carried out at 25 °C.

Flexural modulus and ultimate flexural strength were determined using an RSA-G2 solids analyzer (TA Instruments) according to ASTM D790-10. The three-point bending experiment was performed with a span-to-thickness ratio of 16:1 and a crosshead rate of 1 $mm \cdot min^{-1}$ (0.01 min^{-1} strain rate). The fracture toughness test was performed using a compact tension (CT) method on an Instron 1011 single column system equipped with a 5 kN load cell according to ASTM D5045-99. After having been pre-cracked by tapping with a liquid nitrogen cooled fresh razor blade, all specimens were pulled at 10 $mm \cdot min^{-1}$ crosshead speed until complete failure. In a typical test, five three-point bending and at least ten CT specimens were tested, and the average was reported along with the standard deviation.

The critical stress intensity factor (K_{IC}) was calculated using equation 4.1, and the critical strain energy release rate (G_{IC}) was calculated via equation 4.2.

$$K_{IC} = \frac{P_C}{B\sqrt{W}} \times \frac{\left(2+\frac{a}{W}\right)\left[0.886+4.64\frac{a}{W}-13.22\left(\frac{a}{W}\right)^2+14.72\left(\frac{a}{W}\right)^3-5.6\left(\frac{a}{W}\right)^4\right]}{\left(1-\frac{a}{W}\right)^{\frac{3}{2}}} \quad (4.1)$$

$$G_{IC} = K_{IC}^2\left(\frac{1-\upsilon^2}{E}\right) \quad (4.2)$$

Here, P_C is the critical applied load, B is the specimen thickness, W is the specimen width; a is the crack length, E is the flexural modulus, and υ is the Poisson's ratio of the VE resin, which is taken to be 0.39.

4.3 Results and discussion

4.3.1. Characterization of inorganic fillers and graphene-based toughener

The morphology of the fillers used in this study is shown in Figure 4.1. The ground calcium carbonate sample (GCC, Figure 4.1a) shows a wide distribution of sizes with most of the particles measuring around 3–15 μm and a few over 15 μm in length. The precipitated calcium carbonate (PCC) samples, PCC-700 (Figure 4.1b) and PCC-70 (Figure 4.1c), consist of particles with average sizes around 700 nm and 70 nm, respectively (see also Figure 4.7 for higher magnification images). The kaolinite sample (Figure 4.1d) has typical particle sizes close to those of GCC, but it shows a layered structure, which is characteristic for phyllosilicates. CAB-O-SIL untreated fumed silica, (SC, Figure 4.1e) and AEROSIL PDMS-treated fumed silica, (SA, Figure 4.1f) samples both have primary particle sizes about 15 nm, according to the TEM micrographs. Calcium carbonate, kaolinite, and fumed silica were investigated in this research because they are frequently used in thermosetting resin formulations, and their differences in particle size

and surface polarity were utilized to probe the interference of filler particles with the mGO toughening effect in VE resins.

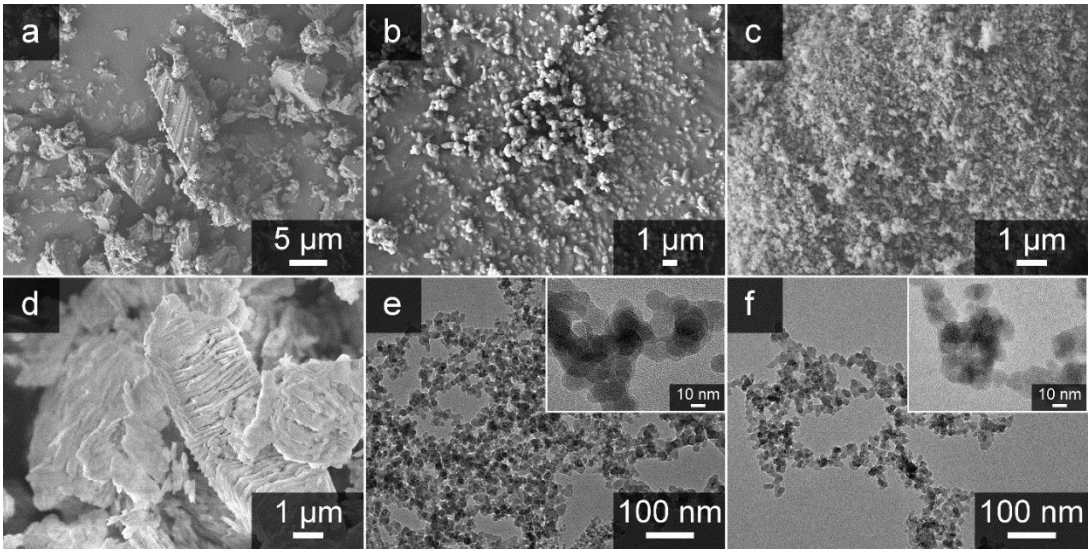

Figure 4.1. Morphology of filler particles. SEM images of (a) ground calcium carbonate (GCC); (b) precipitated calcium carbonate, 700 nm (PCC-700); (c) precipitated calcium carbonate, 70 nm (PCC-70); and (d) Kaolinite (kaolin). TEM images of (e) untreated fumed silica (SC); (f) PDMS-treated fumed silica (SA). The insets show higher magnification TEM images of the samples in (e) and (f).

Figure 4.2a shows the morphology of mGO from a styrene masterbatch that was used to prepare the mGO-toughened resin samples. A detailed description of the mGO material can be found elsewhere.[233] The mGO sample was dispersed in dichloromethane, and then drop cast onto a silicon wafer. The wafer was then slowly dried under dichloromethane vapor. The contrast inside these particles indicates that some mGO sheets restack (darker areas) and aggregate in the styrene masterbatch. The average length of mGO aggregates is 2.21±0.87 µm, determined by measuring the longest distance between two points on the periphery of particles in Figure 4.2. mGO particles of similar sizes were also observed in

TEM micrographs of resin composite samples (Figure 4.2b). This implies that no noticeable change in lateral dimensions of mGO occured during resin composite preparation.

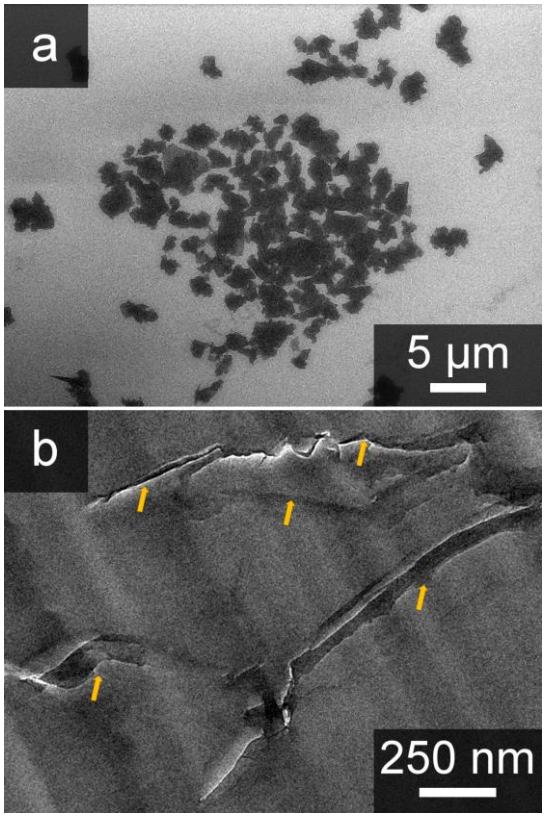

Figure 4.2. SEM image of mGO particles on a silicon wafer (a), and TEM image of mGO particles (yellow arrows) inside a microtomed resin composite sample (b).

4.3.2. Effects of filler–mGO interactions on VE resin toughening

Figure 4.3 shows the mechanical properties of VE resin composites containing GCC, Kaolin, and mGO as filler/toughener. Because the content of mGO and other fillers is low, the change in flexural modulus (Figure 4.3c) and flexural strength (Figure 4.3d) is insignificant. In contrast, all composite samples exhibit a fracture toughness improvement of 16–24% in K_{Ic}, or 27–45% in G_{Ic}, compared to the neat resin. It should be noted that the

toughening effect of mGO, GCC, and kaolin in VE resin is insensitive to filler content in the concentration range studied. A similar phenomenon has also been observed by other researchers in inorganic particle/VE resin composites.[234, 235] Additional mGO added to GCC or kaolin-filled VE resin does not result in any further toughness improvement, which may indicate that mGO aggregates and GCC/kaolin particles toughen the VE resin matrix via similar mechanisms. This observation implies that the major toughening mechanism in VE resin with inorganic particles is crack-deflection, because crack-pinning mechanisms would lead to a monotonic increase of fracture toughness with respect to mGO loading,[236] whereas toughening effects based solely on crack-deflection reach a plateau with increasing particle number.[237]

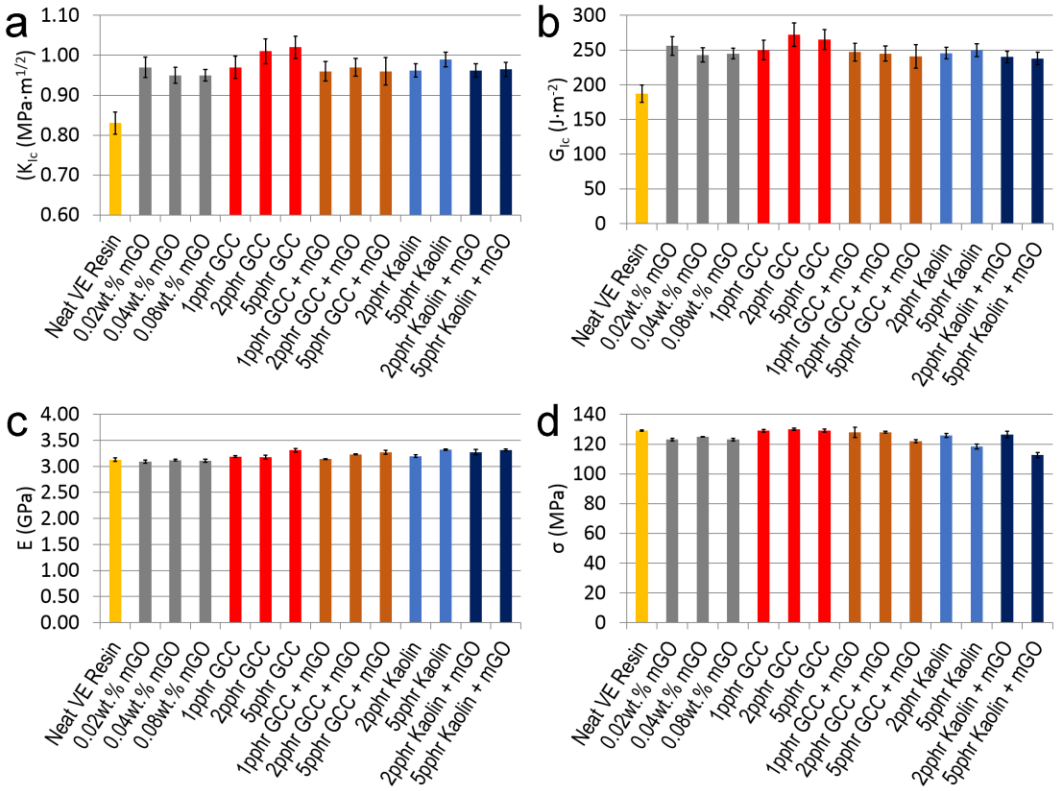

Figure 4.3. Mechanical properties of VE resin composites with inorganic filler and mGO toughener. (a) K_{IC}, (b) G_{IC}, (c) flexural modulus, and (d) flexural strength. The mGO loading level for all filler-containing samples is 0.04 wt %. The notation "pphr" refers to parts per hundred resin.

To better understand the nature of filler interference in toughening processes, the fracture surfaces of post-CT test specimens were analyzed using SEM, and the corresponding micrographs are shown in Figure 4.4. The introduction of inorganic particles significantly roughens the near-precrack region (Figure 2.9 in Chapter 2 shows the definition for different regions on a crack surface), which is usually an indication of toughness enhancement.[181, 203] A rougher fracture surface means that a larger surface area is created, which dissipates more energy. In general, some surface features also imply

toughening events, such as crack-pinning, crack deflection, multi-cracking, and cavitation, that can further dissipate energy. However, in this study, it is found that addition of mGO into filler-containing VE resin (Figure 4.4 f, h, j, i) or simply adding mGO to VE resin (Figure 4.4 c, d) further increases the fracture surface roughness without changing the fracture toughness of the resin composite (Figure 4.4.3 a, c). The fracture surface of VE/mGO composites lacks the characteristic "river-like" features generated by crack-pinning events.[233] This again leads to the conclusion that the main toughening mechanism in VE/inorganic particle composites is crack-deflection.

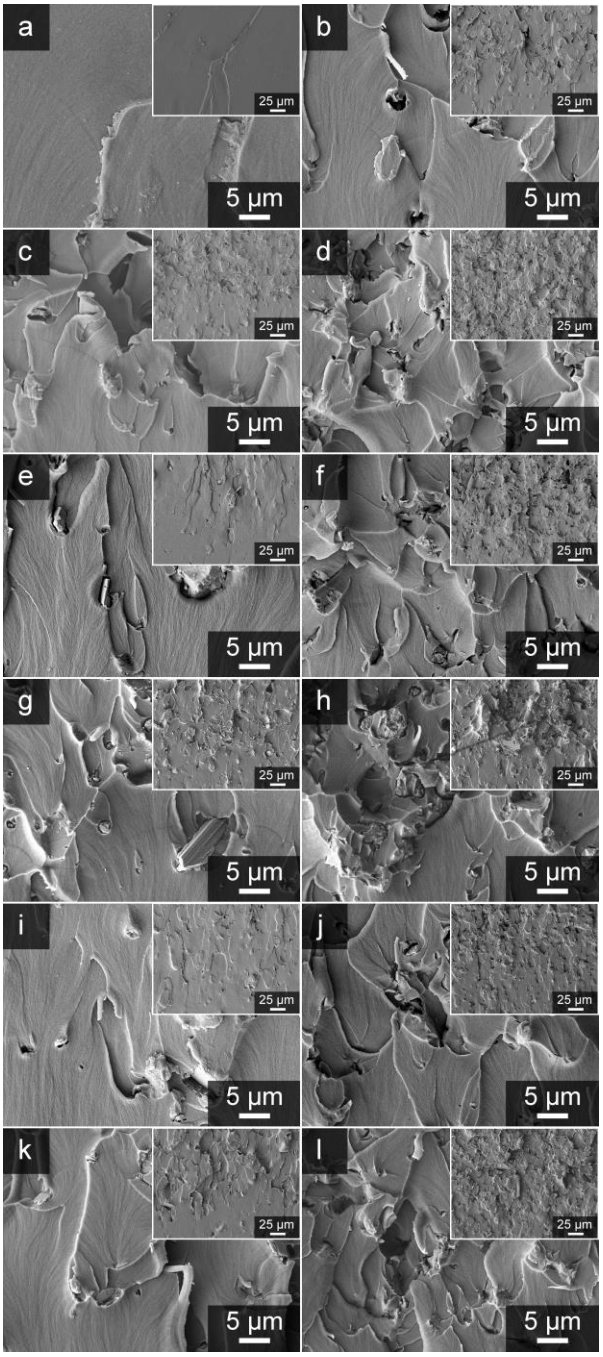

Figure 4.4. SEM fractographs of (a) neat VE resin; VE resin with (b) 0.02 wt % mGO, (c) 0.04 wt % mGO, (d) 0.08 wt % mGO; (e) 2 pphr GCC , (g) 5 pphr GCC (ground calcium carbonate); (f), (h) 0.04 wt % mGO added to (e) and (g), (i) 2 pphr kaolin, (k) 5 pphr kaolin, (j), (l) 0.04 wt % mGO added to (i) and (k). All micrographs were taken in the near-precrack region with the crack propagation direction from bottom to top. The insets show more extended areas in lower magnification SEM images.

To study the dependence of the toughening effect from incorporating mGO toughener on filler particle sizes, a set of VE/calcium carbonate samples were investigated along with VE/calcium carbonate/mGO composites. As shown in Figure 4.5, all calcium carbonate samples exhibit increased toughness compared to the neat resin, with the PCC-700 sample being the least improved. This can be understood by the fact that the strongly associated calcium carbonate particles in the PCC-70 sample form aggregates that are larger in dimension than those in the PCC-700 sample. The morphology difference of different calcium carbonate particles inside the VE resin can be observed in both fractographs (Figure 4.6) and TEM micrographs (Figure 4.7) of resin composite samples.

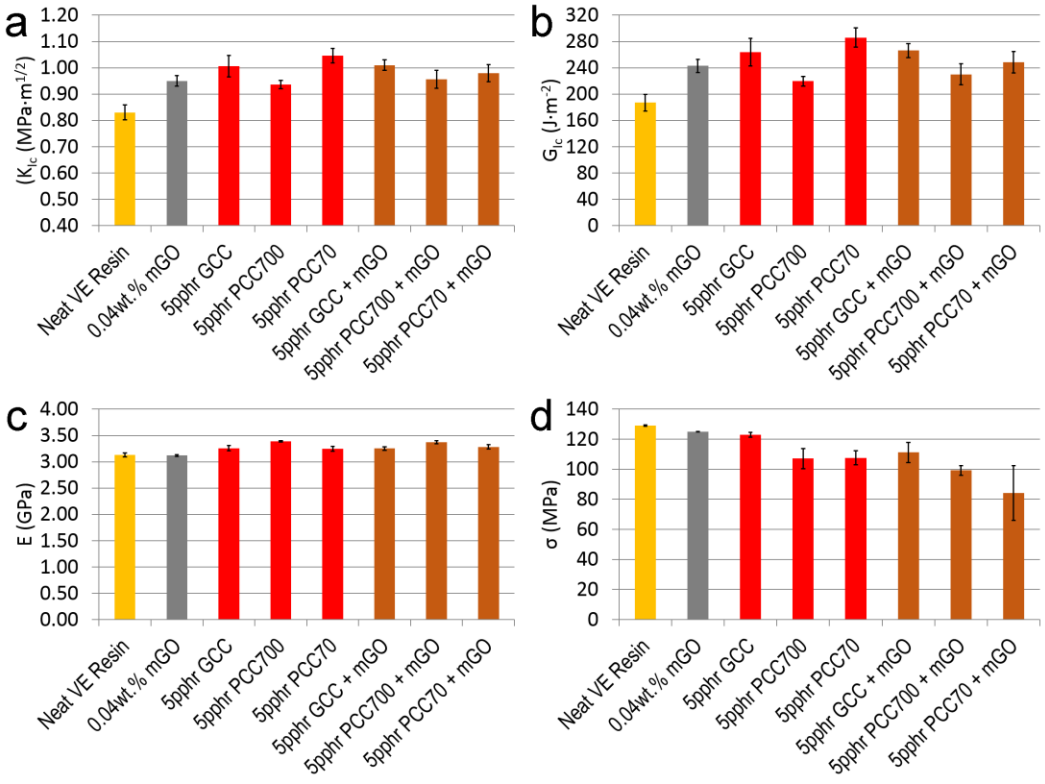

Figure 4.5. Mechanical properties of VE resin composites with calcium carbonate fillers and mGO toughener. (a) K_{IC}, (b) G_{IC}, (c) flexural modulus, and (d) flexural strength. The mGO loading level for all filler-containing samples is 0.04 wt %.

The difference in the sizes of the aggregates can be seen in Figure 4.6e and 4.6g. An aggregation size can be measured by drawing ellipses around particle clusters and averaging the length of major and minor axes. Typically, PCC-700 calcium carbonate forms 5–7 μm aggregates of a few particles, and PCC-70 forms larger aggregates (5–15 μm). The size of different calcium carbonate particles/particle aggregates can be seen in Figure 4.6 and 4.7. GCC itself contains large particles (3–15 μm, see Figure 4.6c) that exceed the dimensions of mGO aggregates, so the corresponding VE resin composites also show improved toughness due to crack deflection. Because all samples have inorganic particle inclusions larger than the aggregate sizes of mGO, the addition of mGO does not further improve the fracture toughness of these composites. Both PCC-700 and PCC-70 composite samples show cavitation around filler particles, which is an indication of poor particle-matrix bonding. Because poorly bonded particles can act as defect sites, a lowered flexural strength for both composite samples is expected, which is consistent with the experimental results (Figure 4.5d).

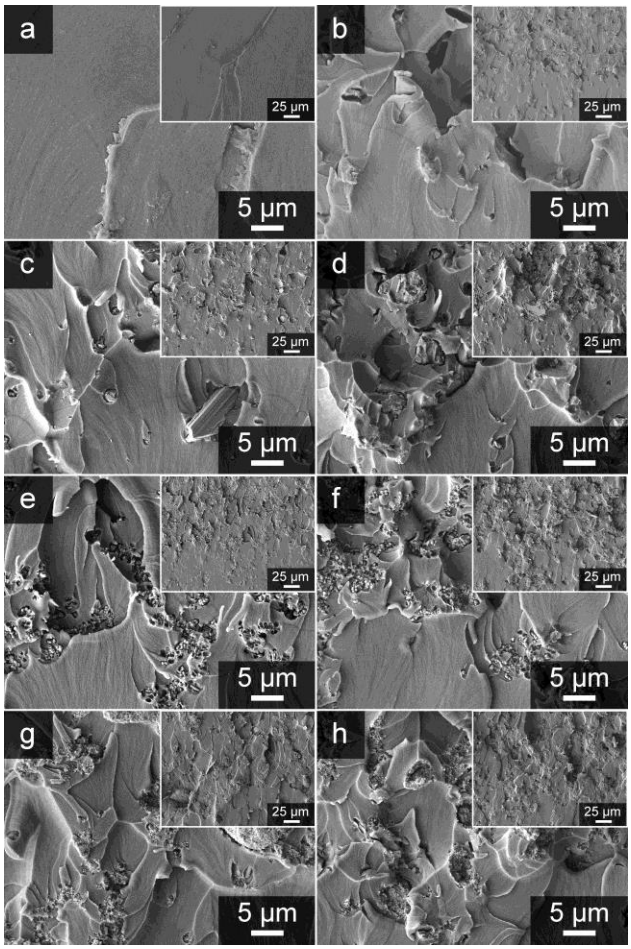

Figure 4.6. SEM fractographs of: (a) neat VE resin, VE resin with (b) 0.04 wt % mGO, (c) 5 pphr GCC, (e) 5 pphr PCC-700, (g) 5 pphr PCC-70, (d), (f), (h) with 0.04 wt % mGO added to (c), (e), and (g). All micrographs were taken in the near-precrack region with the crack propagation direction from bottom to top. The insets show more extended areas in lower magnification SEM images.

It should be noted that mGO could potentially be adsorbed onto the calcium carbonate particles/aggregates, therefore yielding negligible toughness improvement. To test this possibility, microtomed resin composite samples and uncured resin dispersions were investigated. Figure 4.7 shows the TEM micrographs of the microtomed calcium

carbonate/mGO/VE ternary composite. Because of the large particle size of GCC (Figure 4.7a) and PCC-700 (Figure 4.7b) samples, the microtoming process shatters the filler particles, leaving holes and calcium carbonate debris on the specimens. In contrast, particles can be readily observed in the PCC-70 specimen (Figure 4.7c) because the particle diameter is close to the thickness of the specimen. Both the holes and the slices of particle aggregates provide an indication of the dimensions of the filler inclusions inside the resin. Due to the contrast difference, it is difficult to see mGO aggregates in the presence of calcium carbonate filler. Therefore, higher magnification images of mGO in all three samples are also provided in Figure 4.7. From these images, there is no evidence indicating that mGO has a strong affinity towards calcium carbonate particles, so it is unlikely that the lack of toughening is due to mGO adsorption on the calcium carbonate surfaces.

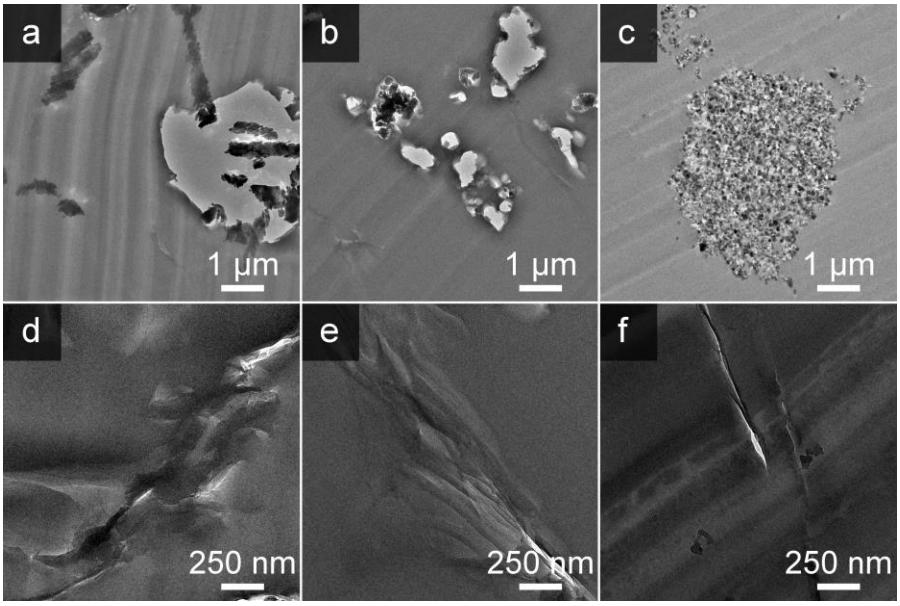

Figure 4.7. TEM micrographs of microtomed calcium carbonate/mGO resin composites at two different magnifications. (a), (d) 5 pphr GCC, (b), (e) 5 pphr PCC-700, (c), (f) 5 pphr PCC-70. All samples contain 0.04 wt % mGO.

Steady shear tests show that the rheological behavior of all calcium carbonate resin dispersions is unaffected by the addition of 0.04 wt.% mGO (Figure 4.8), which implies that there is little surface interaction between mGO toughener and the other filler particles. The higher viscosity of the PCC-70 resin dispersions at low shear stress indicates weak attraction between these small particles, as well as floc formation. As the shear rate increases, the flocs break down. As a result, the viscosity at higher shear rates was close to that of the other two suspensions. These observations are consistent with the results from the fractography and TEM analysis.

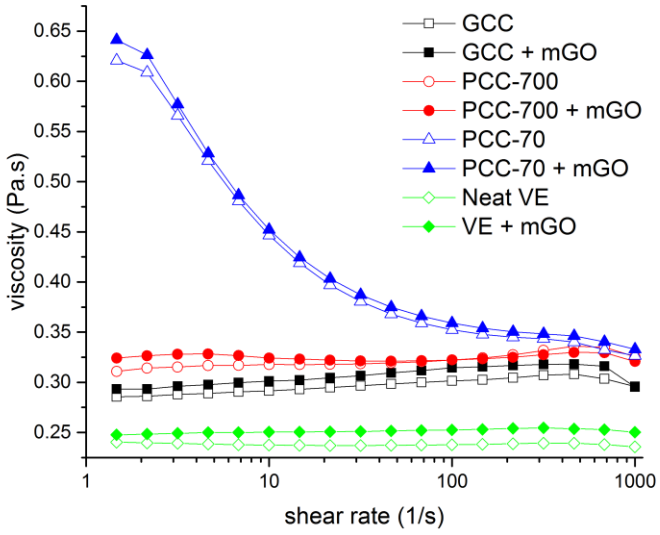

Figure 4.8. Steady shear viscosity of calcium carbonate/VE resin dispersion, with (solid symbol) or without mGO (hollow symbol). The mGO concentration is 0.04 wt %.

Differently surface-treated fumed silica samples behave differently with regards to resin toughening and filler-mGO interference. As shown in Figure 4.9, PDMS-treated silica (SA) significantly toughens the VE resin, but the fracture toughness decreases considerably

after mGO addition. In comparison, untreated fumed silica (SC) has no effect on VE resin fracture toughness, and the filled resin shows the normal toughness increase that is typically seen with mGO. The difference in the toughening effect can be explained as follows. The PDMS-treated fumed silica forms large secondary structures when dispersed in VE resin, and these particle aggregates are capable of changing the crack propagation direction. Untreated silica, however, disperses readily in the VE resin, thus the evenly distributed small particles cannot effectively deflect the propagating crack to toughen the matrix. Further evidence for the better dispersion of SC in VE resin is the slightly higher ultimate flexural strength observed in the SC composite compared to that of the SA composite (Figure 4.9d).

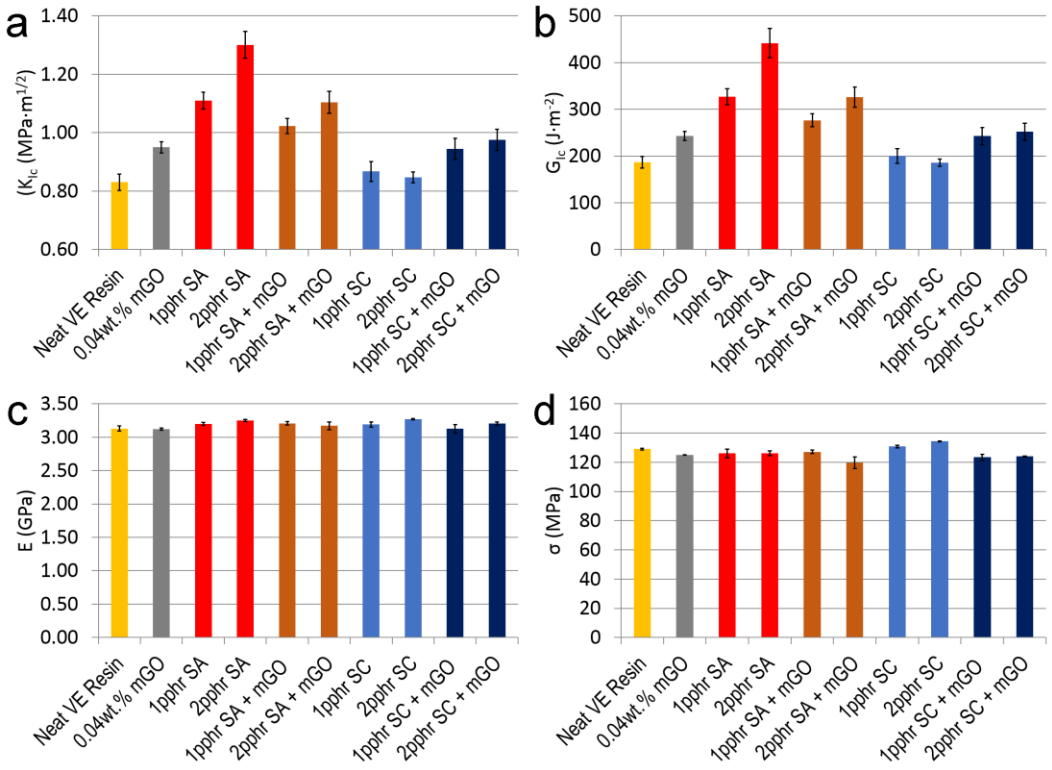

Figure 4.9. Mechanical properties of VE resin composites with different fumed silica materials and mGO toughener. (a) K_{IC}, (b) G_{IC}, (c) flexural modulus, and (d) flexural

strength. The mGO loading level for all filler-containing samples is 0.04 wt %. SC: CAB-O-SIL fumed silica M-5, untreated; SA: Aerosil fumed silica R202, PDMS treated.

The formation of a secondary structure for Aerosil fumed silica in VE resin was confirmed by rheological tests (Figure 4.10). The viscosity of SA, the PDMS modified silica, was strongly shear thinning, dropping by two orders of magnitude with shear stress. The significant difference in viscosity at low shear stress indicates that the SA silica attracts to each other much more than PCC70 and form a weak network in VE resin[238] with a yield stress around 3 Pa. The SC sample shows a Newtonian plateau at low shear stress about twice the viscosity of VE resin. The slight shear-thinning region at higher shear stress also indicates that particles in SC are not simple isolated spheres. Similar viscosities at high shear stress mean that the primary sizes of SA and SC silica are quite close to each other. Similar to the observations for the calcium carbonate dispersions, SA does not preferentially adsorb onto the mGO surface, which explains why the yield stress of SA suspensions does not increase with the presence of mGO. In fact, SC also does not interact strongly with mGO. Additional TEM images of microtomed composite specimens are provided in Figure 4.11.

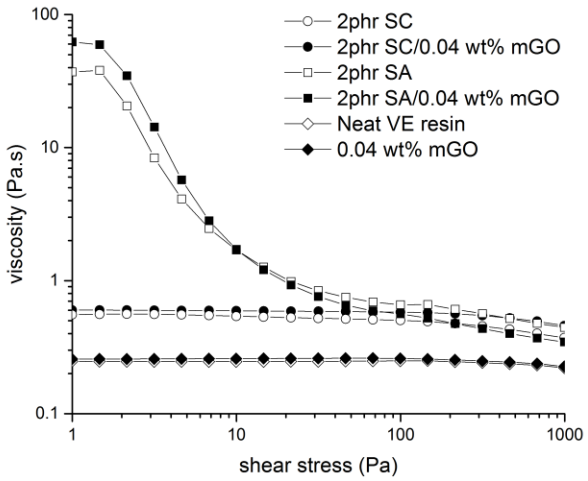

Figure 4.10. Steady shear viscosity of VE resin loaded with different fumed silica materials, with (solid symbol) or without mGO (hollow symbol).

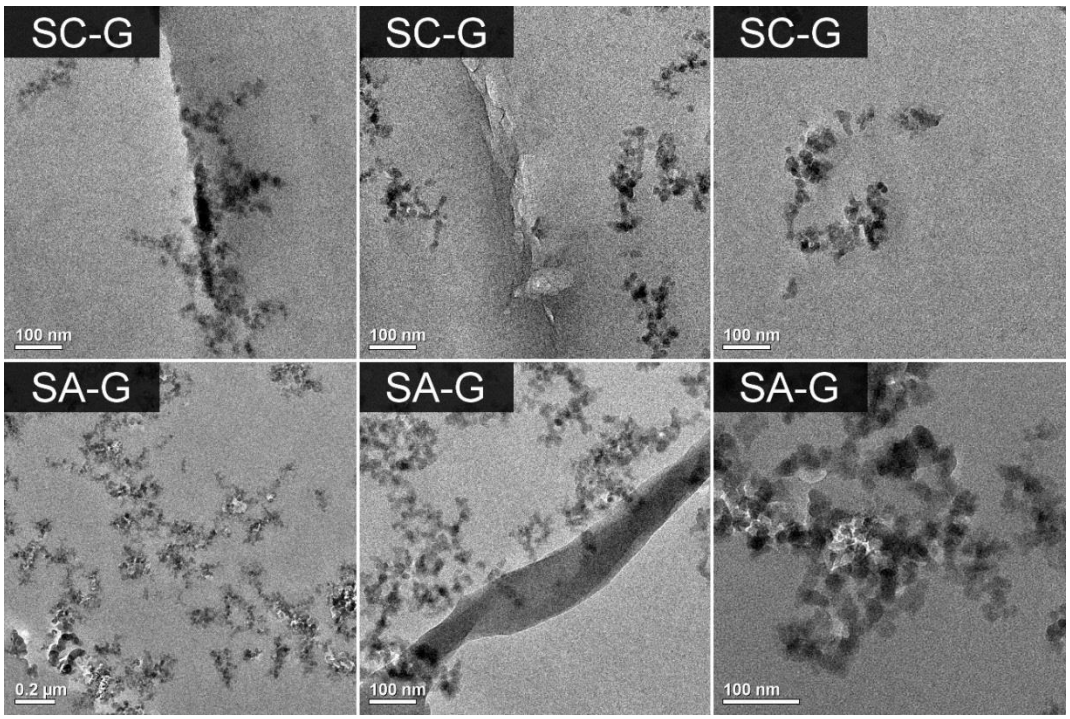

Figure 4.11 TEM micrographs of microtomed samples of different fumed silica (2 pphr) VE resin composites. SC: Cabosil fumed silica M-5, untreated; SA: Aerosil fumed silica R202, PDMS treated; G: with 0.04 wt % mGO.

The difference in particle-crack interactions between the resin sample with SA and that with SC can be observed in SEM fractographs shown in Figure 4.12. VE resin with 2 pphr Aerosil fumed silica exhibits a rough near-precrack fracture surface with plastic deformation features such as blunt edges and irregular surface textures, whereas the resin sample made with CAB-O-SIL fumed silica at the same loading level has a rather smooth fracture surface that lacks evidence for plastic deformation. After adding mGO to the VE/SA sample, features associated with plastic deformation, such as stretched edges and smooth bulges, become less apparent, and the new fracture surface texture resembles that of a VE/mGO composite. Aggregates of treated fumed silica can still be observed, but the network appears to be partially disrupted by mGO sheets, because now there are large areas on the fracture surface that show no silica particles. This may be the reason that VE/SA/mGO samples exhibit fracture toughness values significantly lower than those of the VE/SA composites, but still higher than that of VE/mGO. Silica aggregates are not prominent on the fracture surface of VE/SC/mGO sample, and the small clusters of untreated silica seem incapable of altering the crack propagation direction. Therefore, the fracture toughness of VE/SC/mGO samples is very close to that of the VE/mGO sample.

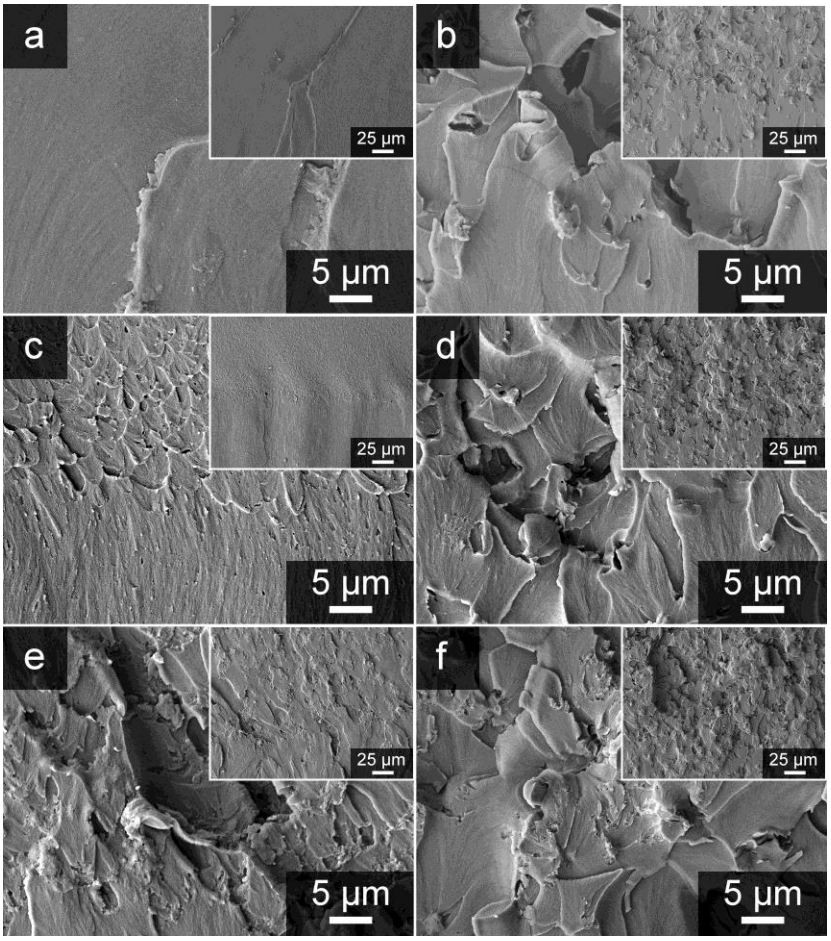

Figure 4.12. SEM fractographs of (a) neat VE resin, VE resin with (b) 0.04 wt % mGO, (c) 2 pphr SC, (d) 2 pphr SC and 0.04 wt % mGO, (e) 2 pphr SA, (f) 2 pphr SA and 0.04wt.% mGO. All micrographs were taken in the near-precrack region with the crack propagation direction from bottom to top. The insets show more extended areas in lower magnification SEM images.

The size effect of the filler particles on thermoset toughening can be explained using plastic zone theory. The plastic zone is the volume around the crack tip that deforms plastically to relieve the crack tip from forming a stress singularity. Although it is difficult to measure the yield stress of a highly crosslinked thermosetting polymer, we can nonetheless estimate the size of the plastic zone in the neat resin by using its flexural

strength value as the yield stress. According to Irwin's model, we can use equation 4.3 to calculate the plastic zone size in the crack propagation direction:[239]

$$r_p = \frac{K_{Ic}^2}{6\pi\sigma_Y^2} \quad (4.3)$$

Here, r_p is the plastic zone radius, K_{IC} is the mode I critical stress intensity factor, σ_Y is the yield stress of the polymer, which, in this case, is assumed to be the flexural strength. The r_p for neat VE resin is calculated to be 2.2 μm. This value implies that inorganic inclusions in the resin need to be a few micrometers in size or larger to show a toughening effect. Small and well dispersed particles are incapable of transfering stress further outside the plastic zone; therefore, no toughening is observed when such particles are incorporated in the resin. Particles or particle aggregates inside the resin matrix whose size is comparable to the plastic zone size of the neat resin will toughen the VE rein to some extent. The composite materials will deviate more from the homogeneous and isotropic assumption if the filler size or loading level further increases, therefore, equation 3 may no longer be applicable.

4.4 Conclusions

Our results show that dodecylamine functionalized GO (mGO) can toughen VE resin at a concentration as low as 0.02 wt.%, which agrees with studies that have demonstrated mGO toughening in other resin systems such as unsaturated polyester and epoxy.[192, 220, 221] The main toughening mechanism in mGO toughened VE resin is found to be crack deflection, which gives a toughness plateau at higher particle concentration. To study how common inorganic fillers interact with mGO in resin toughening, three types of filler, namely fumed silica, calcium carbonate, and kaolin clay, were investigated. The results

indicate that these fillers themselves can provide toughening effects when incorporated in VE resin, if the size of the particle or the particle aggregates is comparable to or larger than the plastic zone size of the vinyl ester resin (1–3 micrometers). For calcium carbonate fillers of different particle sizes between 70 nm and 15 μm, the smallest particles brought about the greatest enhancement in fracture toughness, even though these nanoparticles formed agglomerates in the resin. For a given particle size, the surface chemistry also has an important influence on toughness of a VE resin, as was demonstrated for silica nanoparticles: fumed silica significantly toughened the VE resin only if its surface had been treated with PDMS. When additional mGO is added to the filler-containing VE resin, the change in fracture toughness depends on how the size of the biggest particle aggregates changes. If the addition of mGO disrupts the formation of filler aggregates, a decrease in toughness can be observed. If the filler particles or aggregates are significantly smaller than mGO aggregates, adding mGO will improve the toughness. If the filler aggregates are comparable in size with mGO, there will be no change in toughness with additional mGO incorporation. This agrees well with plastic zone theory in which the size of plastic zone is estimated to be close to the size of mGO sheets. The relative particle/particle aggregation sizes of the inorganic filler or toughener to the plastic zone size of the matrix resin determines the observed fracture toughness of particle-filled resin composite. This could be true for all thermosets. Therefore, care must be taken when inorganic nano-toughener is used to toughen filler-containing VE resin systems, and it is important to understand filler–toughener interactions for inorganic tougheners.

Chapter 5*

Effect of Primary Particle Size and Aggregate Size of Modified Graphene Oxide on Toughening of Unsaturated Polyester Resin

5.1 Introduction

Graphene–polymer nanocomposites have recently become a subject undergoing intense study due to their unique properties that include good electrical[92, 97, 98, 100] and thermal conductivity,[240-242] high modulus and strength,[88-90] low gas permeability,[122, 123] and good flame retardancy.[107, 108] These properties are directly related to the structure of graphene, a single layer of honeycomb-arrayed carbon atoms. The strong covalent networks within the graphene plane give it high mechanical strength; the overlapping carbon *p*-orbitals perpendicular to the basal plane result in semi-metallic conductivity; and very high aspect ratio leads to a low percolation threshold and effective gas barrier properties. Among many applications, ranging from electromagnetic shielding[162] to corrosion resistive coatings,[131] graphene-based materials are used to toughen polymers, particularly thermosets.[192, 220-222]

Thermosets are highly crosslinked polymers that have high modulus, good corrosion resistance, low density compared to metal and concrete, and good processability.[134] These properties render thermosets very good candidates for light and strong structural materials, and, therefore, they are widely used in chemical, transportation, and recreational industries.[134, 231] However, thermosets are brittle materials that can crack and fail fast once

* Mechanical data used in this chapter were collected and processed by Kunwei Liu.

a small damage or defect appears, thus toughening agents are often added. Commercial tougheners for thermosets, including liquid rubbers,[155] core-shell rubbers,[161] and block copolymers,[167] can significantly improve the fracture toughness of a resin, but an increase in viscosity and a decrease in modulus and glass transition temperature are often the trade-off. Unlike polymeric tougheners, toughening thermosets with graphene derivatives usually results in no viscosity change, no modulus reduction, and no T_g reduction of the matrix resin, all of which is advantageous.[192, 220-222]

Since the first discovery of graphene-toughening of resins, researchers have developed many new functionalization processes and optimized composite fabrication processes to achieve better toughening of the composites.[89, 223, 243] The community generally accepts that strong particle–matrix interfaces and better dispersion will increase the fracture toughness improvement for resins toughened with inorganic particles, so most surface modifications are designed to achieve these goals. But some contradictory results suggest that these rules do not always hold true for graphene composites.[176, 177, 233, 244] Therefore, it is still unclear what can cause a change in the toughening effect. Also, as a high-aspect-ratio nanomaterial, the lateral dimensions of modified graphene oxide sheets may influence the toughening effect, but very few studies on this issue have been carried out.

To address these questions, graphene oxide (GO) samples with identical chemical composition but different sheet sizes were chemically modified and dispersed into an unsaturated polyester (UP) resin to prepare polymer composites. The composites were then tested for fracture-related mechanical properties to help understand how the size of GO particles changes the toughening effect of the corresponding surface-modified GO. In addition, three different surface modifications were employed to prepare modified GO

samples with the same particles size. These modifications were designed to produce different aggregate sizes of mGO in the UP resin to study how different aggregation behaviors inside a UP resin are related to different toughening responses with respect to mGO loading levels. Scanning electron microcopy-based particle size analysis and postmortem fracture surface analysis, in addition to mechanical tests, were used to elucidate the toughening mechanisms in various mGO-UP resin composites.

5.2 Experimental

Materials

N,*N*'-dimethylformamide (DMF, 99.8%, anhydrous), dichloromethane (DCM, 99%), 2-butanol (99%), cobalt(II) 2-ethylhexanoate solution (65 wt % in mineral spirits), 4-*tert*-butylcatechol (98%), styrene (99%), 2-butanone peroxide (Luperox DDM-9, 35 wt % in 2,2,4-trimethyl-1,3-pentanediol diisobutyrate), 2,4-toluene diisocyanate (TDI, 95%), dihexylamine (DHA), and octadecylamine were purchased from Sigma-Aldrich. Dodecylamine (DDA, 98%) was obtained from Alfa-Aesar. Deionized (DI) water with a resistivity of 18 MΩ·cm was produced onsite using a Barnstead purification system. The AROPOL 8422 unsaturated polyester resin was supplied by Ashland Inc. GO in water slurry (about 1.5 wt.%) was purchased from Graphenea.

Synthesis of modified GO

The stock GO slurry purchased from Graphenea was diluted to 4 mg/mL by adding DI water and then pH was adjusted to 9 using 4 wt % sodium hydroxide solution. The solution was then sonicated for 2 h in a bath sonicator (Branson 3510, 135W input power). The resulting GO dispersions were used directly for dodecylamine or octadecylamine

functionalization or freeze-dried for TDI-dihexylamine functionalization (Freezemobile, SP Scientific).

A detailed procedure for the synthesis of dodecylamine-modified GO can be found elsewhere.[233] Briefly, one part by volume of an aqueous dispersion of GO (4 mg/mL) prepared by sonication was rapidly mixed with two parts by volume of a solution of 6 g/L dodecylamine in ethanol. The mixture was then heated to 70 ˚C and allowed to react for 24 h under stirring. The crude product was washed 4 times with ethanol and 3 times with styrene by mixing and centrifugation to obtain the final product. Purified dodecylamine-modified GO (DDA-GO) was redispersed in styrene at approximately 1 wt % with 30 min bath sonication to prepare the styrene masterbatch.

The octadecylamine modification procedure was similar to that of the dodecylamine modification. The GO dispersion was quickly mixed with 6.12 g/L octadecylamine in 2-butanol at a 1:3 volume ratio. The resulting suspension was heated to 70 ˚C under stirring for 24 h. The reaction mixture was then centrifuged to collect the crude product, and the product was washed 4 times with ethanol and 3 times with styrene by repeated vortex mixing and centrifugation. The final product (ODA-GO) was also dispersed in styrene.

For TDI-dihexylamine modification, freeze-dried GO was used. In a typical synthesis, 300 mg of GO was dispersed in 150 mL of anhydrous DMF by bath sonication for 1 h. The resulting GO dispersion was purged under dry nitrogen for 1 h. Subsequently, 6 mL of TDI was added, and the mixture was heated at 60 ˚C with stirring for 24 h under nitrogen. The reaction mixture was cooled to 40 ˚C, and 12 mL of dihexylamine was added. After another 24 h reaction at 40 ˚C, the suspension was mixed with diethyl ether at a 1:2 volume ratio.

The ether-diluted suspension was centrifuged at 8000 rpm for 1 h to collect the crude product as the sediment. Crude modified GO was then purified by washing with styrene 4 times and redispersing it in styrene (TDI-DHA-GO) to prepare a styrene masterbatch.

To further suppress aggregation of TDI-DHA-GO, a resin masterbatch was prepared. For a typical synthesis, 160 mg of TDI-DHA-GO (12.15 g styrene masterbatch, 1.32 wt %) was dispersed in 100 mL of DCM. Then the dispersion was homogenized by probe sonication for 15 min (Misonix S-4000, 4 s pulse, 2 s pause, 100% amplitude at 600 W, 1/4" probe) together with constant mechanical stirring. To this dispersion, 10.5 g of stock UP resin (71% UP prepolymer and 29% styrene) in 50 mL DCM was added under vigorous stirring. Finally, the mixture was vacuum distilled to remove most of DCM and some styrene to obtain the resin masterbatch (RMB) of TDI-DHA-GO. A typical composition of this resin masterbatch is consisted of 0.9 wt % modified GO, 41.2 wt % UP prepolymer, and 57.9 wt % of styrene.

Preparation of resin composite

To prepare formulated AROPOL 8422 UP resin containing 45% styrene, stock resin was first diluted with styrene. To 100 g diluted resin, 20 mg of 4-*tert*-butylcatechol inhibitor and 100 mg of 65% cobalt(II) 2-ethylhexanoate promoter solution were added. For all DDA-GO and ODA-GO samples, a styrene masterbatch was used to prepare the resin dispersion. Thus, the extra styrene contributed by the masterbatch was counterbalanced by the corresponding reduction of the amount of styrene added during the dilution step. A similar formulation adjustment was made when a resin masterbatch was used for preparing TDI-DHA-GO samples. All resin dispersion samples were shear-mixed

with a 1" Cowles blade at 2000 rpm for 15 min (Eurostar power-b, IKA) to obtain a uniform dispersion. Subsequently, dispersions were initiated with 1.25 g 2-butanone peroxide initiator per 100 g resin and allowed to react for 10 min with magnetic stirring at a moderate speed, followed by 10 min degasing in vacuum. Resins were then poured into glass molds made by sandwiching U-shaped, high temperature silicon rubber cords (3-mm in diameter for compact tension specimens, and 1.5-mm for flexural modulus/strength testing specimens) between pairs of 3/16-inch-thick borosilicate glass plates. Samples were cured at room temperature for 24 h before post-curing for 3 h at 70 °C and 3 h at 120 °C. For mechanical testing, fully cured resin plaques were cut into test specimens according to ASTM D790-10 and ASTM D5045-99. A detailed description of specimen dimensions can be found in our previous publication.[220]

Characterization

A JEOL 6700 field emission scanning electron microscope (SEM) with a tungsten filament source was used for imaging. SEM images were taken using an acceleration voltage of 5 kV. Fractography samples were coated with 5 nm Pt prior to imaging. GO and mGO samples were made by dip coating DCM diluted particle suspensions onto silicon wafer chips (Ted Pella lnc.). For GO/mGO particle analysis, Gwyddion[245] software was used to remove background and scanning artifacts in a SEM micrograph, and Image J[246] was used to binarize the micrographs and analyze the particles.

Flexural modulus and ultimate flexural strength were determined using an RSA-G2 solids analyzer (TA Instruments) according to ASTM D790-10. The three-point bending experiment was performed with a span-to-thickness ratio of 16:1 and a crosshead rate of 1

mm·min^{-1} (0.01 min^{-1} strain rate). The fracture toughness test was performed using a compact tension (CT) method on an Instron 5966 single-column system equipped with a 500 N load cell according to ASTM D5045-99. After having been pre-cracked by tapping with a liquid-nitrogen-cooled fresh razor blade, all specimens were pulled at 10 mm·min^{-1} crosshead speed until complete failure. In a typical test, five three-point bending and at least ten CT specimens were tested, and the average was reported along with the standard deviation.

The critical stress intensity factor (K_{IC}) was calculated using equation 5.1, and the critical strain energy release rate (G_{IC}) was calculated via equation 5.2.

$$K_{IC} = \frac{P_C}{B\sqrt{W}} \times \frac{\left(2+\frac{a}{W}\right)\left[0.886+4.64\frac{a}{W}-13.22\left(\frac{a}{W}\right)^2+14.72\left(\frac{a}{W}\right)^3-5.6\left(\frac{a}{W}\right)^4\right]}{\left(1-\frac{a}{W}\right)^{\frac{3}{2}}} \quad (5.1)$$

$$G_{IC} = K_{IC}^2\left(\frac{1-\upsilon^2}{E}\right) \quad (5.2)$$

Here, P_C is the critical applied load, B is the specimen thickness, W is the specimen width; a is the crack length, E is the flexural modulus, and υ is the Poisson's ratio of the VE resin, which is taken to be 0.39.

5.3 Results and discussion

To study how the sheet size of the precursor GO affects the toughening of mGO, four GO samples with different sheet sizes were prepared. Equal portions of GO slurry from an identical batch were diluted to 4 mg/mL, and each sample was sonicated in a bath sonicator for different time durations. The size of GO sheets was characterized by SEM, and representative micrographs are shown in Figure 5.1.

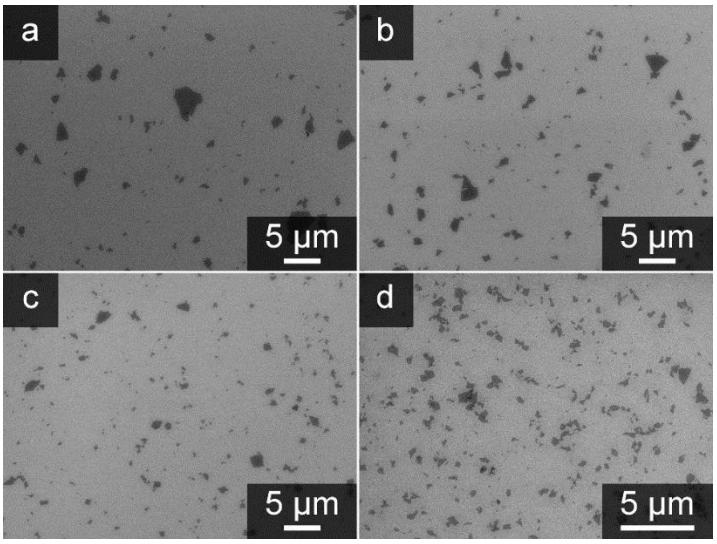

Figure 5.1. SEM micrographs of GO samples subject to sonication for different durations: (a) 15 min, (b) 30 min, (c) 60 min, and (d) 120 min.

It is obvious that sonication breaks down GO and reduces its lateral sizes. The lack of contrast within and between the irregularly-shaped gray spots in a SEM image hints that these spots are single-layered GO. AFM data also indicate that samples sonicated for at least 15 min contain predominantly monolayered GO, which means that the GO thickness is not a variable in this study. A set of typical AFM data of samples sonicated for 15 min and 60 min sonicated samples is presented in Figure 5.2.

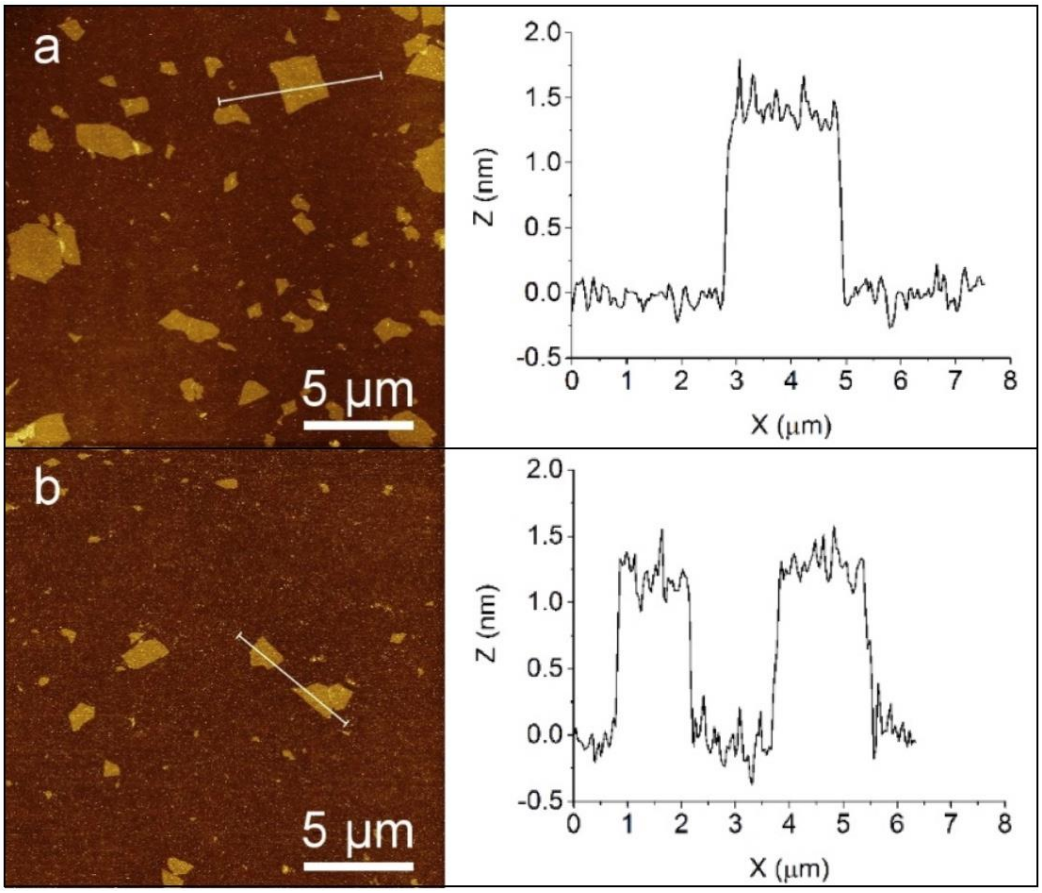

Figure 5.2. AFM Z-plots of GO samples subjected to sonication for different durations: (a) 15 min, and (b) 60 min. The profile plots on the right correspond to the data marked in the Z-plots with white lines. The observed heights correspond to monolayers of GO.

To quantitatively analyze the difference between differently sonicated GO samples, multiple SEM micrographs were analyzed using software and the distributions of GO sheet sizes are presented in Figure 5.3.

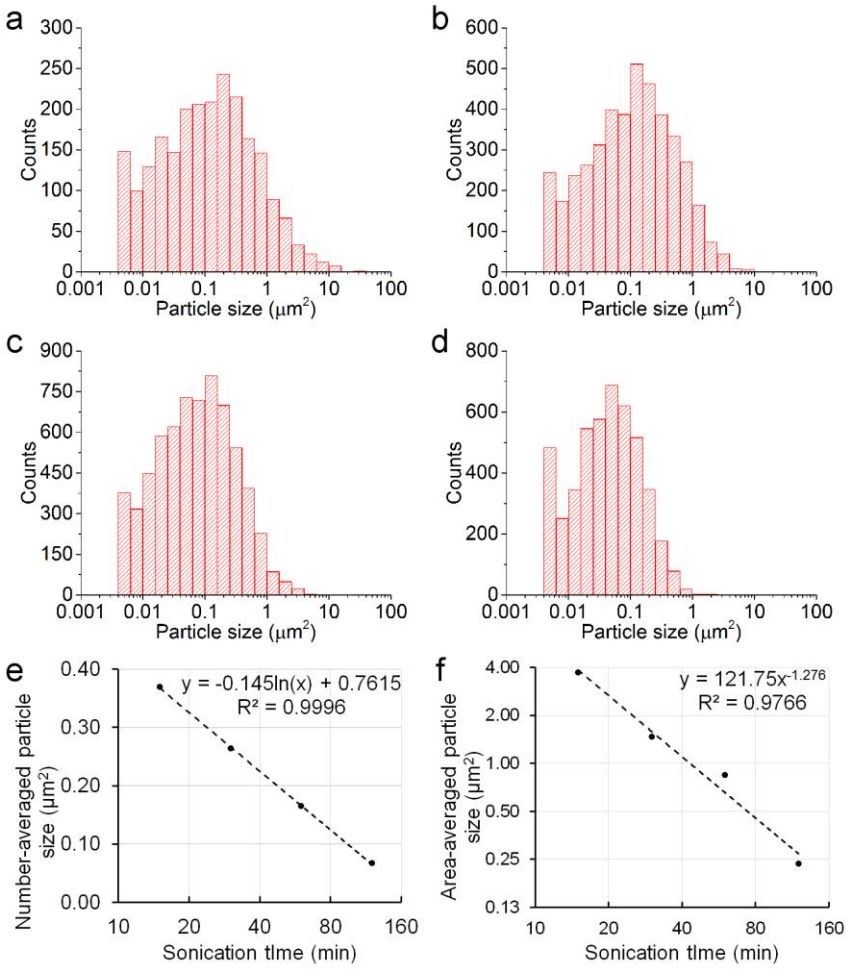

Figure 5.3. Effect of sonication time on particle size distributions of GO: (a) 15 min, (b) 30 min, (c) 1 h, and (d) 2 h. (e) Number-averaged and (f) area-averaged particle size with respect to sonication time. The particle size limit in this plot is 0.004 μm^2 due to the resolution of the SEM micrographs.

As the sonication time becomes longer, the tail of the size distribution curve diminishes, and the frequency curve shifts towards smaller sizes. To describe the average sizes of GO samples, two values are given here: number-averaged particle area, N_A, (5.3a) and area-averaged particle area, S_A (5.3b).

$$N_A = \frac{\sum N_i A_i}{\sum N_i} \quad (5.3a)$$

$$S_A = \frac{\sum N_i A_i^2}{\sum N_i A_i} \quad (5.3b)$$

Here, N is the number of particles counted, and A is the area of a particle in pixels on SEM micrograph. N_A shows how sheets break down during sonication, and S_A depicts the size differences among samples. The plot of area-averaged particle area is provided here because the size follows a Γ-distribution and N_A underestimates the contribution from large particles.

This analysis shows that N_A has a linear relationship with respect to logarithmic sonication time, and S_A shows an exponential decay with respect to sonication time. This is in good agreement with previously published work.[247] S_A better represents the information obtained from the SEM micrographs, because tiny fragments generated by sonication contribute much less to the mean. In addition, particles that are much smaller than the plastic zone size of the polymer matrix do not show any toughening effect in a resin composite. Thus, for the rest of the paper, S_A will be used to describe average particle sizes. GO samples with different sizes were then modified with dodecylamine, and the resulting DDA-GO products were added to UP resin at different loading levels to prepare composite samples. This modification was chosen because it can generate a modified GO that disperses well in the UP resin. The normalized fracture toughness and flexural strength values are plotted in Figure 5.4.

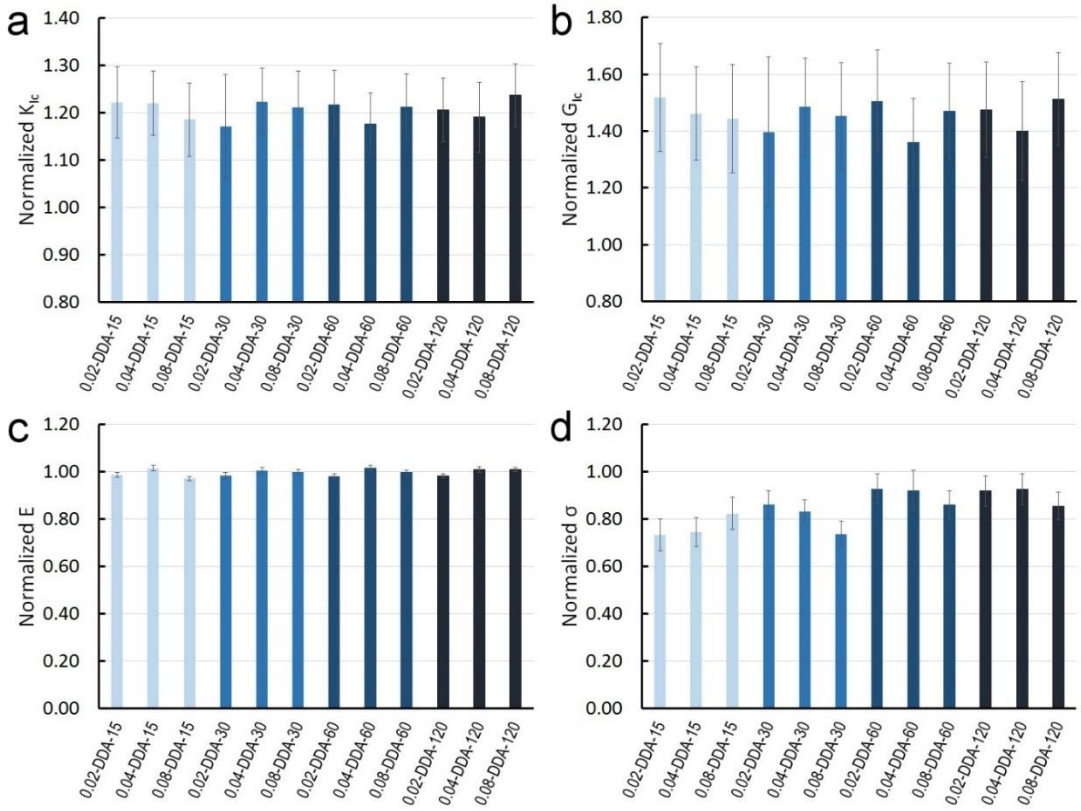

Figure 5.4. (a) Fracture toughness values, (b) fracture energy, (c) modulus, (d) flexural strength of mGO-toughened UP resins with various GO sizes, normalized to corresponding values for the neat resin. All samples are named using the notation "loading in wt %–DDA–sonication time in minutes."

The fracture toughness test shows that the size difference in GO has no direct effect on the toughening of DDA-GO. Flexural moduli (Figure 5.4c) of all samples are very close to each other due to the low mGO loading level. Consequently, G_{1C} values (Figure 5.4b) of these composites follow similar trends as K_{1C} values. Compared to K_{1C}, flexural strength is more sensitive to filler particle sizes. Indeed, a small difference in ultimate strength is observed when comparing DDA-15 and DDA-120, DDA-120 showing higher values for loadings of 0.02 and 0.04 wt %. The observation of similar mechanical properties of DDA-

120 and DDA-60 samples suggests that the actual mGO particle sizes of these two samples may be very close to each other, despite the precursor GO differing in size by a factor of almost 16. If this is the case, aggregation of mGO sheets must have occurred, and the actual aggregate sizes of DDA-GO samples are insensitive to the starting GO particle size. Unfortunately, it is very difficult to directly measure filler aggregate sizes inside a polymer composite, especially in a statistically meaningful way. To estimate the aggregate sizes, we, therefore, assumed that for particles with identical surface treatment, the aggregate sizes in composites are related to the particle sizes in a styrene masterbatch. Thus, a size analysis of DDA-GO in a masterbatch was carried out similar to that for pristine GO samples, and some representative SEM micrographs are shown in Figure 5.5.

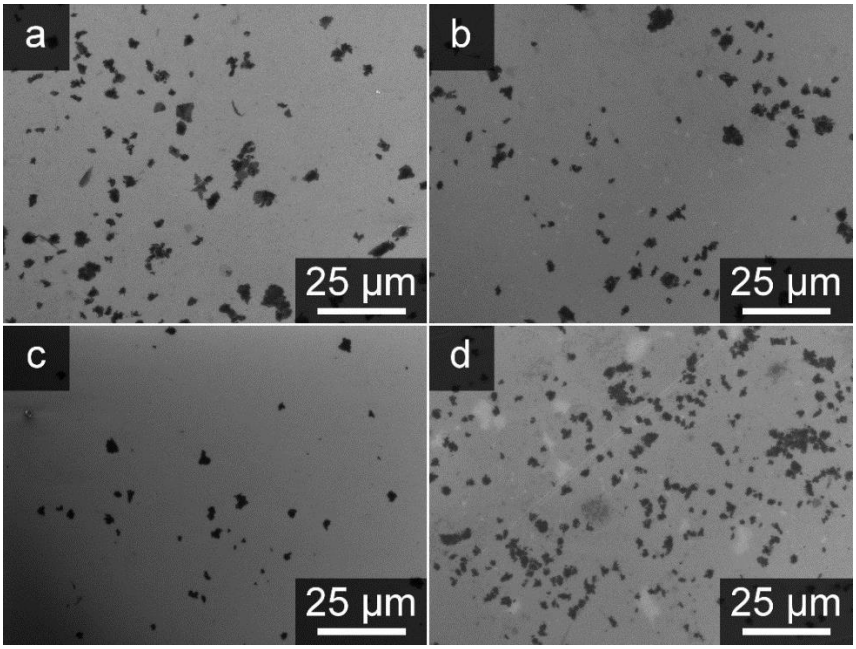

Figure 5.5. SEM images of DDA samples made with GO of different sizes, which had been varied by changing sonication times. (a) DDA-GO made with 15-min sonicated GO, (b) 30 min, (c) 1 h, and (d) 2 h.

The sizes of all DDA-GO samples increased significantly compared to those of the precursor GO. The DDA-15 sample has an average particle size of 11.9 μm^2, but the average sheet size for its precursor was only 3.72 μm^2. The particle size of DDA-120 sample also changed from 0.235 μm^2 to 6.92 μm^2 after chemical modification. Size differences in these two GO samples diminish from about 16 times to about 0.6 times after dodecylamine modification, and the contrast within each particle indicates that these particles are aggregates of many smaller mGO sheets (Figure 5.6). This result supports the hypothesis that surface modification of GO can cause aggregation, and modification methods, including post-synthesis processing, have a greater influence on mGO aggregate size than does the size of starting materials.

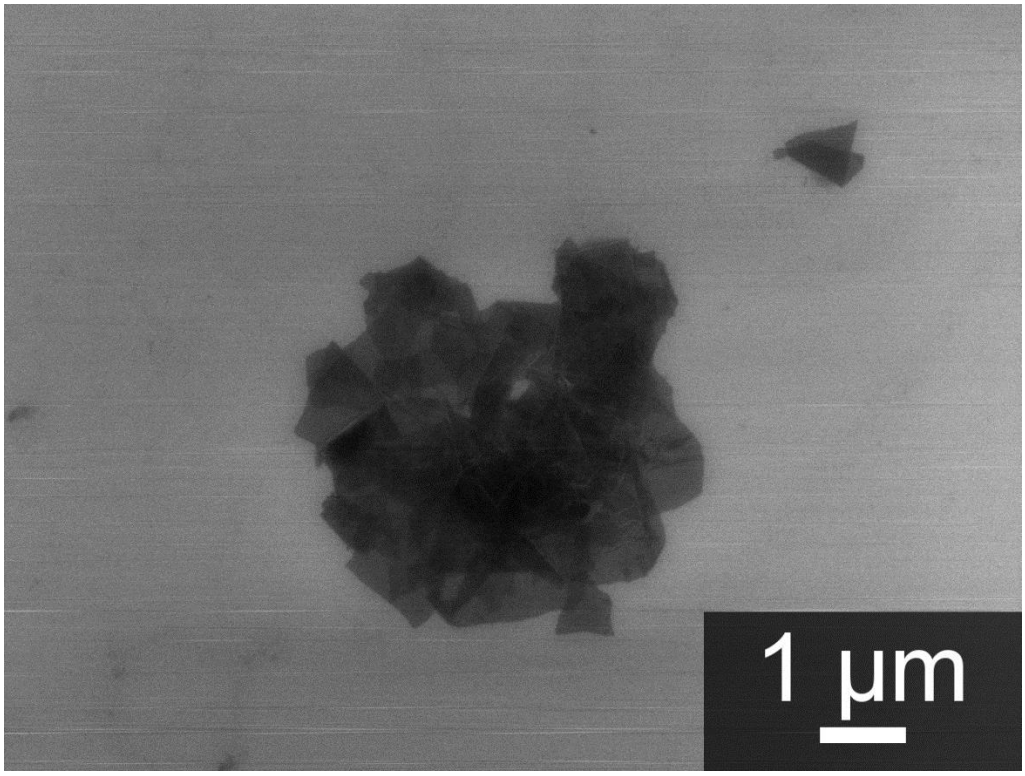

Figure 5.6. A high magnification SEM micrograph of the DDA-30 sample. The aggregate in the center is comprised of many smaller mGO sheets.

Another strong evidence for similar aggregate sizes in all DDA samples can be seen from the SEM fractography analysis of DDA-GO composites. Shown in Figure 5.7 are the crack surfaces of failed compact tension samples. According to the nature of crack propagation, a fracture surface has two distinctive regions: a near-precrack region, where the resting crack front starts to move under stress, and a fast propagation region, where the moving crack front becomes unstoppable. A sample micrograph of different areas of a crack surface can be found in Figure 2.9 in Chapter 2. These fracture surfaces of composites loaded with different DDA-GOs are similar to each other. All near-precrack regions (Figure 5.7c, e, g, and i) show crack-deflection events that appear as many small irregular fracture surfaces tilted randomly. This is because the crack plane tilts as it encounters a randomly oriented graphene particle in the near-precrack region. A crack plane becomes hard to perturb in the fast propagation region, and the pits and bulges on a crack surface here show where the particles are located and the relative sizes of them. It can be seen from Figure 5.7 that both the features on the near-precrack regions and fast propagation regions are similar for all DDA samples, which suggests that the mGO aggregate sizes and the quality of dispersion are also very close across the series. Fractography analysis shows that the aggregate size, not the GO sheet size, is more important in determining the fracture toughness of a graphene composite.

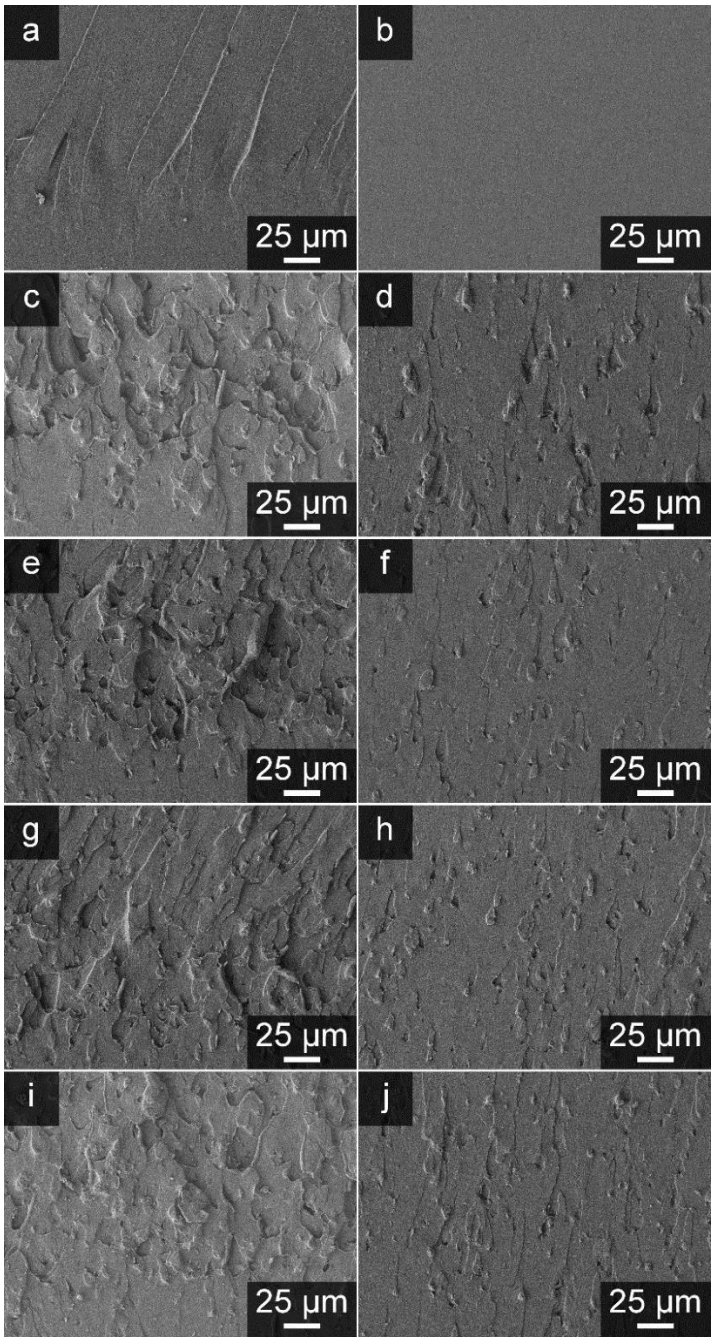

Figure 5.7. SEM fractographs of (a), (b) neat UP resin, (c), (d) DDA–15, (e), (f) DDA–30, (g), (h) DDA–60, (i), (j) DDA–120. Panels (a), (c), (e), (g), and (i) show the near-precrack regions, and panels (b), (d), (f), (h), and (j) show the fast propagation region. All composites were loaded with 0.04 wt % DDA–GO, and the crack propagation direction is from the bottom to the top.

To control the aggregate sizes of mGO, two new surface modifications were introduced. Compared to dodecylamine modifications, TDI-dihexylamine modification produces GO derivatives (TDI-DHA-GO) with less aggregation, and octadecylamine modification yields a product (ODA-GO) that aggregates even more inside the UP resin. Because the synthesis of TDI-DHA-GO requires freeze-dried GO, the product after purification contains large aggregates. Thus, some extra post-synthesis processing steps were added to decrease the aggregate size. These include diluting and sonicating the product in dichloromethane, rapid mixing with dichloromethane-diluted stock UP resin, and vacuum distillation to fully remove dichloromethane and partly remove styrene. The final product is in a resin masterbatch, which typically contains 1 wt % mGO. A SEM size comparison of DDA-GO, ODA-GO and TDI-DHA-GO samples made with 2-h sonicated GO is shown in Figure 5.8.

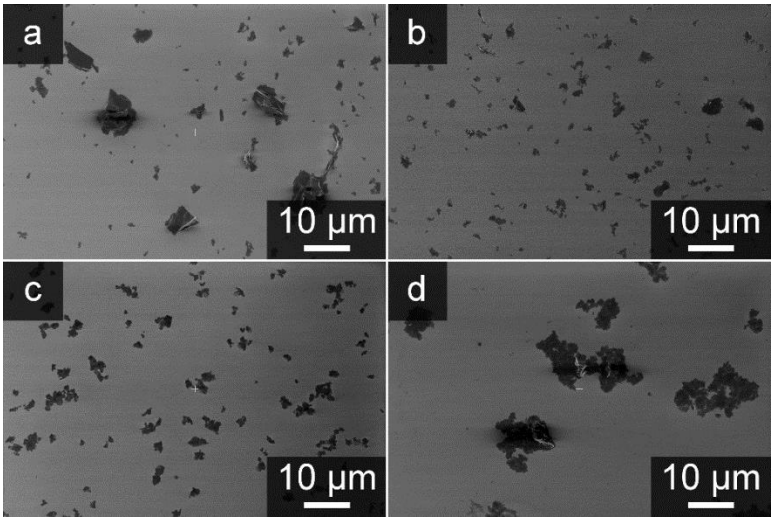

Figure 5.8. SEM images of (a) TDI-DHA-GO from a styrene masterbatch, (b) TDI-DHA-GO from a sonicated DCM suspension, which was used for preparing resin masterbatch, (c) DDA-GO from a styrene masterbatch, and (d) ODA-GO from a styrene masterbatch. All samples had been sonicated for 2 h.

Particle size analysis indicates that the average sizes of TDI-DHA-GO, sonicated TDI-DHA-GO, DDA-GO, and ODA-GO are 47.7, 2.32, 6.01, and 109 μm^2 respectively. It should be noted that all chemically modified GO particles are highly aggregated, so the size measured in SEM analysis is based on the projections of flattened three-dimensional aggregates. The average size of DDA-GO made with 2h sonicated GO differs slightly from the value provided in the previous section, because the SEM specimens are made from different batches of DDA-GO. Differently modified GO were added to UP resin at different loading levels for testing mechanical properties, and values of mechanical properties, normalized to the neat resin, are shown in Figure 5.9.

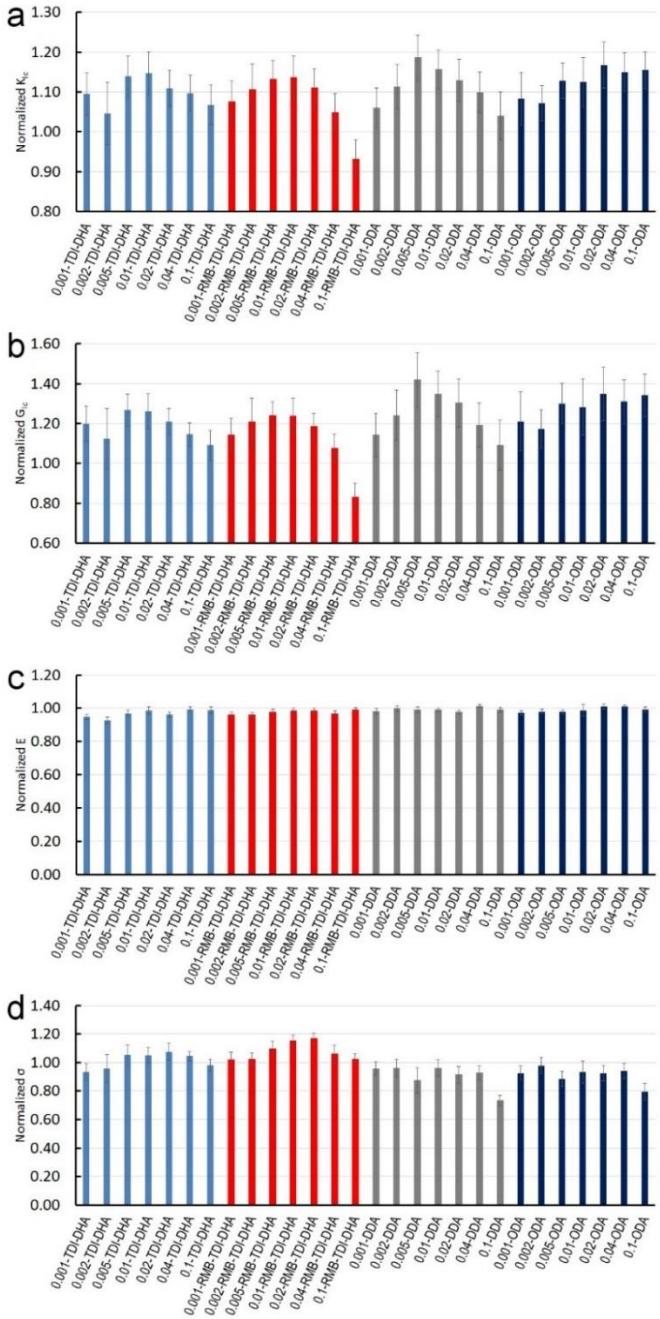

Figure 5.9. (a) Fracture toughness (b) fracture energy, (c) modulus, and (d) flexural strength values of mGO-toughened UP resins with differently modified GO (sonicated for 2 h), normalized to corresponding values for the neat resin. All samples are named using the notation "loading in wt %–GO modification method", and RMB refers to "resin masterbatch".

The fracture toughness test results indicate that the toughening effect introduced by adding graphene derivatives has little dependence on the surface chemistry of mGO, but the difference in GO aggregate size affects optimal loading levels of toughener. Modified GO samples with larger aggregate sizes, such as TDI-DHA-GO and ODA-GO, show less decrease in toughness with higher loading compared to RMB-TDI-DHA-GO and DDA-GO, which contain much smaller aggregates. All three mGOs show a toughening effect even at 0.001 wt % loading, and fracture toughness of all composites except the ODA-GO samples improves at first and decreases after an optimum point (0.005 wt %-0.01 wt %) with increasing loading level. ODA-GO has the largest aggregate size, thus the optimal loading level may fall beyond 0.1 wt %, the highest loading tested. The toughening behavior of various mGOs is similar to the size effects of aluminum particles on fracture toughness of a polyester composite at high volume ratio.[191] In that study, 100 nm aluminum particles behave like RMB-TDI-DHA-GO with the optimal loading of 2 wt %. Aluminum particles of 3.5 μm and 20 μm in diameter sizes resemble TDI-DHA-GO and ODA-GO in terms of toughening.

In contrast to fracture toughness, the ultimate strength of polymer-mGO composites appears to depend on the GO surface chemistry. Both TDI-DHA-GO series show an overall improved ultimate strength, and the smaller sized resin masterbatch TDI-DHA-GO samples have even better strength. DDA-GO and ODA-GO samples show a decreased strength compared to the neat resin, and the strength values are very close to each other. This can be explained by the better compatibilization of TDI-DHA-GO with UP resin, which results in a stronger interface that leads to higher ultimate strength. For mGOs with identical surface treatment, a smaller aggregate size translates into less strength reduction.

ODA and DDA modifications yield similar mGO-matrix interfaces, so the counterbalance between fewer particles and larger particle sizes gives ODA-GO similar strength reduction compared to DDA-GO.

To study how the toughening effect changes with mGO loading, SEM fractography analysis was performed, and representative fractographs are displayed in Figure 5.10. At 0.005 wt % loading, the primary toughening effect is crack pinning for all four samples shown. The mGO aggregates pin and retard the crack front to increase the critical stress for crack propagation. As the stress continues to build up, the crack front finally starts to move and is forced to go around the pinning point. The split crack surfaces rejoin after the pinning point and form a ridge that appears brighter in the SEM image. At this stage, a rougher near-precrack region correlates with higher fracture toughness. As the mGO loading is increased to 0.1 wt %, a crack deflection mechanism starts to dominate, so the near-precrack region becomes chaotic. The roughness-toughness correlation starts to break down if this stage is reached. Any further increase in mGO loading leads to toughness reduction, which appears on fractographs as diminishing borders between precrack and near-precrack regions (Figure 5.10d, f). This toughness reduction can be explained by the coalescence of microcracks formed around mGO particles that reduces the toughening effect.[192]

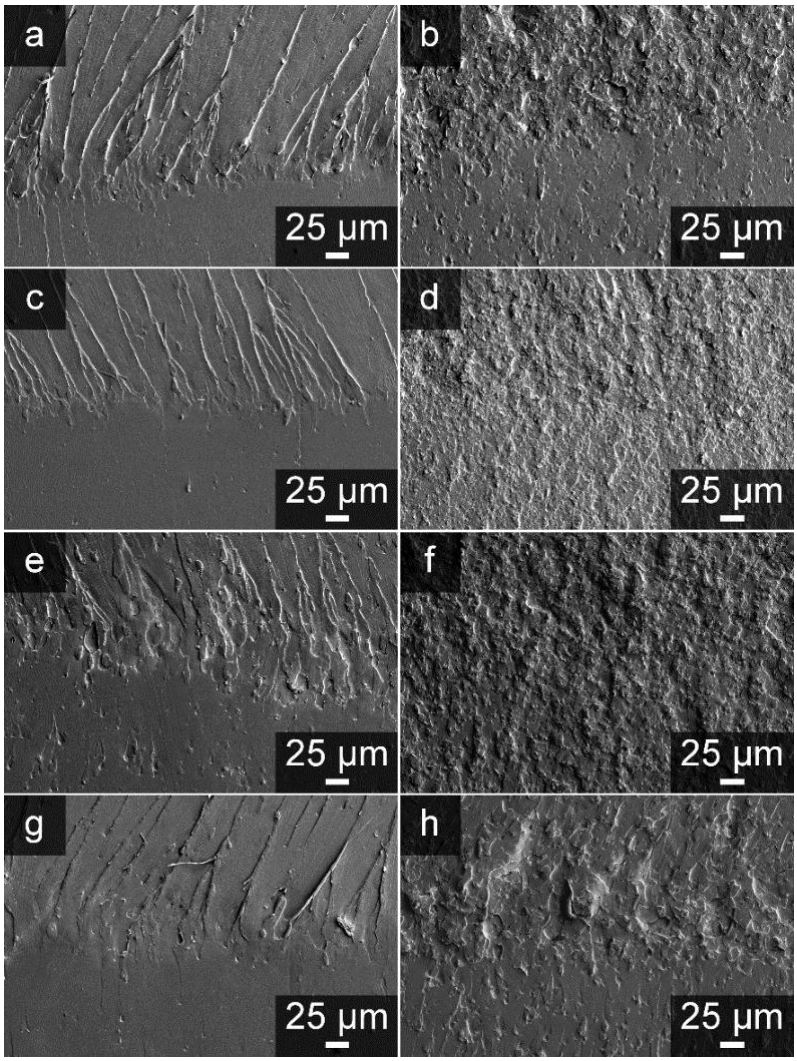

Figure 5.10. SEM fractographs from the near-precrack regions of (a), (b) TDI-DHA-GO, (c), (d) TDI-DHA-GO from RMB, (e), (f) DDA-GO, (g), (h) ODA-GO. Panels (a), (c), (e), and (g) show samples with 0.005 wt % mGO loading, and panels (b), (d), (f), and (h) show samples with 0.1 wt % mGO loading. The crack propagation direction is from the bottom to the top in all SEM micrographs.

5.4 Conclusions

The question how primary particle size and aggregate size of mGO affect toughening of a UP resin was addressed using GO modified with three different surface modifiers

and reduced to various sizes through sonication. DDA modification was chosen because it had previously been demonstrated to improve dispersion in UP resins [28]. TDI-DHA was chosen because it can improve GO matrix interactions, while ODA was selected as a control sample with extended particle aggregation. The study showed that primary particle size had little effect on how mGO toughens a UP resin, but the size of mGO aggregates affected how the toughness of mGO-UP composites changed with varying mGO loadings. RMB-TDI-DHA-GO and DDA-GO toughened UP resin at optimal loading levels of 0.005 to 0.01 wt %, but this toughening effect was lost at a concentration above 0.1 wt %. Highly aggregated mGO, such as ODA-GO, produced a gradual increase in toughness improvement with increased loading, and appeared to be insensitive to loading of toughener beyond 0.02 wt %. GO modified with TDI-DHA or DDA showed a toughening effect at very low concentration, about one order of magnitude lower than what was reported before.[220, 223] This has some advantage if transparency of a toughened composite is desired. The lack of response to different GO surface chemistry in resin toughening also suggests that the maximum achievable toughness for a resin is determined solely by the resin, and this value cannot be changed by new GO modification methods or by increasing mGO loading. However, other properties, such as dispersibility, processability, and ultimate strength may be influenced by surface functionalization of GO.

Chapter 6*

Nanoparticles in Glass Fiber-Reinforced Polyester Composites: Comparing Toughening Effects of Modified Graphene Oxide and Core-shell Rubber

6.1 Introduction

Thermosetting resins, including epoxy, unsaturated polyester, and vinyl ester, are widely used as structural materials, coating, adhesives, and insulation materials.[248] These thermosetting resins possess properties such as high modulus, high strength, and chemical resistance, which are desirable for manufacturing fiber-reinforced plastics (FRPs). However, the high crosslink density intrinsic to these thermosetting resins also renders them brittle, limiting the applications where fracture toughness is critical. To address this weakness, many studies have been dedicated to toughening thermosets. The most common toughening method is to incorporate soft, low T_g materials, such as carboxyl-terminated butadiene acrylonitrile (CTBN) and amine-terminated butadiene acrylonitrile (ATBN),[249-252] core-shell rubber (CSR),[253-256] and block copolymers.[221, 257, 258] Rubber modifiers are very effective tougheners due to their inherent ductility. The toughening mechanisms of rubber modified polymers are cavitation, crack blunting, and rubber induced shear yielding.[152] It has been reported that rubber tougheners can increase the mode-I fracture energy of a resin (G_{IC}) by as much as 3500%.[259, 260] However, adding rubber modifiers generally results in a reduction of modulus, strength, and glass transition temperature

* The author is responsible for mGO synthesis, the unreinforced resin toughening, and fiber composites fracture analysis in this chapter.

(T_g).[259, 260] Another strategy to toughen the resin is the utilization of rigid inorganic particles, such as silica,[261, 262] clay,[263, 264] carbon nanotubes,[265] graphene or graphene oxide.[181, 182, 192, 222] Crack pinning, crack deflection, and/or matrix-particle debonding have been identified as the toughening mechanisms of rigid particles.[192] The toughening effect brought by adding rigid inorganic particles is typically less pronounced than that of the polymer modifiers, but the modulus and T_g are usually improved.

Graphene and graphene oxide (GO) have attracted a tremendous amount of interest due to their exceptional mechanical properties, high specific surface areas, and the high electrical conductivity.[266] The oxygen-containing functional groups on GO, such as epoxide, hydroxyl, and carboxylic acid groups, provide opportunities for a variety of chemical modifications. Our previous research demonstrated that thermosetting resins, including epoxy and unsaturated polyester resin (UPR), can be toughened by extremely low loadings of modified graphene oxide (mGO).[192, 220, 221, 223] At such low loading levels, incorporation of GO-based tougheners becomes economically attractive. In addition, the optically clear resin will still be transparent at low loadings, which is advantageous for FRP parts quality inspection. While many other inorganic tougheners or rubber particles significantly increase the viscosity of the resin,[267, 268] mGO at low loadings does not significantly increase the resin viscosity as shown in Table 6.1. In our previous studies, ATBN was attached to GO using diisocyanate as the coupling agent, and incorporating 0.04 wt% of ATBN-modified GO yielded a 240% increase in G_{IC} in epoxy without sacrificing modulus, strength, and T_g.[192] We also showed that 0.04 wt% of GO functionalized with a combination of 3-isopropenyl-α,α-dimethylbenzylisocyanate and dodecylamine (TMI-12C-GO) can increase the G_{IC} of an UPR by as much as 55%.[220] The

double-bond on isopropenyl-α,α-dimethylbenzylisocyanate (TMI) may introduce covalent bonding between GO and the polyester matrix, while the dodecylamine functionalization prevents particle aggregation. Recently, we also showed that the toughening performance of dodecylamine-modified GO (12C-GO) in UPR or vinyl ester resin (VER) is similar to that of TMI-12C-GO.[244] The toughening mechanisms in mGO containing resin composites were identified to be crack pinning and crack deflection.[220]

Table 6.1. Viscosity of UPR, UPR/0.04 wt% 12C-GO mixture, UPR/5 wt% CSR mixture, and the as-received CSR concentrate. Viscosity values were obtained at room temperature.

Materials	Viscosity (cP)
Neat UPR	120
UPR/0.04 wt% 12C-GO	121
UPR/5 wt% CSR	221
CSR Concentrate	12,900

As mentioned earlier, one primary application for toughened thermosetting resin is to prepare FRPs. FRPs are a very important class of structural materials due to their excellent strength-to-weight and modulus-to-weight ratio, leading to their extensive use in the aerospace, automotive, sporting goods, marine, and infrastructure industries.[269] Despite their advantages in stiffness and strength, FRPs are prone to delamination failure, which is a process when cracks propagate between the plies of FRPs. To mitigate delamination, tougheners such as rubber particles and inorganic particles can be incorporated into the matrix to produce FRPs with high mode-I interlaminar fracture toughness. However, FRP laminates-based tests are time consuming, and they also require a large amount of materials for laminate preparation. Thus, the majority of research papers in this field are focused on

toughening the base resin without any fiber. Even though the community generally accepts that toughened resin leads to toughened fiber composites, it is still important to understand the toughness translation from unreinforced resin to FRPs. To distinguish the fracture energy of a toughened resin and interlaminar fracture toughness, we refer to the former as G_{IC_Resin} and to the latter as G_{IC_Comp}.

Many publications describe the toughening translation of epoxy FRPs. It has been reported that incorporating CTBN,[252, 270, 271] CSR,[256, 271, 273] nanosilica,[256, 272] a combination of CTBN and nano-silica,[270, 274] nanoclay,[275, 276] carbon black,[277-279] carbon nanotubes,[280, 283] graphene, and graphene oxide,[284, 285] and halloysite[286, 287] in epoxy resin can increase G_{IC_Resin} and lead to an increase in G_{IC_Comp}. Despite the much larger production of polyester-based FRPs, research focused on improving G_{IC_Comp} of polyester-based FRPs by increasing matrix fracture toughness is limited. Miller et al. reported that 6 parts per hundred resin (pphr) of ATBN increased the fracture toughness of a very brittle UPR (with G_{IC_Resin} around 10 J/m^2) by approximately 87%, while the G_{IC_Comp} of the corresponding showed 130%–160% enhancement.[288] Compston et al. produced VER-based glass fiber reinforced plastics (GFRPs) with different matrix toughness and found a 1:1 relationship between G_{IC_Resin} and G_{IC_Comp}.[289] A similar extent of G_{IC_Comp} improvement was also reported by Burchill et al. in VER/CSR glass fiber woven laminates.[290] Kobayashi and Kitagawa used 5 wt% and 10 wt% of silicone rubber with a diameter of 2 μm to toughen a VER, but the increase in G_{IC_Comp} was not significant.[291] Recently, Klingler et al. found that adding 2 wt% of CSR with a diameter of 200 nm increased G_{IC_Resin} of a UPR system by 64%, but G_{IC_Comp} of the corresponding glass fiber continuous filament mat composites only increased by 19%.[292] Seyhan et al. found that adding amino-functionalized multiwall

carbon nanotubes could increase the G_{IC_Resin} of VER by 8%, but the G_{IC_Comp} remained unchanged compared to the neat FRP due to weak fiber-matrix adhesion and non-uniform carbon nanotube distribution.[234, 293] Carbon nanofibers[294] and clay[295] were also used to increased G_{IC_Comp} of VER-based GFRPs, and the fracture toughness of the resin was not reported.

To the best of our knowledge, there is no publication dedicated to investigating the effect of very low loadings of GO in GFRPs yet. We wanted to investigate if the toughening effect provided by mGO (TMI-GO and 12C-GO) in polyester resins[220, 233] can be translated to GFRPs. In addition, very limited literature was found on glass-fiber reinforced polyester resin toughened by CSR.[289, 290] In this work, we studied the effects of incorporating very low loadings (<0.2 wt%) of mGO and 1 to 5 wt% of CSR on the mechanical properties and fracture toughness in two different thermosetting resins, namely, UPR and VER. Flexural properties, Izod impact strength, interlaminar shear strength (ILSS), and G_{IC_Comp} of GFRPs were measured. The correlation between the G_{IC_Resin} and G_{IC_Comp} is discussed in comparison with literature results.

6.2 Experimental

Materials

Sodium hydroxide (NaOH) and 200-proof ethanol were purchased from Fisher Scientific. Styrene (99%), dodecylamine (DDA, 98%), *N*,*N*-dimethylformamide (98%, anhydrous), 3-isopropenyl-α,α-dimethylbenzylisocyanate (TMI, 95%), 1,4-diazabicyclo(2.2.2)octane (99%), cobalt (II) 2-ethylhexanoate solution (65 wt% in mineral spirits), 4-*tert*-butylcatechol (99%), *tert*-butanol, 2-butanone peroxide solution (Luperox

DDM-9, 35 wt% in 2,2,4-trimethyl-1,3-pentanediol diisobutyrate) were obtained from Sigma Aldrich. GO was purchased from Graphenea (San Sebastian, Spain). The GO was supplied as a concentrated slurry (2.74 wt%) in water. The UPR used in this study was Aropol 8422 from Ashland. The Aropol 8422 resin is an orthophthalic polyester resin with 29 wt% styrene. Hetron 922 vinyl ester resin from Ashland was purchased from Express Composites, Inc (Minneapolis, MN), and its styrene content is 45 wt%. Kane Ace MX-020 core-shell rubber was supplied by Kaneka North America. This CSR is tailored for polyester resin, and it was supplied as a 40 wt% concentrate in a free-radical curable polyester resin. The particle size of the CSR is approximately 100 nm with a styrene-butadiene rubber core and a proprietary shell. Frecote 700-NC mold release agent was purchased from Henkel. All chemicals were used as received without further purification.

Two types of fiberglass mats were used in this study. The random chopped strand mats (CSM) (13.5 oz/ yd^2) were manufactured by ORCA and purchased from Fiberlay (Sarasota, FL). The woven roving (17 oz/yd^2) mats were purchased from Fibre Glast Developments Corp (Brookville, OH). The fiber diameter was between 10 and 15 μm. All the glass fiber mats used in this study are compatible with UPR and VER according to the information provided by the suppliers.

Synthesis of modified graphene oxide

The synthesis of TMI-GO can be found in Chapter 2, except that GO used in Chapter 2 was synthesized in-house using Hummer's method, whereas the GO used in this study was purchased from Graphenea. To synthesize TMI-GO, 300 mg of freeze-dried GO was added into 75 mL of *N*,*N*-dimethylformamide, followed by 1 h of bath sonication. 3 mL of TMI was added and allowed to react at 40 ˚C for 24 h under nitrogen atmosphere, followed

by the addition of 3 mL toluene to quench the reaction. The mixture was then centrifuged at 3000 rpm for 15 min, and the sediment was collected and washed 3 times with toluene and 2 times with *tert*-butanol. The TMI-GO powder was obtained by freeze-drying its slurry in *tert*-butanol.

As described in early chapters, we developed an efficient styrene masterbatch process for synthesizing 12C-GO, which allows easy dispersion of 12C-GO into UPR and VER without further sonication. To synthesize 12C-GO, the GO slurry was diluted to 4 mg/mL with deionized water in a 100 mL flask, then 4% NaOH aqueous solution was added to adjust the pH value of the aqueous GO dispersion to 9. The aqueous GO dispersion was bath sonicated for 30 min. Dodecylamine was added to ethanol to create a 6 mg/mL solution, then 2 parts by volume of dodecylamine/ethanol solution were added to one part by volume of GO dispersion. To facilitate the dodecylamine reaction with GO, the mixture was heated at 70 ˚C and stirred for 24 h. The reaction mixture was then centrifuged at 3000 rpm for 15 min, and the sediment was collected. The sediment was washed 4 times with ethanol, followed by 3 times of washing with styrene. At every washing step, ethanol or styrene was thoroughly mixed with the sediment, followed by centrifugation using the above-mentioned condition. Styrene was added to the purified 12C-GO make ~1 wt% dispersion, followed by 30 min bath sonication to prepare the masterbatch in styrene. Additional details about synthesis and characterization of TMI-GO and 12C-GO can be found in our previous publications.[220, 233]

Fabrication of nanocomposites

In a glass jar, TMI-GO powder, 12C-GO styrene masterbatch, or CSR was added into Aropol 8422 UPR, followed by the addition of styrene to adjust the total styrene content to

45 wt%. In the case of UPR/12C-GO nanocomposites, three toughener loadings were used: 0.04 wt%, 0.08 wt%, and 0.16 wt%. Since the optimal loading level of mGO was found to be 0.04%, unless otherwise specified in this chapter, the loading level of mGO in the composites is 0.04 wt%. For UPR/CSR nanocomposites, the total weight of the resin includes the weight of added CSR solution. The concentrations of CSR particles used in this study were 1 and 5 wt%. A CSR loading higher than 5 wt% resulted in a significant viscosity increase (see Table 6.1).

For UPR formulation, 0.03 wt% of 4-*tert*-butylcatechol inhibitor and 0.1 wt% of cobalt (II) 2-ethylhexanoate solution (65 wt% in mineral spirits) promoter was added. The mixture was rigorously stirred using a 1" Cowles blade at a speed of 2000 rpm for 30 min. Unlike the 12C-GO, TMI-GO did not disperse easily in polyester resin. To disperse TMI-GO in polyester resin, the TMI-GO/polyester mixture was probe sonicated for 2 h (Misonix S-4000, 4 s pulse, 2 s pause, 35% intensity) with mechanical stirring. The curing process starts with the addition of 1.25 wt% of Luperox DDM-9 free radical initiator, followed by 10 min of stirring and 10 min of vacuum degassing. The fabrication procedure of VER plaques was similar to that of UPR resin plaques, except that the styrene content was adjusted to 50 wt% and the as-received VER was already formulated. The amount of Luperox DDM-9 initiator added to cure VER was 1.5 wt%.

Glass molds were prepared by clamping two glass plates with a rubber cord in between, and the resin mixture was then poured into the glass molds. Resin plaques with a thickness of 1.5 mm and 3 mm were prepared for the flexural tests and compact tension tests, respectively. After 24 h of room temperature curing, the UPR plaques were post-cured for 3 h at 70 ˚C followed by 3 h at 120 ˚C. The VER plaques were post-cured at 90 ˚C for 4 h

after 24 h of room temperature curing. The heating and cooling rates were controlled to be 2 ˚C/min. The temperature during curing was regulated by the Thermo Fisher Scientific Heratherm programmable oven. The test specimens were cut from the nanocomposites plaques using a milling machine. The dimensions of flexural test specimen were approximately 35 mm in length, 3 mm in width, and 1.5 mm in thickness. The compact tension specimen were about 15 mm in length, 12 mm in width, and 3 mm in thickness.

Fabrication of glass fiber-reinforced polyester composites

In this study, GFRPs were fabricated using a hand lay-up process. For this process, a thick glass plate (12.7 mm) coated with mold release agent was used as the substrate. An LED light panel was placed under the glass plate so that gas bubbles and voids could be easily observed and eliminated during the hand lay-up process. After the resin mixture was free-radically initiated and degassed, a portion of the resin was poured onto the glass plate and spread evenly using a plastic squeegee; then the first layer of glass fiber mat was placed on the glass plate. Additional resin was poured and spread on the glass fiber mat until the mat was fully wetted. By gently rolling the lay-up with a grooved aluminum roller, air bubbles, voids, and excess resin were removed. These steps were repeated for the remaining plies. A 15 μm thick non-perforated Teflon sheet was partially inserted between the two center plies to serve as the delamination initiator for the mode I interlaminar fracture test. The number of plies for CSM and woven laminates was set to be 4 and 6, respectively, in order to keep the thickness of all laminates similar, around 3.2 mm. The curing profile for GFRPs was the same as that of unreinforced polyester nanocomposites, except that the heating rate and cooling rate were set to 1 ˚C to minimize residual thermal stress. The fiber weight percentage was ~35 wt% for CSM and ~60 wt% for woven

laminates. The laminates for mechanical testing were machined to the standard dimensions using a waterjet cutter. Dual cantilever beam (DCB) specimens with length of 127 mm and width of 25.4 mm were used. The dimension of flexural test specimens were about 127 mm in length and 12.7 mm in width.

Material characterization

The flexural properties of the nanocomposite plaques were determined utilizing an RSA-G2 solid analyzer (TA Instruments) according to ASTM D790-10. The flexural tests were performed with a span of 25 mm (16:1 span-to-thickness ratio) and a speed of 1mm/min. At least five specimen were tested, and flexural modulus, flexural strength, and ductility (strain at break) of the unreinforced polymer were reported. Dynamic mechanical analysis (DMA) was performed using the same flexural fixture with an oscillating strain of 0.02% at 1 Hz from room temperature to 150 ˚C.

Compact tension (CT) tests were performed per ASTM D5045-14 to obtain the mode I critical stress intensity factor (K_{IC}). CT specimens were machined into the geometry specified by ASTM D5045-14, and a liquid nitrogen-cooled razor blade was used create the pre-crack. All CT specimens were tested using an Instron 5966 Universal Tester under a speed of 10 mm/min. At least 10 specimens were tested for each CT test. The K_{IC} and the critical strain energy release rate (G_{IC}) were calculated using Equation 6.1 and Equation 6.2, respectively:

$$K_{IC} = \frac{P_C}{B\sqrt{W}} \times \frac{\left(2+\frac{a}{W}\right)\left[0.886+4.64\frac{a}{W}-13.22\left(\frac{a}{W}\right)^2+14.72\left(\frac{a}{W}\right)^3-5.6\left(\frac{a}{W}\right)^4\right]}{\left(1-\frac{a}{W}\right)^{\frac{3}{2}}} \quad (6.1)$$

$$G_{IC} = K_{IC}^2\left(\frac{1-\upsilon^2}{E}\right) \quad (6.2)$$

where P_c is the critical load during the CT test, B is the thickness of the specimen, W is the width of the specimen, a is the crack length (including notch length and pre-crack length), v is the Poisson's ratio, which is assumed to be 0.39,[134] and E is the flexural modulus.

The flexural modulus and strength of GFRPs were measured using an Instron 5966 Universal Tester under 3-point-bend mode in accordance with ASTM D7264-15. A span-to-thickness ratio of 32:1 was used to minimize the possibility of interlaminar shear failure. To obtain the interlaminar shear strength, short beam shear tests were also carried out per ASTM D2355-16 using the same equipment and fixture as the flexural tests but with a span-to-thickness ratio of 4:1. The crosshead speed for flexural tests and short-beam shear tests was set to 1 mm/min.

Mode I interlaminar fracture toughness tests were performed according to ASTM D5528 utilizing an Instron 5966 Universal Tester. Dual cantilever beam (DCB) specimens with a length of 127 mm were used. The length of the Teflon insert was controlled to be around 64 mm. The end of the DCB specimens with the Teflon insert was roughened using sandpaper to promote adhesion to the piano hinges. A two-part epoxy adhesive was used to bond the piano hinges to the end of the specimen. To visualize crack propagation, a thin layer of white paint was applied on the side of the specimen, and the first 5 mm from the Teflon insert were marked with thin vertical lines every 1 mm, followed by a vertical line at every 5 mm interval up to the end of the specimen. The specimen was loaded at a rate of 3 mm/min until the crack propagated 3 to 5 mm from the tip of the Teflon insert, and then the load was released. The specimen was reloaded using the same speed until the crack had propagated for 50 mm. The crack propagation was videotaped using a traveling microscope camera while the load vs. crosshead displacement curve was recorded by the

Universal Tester. The mode I interlaminar strain energy release rate (G_{I_Comp}) was calculated using modified beam theory, as shown in Equation 6.3:

$$G_{I\_Comp} = \frac{3P\delta}{2b(a+|\Delta|)} \tag{6.3}$$

where: P is the load, δ is the crosshead displacement, b is specimen width, a is the delamination length, and Δ is the correction factor accounting for the rotation of the beam. Δ is determined by plotting the cube root of compliance, $\sqrt[3]{\frac{\delta}{P}}$, as a function of delamination length; the best-fit linear relationship is found for such plot, and the intercept on the abscissa is the value of Δ.

Due to the relatively low thickness of the specimens, the large displacement correction factor should be applied to Equation 6.3 according to ASTM D5528-13. The large displacement correction factor is calculated using Equation 6.4:

$$F = 1 - \frac{3}{10}\left(\frac{\delta}{a}\right)^2 - \frac{3}{2}\left(\frac{\delta t}{a^2}\right) \tag{6.4}$$

where t is the sum of the distance from the center of the piano hinge pin (which is 2.5 mm) and 0.25 times of DCB specimen thickness. After applying the large displacement correction factor, the interlaminar strain energy release rate is calculated as shown in Equation 6.5:

$$G_{I\_comp} = \frac{3P\delta}{2b(a+|\Delta|)} \times F \tag{6.5}$$

The critical strain energy release rate (interlaminar fracture toughness, G_{IC_Comp}) for the initiation region and the propagation region were determined as follows: after the specimens were pulled until the crack has propagated 3 to 5 mm beyond the tip of the

Teflon insert, the load was released and then reapplied. During the second loading cycle, the force vs. crosshead displacement curve became nonlinear, and the point at which the curve became nonlinear is called the nonlinear point. The load, crosshead displacement, crack length, and correctional factors corresponding to the nonlinear point were used to calculate the initiation G_{IC_Comp} according to Equation 6.5. As the crack propagated further, sudden load drops after certain periods of stable crack propagation were observed. A sudden load drop was usually accompanied by a relatively long crack extension. Composites made with glass fiber mats generally exhibit this type of "stick-slip" crack growth behavior due to the presence of non-uniform interlaminar layer and fiber bridging.[296, 297] The load at the onset of the sudden load drop, and the crack length after the sudden crack extension was used to calculate G_{IC_Comp} in the propagation region according to Equation 6.5. The value of G_{IC} at each sudden load drop was calculated and averaged, and the average value is the propagation G_{IC_Comp}.

Izod impact tests were carried out according to ASTM D256-10. Specimens with a length of 63.5 mm and a width of 12.7 mm were cut from the 3.2 mm-thick laminates using a waterjet cutter, and a 2.54 mm deep notch with a radius of 0.25 mm was generated using a single-tooth slitting saw. At least 6 specimens were tested for each laminate. The fracture surfaces of failed CT specimens and DCB specimens were analyzed using a JEOL 6700 field emission scanning electron microscope (SEM). The specimen were coated with 50 Å of platinum prior to imaging, and an accelerating voltage of 5kV was used during imaging. To evaluate the dispersion of mGO in polyester resin, 1.5 mm-thick cured resin plaques were observed in transmission mode using a Nikon Eclipse Ti-e optical microscope.

6.3. Result and discussion

In this chapter, the discussion will be divided into three sub-sections. The first part of the discussion presents the results and analysis for graphene-resin composites without glass fiber reinforcement, and the second part of the discussion focuses on the toughening of GFRPs. The last part will be mainly the translation from resin to GFRPs.

6.3.1 Nanoparticle toughening of unreinforced resins

Dispersion of nanoparticles

GO sheets are mechanically strong, with a modulus of several hundred GPa and a strength of above 30 GPa.[298] However, these impressive mechanical properties do not always translate to the same properties of GO-polymer nanocomposites, especially if the nanoparticles aggregate. The goal of functionalizing GO particles with long alkyl chains (12C-GO) is to improve dispersion in a resin, and that of adding TMI groups is to introduce covalent bonding between polyester matrix and GO. Figure 6.1 shows the transmission optical microscopy images of polyester/GO and polyester/mGO composites. Unmodified GO was not well exfoliated in the polyester resin, and large aggregates can be observed. The size of aggregates of TMI-GO is close to that of unmodified GO. Dodecyl amine modification improves particle-matrix compatibility and thus the mGO dispersion, which is evident by the smaller aggregate size compared to unmodified GO or TMI-GO. Even though the composites were prepared through the same process, the dispersion of 12C-GO in VER seemed to be slightly better compared to that of UPR. In Figure 6.1c (UPR/12C-GO), some GO is aggregated into 10–20 μm diameter particles, while in Figure 6.1d (VER/12C-GO), the aggregates are much finer.

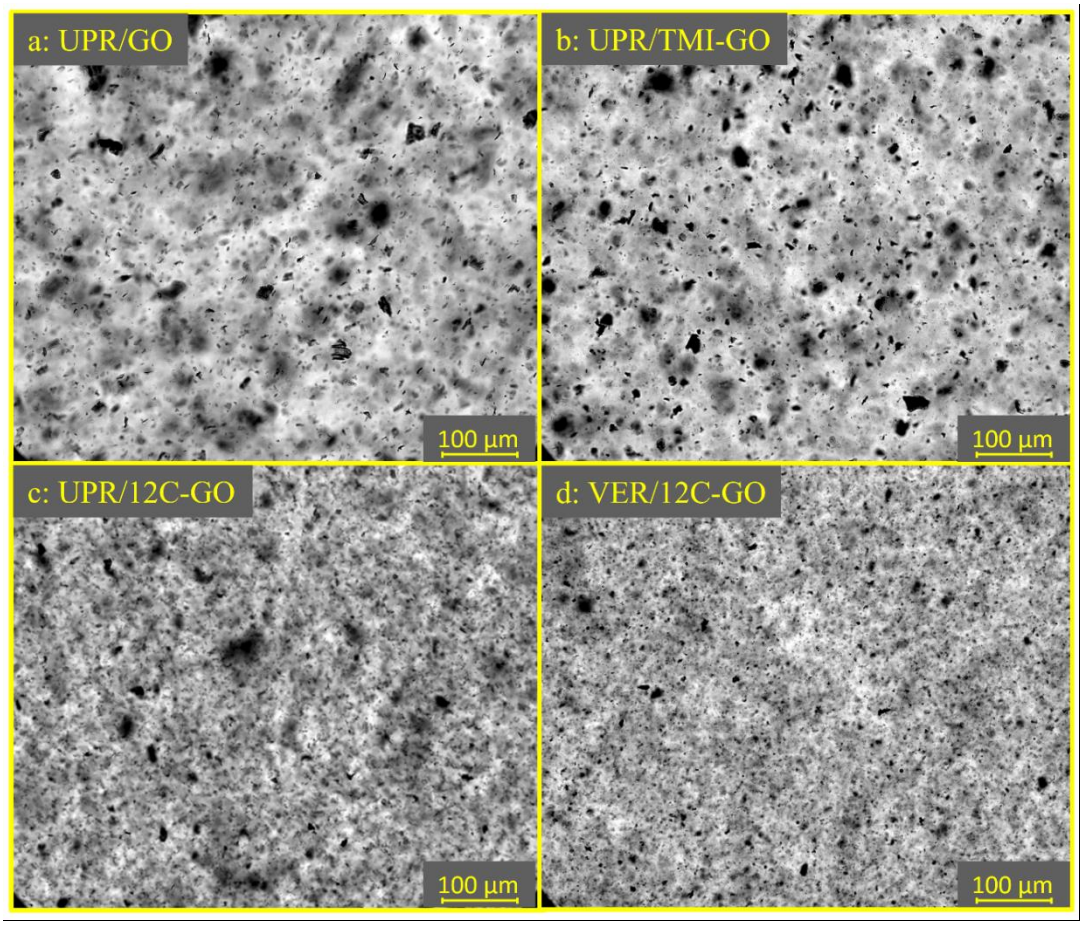

Figure 6.1. Transmission optical micrographs of polyester/GO and polyester/mGO nanocomposites. The loading is 0.04 wt% in all samples.

Flexural properties and dynamic mechanical analysis (DMA)

The flexural modulus, flexural strength, and the resin ductility (strain at break during flexural testing) of the nanocomposites are shown in Table 6.2. The flexural modulus of both UPR and VER resin remains unchanged after adding 0.04 wt% of TMI-GO or 0.04–0.16 wt% of 12C-GO. Even though GO possesses high modulus, the concentration of mGO is too low to show an observable increase in flexural modulus. Adding 5 wt% of CSR decreases the flexural modulus of UPR and VER by 20% and 12% respectively, which is due to the low modulus of CSR. Figure 6.2 shows the storage modulus and tan δ curves

obtained from DMA. Similar to the flexural modulus, the change in storage modulus and T_g of polyester/mGO composites after adding 0.04 wt% of mGO is negligible. On the other hand, adding CSR decreased the storage modulus of the resin across the entire temperature range and shift the glass transition of the composites by 8–10˚C.

Table 6.2. Mechanical properties of mGO and CSR toughened polyester nanocomposites

Materials	K_{1C} **(MPa m$^{0.5}$)**	$G_{IC\text{-}Resin}$ **(J/m^2)**	**Flexural Modulus (GPa)**	**Flexural Strength (MPa)**	**Strain at Break (%)**	**T_g (˚C)** (a)
Neat UPR	0.69 (0.03)	100.3 (10.1)	3.99 (0.03)	136.1 (7.5)	4.1 (0.3)	96
UPR/0.04 wt% 12C-GO	0.84 (0.02)	149.2 (8.3)	4.00 (0.05)	115.4 (3.8)	2.9 (0.1)	95
UPR/0.08 wt% 12C-GO	0.83(0.02)	148.9 (6.2)	3.93 (0.01)	110.2 (3.1)	3.0 (0.1)	-
UPR/0.16 wt% 12C-GO	0.83(0.01)	160.1 (4.5)	3.80 (0.03)	82.3 (3.2)	2.1 (0.2)	-
UPR/0.04 wt% TMI-GO	0.74 (0.02)	114.5 (8.3)	4.05 (0.05)	111.0(6.1)	2.9 (0.2)	94
UPR/1 wt% CSR	0.87 (0.03)	189.4 (11.8)	3.39 (0.04)	76.0(1.5)	2.6 (0.6)	-
UPR/5 wt% CSR	1.19 (0.03)	379.8 (20.8)	3.18 (0.05)	94.5 (1.3)	5.1 (0.7)	86
Neat VER	0.81 (0.02)	169.9 (6.3)	3.32 (0.03)	135.6 (1.2)	10.3 (1.4)	116
VER/0.04 wt% 12C-GO	0.95 (0.03)	229.2 (16.0)	3.35 (0.08)	135.9 (2.7)	7.2 (0.7)	117
VER/5 wt% CSR	2.03 (0.05)	1204.4 (54.6)	2.91 (0.02)	100.7 (0.3)	16.9 (2.2)	108

Values in parenthesis are standard deviations.

(a) from the peak in tan δ.

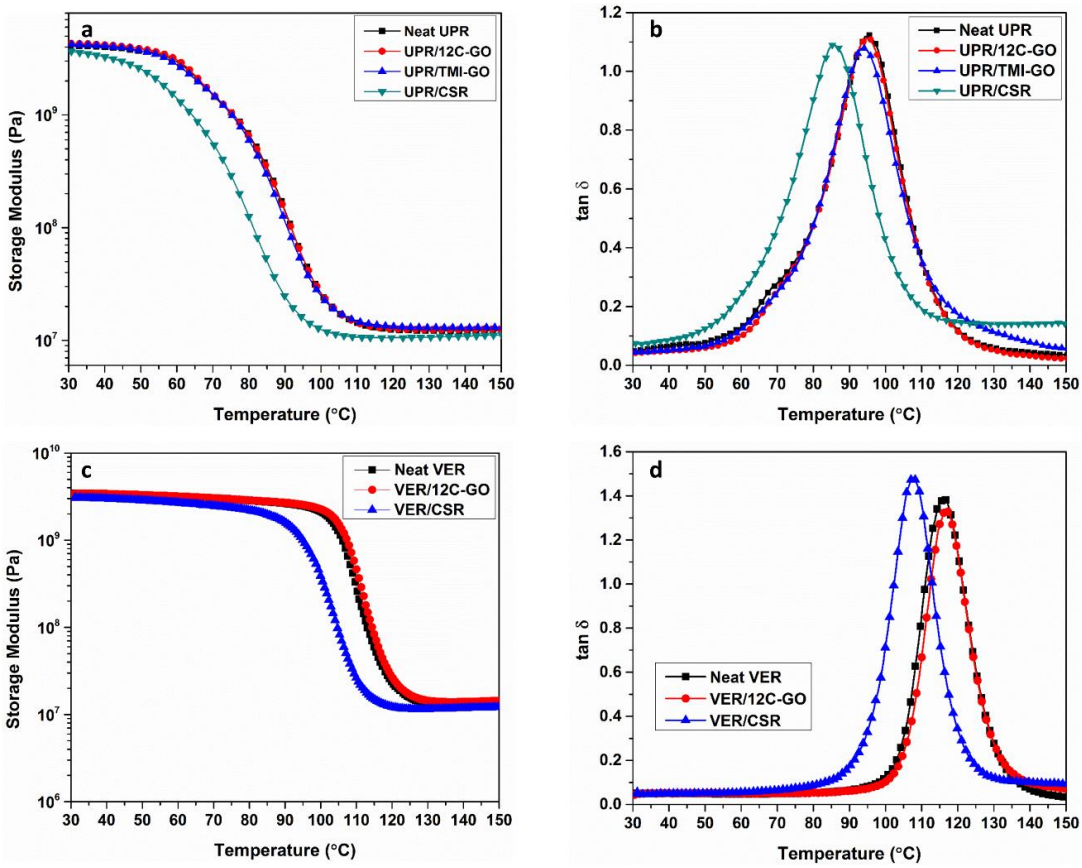

Figure 6.2. Plots of storage modulus (a, c) and tan δ (b, d) as a function of temperature. The loading of mGO is 0.04 wt%, and the loading of CSR is 5 wt%.

A flexural strength reduction of 15% to 57.3% was observed after adding 0.04 wt% to 0.16 wt% of 12C-GO or TMI-GO to the UPR. The decrease of flexural strength and resin ductility suggests that the mGO aggregates can act as stress concentrators and defects in UPR, so higher mGO loading leads to poorer strength of the composites. In contrast, adding 0.04 wt% of 12C-GO has no negative impact on the flexural strength of VER, which can be ascribed to the better dispersion and surface compatibility of 12C-GO in VER when compared to URP, as discussed in the previous section.

The incorporation of CSR also decreased the flexural strength of UPR and VER significantly. The reductions in flexural properties are expected because relatively high loadings of low strength rubbery particles are added into the rigid polyester crosslinked network. However, at 1 wt% of CSR loading, the flexural strength of the composite decreased by about 50% compared to the neat. This is because CSR forms large aggregates inside these resins, and the millimeter-sized aggregates became crack initiators in addition to structural defects, causing a great reduction in flexural strength.

Fracture behavior

The K_{IC} and G_{IC_Resin} values of the unreinforced samples obtained using CT tests are presented in Table 6.2. In UPR resin, adding 0.04 wt% of 12C-GO raised the G_{IC} by 49%, but adding the same amount of TMI-GO improved the G_{IC_Resin} of neat UPR by only 15%. The better toughening provided by 12C-GO can be attributed to the better dispersion of 12C-GO in UPR. Similar magnitudes of toughness improvement 12C-GO can also be observed in VER. Increasing the 12C-GO concentration in UPR to 0.08 wt% and 0.16 wt% did not provide any additional increase in fracture toughness compared to 0.04 wt%. However, as mentioned previously, an undesirable decrease in flexural strength was observed. A plateau in G_{IC_Resin} improvement in polyester resin after adding rigid fillers was also found by Grishchuk *et al.* in VER/organoclay (from 0.25 wt% to 5 wt% organoclay)[235] and Seyhan *et al.* in polyester/carbon nanotube nanocomposites (from 0.05 wt% to 0.3 wt%).[234] After taking the values of fracture toughness and flexural strength at various 12C-GO concentrations into consideration, 0.04 wt% loading of mGO seemed to be the optimal loading level. The improvement in fracture toughness after adding 0.04 wt% of mGO in polyester is comparable to polyester resin toughened by other inorganic fillers

at low concentrations (around or below 1 wt%) such as aluminum particles,[191] silane treated alumina particles,[171] and organoclay,[235, 299] but lower than that of resin toughened by inorganic fillers at much higher loading (2 wt% to 5 wt%). Adding 5% CSR increases the G_{IC_Resin} values by 280% for UPR and 600% for VER. These values are comparable to what was reported in the literature for toughening UPR and VER with CSR or liquid rubber.[160, 161, 300, 301]

Fracture surface analysis

Figure 6.3 and Figure 6.4 contain SEM images of the near-precrack regions (a definition is given in Figure 2.8 in Chapter 2) of failed CT specimens. Our previous work demonstrated that adding small amount of mGO improved toughness by crack deflection and crack pinning mechanisms.[192, 220] These toughening mechanisms are also used here to explain the fracture surface features. When the crack encounters GO, the crack tends to be deflected by these rigid particles, forcing the crack to go around the particles before rejoining the main crack plane, and this creates an uneven fracture surface as shown in the SEM images. The UPR/TMI-GO specimen showed increased surface roughness compared to the neat UPR specimen, and some GO aggregates ranging from 10 to 40 μm in size can be seen. The fracture surfaces of 12C-GO composites are even rougher than those of the UPR/TMI-GO specimens. The rougher topology can be attributed to the better dispersion of 12C-GO in the UPR matrix, leading to more crack deflection events.

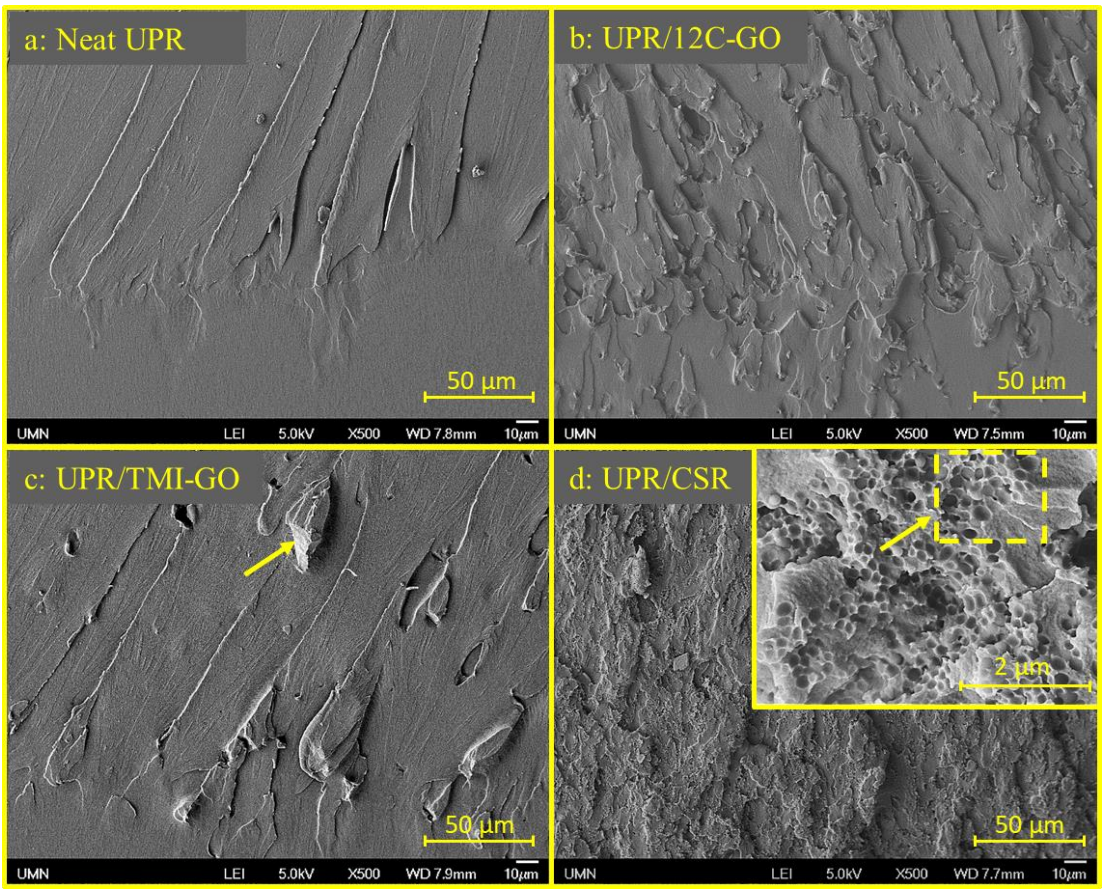

Figure 6.3. SEM micrographs of the fracture surfaces of UPR (a) neat resin and composites with (b) 0.04 wt% 12C-GO (c) 0.04 wt% TMI-GO (arrow indicates GO particle aggregates), and (d) 5wt% CSR (the arrow indicates aggregation of CSR particles).

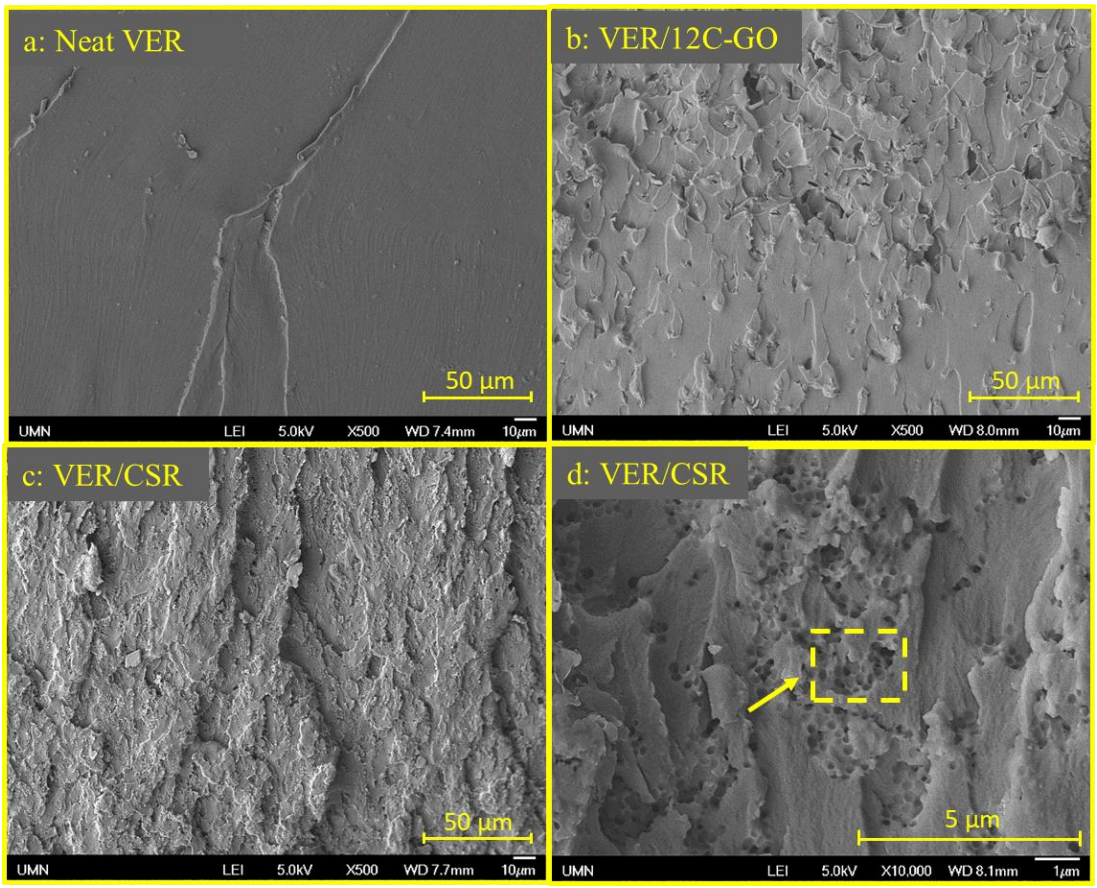

Figure 6.4. SEM micrographs of the fracture surfaces of VER a) neat and with b) 0.04 wt% 12C-GO, and c) 5 wt% CSR; d) is a magnification of c) The arrow indicates aggregation of CSR particles.

For polyester/CSR nanocomposites, the fracture surface is even rougher than those of polyester/mGO nanocomposites, and the fracture surface is covered with circular voids. These voids are likely caused by CSR shell/matrix debonding.[255] The typical diameter of these circular pits is around 100 nm, which agrees with the CSR particle size given by the supplier. Thus, cavitation is the main toughening mechanism in CSR toughened UPR composites. As shown in Table 6.2, the toughening effect of CSR particles is more pronounced in the more ductile VER resin, which agrees well with what was reported by Arias *et al.*[302]

To illustrate the difference in toughening performance of mGO and CSR, the stress-strain curves of mGO and CSR toughened UPR and VER are compared in Figure 6.5, and the strain at break values are also given in Table 6.2. The neat UPR specimen broke without yielding, while the VER specimen showed a typical yielding behavior. As discussed earlier, the incorporation of mGO has an adverse effect on the resin ductility (strain at break) of the resin, while the modulus was unaffected. The incorporation of CSR softens both resins, and induces more yielding in VER. In rubber-toughened thermosets, the major mechanisms are localized shear yielding of the matrix around the rubber particles and rubber particle cavitation.[152, 303, 304] The process of rubber cavitation relieves the tri-axial stress and promote large-scale plastic deformation of the matrix.[305] The lack of ability for the UPR to yield limited the large-scale matrix deformation even when the tri-axial stress was relieved, thus the toughening effect of CSR in UPR was much lower than that of VER. It is also important to note that CSR particles aggregated slightly in the resin, as indicated by arrows in Figure 6.3d and Figure 6.4d.

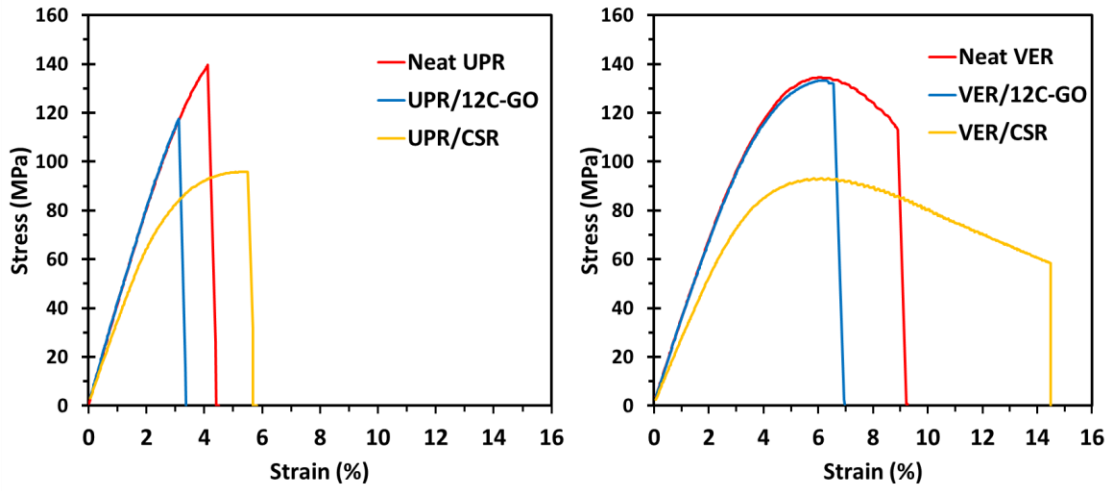

Figure 6.5. (a): Stress-strain curves of neat UPR and toughened resin specimen; and (b) stress-strain curves of neat VER and toughened resin specimen.

To summarize, incorporating 0.04 wt% of 12C-GO yields 49% and 35% increase in fracture toughness for UPR and VER, without lowering T_g and modulus. On the other hand, adding 5 wt% of CSR particles to UPR and VER increases the resin fracture toughness by 280% and 600%, respectively, but significant decreases in modulus and T_g were observed.

6.3.2. Nanoparticle toughening of glass fiber reinforced composites

Flexural properties

Table 6.3 summarizes the flexural properties, interlaminar shear strength (ILSS), and Izod impact strength of all GFRP samples. The flexural modulus and strength of the GFRPs with toughening agent are very close to that of the neat GFPRs, regardless of toughener type, resin type, and fiber architecture. Although adding mGO decreased the flexural strength of UPR plaques (see Table 6.2), and CSR reduced both flexural modulus and strength significantly in UPR and VER, these properties of GFRPs remain unaffected because flexural properties of GFRPs are generally dominated by the glass fibers. Only the

UPR/CSR woven laminate showed much lower flexural strength than the neat UPR woven laminates. This unexpected low flexural strength of UPR/CSR woven laminates may be attributed to uneven dispersion of CSR in UPR.

Table 6.3. Flexural properties, interlaminar shear strength, and Izod impact strength of glass fiber- reinforced polyester laminates.

Fiber Architecture	**Matrix Materials**	**Flexural Modulus (GPa)**	**Flexural Strength (MPa)**	**Interlaminar Shear Strength (MPa)**	**Izod Impact Strength (kJ/m^2)**
Chopped Strand Mats (CSM)	Neat UPR	9.8 (0.3)	216.9 (14.7)	39.6 (1.7)	0.86 (0.08)
	UPR/TMI-GO	10.3 (0.1)	198.3 (12.0)	34.9 (2.1)	0.99 (0.10)
	UPR/12C-GO	10.0 (0.2)	222.9 (12.5)	32.7 (0.7)	1.00 (0.09)
	UPR/CSR	10.0 (0.2)	209.2 (5.1)	29.0 (0.9)	1.24 (0.14)
Woven Roving	Neat UPR	20.6 (0.4)	511.2 (22.5)	42.8 (2.1)	2.90 (0.37)
	UPR/TMI-GO	21.6 (0.6)	478.0 (11.8)	32.8 (1.4)	3.22 (0.50)
	UPR/12C-GO	19.9 (0.7)	474.0 (13.7)	41.9 (1.4)	2.58 (0.34)
	UPR/CSR	19.7 (0.5)	432.1 (27.0)	25.1 (1.3)	2.85 (0.48)
	Neat VER	19.8 (0.7)	511.6 (19.8)	58.2 (3.5)	2.22 (0.26)
	VER/12C-GO	19.1 (0.5)	481.8 (11.4)	54.8 (2.8)	2.03 (0.25)
	VER/CSR	20.9 (0.4)	526.3 (12.8)	46.3 (4.5)	2.52 (0.53)

Values in parenthesis are standard deviations. All mGOs added at 0.04 wt%, CSR at 5 wt% based on resin.

Resin content is 65 wt% in CSM and 40 wt% in woven roving laminates.

Interlaminar shear strength

None of the toughenners used in this study improved the ILSS of the GFRPs. Generally, an increase in ILSS of GFRPs is related to an enhanced fiber-matrix interface, which can be obtained by silane modification[306-308] or electrochemical oxidation[309] of fibers. The lack of ILSS improvement for the toughenners used in this study can be understood as both CSR

and mGO lack functional groups that can bond to the glass fiber or change the fiber-matrix interface.

However, adding CSR caused a significant decrease in ILSS for all fiber architectures and resin types. The decrease in ILSS caused by the incorporation of rubber toughener can be attributed to the reduction of matrix stiffness and strength.[310] Similar to our observation, a decrease of ILSS was reported by Ozdemir *et al.* in nano carboxylic acrylonitrile butadiene rubber and nano acrylonitrile butadiene rubber (particles size: 50–150 nm) toughened carbon fiber-reinforced epoxy composites (CFRP).[311] In addition, Kim *et al.* found that carboxyl-terminated acrylonitrile rubber (CTBN) reduced ILSS in a high resin content CFRP.[311] Pantano *et al.* evaluated ILSS for vinyl ester/glass fiber composites with different G_{IC_Resin} (ranging from 160 J/m^2 to 1970 J/m^2) and found that ILSS was inversely proportional to G_{IC_Resin}, although no detailed explanation was presented.[312]

UPR CSM laminates with mGO also showed a decrease in ILSS compared to the corresponding neat resin laminates, and this reduction may be attributed to the incompatibility between the mGO and the binders on CSM. It is also possible that the high resin content in CSM laminates played a role in the reduction of ILSS because mGO reduced the flexural strength of UPR. UPR/TMI-GO and UPR/12C-GO CSM laminates have similar ILSS values, indicating that both types of chemical functionalization of GO have a similar effect on the fiber-matrix interface. In the woven laminates, the UPR/TMI-GO displayed significantly lower ILSS than the neat laminates, while the UPR/12C-GO CSM laminate has a similar value compared to the neat laminate. The difference may be due to the better dispersibility of 12C-GO compared to TMI-GO in UPR. For the woven

laminates, the VER laminates possessed higher ILSS values than UPR laminates, which suggests that the VER has a better fiber-matrix interfacial adhesion compared to UPR.

Izod impact strength

The mGO toughened GFRPs showed no significant improvement or degradation of Izod impact strength when compared to the neat GFRPs in this study. This result implies that the mGO does not affect the fiber-matrix interface, and the extremely low loadings of mGO are not able to change the impact behavior of GFRPs. The CSR increased Izod impact strength of the UPR CSM laminate by 43%, while no improvement of Izod impact strength was observed in UPR and VER woven laminates. Carvelli *et al.* reported similar findings that their carbon plain weave reinforced epoxy composites modified with carboxylated nitrile-butadiene rubber nanoparticles showed little difference compared to the unmodified composites in impact strength.[313]

It is interesting to observe that even though VER has higher ductility and higher fracture toughness than UPR (see Table 6.2), the Izod impact strength of UPR woven laminates is similar to that of VER woven laminates. Gaggar *et al.* found that the Izod impact strength is independent of matrix ductility (fracture toughness of resin was not provided) in epoxy/CSM laminates.[314] Schrauwen *et al.* compared the falling weight impact test results of woven laminates and stitched laminates made with a brittle UPR and a toughened VER and concluded that the fiber architecture plays a major role in the impact resistance of composites, while the matrix ductility showed no clear effect.[315]

The difference of toughening effects of CSR in CSM and woven laminates can be attributed to the different fiber architectures of GFRPs and resin content between these two

fiber architectures. In this study, the value of impact strength of the neat UPR woven laminates is 3.4 times higher than that of neat UPR CSM laminates, and this result suggests that in woven laminates, the fiber bundles perpendicular to crack propagation direction consume most of the impact energy by fiber breakage. Therefore, the matrix has little influence on the impact resistance of woven laminates. On the other hand, in CSM laminates, there are regions where fibers are parallel or nearly parallel to the crack direction; in these regions, fibers provide little resistance to crack propagation while the matrix consumes most of the impact energy. As a result, the matrix plays a larger role in impact resistance in CSM laminates compared to the woven laminates. Moreover, the resin content of CSM laminates and woven laminates were about 65 wt% and 40 wt%, respectively. In short, the larger influence of matrix in CSM laminates, combined with the higher resin content, improved Izod impact strength of UPR/CSR CSM laminates when compared to the neat UPR CSM laminates.

Mode-I interlaminar fracture toughness

Figure 6.6 summarizes the mode I interlaminar fracture toughness values obtained from DCB tests. In all laminates, the initiation G_{IC_Comp} is lower than the propagation G_{IC_Comp}. The region close to the Teflon crack starter is generally considered as resin-rich. In this region, the deformation and fracture of the matrix consumed most of the energy.[316] When the crack extends beyond the initial resin-rich region, additional toughening is provided by the fiber reinforcement. This fiber-based toughening includes fiber bridging, fiber debonding, and fiber fracture, which can dissipate additional energy.[317] UPR laminates toughened by mGO or CSR showed no significant change in either initiation G_{IC_Comp} or propagation G_{IC_Comp} compared to the neat UPR laminates. G_{IC_Comp} values for

UPR woven laminates did not change in the 12C-GO loading range from 0.04 wt% to 0.16 wt% (Figure 6.6b). This trend is consistent with those in UPR/mGO nanocomposites without fiber reinforcement. Adding mGO also did not increase the G_{IC_Comp} of VER woven laminates, while 5 wt% of CSR produced a 33% increase in G_{IC_Comp} (see Figure 6.6d).

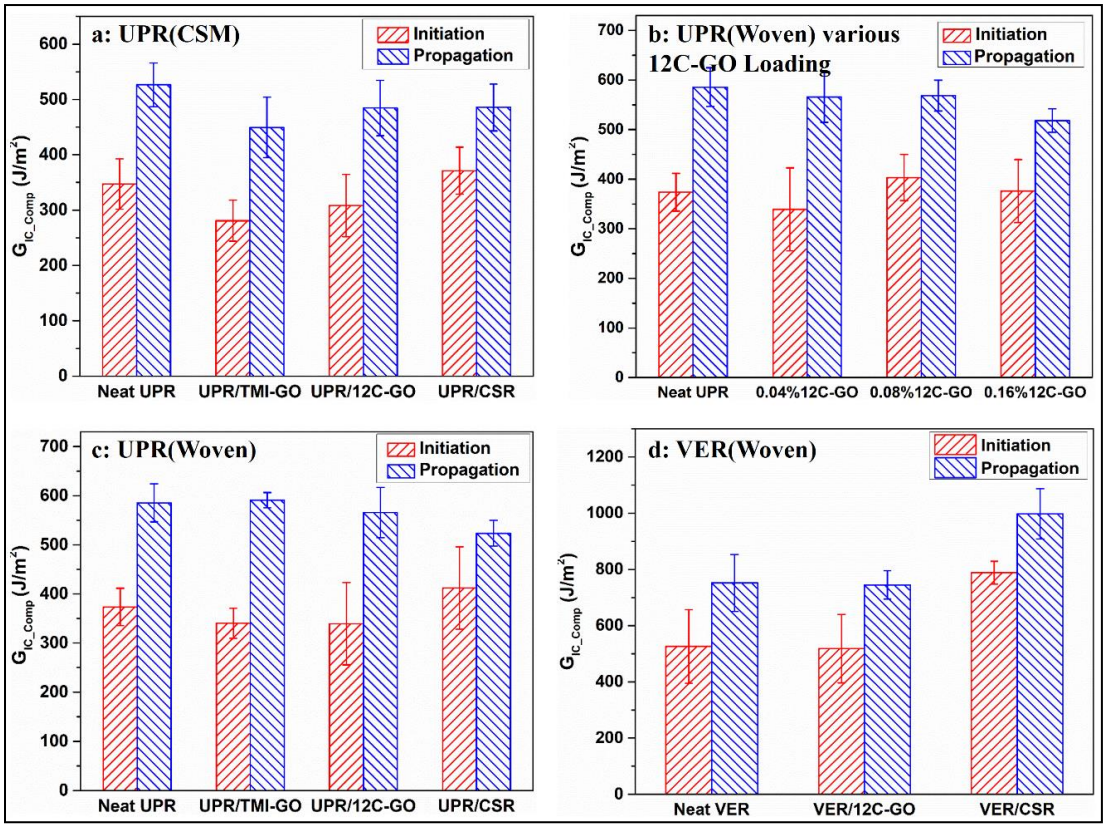

Figure 6.6. Mode I interlaminar fracture toughness of GFRP specimen. Except for samples in (b), the loading level of mGOs is 0.04 wt%, and the loading for CSR is 5 wt%.

The SEM fractographs of the DCB specimen are shown in Figures 6.7–6.9. The opposing surfaces of fractured DCB specimens are very different: one surface is covered mostly by fibers, while the opposite surface is predominantly resin. In all SEM micrographs, the separation of fibers from resin is very clean, suggesting that the fiber-matrix bonding is very weak. For the fibers parallel to the fracture surface, large gaps can be seen between

the resin and fibers, especially for UPR laminates, which is another sign for weak fiber-matrix interactions. The SEM images for VER laminates also show large areas of bare fibers; but in some regions, the matrix adheres to the fiber strongly (Figure 6.9), implying that the VER GFRP has a better fiber-matrix adhesion compared to UPR GFRP.

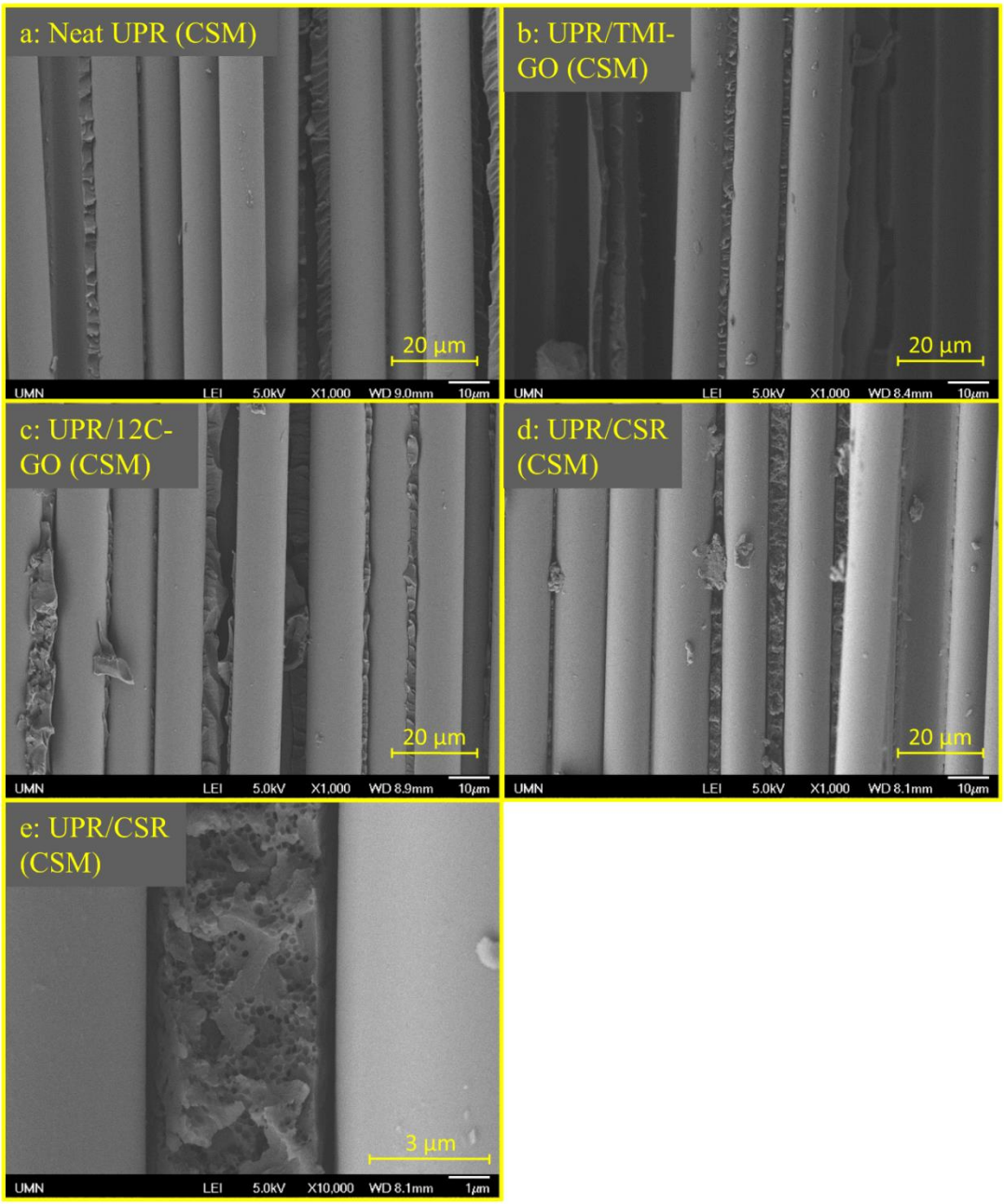

Figure 6.7. SEM micrographs of fracture surfaces of UPR CSM laminates after DCB testing. Images (d) and (e) are UPR/CSR images of chopped strand mats laminates at different magnifications. The loading level of mGOs is 0.04 wt%, and the loading for CSR is 5 wt%.

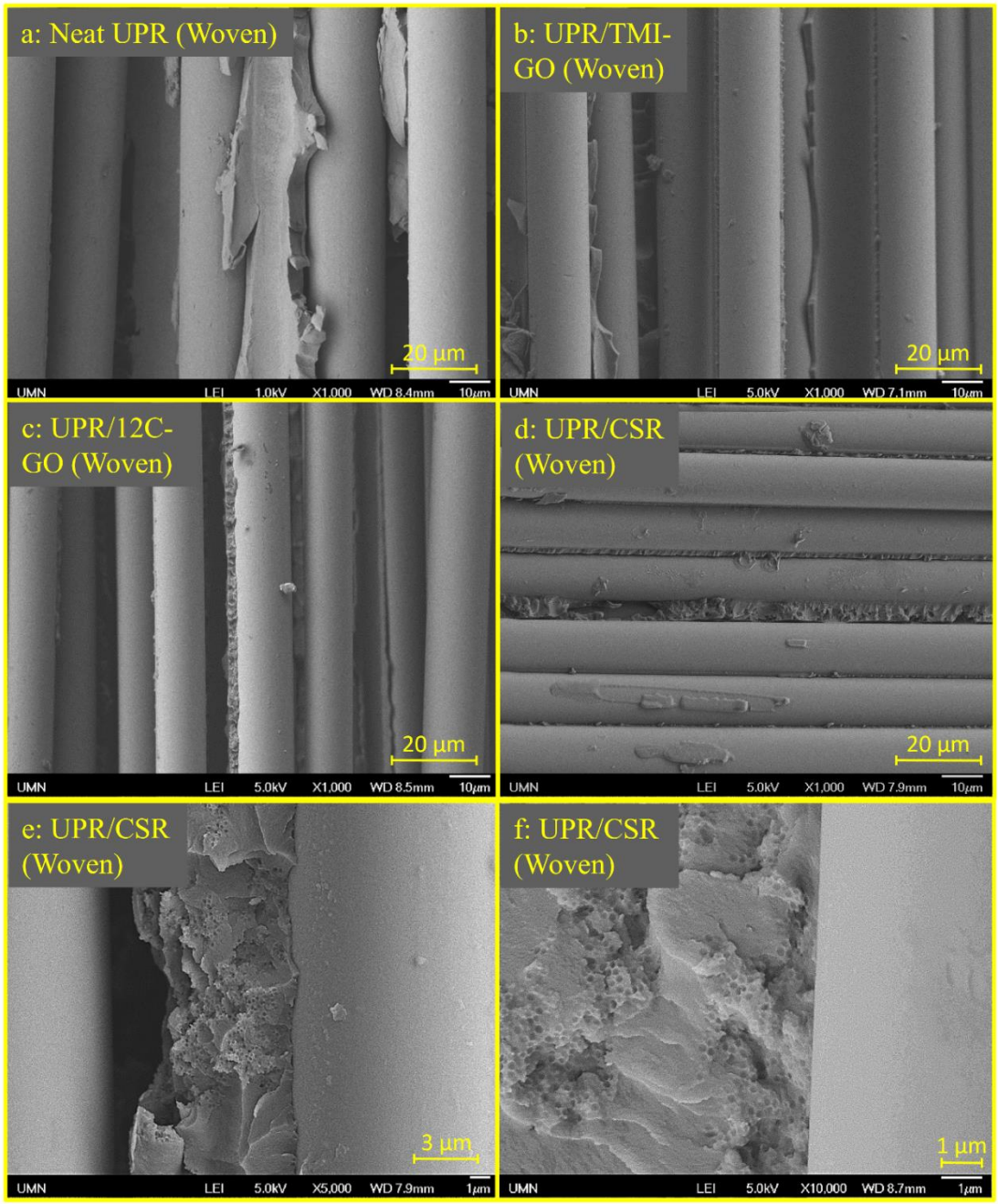

Figure 6.8. SEM micrographs of fracture surfaces of UPR woven laminates after DCB testing. Images (d), (e), and (f) are images UPR/CSR woven laminates at different magnifications. The loading level of mGOs is 0.04 wt%, and the loading for CSR is 5 wt%.

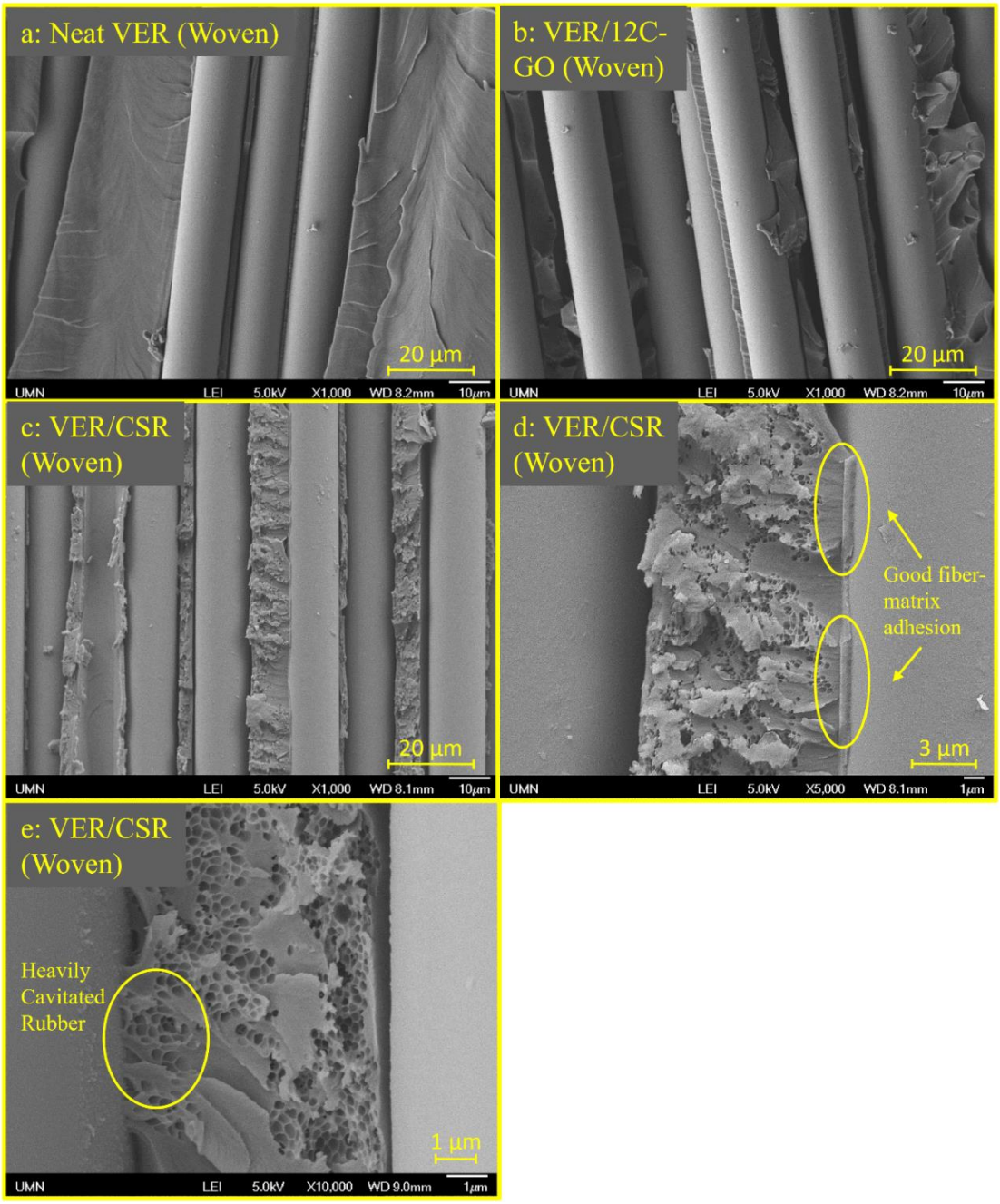

Figure 6.9. SEM micrographs of fracture surfaces of UPR woven laminates after DCB testing. Images (d) and (e) are images VER/CSR woven laminates at different magnifications. The loading level of mGOs is 0.04 wt%, and the loading for CSR is 5 wt%.

For the GFRPs containing CSR, the fracture surface of the resin was rougher than that of the neat or mGO modified matrix owing to the additional toughening mechanisms

offered by rubber particles. CSR was not able to provide G_{IC_Comp} enhancement in the UPR laminates with either CSM or woven roving as the fiber constructions. However, as mentioned above, CSR was able to increase the initiation G_{IC_Comp} and propagation G_{IC_Comp} of the VER woven laminates by 50% and 33%, respectively. The difference of toughening effects may be explained by the difference in fiber-matrix adhesion, and the degree of cavitation and matrix yielding around the rubber particles. When comparing Figure 6.8f (UPR/CSR woven roving) and Figure 6.9e (VER/CSR woven roving), the VER matrix has a better adhesion to the glass fibers. It is possible that CSR acted as a "compatibilizing agent" between the VER and the glass fibers and improved the fiber-matrix adhesion.[252, 288] In addition, the voids are more deformed in the VER matrix, while in UPR the voids remained nearly circular in shape; this difference can be ascribed to the higher degree of CSR particle cavitation and local matrix yielding in the VER matrix. Even though CSR particles have partially cavitated in the VER laminates, the toughening effect exhibits a very poor translation from resin to GFRPs, where a 600% increase in G_{IC_Resin} of VER led to only a 50% enhancement in initiation G_{IC_Comp} and a 33% enhancement in propagation G_{IC_Comp}.

6.3.3 Toughness translation from resin to composites:

The lack of G_{IC_Comp} improvement, especially in the UPR laminates, encouraged us to compare our results to those found in the literature. The relative improvement in fracture toughness after adding toughners over the unmodified counterparts can be represented by improvement ratios. The toughness improvement ratio of FRPs (I_C) and the toughness improvement of resin (I_R) after adding the toughners can be defined as the following:

$$I_C = Toughness\ improvement\ ratio\ of\ FRPs = \frac{Initiation\ G_{IC\_Comp}\ of\ modified\ resin}{Initiation\ G_{IC\_Comp}\ of\ unmodified\ resin}$$

(6.6)

$$I_R = Toughness\ improvement\ ratio\ of\ resin = \frac{G_{IC\_Resin}\ of\ modified\ resin}{G_{IC\_Resin}\ of\ unmodified\ resin}$$

(6.7)

The plot of I_C and I_R for the data compiled from the literature and the data for the woven laminates in this paper are shown in Figure 6.10. The slopes in this plot indicate the toughness transfer from resin to FRPs. Most of the data in literature fall within the area between slope of 1 and slope of 0.25 lines. The UPR/CSR and VER/CSR woven laminates presented in this paper are very close to or below the slope of 0.25, indicating relatively poor toughness transfer compared to the rest of the literature, which is mainly due to the weak fiber-matrix interface.

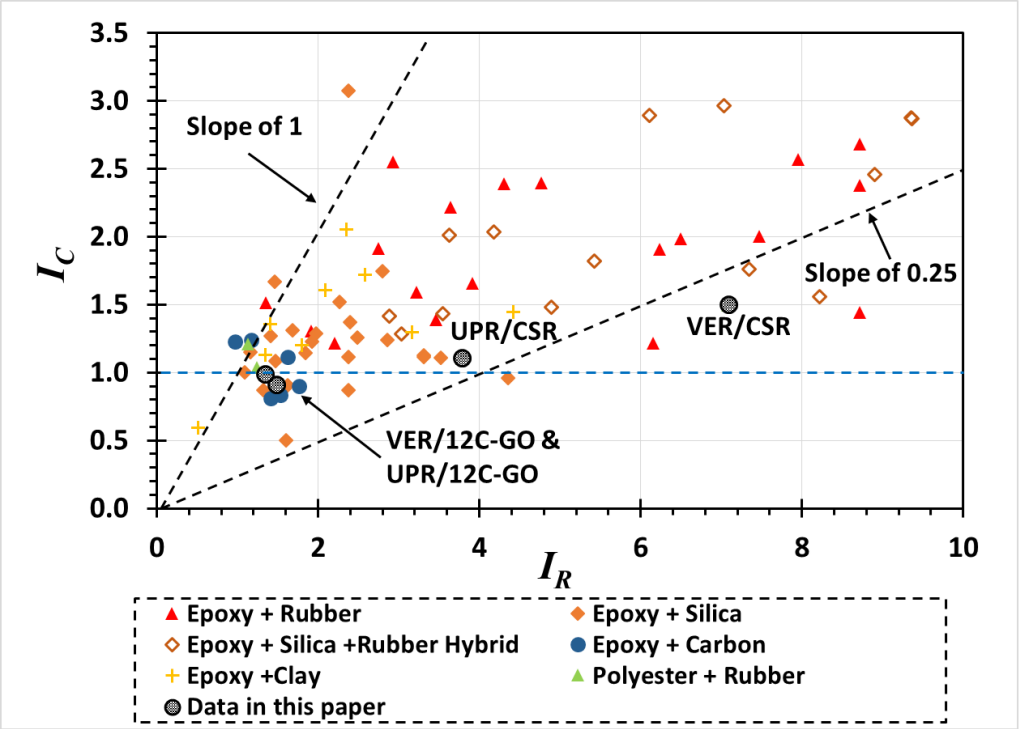

Figure 6.10. The relationship between toughness improvement ratio of FRPs and the toughness improvement ratio of the resin after adding toughenners. The references and data associated with this plot can be found at.[318] The data for woven laminates in the present paper is also plotted. Data above the blue horizontal line indicates that the G_{IC_Comp} is improved by adding toughenners.

The initiation G_{IC_Comp} is strongly influenced by matrix-fiber interface strength.[319] As bonding strength between matrix and fiber increases, the crack has a higher tendency to propagate through the matrix, resulting in high initiation G_{IC_Comp} values.[319] The SEM in the previous section showed that laminates with mGO did not enhance the fiber-matrix interfacial adhesion of both UPR and VER. This can explain why the initiation G_{IC_Comp} for the laminate with mGO did not increase significantly compared to the neat laminates. The TMI and 12C function groups do not react with the functional groups on the fiber sizing, thus even though the matrices were toughened by mGO, the weak fiber-matrix interface

encourages the crack propagates at the interface instead of through the resin. Comparing Figure 6.8 with Figure 6.9, the VER laminates have slightly better interfacial adhesion compared to the UPR laminates. The interfacial adhesion of VER/CSR woven laminate is even better than that of neat VER laminate, while adding CSR into UPR laminate did not improve interfacial adhesion. Based on the SEM images, the fiber-matrix interfacial adhesion can be qualitatively ranked as follows, with the corresponding initiation G_{IC_Comp} values in the pretenses: VER/CSR (787 J/m^2) > neat VER (518 J/m^2) = VER/12C-GO (526 J/m^2) > all UPR laminates (340 – 373 J/m^2). The initiation G_{IC_Comp} values correlate well with interfacial adhesion.

In this chapter, the toughness improvement ratio (I_C) of VER/CSR woven laminate is 1.5, which is less than those typically found in epoxy laminates modified with inorganic or rubber tougheners. The low I_C value may be attributed to the large extent of interfacial failures of GFRPs. The SEM images in Figure 6.9c and 9d revealed that only some areas have good fiber-matrix adhesion, while the majority of the fibers were bare or with a large gap between resin and fibers. By comparing the SEM images in this study to those in references,[252, 256, 271-274] it is obvious that the interfacial adhesion between epoxy and fiber reinforcements is better than the polyester/glass interface in this study, as evident by larger amount of residual resin adhere to the fibers. In addition, polyester resins generally have higher volumetric shrinkage than epoxy resins upon crosslinking,[320] and the residual stress caused by shrinkage may also negatively impact the fiber-matrix interfacial adhesion and/or the interlaminar fracture toughness.[321] To the best of our knowledge, no one has addressed the effect of shrinkage to interfacial bonding and interlaminar fracture toughness experimentally.

Even though the initiation G_{IC_Comp} showed a very weak correlation to G_{IC_Resin} in this study (see Figure 6.11a), we have found a better correlation between G_{IC_Comp} and resin ductility, which is shown in Figure 6.11b. As mentioned in the previous section, adding mGO decreased the ductility of the polyester resin. Interestingly, CSR did not increase the ductility of UPR even though the fracture toughness of the UPR increased dramatically after adding CSR, indicating that CSR did not introduce extensive shear yielding in UPR resin. As depicted in Figure 6.11b, all UPR laminates showed similar G_{IC_Comp} values and similar resin ductility values. Because CSR can introduce shear yielding in VER, the ductility of VER was increased. A high resin ductility increases the degree of matrix shear yielding, crack tip blunting, and stress redistribution caused by non-linear deformation of the matrix, thus, the G_{IC_Comp} increased with increasing resin ductility.[322, 323]

The importance of resin ductility in the interlaminar fracture toughness was also reported by Jordan *et al.* [323] However, in Jordan's study, the fracture toughness of the resin correlated well with resin ductility. A strong dependence of G_{IC_Comp} on resin ductility was also reported by Yan *et al.* in epoxy toughened by liquid rubber or CSR.[271] In Yan's study, even though epoxy toughened by 15 wt% of CSR showed 400% higher G_{IC_Resin} value compared to epoxy toughened by the same amount of CTBN, the epoxy/CTBN specimen showed 350% higher resin ductility and 65% higher G_{IC_Comp} than the epoxy/CSR specimen. Although many examples have been reported in the literature of enhancing G_{IC_Comp} of fiber-reinforced epoxy composites using rubber particles or rigid inorganic particles, increasing the interlaminar fracture toughness of polyester resins, especially UPR, remains a difficult task.

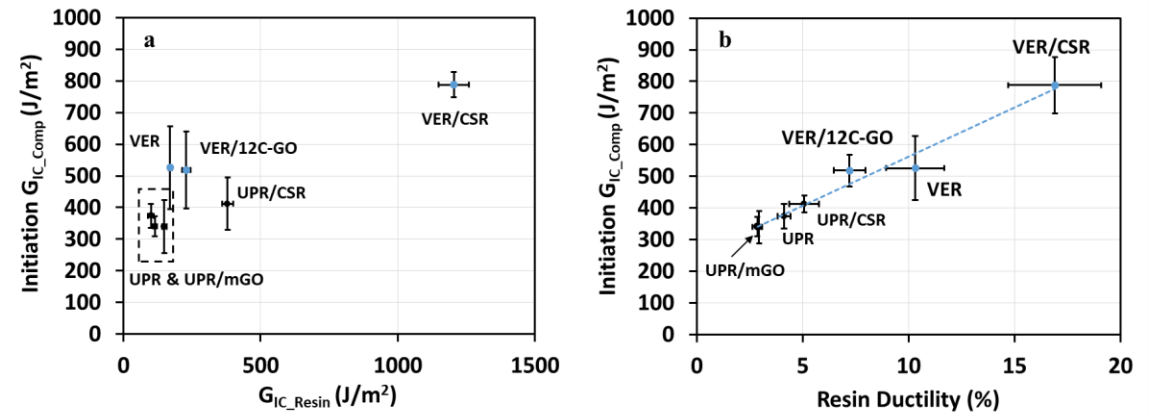

Figure 6.11. (a): The relationship between interlaminar fracture toughness (G_{IC_Comp}) of woven laminates at the initiation region and the fracture toughness of resin (G_{IC_Resin}); and (b) Correlation between mode-I interlaminar fracture toughness (G_{IC_Comp}) of woven laminate at the initiation region and resin ductility.

6.4 Conclusion

The mechanical properties of unsaturated polyester resin (UPR) and vinyl ester resin (VER) toughened with modified graphene oxide (mGO) or core-shell rubber (CSR) were measured. We then investigated whether this toughness translated to glass fiber-reinforced polyester composites (GFRPs) fabricated using the toughened resin. The following conclusions can be made:

(1) Incorporating very low loadings (0.04 wt%) of TMI-GO and 12C-GO, and 5 wt% of CSR can increase the fracture toughness of UPR and VER. Adding 12C-GO increased the fracture toughness of UPR and VER by 49% and 35%, but TMI-GO shows much less toughening effect in the resins. This is because 12C-GO disperses better in the polyester matrix. Increasing the loading of 12C-GO in the polyester resin beyond 0.04 wt% did not provide additional toughening effects. The flexural modulus and glass transition

temperatures of the nanocomposites were unaffected by the addition of mGO. The flexural strength was decreased by 15% in the UPR/12C-GO nanocomposites, but no strength reduction was observed in VER/12C-GO nanocomposites. The toughening mechanisms in mGO/resin composites are crack pinning and crack deflection. On the other hand, 5 wt% of CSR enhanced fracture toughness of the UPR and VER by 280% and 600%, respectively, but the flexural modulus, flexural strength, and glass transition temperature were decreased. The toughening mechanisms are associated with rubber cavitation, rubber/matrix debonding, and matrix shear yielding.

(2) The flexural properties of the GFRPs made with mGO or CSR toughened polyester matrices did not improve compared to the GFRPs with unmodified resin. Even though 12C-GO showed a better dispersion and provided more fracture toughness enhancement in UPR compared to TMI-GO, the toughening performance of these two types of mGO in GFRPs was not differentiable. In the UPR chopped strand mats (CSM) laminates, mGO did not increase the Izod impact strength, but CSR enhanced the Izod impact strength by 44%. This enhancement can be ascribed to the random fiber orientation in the CSM laminates allowing the matrix to play a larger role in impact energy consumption. In woven laminates, Izod impact strength of both the UPR and VER was not affected by the incorporation of either mGO or CSR. In woven roving fiber construction, the Izod impact strength was mainly controlled by the fiber. No improvement, and in some cases, reductions in interlaminar shear strength were observed.

(3) The enhancement of the fracture toughness in polyester resins (G_{IC_Resin}) showed very poor translation to the mode-I interlaminar fracture toughness (G_{IC_Comp}) in GFRPs, and the improvement in G_{IC_Comp} after adding toughgeners was less than what was observed

in the epoxy resin based FRPs. We attribute this to weak fiber-matrix interfacial adhesion. SEM images of fracture surfaces revealed that the fibers that were pulled out of the resin have little residual resin sticking to them, which is indicative of weak fiber-matrix adhesion. The very low loadings of mGO did not increase G_{IC_Comp}, regardless of resin type and fiber architecture. Even 5 wt% loading CSR, which increased the fracture toughness of polyester resin significantly (280% for UPR and 600% for VER), was not able to enhance G_{IC_Comp} of UPR laminates and only increased the initiation G_{IC_Comp} and propagation G_{IC_Comp} of VER woven laminate by 50% and 33%, respectively. The increase in G_{IC_Comp} for VER/CSR woven laminate can be attributed to the enhanced fiber-matrix adhesion due to the additional of CSR, and the ability of CSR to introduce matrix shear deformation, and possibly crack tip blunting and stress redistribution.

The correlation between G_{IC_Comp} and G_{IC_Resin} is very weak compared to the literature values for epoxy fiber-reinforced composites, especially for the UPR laminates. On the other hand, the correlation between G_{IC_Comp} and resin ductility is strong. Because of the weak fiber-matrix bonding in the polyester/glass fiber composite systems, the crack preferentially propagated through the fiber-matrix interface; as a result, toughening the matrix alone is a not very effective method for increasing G_{IC_Comp} in polyester/glass-fiber composite systems. The fiber-matrix interface must be improved in order to realize the benefit of a toughened matrix and maximize the interlaminar fracture toughness of polyester/glass fiber composite systems.

Chapter 7*

Graphene-polyethylene Nanocomposites: Effect of Graphene Functionalization

7.1 Introduction

Electrically conductive composites composed of polymers and conducting fillers have been broadly studied over the past few decades.[13, 266, 324] These materials can be employed as antistatic or electromagnetic shielding materials to avoid damage to electronics by electrostatic discharge or electromagnetic interference. Polyethylene (PE) is a low-cost, general-purpose polymer which shows good mechanical properties and high chemical resistance. It can be used for numerous applications, for example, as a packaging material for electronics, if it is modified to have enhanced electrical conductivity.

Conventional conductive fillers are usually micrometer-scale metal powders or carbonaceous materials such as carbon black. In order to reach the percolation threshold with these fillers, the filler content needs to be as high as 10–50 wt%.[325, 326] Such high filler loading results in poor mechanical properties and processing difficulties of the composites, and the sloughed-off carbon black particles could contaminate electronics. Unlike traditional polymer composites, which contain micron-scale fillers, polymer composites made with well dispersed carbon nanotubes (CNTs) offer a fascinating solution to the aforementioned problems. CNTs have high aspect ratios and excellent electrical

* This chapter was reproduced from *Polymer* **2016**, *104*, 1 with permission. © Copyright 2016, Elsevier. The author is responsible for the mGO design and synthesis, and the characterization of graphene and mGO.

conductivity, which facilitate the formation of conducting networks in a composite. Therefore, an insulating polymer can be converted to a conducting composite at a CNT content as low as 0.5 wt%.[327-330] Many distinctive properties of CNTs, such as electrical, thermal, optical and damping properties along with their excellent mechanical properties can translate to the composites, so CNT/polymer composites can find their applications in chemical sensing, electrical and thermal management, photoemission, electromagnetic absorption and energy storage.[325, 331, 332] However, owing to the low yield and high cost of the production and purification of CNTs, commercial application of CNT-based conducting composites is still limited. In addition, difficulties of dispersing CNTs into polymers and flow-induced orientation during processing remain challenging problems.[325, 327, 330]

Graphene has attracted much attention due to its high aspect ratio, and desirable mechanical, electrical, and thermal properties.[13, 266, 324] Bulk production of graphene sheets from graphite oxide based on a chemical method may prove to be cheaper than production of CNTs.[333-335] These unique attributes make graphene promising for applications in many technological areas, such as thermally and electrically conducting composites, reinforced polymer composites, electronic circuits, and transparent and flexible electrodes for displays.[13, 266, 324]

One challenge in creating graphene/polyethylene composites is that the low polarity of polyethylene leads to poor dispersion of graphene.[336, 337] To overcome this difficulty, we started with graphite oxide, which can be produced from graphite using strong oxidizing conditions.[34] Graphite oxide has ample covalently-attached hydroxyl, epoxy, carbonyl and carboxyl groups on its surface, which makes it hydrophilic and easily swellable in water.

The exfoliated graphite oxide is graphene oxide, and it has structural similarity with graphene, except some defects and surface oxygen-containing groups. Graphene oxide (GO) is not electrically conductive, but conductivity can be partially restored by heating it at relatively low temperatures.[338, 339] The functional groups of GO provide means for covalent functionalization,[33] and subsequently allows for improving GO dispersion in various polymers.

Here we report the processing and properties of PE nanocomposites made with functionalized GO (FGO). Methylstyrene moieties and 18-carbon alkyl chains were attached to GO via urethane linkages and amide bond formation, respectively. The alkyl chains and methylstyrene moieties lower the GO polarity and help FGO to be exfoliated and disperse better in PE. Linear low-density PE (LLDPE), relatively high-density PE (PE_A), and oxidized PE (OPE) were selected as polymer matrices. Dispersion of FGO in LLDPE, PE_A, and OPE was compared to that of the unfunctionalized GO and thermally reduced GO (TRG). We characterized these composites using optical microscopy, conductivity measurements, and mechanical tests. We compared the conductivity of the FGO nanocomposites before and after reduction to determine the efficiency of thermal treatment at moderate temperatures.

7.2. Experimental

Materials

PE_A was obtained from Sigma-Aldrich (product # 428108). It is a random copolymer containing 5–10 wt% hexene *co*-monomer. LLDPE, provided by Dow Chemicals, is a linear low-density PE copolymer of ethylene and octene (ENGAGE™ 8200 CAS 26221-

73-8). OPE was purchased from Honeywell. It is an oxidized PE with 3.3 wt% oxygen content (A-C® 656, oxidized PE homopolymer). Molecular characteristics of PE_A, LLDPE and OPE, including number averaged molecular weight (M_n), polydispersity index (PDI), viscosity, density, melting point, composition and crystallinity are summarized in Table 7.1. M_n values of three different PE samples were measured via gel permeation chromatography (GPC, PL-GPC 220 High Temperature Chromatograph) using trichlorobenzene as the eluent at 135 ˚C. TRG in this study was produced by rapid thermal reduction of graphite oxide,[337] and it was kindly provided by Vorbeck Materials. Sodium nitrate (ACS grade), potassium permanganate (ACS grade), hydrogen peroxide (30% solution in water, ACS grade), toluene (HPLC grade), and potassium bromide (IR grade) were obtained from Fisher Scientific. Octadecylamine (98%), *N*,*N*-dimethylformamide (anhydrous, 99.8%), 3-isopropenyl-α,α-dimethylbenzylisocyanate (TMI, 95%), 1,2-dichlorobenzene (ReagentPlus® Grade) and 1,4-diazabicyclo[2.2.2] octane (99%), were purchased from Sigma-Aldrich. Ammonium hydroxide (28-30% in water, ACS grade) and *tert*-butanol (99%) were purchased from Macron. Sulfuric acid (98%, ACS grade) and hydrochloric acid (37%, ACS grade) were purchased from BDH. Graphite flakes (SP1 grade) were sourced from Bay Carbon. Deionized (DI) water with a resistivity of 18 $M\Omega \cdot cm^{-2}$ was produced onsite using a Barnstead purification system.

Table 7.1. Molecular characteristics of PEs.

Sample code	M_n[a] g/mol	PDI	Viscosity Pa·s	Density[d] g/mL	T_m[e] ˚C	Composition[d]	Crystallinity[f]
PE from Aldrich (PE_A)	9600	5.6	200[b] 70[c]	0.93	122	Hexene 5-10 wt%	0.49
EG8200 from Dow (LLDPE)	42000	3.0	7300[b] 1200[c]	0.87	65	Octene 7.3 wt%	0.16
Oxidized PE from Honeywell (OPE)	450	10.2	1.0[b] 0.8[c]	0.92	92	Oxygen 3.3 wt%	0.29

[a] GPC, trichlorobenzene, RI detector, PS standards
[b] at 140 ˚C.
[c] at 210 ˚C
[d] Data provided by supplier
[e] DSC, second heating, 10 ˚C /min
[f] Determined by dividing the heat of fusion by 293 J/g

7.2.1 Graphene synthesis and characterization

Synthesis of GO

The method of GO synthesis was adapted from Hummers' method[34] with modifications. In a typical synthesis, 2.5 g $NaNO_3$ was dissolved in 115mL concentrated sulfuric acid in an ice bath, and 5 g of graphite was then added to the solution. Under moderate stirring, 5 g $KMnO_4$ was added every 10 min during 30 min for 15 g total (includes 10 min stirring after last addition). The ice bath was then replaced by a room temperature water bath, and the mixture was allowed to react at 35 ˚C for 1 h. Later, 230 mL of DI water was added to the reaction mixture and the temperature increased to 80 ˚C. After stirring for 15 min, the mixture was further diluted to 1 L. The reaction was quenched by adding hydrogen peroxide dropwise until the effervescence stopped and the mixture turned light brown.

After overnight sedimentation, 600 mL of the supernatant was decanted, and the rest of the mixture was divided into eight portions for purification.

To purify the GO, 40 mL of DI water was added to each portion with 1.5 mL concentrated hydrochloric acid. After stirring and shaking inside the centrifuge tube, the GO was spun down (Marathon 8 k) at 3000 rpm for 15 min. This procedure was repeated for a total of 10 times to remove metal ions and sulfate ions (no precipitation in 0.1 M $BaCl_2$). The resulting material was then dialyzed against DI water with cellulose dialysis tubing (Fisherbrand, MWCO: 6000-8000) until no precipitate was observed upon mixing the dialyzing solvent with 0.1 M silver nitrate solution. The GO was then redispersed in DI water and neutralized with ammonium hydroxide. After 1 h sonication in a bath sonicator (Branson 3510 ultrasonic cleaner, Emerson Electric Co.), the GO dispersion was centrifuged at 1500 rpm for 10 min to remove any poorly oxidized graphite. The supernatant was collected as the GO stock solution (2 mg/mL). Later, the stock solution was freeze-dried (Freezemobile, SP Scientific) to obtain the solid GO for further modification.

Synthesis of TMI/octadecylamine-functionalized GO (FGO)

To synthesize functionalized GO, 300 mg of the dried GO was dispersed in 75 mL anhydrous *N*,*N*-dimethylformamide (DMF) and then sonicated in a bath sonicator (Branson 3510) for 1 h. The resulting homogenous dispersion was transferred into a 150 mL two-necked round bottom flask and 1,4-diazabicyclo[2.2.2] octane (DABCO, 5 mg per 100 mg GO) was added as the catalyst. The dispersion was purged under nitrogen flow for 2 h with 300 rpm stirring. After that, 6 mL of 3-isopropenyl-α,α-dimethylbenzylisocyanate (TMI)

was injected and the mixture was allowed to react at 60 ˚C for 24 h under nitrogen. The reaction was quenched by adding 225 mL dry toluene, and the resulting mixture was then centrifuged at 3000 rpm for 15 min. The precipitate from the centrifugation was washed 3 times with toluene and twice with tert-butanol followed by freeze drying to obtain the intermediate product (TMI-GO).

The resulting TMI functionalized GO was redispersed in DMF in the same way as described before (2 mg/mL). The octadecylamine was then added (4 mg per 1 mg GO) and the reaction was kept at 70 ˚C for 24 h while stirring at 300 rpm. The reaction was terminated by pouring the mixture into ethanol, and the functionalized GO flocculated immediately. The crude product was collected by centrifugation and purified by 4 washes in dry ethanol and 2 washes in DI water. The purified product, TMI-octadecyl-GO, referred to hereafter as FGO, was freeze dried to obtain a powder. Figure 7.1 illustrates the steps of the FGO synthesis.

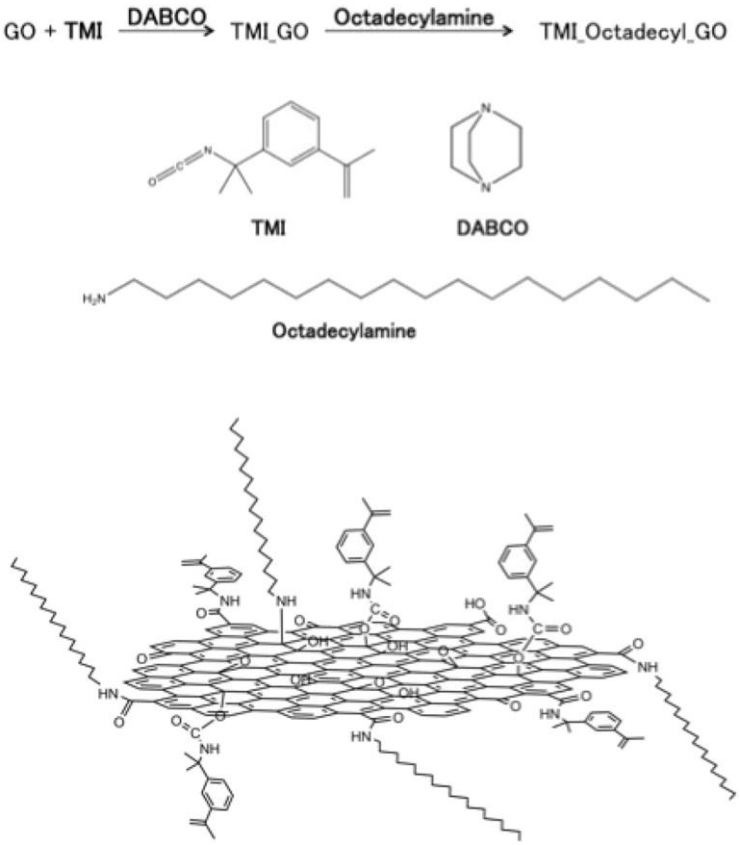

Figure 7.1. Synthesis and schematic structure of FGO.

Characterization

The viscosity of PE was measured using parallel-plate frequency sweep tests at 140 ˚C and 210 ˚C with an ARES rheometer (TA instrument). The melting point and degree of crystallinity of PE were determined by differential scanning calorimetry (DSC, TA Instruments Q1000) using TA Universal Analysis software. 4.0–6.0 mg of PE was loaded into hermetic aluminum pans. The scanning procedure was performed from 40 ˚C to 150 ˚C with a heating/cooling rate of 10 ˚C/min. Crystallinity was calculated by dividing the heat of fusion obtained from integrating the area of the melting endothermic peak by 293 J/g,[340] the heat of the fusion for a 100% crystalline PE.

Transmission infrared (IR) spectra of GO, FGO and TRG were obtained using a Fourier-transform-IR (FT-IR) spectrometer (Magna-FTIR 760, Nicolet). The spectra were collected from 4000 cm^{-1} to 400 cm^{-1}. Powder X-ray diffraction (XRD) experiments were performed with a PANalytical X'Pert Pro diffractometer. This instrument utilized a Co anode (Kα radiation, 1.79 Å) and X'celerator detector, and it was operated at 45 kV accelerating voltage with a 40 mA emission current. Transmission electron microscopy (TEM, FEI Tecnai T12) images were obtained to survey the sizes and morphologies of the FGO and TRG sheets. Each sample was stirred in ethanol and sonicated with a bath sonicator for 5 min. Lacey carbon TEM grids were dipped into the dispersions and allowed to air-dry before imaging.

7.2.2 Preparation and characterization of graphene/PE composites

Preparation of PE nanocomposites

Graphene/PE nanocomposites were prepared by solvent blending three GO samples (untreated GO, FGO and TRG) with three PE samples (PE_A, LLDPE, and OPE) using 1,2-dichlorobenzene (DCB) as the solvent. Up to 50 mg of graphene was added to 10 mL of DCB and stirred for 48 h at room temperature. About 1.0 g of PE solid was then added, and the mixture was heated in an oil bath at ~130 ˚C for at least 2 h. Graphene/PE mixtures in DCB were then cast on glass plates to prepare composite films. After the film casting, solvent removal continued for at least 48 h at room temperature and another 72 h in a

vacuum oven (24 ˚C, 5 mbar). These films were annealed at 210 ˚C in an oven for up to 1 h. Figure 7.2 shows the steps of the dispersion process.

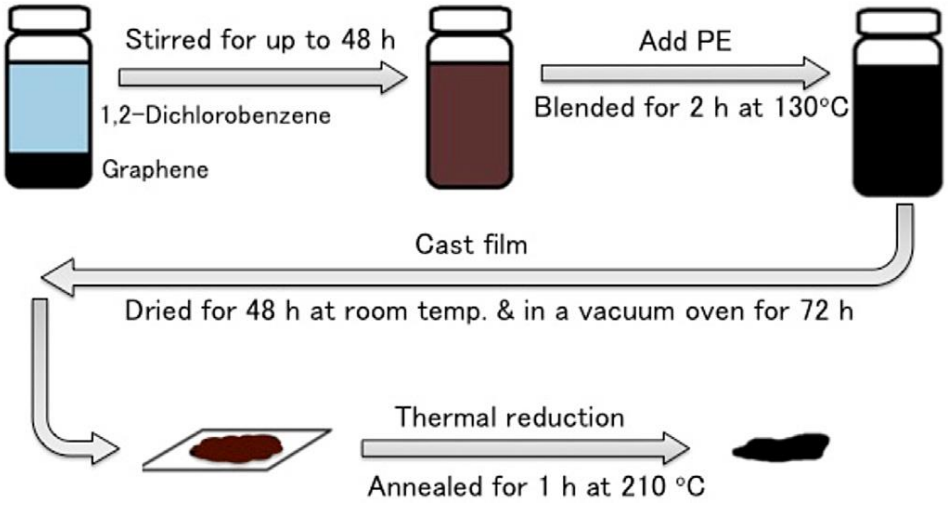

Figure 7.2. Schematic diagram of preparation of graphene/PE nanocomposites.

Characterization of nanocomposites

Optical microscopy was applied to investigate the dispersion of graphene in PE. Approximately 1 mg of composite was loaded between two glass slides placed in an oven at 130 ˚C for 2 min which caused it to melt. It was then compressed to a thickness of about 100 μm measured with a digital micrometer (Mitutoyo). Optical microscopy images were taken (Eclipse Ti, Nikon), and these images were binarized to create black and white images using ImageJ software. Tensile moduli of the composites were measured with an RSA-G2 rheometer (TA instruments). Composite samples were cut to rectangular strips 4–6 mm in width, then clamped between two film fixtures of the rheometer. The displacement

rate of the fixtures was 0.01 mm/s, and the modulus was evaluated based on the slopes of stress-strain curves from 0.05 to 0.25% strain.

Surface resistance was measured using an 11-probe meter (PRS-801, Prostat). The conductivity was reported as the geometric mean which was estimated based on 3 to 4 different spots of on a sample film. Crystallinity was measured using differential scanning calorimetry (DSC, Q1000 TA Instruments) by heating a sample at 10 ˚C/min from room temperature to 200 ˚C.

7.3 Results and discussion

The properties of polymer nanocomposites depend strongly on how well nano-fillers are dispersed in the polymer matrix. However, in our case, the surface energy mismatch between PE and graphene have made effective dispersion of graphene difficult without compatibilization. To solve this problem, we resort to chemically functionalizing GO to improve dispersion. The hydroxyl and epoxide groups on GO are sites for attaching functional groups like methylstyrene and alkane. We covalently attached methylstyrene moieties by reacting TMI isocyanate with hydroxyl and carboxy groups to form urethane and amide linkages and 18-carbon alkyl chains via epoxy ring-opening addition with octadecylamine. TMI modification helps exfoliation of GO sheets in the organic solvent, which benefits the subsequent octadecyl functionalization. Also, the unsaturated moiety in TMI molecules may be able to bond to PE chains at elevated temperature to improve the particle-matrix adhesion. The long alkyl chains attached to GO sheets can increase the hydrophobicity of GO, leading to better compatibilization with PE.

7.3.1. Characterization of FGO sheets

TEM images indicate that the ultrathin sheets of TRG and FGO have paper-like structures (Figure 7.3a and b). In general, TRG shows more wrinkles than FGO. This has been attributed to the thermal reduction process rapidly generates gas with the elimination of oxygen, which separates the graphene layers.[341, 342] Unlike functional groups such as hydroxyls or carboxyls, epoxy groups generate strain on the C-C bond of the three-membered epoxide ring. When several epoxy groups line up, the sheet can form a kink that partially releases this strain energy and makes this configuration energetically favored. Amine functionalization releases the above-mentioned strain by breaking the epoxy rings, and thus a less wrinkled but more stacked structure should form after modification. The selected area electron diffraction (SAED) patterns of FGO show only weak and diffuse rings, indicating that the FGO particle is multilayered. The diffraction spots of TRG suggest that it consists of single or a few layers, in agreement with the observed wrinkled morphology.

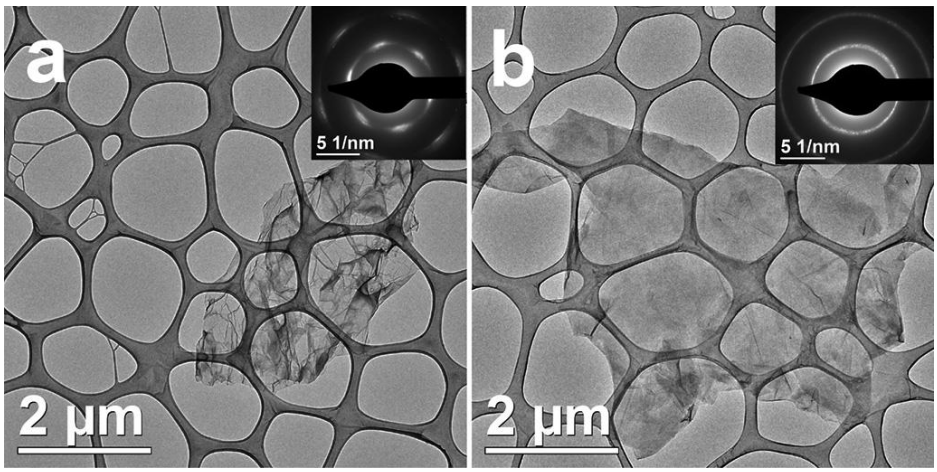

Figure 7.3. TEM micrographs and electron diffraction patterns (insets) of (a) TRG and (b) FGO.

The functionalization of GO was confirmed by IR spectroscopy (Figure 7.4a). The absorption peaks at 2920 and 2850 cm^{-1} in FGO represent the antisymmetric and symmetric stretching vibrations, respectively, of methylene groups in the long alkyl chains grafted onto GO.[199] The corresponding methylene scissoring and rocking bands appear at 1460 and 721 cm^{-1}, respectively. Absorptions due to amide C=O stretching and amide N-H bending vibrations at 1650 and 1580 cm^{-1}, respectively, and the absence of the carboxylate peak that was present in the original GO (1721 cm^{-1}), confirm the amide linkage between the long-chain alkyl amine and the GO surface. Peaks at 1105 and 1070 cm^{-1} in the FGO spectrum can be ascribed to mixed skeletal modes of C-C and C–O bonds in GO.[198, 199] The peak at 1236 cm^{-1} is attributed to epoxide groups and that at 1370 cm^{-1} to bending of C–OH phenolic groups in GO.[198]

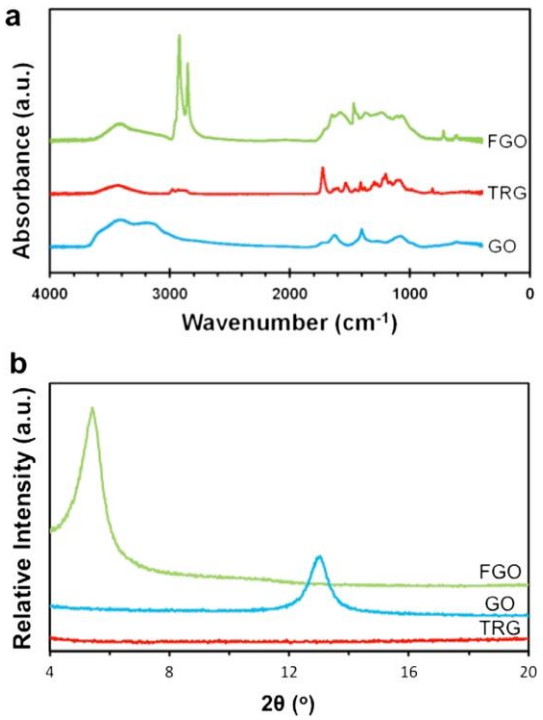

Figure 7.4. (a) Transmission FT-IR absorbance spectra of FGO, GO and TRG. (b) X-ray diffraction (XRD) patterns of FGO, GO and TRG.

The presence of these absorption peaks indicates that not all available oxygen groups on GO have been utilized in the functionalization process. Because of the relatively low density of TMI functional groups on the FGO, as well as the overlapping of its characteristic absorption peaks with those of alkyl groups and GO, we cannot observe IR absorptions corresponding to TMI in the spectrum. A broad peak between 3700 and 3000 cm^{-1}, which is apparent in all three spectra, arises from the stretching vibration of OH groups of water molecules adsorbed on GO.

The structural change in FGO was observed by X-ray diffraction as shown in Fig. 4b. Upon functionalization, the (001) diffraction peak of GO located at ~13˚ 2θ shifts to ~5˚ 2θ, indicating an increase of the interlayer spacing from ~0.72 nm to ~1.61 nm due to the incorporation of long alkyl functional groups. TRG does not display any prominent diffraction peaks in the range of 4˚ to 20˚ 2θ due to more complete exfoliation, in agreement with previous characterization of TRG.[337] The lack of X-ray diffraction peaks signifies loss of the periodic order in GO layer exfoliation and agrees with the TEM observation of one or a few layers in TRG.

7.3.2. Dispersion of FGO in PE

In addition to the thermodynamic compatibility of filler sheets with polymers, processing has a substantial impact on the dispersion and properties of graphene reinforced polymer composites. Due to the intrinsic low surface compatibility between PE and graphene, hindered polymer chain diffusion and compressive flow fields in high viscosity polymer melts may result in macroscopic aggregation in melt-compounded samples.[337]

Therefore, solution blending was employed in this study as it facilitated material transport in low viscosity solvents.[207, 337]

The crystallinity of FGO/PE nanocomposites was obtained from DSC analysis. The degree of crystallization slightly decreased at 3wt % FGO loading in PE compared to pure PE (Table 7.2). We speculate that the large amount of FGO and its good dispersion significantly hinders the diffusion of polymer chains to the growing crystallites.

Table 7.2. Properties of graphene/PE composites.

Matrix	Loading (wt%)	Surface resistance (Ohm)	Tensile modulus (MPa)
	FGO		
PE_A	0	3.10×10^{12}	145.0 ± 39.9
	1	1.78×10^{9}	120.1 ± 25.5
	3	1.89×10^{7}	146.6 ± 2.8
	5	7.19×10^{4}	480.4 ± 56.3
LLDPE	0	4.80×10^{11}	5.5 ± 0.9
	1	1.14×10^{12}	6.9 ± 0.4
	3	1.19×10^{6}	27.4 ± 1.1
	5	5.20×10^{5}	70.3 ± 7.7
OPE	0	2.47×10^{13}	61.6 ± 7.7
	1	1.09×10^{13}	58.8 ±1.8
	3	7.44×10^{12}	72.5 ± 32.1
	5	9.42×10^{9}	117.2 ± 20.5
	TRG		
PE_A	0	3.10×10^{12}	145.5 ± 39.9
	1	2.78×10^{13}	240.3 ± 21.3
	3	9.46×10^{12}	307.7 ± 35.7
	5	1.30×10^{13}	392.0 ± 53.0
LLDPE	0	4.80×10^{11}	5.4 ± 0.9
	1	1.10×10^{13}	9.1 ± 0.5
	3	2.32×10^{13}	16.1 ± 2.9
	5	1.30×10^{13}	18.6 ± 3.8
OPE	0	2.47×10^{13}	61.6 ± 7.7
	1	9.14×10^{12}	50.0 ± 12.8
	3	1.49×10^{13}	50.9 ± 2.9
	5	1.63×10^{13}	33.0 ± 11.9
	GO		
PE_A	0	3.10×10^{12}	145.5 ± 39.9
	5	2.02×10^{13}	266.0 ± 53.0
LLDPE	0	4.80×10^{11}	5.4 ± 0.9
	5	1.93×10^{12}	46.5 ± 3.8
OPE	0	2.47×10^{13}	61.6 ± 7.7
	5	1.26×10^{13}	46.7 ± 11.9

All samples were measured after 1 h annealing.

Optical microscopic images of the different composites reveal the morphology of FGO and TRG dispersed in different PE matrices. Images of PE_A films containing TRG and FGO with 1 and 3 wt% are shown in Figure 7.5. The morphology of 1 wt% TRG in the PE_A matrix can be described as partially exfoliated with significant occurrence of graphene aggregation (Figure 7.5a). The strong segregation of 3 wt% TRG from PE_A is clearly observed (Figure 7.5b). Apparent localization of TRG aggregates signifies phase separation due to intrinsic incompatibility. However, macroscopic distribution of FGO is significantly improved in PE_A (Figure 7.5c and d). Enhanced FGO dispersion was also found in LLDPE and OPE matrices (see Figure 7.6 and 7.7). The functionalization of GO appears to be critical for the generation of evenly distributed graphene in polyethylene. Figure 7.8a and b compare the dispersion of LLDPE with 3 wt% of TRG and FGO, respectively, after adjusting the color threshold. From images like these, relative dispersion indices were calculated.

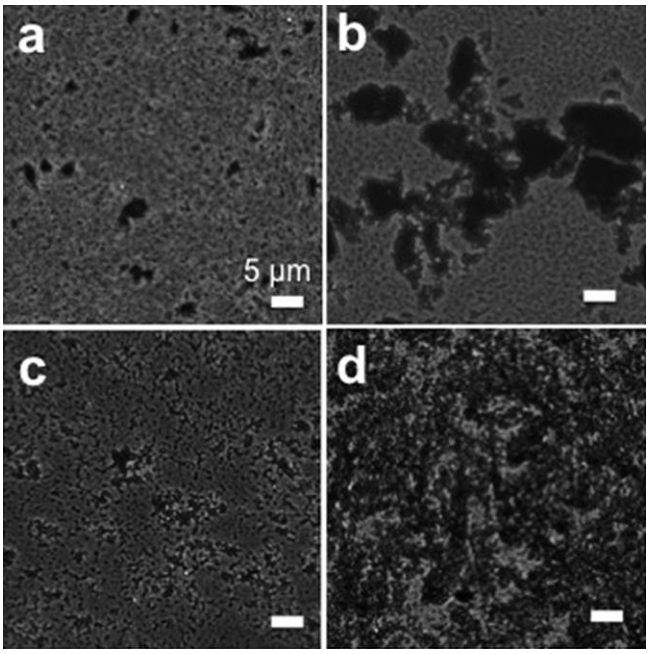

Figure 7.5. Optical microscopy images of PE_A with (a) 1 wt% TRG, (b) 3 wt% TRG, (c) 1 wt% FGO, and (d) 3 wt% FGO.

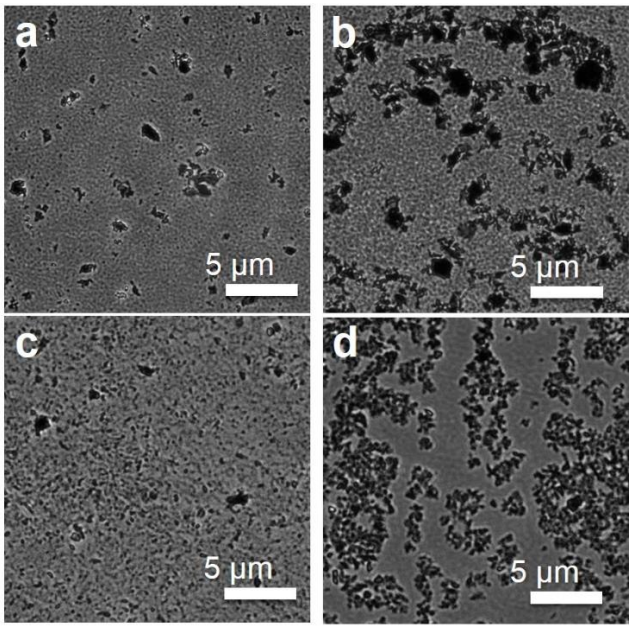

Figure 7.6. Optical microscopic images of OPE with (a) 1 wt% TRG, (b) 3 wt% TRG, (c) 1 wt% FGO and (d) 3 wt% FGO.

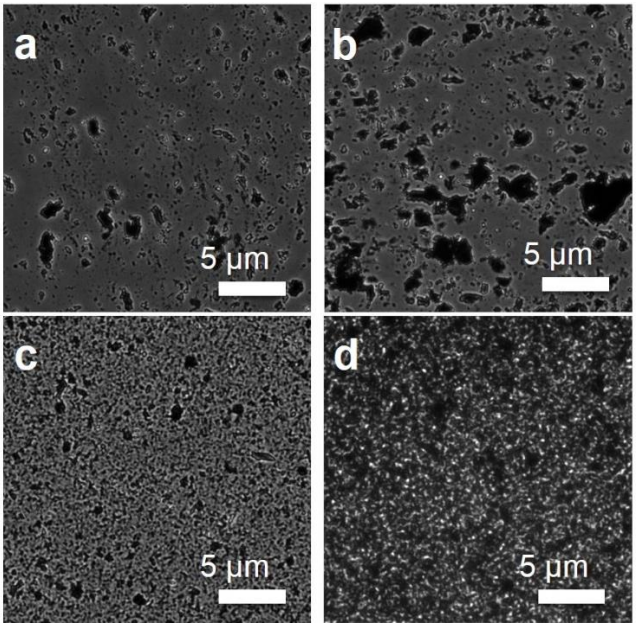

Figure 7.7. Optical Microscopic images of LLDPE with (a) 1 wt% TRG, (b) 3 wt% TRG, (c) 1 wt% FGO and (d) 3 wt% FGO.

The dispersion index results, defined as the area occupied with the filler divided by total area, are shown in Figure 7.8c. A high index indicates a more homogeneous dispersion because the fillers uniformly cover the whole surface of the microscopic samples. Judging from these thresholded images, FGO is well dispersed throughout all PE matrices. In contrast, TRG is not homogeneously dispersed into PE, leading to a comparatively low dispersion index. This verifies the compatibilization of the FGO/PE blends by GO functionalization. In addition, OPE and LLDPE seem to lead to better dispersion with TRG and FGO than PE_A. The effect of different PEs on dispersion and on electrical conductivity does not coincide because the specific properties of PE also can affect the electrical conductivity of the composites. The relation between morphological difference and differences in electrical conductivity are described in the next section.

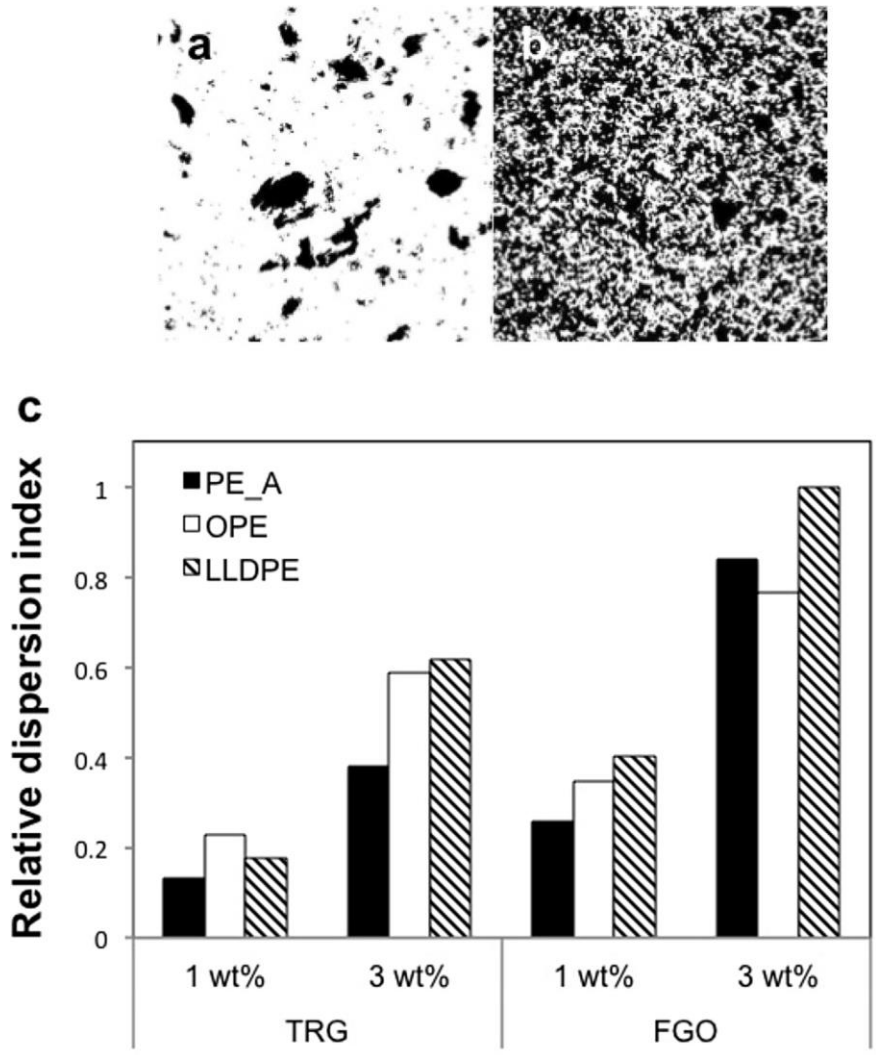

Figure 7.8. Optical microscopic images of LLDPE with (a) 3 wt% TRG and (b) 3 wt% FGO. Images were thresholded using ImageJ. (c) Relative dispersion index of 1 wt% and 3 wt% of TRG and FGO in PEs. Values are scaled to FG) with PE-A.

7.3.3. Properties of nanocomposites

PE can become electrically conductive and mechanically more robust by graphene reinforcement. Results of electrical resistance and tensile modulus measurements are summarized in Table 7.2.

Electrical conductivity

The surface resistance of 3 wt% FGO, TRG, and GO in PE after 1 h annealing is compared in a Figure 7.9. Even at the same filler concentration, the surface resistance differs considerably depending on graphene and PE compatibility. FGO composites with PE_A and LLDPE revealed substantially improved electrical conductivity. Figure 7.9b and c summarize surface resistance of composites as a function of graphene loading. While TRG/PE composites do not become electrically conductive up to 5 wt% of TRG, FGO incorporation into PE_A or LLDPE leads to a great decrease in electrical resistance. A negative influence of PE oxidation on conductivity was detected from FGO/OPE composites. Electrical conduction pathways are formed via the formation of graphene networks in the polymer matrix. Dispersion of graphene in PE inferred from conductivity enhancement generally correlated with the morphological characterization by optical microscopy seen in Figure 7.8. However, even with seemingly better dispersion from optical images (Figure 7.8c and Figure 7.6) the decrease in resistance for FGO in OPE was only observed above 3 wt%. This is likely due to the abundant oxidized groups on PE hindering the electron transport through graphene sheets in the composites.[343, 344]

Effect of thermal reduction on electrical conductivity

The most economical route to produce large quantities of graphene sheets for polymer composites appears to be reducing exfoliated GO.[333-335, 339] The oxidation step in GO synthesis gives rise to the loss of electric conductivity, thus a reduction has to be performed to recover conductivity in PE/graphene nanocomposites. Different approaches, such as thermal treatment,[345-348] chemical reduction,[347] and UV irradiation[349, 350] have been

employed to reduce GO. In this study, thermal reduction was achieved in-situ by heating the nanocomposites. Generally, temperatures above 600 ˚C are needed to perform optimal thermal reduction.[345-347] However, the practical temperature of in-situ thermal reduction is restricted by the degradation temperature of polymers.[347] Hence, simple thermal reduction of the FGO sheets dispersed in PE at moderate temperature, 210 ˚C, was employed to partially reduce FGO and to obtain reasonable electrical conductivity without any damage to the functional grafts on FGO or the PE matrices. In order to identify the time required for thermal reduction, FGO/LLDPE samples were treated at 210 ˚C for 5 min, 30 min, and 1 h (Figure 7.9). The reduction of GO started to occur even after only 5 min, leading to the restoration of electrical conductivity of FGO/LLDPE composites. As the annealing time increased, the electrical conductivity of GO in PE matrix improved further until 1 h. In case of 5 wt% FGO, 5 min reduction was already enough to obtain good electrical conductivity in FGO/LLPDPE composites. As the annealing time increased, the electrical conductivity of the composites improved further until 1 h. Therefore, 1 h annealing was selected as the condition of GO reduction for the composites.

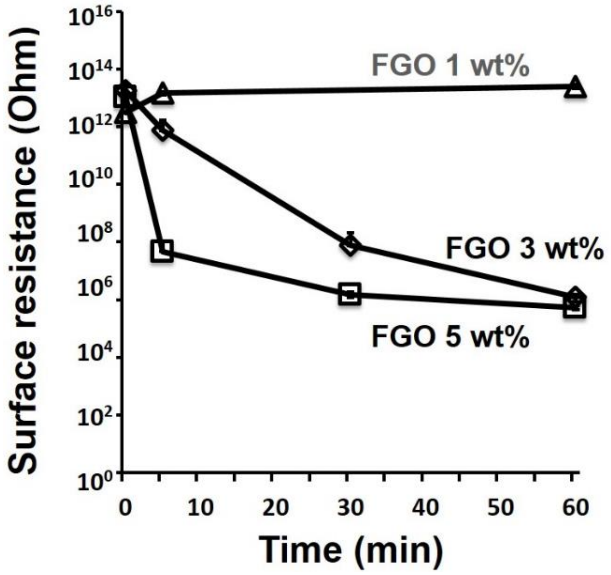

Figure 7.9. Electrical resistance of FGO/LLDPE composites after different thermal reduction time.

Figure 7.10 shows the surface resistance of FGO/LLDPE and FGO/PE_A with different FGO concentration. There was no change in the as-cast samples but an obvious decrease in resistance after 1 h annealing at 210 ˚C. The dramatic change in electrical conductivity was achieved at an FGO content of 3 wt% because at this loading FGO reached a percolation threshold through uniform dispersion within the PE matrix. The high viscosity of the polymer matrix surrounding FGO helped to prevent reaggregation of reduced FGO in the composites.[345, 351]

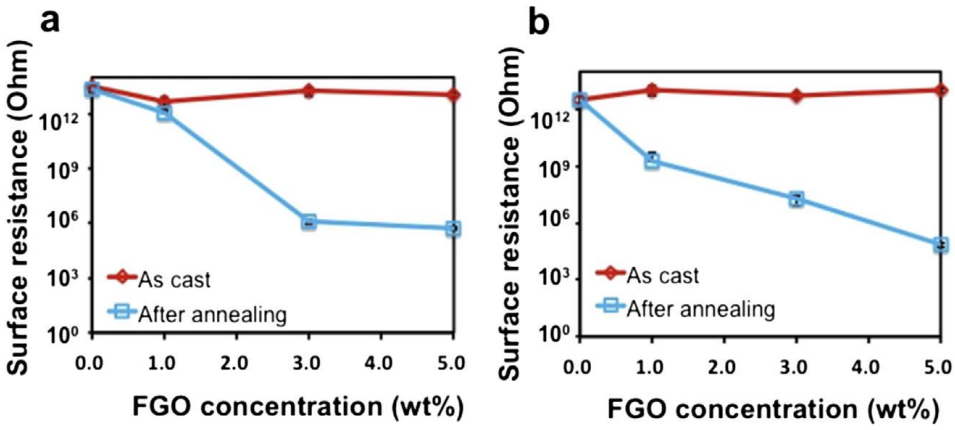

Figure 7.10. Surface resistance of (a) LLDPE and (b) PE_A with different FGO concentrations, comparing as-cast samples with those that had been annealed for 1 h

Tensile modulus

Mechanical properties of the PE polymers in this study were improved considerably via dispersion of graphene. At the same graphene concentration (5 wt%), the tensile moduli depend on the compatibility between the filler and matrices (Table 7.2). Tensile moduli were enhanced significantly by blending with FGO in all types of PE. The highest modulus was achieved with the FGO/PE_A composite (480 MPa). TRG and GO showed less increase in all PE's and even a slight modulus decrease with OPE. Tensile moduli normalized by modulus E_0 of unfilled PE are plotted in Figure 7.11.

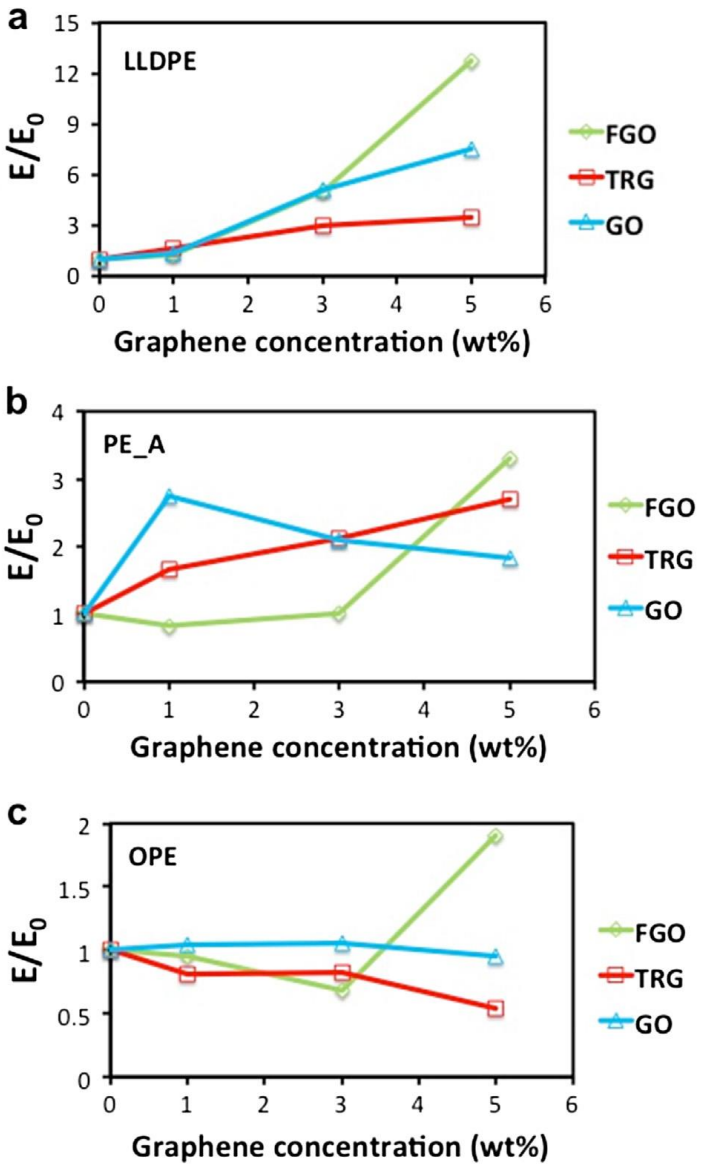

Figure 7.11. Tensile modulus of (a) graphene/LLDPE composites, (b) graphene/PE_A composites and (c) graphene/OPE composites.

Graphene/LLDPE and graphene/PE_A composites show an overall uniform increase in accordance with the graphene composition, whereas the trend is less uniform for the PE composite with GO. Particularly, GO does not show any consistent increase in the normalized tensile moduli with graphene concentration in all PEs due to the poor dispersion in PE. Another point to note is that, although all graphene/graphene derivatives show a

good dispersion in OPE, none of the graphene-based nanomaterial shows significant effect on composite modulus. We attribute this result to the relatively low molecular weight, low viscosity (shown in Table 7.1), and the presence of ample oxygen-containing groups of OPE. These factors determine that the OPE composites will phase-separate and form co-continuous structure which graphene-rich and graphene-poor domains.

7.4 Conclusions

In this study, we dispersed GO, TRG, and FGO into three PEs: linear low density LLDPE, high density PE_A, and an oxidized PE (OPE) via solvent blending. Dispersion of GO can be difficult in highly hydrophobic and non-polar matrices such as PE. In order to improve particle-matrix compatibility, GO was functionalized with 18-carbon alkyl chains and TMI moieties. This FGO was blended into the PE matrices and composite films were obtained by casting from the solution. Graphene/ PE composites were also produced from a thermally reduced GO (TRG) and unfunctionalized GO using solvent blending. At the same loading, nanocomposite properties strongly depend on the quality of filler dispersion. Visual observation of cast films indicates that FGO disperses more homogeneously in PE than GO or TRG in the same matrices.

A simple thermal treatment of the FGO nanocomposites at moderate temperature (210 ˚C) following solvent casting resulted in greatly enhanced electrical conductivity in these composites. We achieved a surface resistance of a composite lower than 10^5 Ω at an FGO content of 5 wt%. This thermal treatment yielded an improvement similar to what was observed for poly(methyl methacrylate)/GO[347] and TRG/PE nanocomposites.[337] This simple process recovered electrical conductivity at a moderate temperature without any

additional environmental control such as nitrogen atmosphere. Its effectiveness in conductivity recovery also appeared to be comparable to chemical reduction with hydrazine.[347]

Regardless of PE types, FGO increases the tensile modulus of PE more effectively than that of TRG. The modulus increased 12 times for LLDPE and 3 times for PE_A with 5 wt% FGO. Enhancements in electrical conductivity and tensile modulus are more pronounced for FGO/ LLDPE and FGO/PE_A composites than for FGO/OPE. We attribute this result to the oxidization of PE which hinders the electron transfer through graphene sheets, even though the oxide groups of OPE help the graphene disperse well in PE matrices.

Chapter 8

Summary and Outlook

8.1 Summary of modified graphene oxide toughening of unsaturated polyester resin and vinyl ester resin

Generalizing from all previous chapters in this thesis, our research has demonstrated that modified graphene oxide can be used to toughen unsaturated polyester and vinyl ester resins. Due to their high aspect ratios, mGO-based tougheners show significant toughening effects at extremely low loading levels of 0.002 wt.% to 0.04 wt.%. This type of nano-toughener is able to increase the fracture toughness (K_{IC}) of an UPR by up to 25 % and that of a VER by up to 26 %. The low required loading level also influences other aspects of mGO toughners. First, it ensures that mGO is economically viable in the cost-sensitive UPR and VER markets, considering the production cost of mGO is still formidable for most composite additive applications. Second, useful resin properties will not significantly degrade after adding such small amounts of mGO. Since these resins are often used as structural materials, it is not acceptable to have a large reduction in modulus and glass transition temperature when a toughener is added. Our experiments proved that adding mGO barely changes these properties, which is in stark contrast to incorporating polymeric tougheners such as reactive liquid rubber. In addition, unlike the sharp viscosity increase observed in resins with polymeric tougheners (which require about 5 wt.% loading), the viscosity of uncured resins does not change when mGO is used as the toughener. This is an advantage because low resin viscosity is required for building large parts with vacuum assisted resin transfer molding (VARTM).

The low loading requirement is linked with the improved dispersion of mGO in resin matrices. Like other applications, such as improving composite conductivity, toughening of thermosetting resins benefits from a good dispersion of mGO, which can be achieved by GO surface modification and processing optimization. For surface functionalization, we developed dodecylamine, octadecylamine, TMI-dedecylamine, and TDI-dihexylamine modifications. With these modifications, the surface of mGO can be engineered to be compatible with resin, thus mGO can be dispersed well into resin without sonication. Moreover, TMI moieties, which can introduce particle–matrix covalent bonding, were also successfully attached to GO surface to help enhance interfacial interaction. For processing optimization, we developed both a styrene masterbatch route and a reactive resin masterbatch route. The results show that these processing techniques help further suppress mGO aggregation during composite synthesis, which leads to fewer structural defects and better retention of composite flexural strength. In addition, using a mGO masterbatch instead of dry powder reduces inhalation risk and simplifies materials handling.

Although improvement in dispersion minimizes the adverse effect of strength reduction, it does not show a significant influence on the toughening effect. It is shown in this thesis that primary particle size of GO or mGO has little influence on toughening, which is not surprising because mGO tends to form aggregates in resin. Therefore, unlike many schematics in published papers, it is the interaction between the mGO aggregates and a propagating crack front that determines the toughening effect. To study how the aggregation behavior of different mGOs affects toughening, three different surface modifications were employed. The result indicates that mGO that does not tend to aggregate during curing has a much lower optimal loading level of 0.005 wt.%. But, if the

mGO loading becomes higher than the optimum, the resin fracture toughness will decrease sharply. The mGO that has high tendency to aggregate (ODA-GO) during matrix curing shows a delayed optimum when the loading increases, but the fracture toughness plateaus afterwards. This size-dependent toughening behavior resembles typical inorganic filler toughened UPR. The toughening effect of mGO in UPR composites lacks response to differences in particle-matrix interfacial strength. This can be readily seen when comparing the toughening result of TDI-DHA-GO and that of DDA-GO or ODA-GO. The lacks response of toughening effect to different GO surface chemistry suggests that the maximum achievable toughness for a resin is determined solely by the resin, and this value cannot be changed by new GO modification methods or by increasing mGO loading.

When adding mGO to a resin that contains inorganic filler, the toughening effect of mGO depends on the particle size or aggregate size of the inorganic filler. As is well known that some inorganic fillers themselves can provide toughening effects when incorporated. If the size of the inorganic particle aggregates is comparable to or larger than the plastic zone size of the matrix resin, adding mGO will not further improve the fracture toughness. If the addition of mGO disrupts the formation of large-scale secondary structure of filler particles, a decrease in toughness can be observed. If the filler particles or aggregates are significantly smaller than mGO aggregates, adding mGO will improve the toughness. This observation agrees well with plastic zone theory in which the size of plastic zone is estimated to be close to the size of mGO sheets. Thus, the toughening effect provided by any inorganic particles, including mGO, is independent of the materials properties of the particles. The effectiveness of mGO in toughening stems from its large aspect ratio.

Glass-fiber-reinforced composites made with mGO-toughened resin show little toughness improvement over similar composites made with neat resin. The fractography analysis of failed GFRPs indicates that the fiber composite fracture is a result of fiber-resin interfacial failure, thus fracture toughness improvement in resin will not translate to a toughened composite. Instead, we found a correlation between GFRP fracture toughness and resin ductility. Incorporating inorganic particles into UPR and VER slightly reduces resin ductility, therefore no toughness improvement can be observed. To produce toughening effects in UPR or VER based GFRPs, a better designed fiber-resin interface is a prerequisite.

8.2 Outlook

The study of mGO toughening of UPR and VER leads to the conclusion that mGO alone will not likely to be a practical toughening agent for this proposed market. However, a collaborative study on synergistic toughening of epoxy with mGO and block copolymers yielded a very promising result. In this study Dr. Tuoqi Li and I prepared a series of epoxy composites with tunable crosslink density and incorporated both mGO and a PEO-*b*-PEP block copolymer to study the fracture toughness improvement. It is interesting that, by adding 5 wt.% BCP and 0.04 wt.% mGO, the GIC of this ternary composite becomes 17 times higher than the neat resin, which is more than the sum of individual toughening contributions (13 times increase in GIC). A detailed analysis of this composite showed that there is no association between mGO and BCP, and the modulus and T_g of the composite is very close to that of the neat resin. This discovery offered us a new opportunity for designing resins with both high modulus and high toughness. We propose that mGO in this case transduces the stress around the crack tip deeper into the resin, which promotes BCP

micelle caviation in a large composite volume. This finding opens new possibilities for mGO to be a synergistic toughening additive, which may potentially solve the issue of modulus and T_g reduction when a polymeric toughener is used. It will be beneficial to know how mGO changes the toughening effect of commercially available products, such as liquid rubber and CSR. Also, by studying the mechanism of this synergy, we can better design new functionalization and processing techniques for mGO to maximize the toughening effect.

Bibliography

(1) Winey, K. I.; Vaia, R. A. *MRS Bull.* **2007**, *32*, 314.

(2) Shen, C.; Zhou, Y.; Dou, R.; Wang, W.; Yin, B.; Yang, M. B. Effect of the Core-Forming Polymer on Phase Morphology and Mechanical Properties of PA_6/EPDM-*g*-MA/HDPE Ternary Blends. *Polymer.* **2015**, *56*, 395.

(3) Huang, A.; Peng, X.; Turng, L. S. In-Situ Fibrillated Polytetrafluoroethylene (PTFE) in Thermoplastic Polyurethane (TPU) via Melt Blending: Effect on Rheological Behavior, Mechanical Properties, and Microcellular Foamability. *Polymer.* **2018**, *134*, 263.

(4) Ferri, J. M.; Fenollar, O.; Jorda-Vilaplana, A.; GarcÃa-Sanoguera, D.; Balart, R. Effect of Miscibility on Mechanical and Thermal Properties of Poly(Lactic Acid)/ Polycaprolactone Blends. *Polym. Int.* **2016**, *65*, 453.

(5) Giannelis, E. Polymer Layered Silicate Nanocomposites. *Adv. Mater.* **1996**, No. 1, 29.

(6) Braun, David D., and Meyer R. Rosen. Rheology modifiers handbook: practical use and application. Elsevier, 2013

(7) Sabzi, M.; Jiang, L.; Nikfarjam, N. Graphene Nanoplatelets as Rheology Modifiers for Polylactic Acid: Graphene Aspect-Ratio-Dependent Nonlinear Rheological Behavior. *Ind. Eng. Chem. Res.* **2015**, *54*, 8175.

(8) Wong, C. P.; Bollampally, R. S. Thermal Conductivity, Elastic Modulus, and Coefficient of Thermal Expansion of Polymer Composites Filled with Ceramic Particles for Electronic Packaging. *J. Appl. Polym. Sci.* **1999**, *74*, 3396.

(9) Bauhofer, W.; Kovacs, J. Z. A Review and Analysis of Electrical Percolation in Carbon Nanotube Polymer Composites. *Compos. Sci. Technol.* **2009**, *69*, 1486.

(10) Kuhn, J.; Ebert, H. P.; Arduini-Schuster, M. C.; Büttner, D.; Fricke, J. Thermal Transport in Polystyrene and Polyurethane Foam Insulations. *Int. J. Heat Mass Transf.* **1992**, *35*, 1795.

(11) Liao, K. H.; Qian, Y.; Macosko, C. W. Ultralow Percolation Graphene/Polyurethane Acrylate Nanocomposites. *Polymer.* **2012**, *53*, 3756.

(12) Sandler, J.; Shaffer, M. S. P.; Prasse, T.; Bauhofer, W.; Schulte, K.; Windle, A. H. Development of a Dispersion Process for Carbon Nanotubes in an Epoxy Matrix and the Resulting Electrical Properties. *Polymer.* **1999**, *40*, 5967.

(13) Stankovich, S.; Dikin, D. A.; Dommett, G. H. B.; Kohlhaas, K. M.; Zimney, E. J.; Stach, E. A.; Piner, R. D.; Nguyen, S. B. T.; Ruoff, R. S. Graphene-Based Composite Materials. *Nature* **2006**, *442*, 282.

(14) Noh, Y. J.; Joh, H. I.; Yu, J.; Hwang, S. H.; Lee, S.; Lee, C. H.; Kim, S. Y.; Youn, J. R. Ultra-High Dispersion of Graphene in Polymer Composite via Solvent Free Fabrication and Functionalization. *Sci. Rep.* **2015**, *5*, 1.

(15) Land, T.; Michely, T.; Behm, R. STM Investigation of Single Layer Graphite Structures Produced on Pt (111) by Hydrocarbon Decomposition. *Surf. Sci.* **1992**, *264*, 261-270.

(16) Li, X.; Cai, W.; An, J.; Kim, S.; Nah, J.; Yang, D.; Piner, R.; Velamakanni, A.; Jung, I.; Tutuc, E.; *et al.* Large-Area Synthesis of High-Quality and Uniform Graphene Films on Copper Foils. *Science* **2009**, *324*, 1312.

(17) Reina, A.; Jia, X.; Ho, J.; Nezich, D.; Son, H.; Bulovic, V.; Dresselhaus, M. S.; Kong, J. Large Area, Few-Layer Graphene Films on Arbitrary Substrates by Chemical Vapor Deposition. *Nano Lett.* **2009**, *9*, 30.

(18) Sutter, P. W.; Flege, J.-I.; Sutter, E. a. Epitaxial Graphene on Ruthenium. *Nat. Mater.* **2008**, *7*, 406.

(19) Kosynkin, D. V; Higginbotham, A. L.; Sinitskii, A.; Lomeda, J. R.; Dimiev, A.; Price, B. K.; Tour, J. M. Longitudinal Unzipping of Carbon Nanotubes to Form Graphene Nanoribbons. *Nature* **2009**, *458*, 872.

(20) Cano-Márquez, A. G.; Rodríguez-Macías, F. J.; Campos-Delgado, J.; Espinosa-González, C. G.; Tristán-López, F.; Ramírez-González, D.; Cullen, D. a; Smith, D. J.; Terrones, M.; Vega-Cantú, Y. I. Ex-MWNTs: Graphene Sheets and Ribbons Produced by Lithium Intercalation and Exfoliation of Carbon Nanotubes. *Nano Lett.* **2009**, *9*, 1527.

(21) Novoselov, K. S.; Geim, a K.; Morozov, S. V; Jiang, D.; Zhang, Y.; Dubonos, S. V; Grigorieva, I. V; Firsov, a a. Electric Field Effect in Atomically Thin Carbon Films. *Science* **2004**, *306*, 666.

(22) Hernandez, Y.; Nicolosi, V.; Lotya, M. High-Yield Production of Graphene by Liquid-Phase Exfoliation of Graphite. *Nat. Mater.* **2008**, *3*, 563.

(23) Lotya, M.; King, P. J.; Khan, U.; De, S.; Coleman, J. N. High-Concentration, Surfactant-Stabilized Graphene Dispersions. *ACS Nano* **2010**, *4*, 3155.

(24) Lu, J.; Yang, J.; Wang, J.; Lim, A.; Wang, S.; Loh, K. P. One-Pot Synthesis of Fluorescent Carbon Graphene by the Exfoliation of Graphite in Ionic Liquids. *ACS Nano* **2009**, *3*, 2367.

(25) Paton, K. R.; Varrla, E.; Backes, C. Scalable production of large quantities of defect-free few-layer graphene by shear exfoliation in liquids. *Nat. Mater.* **2014**, *13*, 624.

(26) Hernandez, Y.; Lotya, M.; Rickard, D.; Bergin, S. D.; Coleman, J. N. Measurement of Multicomponent Solubility Parameters for Graphene Facilitates Solvent Discovery. *Langmuir* **2010**, *26*, 3208.

(27) Khan, U.; O'Neill, A.; Lotya, M.; De, S.; Coleman, J. N. High-Concentration Solvent Exfoliation of Graphene. *Small* **2010**, *6*, 864.

(28) Ciesielski, A.; Samorì, P. Graphene via Sonication Assisted Liquid-Phase Exfoliation. *Chem. Soc. Rev.* **2014**, *43*, 381.

(29) Soldano, C.; Mahmood, A.; Dujardin, E. Production, Properties and Potential of Graphene. *Carbon* **2010**, *48*, 2127.

(30) Englert, J.; Dotzer, C.; Yang, G.; Schmid, M. Covalent Bulk Functionalization of Graphene. *Nat. Chem.* **2011**, *3*, 279.

(31) Englert, J. M.; Knirsch, K. C.; Dotzer, C.; Butz, B.; Hauke, F.; Spiecker, E.; Hirsch, A. Functionalization of Graphene by Electrophilic Alkylation of Reduced Graphite. *Chem. Commun.* **2012**, *48*, 5025.

(32) Abdelkader, A. M.; Cooper, A. J.; Dryfe, R. A. W.; Kinloch, I. A. How to Get between the Sheets: A Review of Recent Works on the Electrochemical Exfoliation of Graphene Materials from Bulk Graphite. *Nanoscale* **2015**, *7*, 6944.

(33) Dreyer, D. R.; Park, S.; Bielawski, C. W.; Ruoff, R. S. The Chemistry of Graphene Oxide. *Chem. Soc. Rev.* **2010**, *39*, 228.

(34) Hummers, W. S.; Offeman, R. E. Preparation of Graphitic Oxide. *J. Am. Chem. Soc.* **1958**, *208*, 1937.

(35) Marcano, D. C.; Kosynkin, D. V.; Berlin, J. M.; Sinitskii, A.; Sun, Z.; Slesarev, A.; Alemany, L. B.; Lu, W.; Tour, J. M. Improved Synthesis of Graphene Oxide. *ACS Nano* **2010**, *4*, 4806.

(36) Lerf, A.; He, H.; Forster, M.; Klinowski, J. Structure of Graphite Oxide Revisited. *J. Phys. Chem. B* **1998**, *5647*, 4477.

(37) Cai, W.; Piner, R.; Stadermann, F.; Park, S. Synthesis and Solid-State NMR Structural Characterization of 13C-Labeled Graphite Oxide. *Science* **2008**, *321*, *1815*.

(38) Georgakilas, V.; Otyepka, M.; Bourlinos, A. B.; Chandra, V.; Kim, N.; Kemp, K. C.; Hobza, P.; Zboril, R.; Kim, K. S. Functionalization of Graphene: Covalent and Non-Covalent Approaches, Derivatives and Applications. *Chem. Rev.* **2012**, *112*, 6156.

(39) Lomeda, J. R.; Doyle, C. D.; Kosynkin, D. V.; Hwang, W. F.; Tour, J. M. Diazonium Functionalization of Surfactant-Wrapped Chemically Converted Graphene Sheets. *J. Am. Chem. Soc.* **2008**, *130*, 16201.

(40) Zhu, Y.; Higginbotham, A. L.; Tour, J. M. Covalent Functionalization of Surfactant-Wrapped Graphene Nanoribbons. *Chem. Mater.* **2009**, *21*, 5284.

(41) Fang, M.; Wang, K.; Lu, H.; Yang, Y.; Nutt, S. Covalent Polymer Functionalization of Graphene Nanosheets and Mechanical Properties of Composites. *J. Mater. Chem.* **2009**, *19*, 7098.

(42) Jin, Z.; McNicholas, T.; Shih, C. Click Chemistry on Solution-Dispersed Graphene and Monolayer CVD Graphene. *Chem. Mater.* **2011**, *23*, 3362.

(43) Park, O.-K.; Hahm, M. G.; Lee, S.; Joh, H.-I.; Na, S.-I.; Vajtai, R.; Lee, J. H.; Ku, B.-C.; Ajayan, P. M. In Situ Synthesis of Thermochemically Reduced Graphene Oxide Conducting Nanocomposites. *Nano Lett.* **2012**, *12*, 1789.

(44) Wei, G.; Yan, M.; Dong, R.; Wang, D.; Zhou, X.; Chen, J.; Hao, J. Covalent Modification of Reduced Graphene Oxide by Means of Diazonium Chemistry and Use as a Drug-Delivery System. *Chem. Eur. J.* **2012**, *18*, 14708.

(45) Lu, Y.; Jiang, Y.; Wei, W.; Wu, H.; Liu, M.; Niu, L.; Chen, W. Novel Blue Light Emitting Graphene Oxide Nanosheets Fabricated by Surface Functionalization. *J. Mater. Chem.* **2012**, *22*, 2929.

(46) Georgakilas, V.; Bourlinos, A. B.; Zboril, R.; Steriotis, T. A.; Dallas, P.; Stubos, A. K.; Trapalis, C. Organic Functionalisation of Graphenes. *Chem. Commun.* **2010**, *46*, 1766.

(47) Vadukumpully, S.; Gupta, J.; Zhang, Y.; Xu, G. Q.; Valiyaveettil, S. Functionalization of Surfactant Wrapped Graphene Nanosheets with Alkylazides for Enhanced Dispersibility. *Nanoscale* **2011**, *3*, 303.

(48) Zhong, X.; Jin, J.; Li, S.; Niu, Z.; Hu, W.; Li, R.; Ma, J. Aryne Cycloaddition: Highly Efficient Chemical Modification of Graphene. *Chem. Commun.* **2010**, *46*, 7340.

(49) Georgakilas, V.; Tiwari, J. N.; Kemp, K. C.; Perman, J. A.; Bourlinos, A. B.; Kim, K. S.; Zboril, R. Noncovalent Functionalization of Graphene and Graphene Oxide for Energy Materials, Biosensing, Catalytic, and Biomedical Applications. *Chem. Rev.* **2016**, *116*, 5464.

(50) An, X.; Simmons, T.; Shah, R.; Wolfe, C.; Lewis, K. M.; Washington, M.; Nayak, S. K.; Talapatra, S.; Kar, S. Stable Aqueous Dispersions of Noncovalently Functionalized Graphene from Graphite and Their Multifunctional High-Performance Applications. *Nano Lett.* **2010**, *10*, 4295.

(51) Mann, J. A.; Rodríguez-López, J.; Abruña, H. D.; Dichtel, W. R. Multivalent Binding Motifs for the Noncovalent Functionalization of Graphene. *J. Am. Chem. Soc.* **2011**, *133*, 17614.

(52) Liu, Y.; Zhou, J.; Zhang, X.; Liu, Z.; Wan, X.; Tian, J.; Wang, T.; Chen, Y. Synthesis, Characterization and Optical Limiting Property of Covalently Oligothiophene-Functionalized Graphene Material. *Carbon* **2009**, *47*, 3113.

(53) Yu, D.; Yang, Y.; Durstock, M.; Baek, J.; Dai, L. Soluble P3HT-Grafted Graphene for Efficient Bilayer-Heterojunction Photovoltaic Devices. *ACS Nano* **2010**, *4*, 5633.

(54) Liu, Z.; Robinson, J. T.; Sun, X.; Dai, H. PEGylated Nanographene Oxide for Delivery of Water-Insoluble Cancer Drugs. *J. Am. Chem. Soc.* **2008**, *130*, 10876.

(55) Liu, Z.-B.; Xu, Y.-F.; Zhang, X.-Y.; Zhang, X.-L.; Chen, Y.-S.; Tian, J.-G. Porphyrin and Fullerene Covalently Functionalized Graphene Hybrid Materials with Large Nonlinear Optical Properties. *J. Phys. Chem. B* **2009**, *113*, 9681.

(56) Zhang, X.; Feng, Y.; Huang, D.; Li, Y.; Feng, W. Investigation of Optical Modulated Conductance Effects Based on a Graphene Oxide–azobenzene Hybrid. *Carbon* **2010**, *48*, 3236.

(57) Choudhary, S.; Mungse, H. P.; Khatri, O. P. Dispersion of Alkylated Graphene in Organic Solvents and Its Potential for Lubrication Applications. *J. Mater. Chem.* **2012**, *22*, 21032.

(58) Tessonnier, J.-P.; Barteau, M. a. Dispersion of Alkyl-Chain-Functionalized Reduced Graphene Oxide Sheets in Nonpolar Solvents. *Langmuir* **2012**, *28*, 6691.

(59) Jang, J.; Pham, V. H.; Hur, S. H.; Chung, J. S. Dispersibility of Reduced Alkylamine-Functionalized Graphene Oxides in Organic Solvents. *J. Colloid Interface Sci.* **2014**, *424*, 62.

(60) Stankovich, S.; Piner, R. D.; Nguyen, S. T.; Ruoff, R. S. Synthesis and Exfoliation of Isocyanate-Treated Graphene Oxide Nanoplatelets. *Carbon* **2006**, *44*, 3342.

(61) Lerf, A.; Heb, H.; Forster, M.; Klinowskib, J. 13C and 1H MAS NMR Studies of Graphite Oxide and Its Chemically Modified Derivatives. *Solid State Ionics* **1997**, *103*, 857.

(62) Obreja, A. C.; Cristea, D.; Gavrila, R.; Schiopu, V.; Dinescu, A.; Danila, M.; Comanescu, F. Isocyanate Functionalized graphene/P3HT Based Nanocomposites. *Appl. Surf. Sci.* **2013**, *276*, 458.

(63) Saha, U.; Jaiswal, R.; Singh, J. P.; Goswami, T. H. Diisocyanate Modified Graphene Oxide Network Structure: Steric Effect of Diisocyanates on Bimolecular Cross-Linking Degree. *J. Nanoparticle Res.* **2014**, *16*, 2404.

(64) Zhang, M. M. Hyperbranched Polysiloxane Functionalized Graphene Oxide for Dicyclopentadiene Bisphenol Dicyanate Ester Nanocomposites with High Performance. *Express Polym. Lett.* **2014**, *8*, 413.

(65) Li, Z.; Shen, J.; Ma, H.; Lu, X.; Shi, M.; Li, N.; Ye, M. Preparation and Characterization of pH- and Temperature-Responsive Hydrogels with Surface-Functionalized Graphene Oxide as the Crosslinker. *Soft Matter* **2012**, *8*, 3139.

(66) Hou, S.; Kasner, M.; Su, S. Highly Sensitive and Selective Dopamine Biosensor Fabricated with Silanized Graphene. *J. Phys. Chem. C* **2010**, 14915.

(67) Cha, C.; Shin, S. R.; Gao, X.; Annabi, N.; Dokmeci, M. R.; Tang, X. S.; Khademhosseini, A. Controlling Mechanical Properties of Cell-Laden Hydrogels by Covalent Incorporation of Graphene Oxide. *Small* **2014**, *10*, 514.

(68) Yang, H.; Li, F.; Shan, C.; Han, D.; Zhang, Q.; Niu, L.; Ivaska, A. Covalent Functionalization of Chemically Converted Graphene Sheets via Silane and Its Reinforcement. *J. Mater. Chem.* **2009**, *19*, 4632.

(69) Wang, X.; Xing, W.; Zhang, P.; Song, L.; Yang, H.; Hu, Y. Covalent Functionalization of Graphene with Organosilane and Its Use as a Reinforcement in Epoxy Composites. *Compos. Sci. Technol.* **2012**, *72*, 737.

(70) Layek, R. K.; Nandi, A. K. A Review on Synthesis and Properties of Polymer Functionalized Graphene. *Polymer.* **2013**, *54*, 5087.

(71) Gao, J.; Bao, F.; Feng, L.; Shen, K.; Zhu, Q.; Wang, D.; Chen, T.; Ma, R.; Yan, C. Functionalized Graphene Oxide Modified Polysebacic Anhydride as Drug Carrier for Levofloxacin Controlled Release. *RSC Adv.* **2011**, *1*, 1737.

(72) Song, N.; Yang, J.; Ding, P.; Tang, S.; Liu, Y.; Shi, L. Effect of Covalent-Functionalized Graphene Oxide with Polymer and Reactive Compatibilization on Thermal Properties of Maleic Anhydride Grafted Polypropylene. *Ind. Eng. Chem. Res.* **2014**, *53*, 19951.

(73) Salavagione, H. J.; Gómez, M. A.; Martínez, G. Polymeric Modification of Graphene through Esterification of Graphite Oxide and Poly(Vinyl Alcohol). *Macromolecules* **2009**, *42*, 6331.

(74) Yuan, B.; Bao, C.; Song, L.; Hong, N.; Liew, K. M.; Hu, Y. Preparation of Functionalized Graphene Oxide/Polypropylene Nanocomposite with Significantly

Improved Thermal Stability and Studies on the Crystallization Behavior and Mechanical Properties. *Chem. Eng. J.* **2014**, *237*, 411.

(75) Castelaín, M.; Martínez, G.; Marco, C.; Ellis, G.; Salavagione, H. J. Effect of Click-Chemistry Approaches for Graphene Modification on the Electrical, Thermal, and Mechanical Properties of Polyethylene/Graphene Nanocomposites. *Macromolecules* **2013**, *46*, 8980.

(76) Gonalves, G.; Marques, P. A. A. P.; Barros-Timmons, A.; Bdkin, I.; Singh, M. K.; Emami, N.; Grácio, J. Graphene Oxide Modified with PMMA via ATRP as a Reinforcement Filler. *J. Mater. Chem.* **2010**, *20*, 9927.

(77) Ye, Y. S.; Chen, Y. N.; Wang, J. S.; Rick, J.; Huang, Y. J.; Chang, F. C.; Hwang, B. J. Versatile Grafting Approaches to Functionalizing Individually Dispersed Graphene Nanosheets Using RAFT Polymerization and Click Chemistry. *Chem. Mater.* **2012**, *24*, 2987.

(78) García-Valdez, O.; Ledezma-Rodríguez, R.; Saldívar-Guerra, E.; Yate, L.; Moya, S.; Ziolo, R. F. Graphene Oxide Modification with Graft Polymers via Nitroxide Mediated Radical Polymerization. *Polymer.* **2014**, *55*, 2347.

(79) Xu, C.; Wang, X.; Zhu, J. Graphene - Metal Particle Nanocomposites. *J. Phys. Chem. C* **2008**, *112*, 19841.

(80) Ramezanzadeh, B.; Haeri, Z.; Ramezanzadeh, M. A Facile Route of Making Silica Nanoparticles-Covered Graphene Oxide Nanohybrids (SiO2-GO); Fabrication of SiO2-GO/Epoxy Composite Coating with Superior Barrier and Corrosion Protection Performance. *Chem. Eng. J.* **2016**, *303*, 511.

(81) Ma, Y.; Di, H.; Yu, Z.; Liang, L.; Lv, L.; Pan, Y.; Zhang, Y.; Yin, D. Fabrication of Silica-Decorated Graphene Oxide Nanohybrids and the Properties of Composite Epoxy Coatings Research. *Appl. Surf. Sci.* **2016**, *360*, 936.

(82) Yu, Z.; Di, H.; Ma, Y.; He, Y.; Liang, L.; Lv, L.; Ran, X.; Pan, Y.; Luo, Z. Preparation of Graphene Oxide Modified by Titanium Dioxide to Enhance the Anti-Corrosion Performance of Epoxy Coatings. *Surf. Coatings Technol.* **2015**, *276*, 471.

(83) Tong, W.; Zhang, Y.; Yu, L.; Lv, F.; Liu, L.; Zhang, Q.; An, Q. Amorphous TiO_2-Coated Reduced Graphene Oxide Hybrid Nanostructures for Polymer Composites with Low Dielectric Loss. *Chem. Phys. Lett.* **2015**, *638*, 43.

(84) Feng, X.; Xing, W.; Song, L.; Hu, Y.; Liew, K. M. TiO2loaded on Graphene Nanosheet as Reinforcer and Its Effect on the Thermal Behaviors of Poly(Vinyl Chloride) Composites. *Chem. Eng. J.* **2015**, *260*, 524.

(85) Daud, M.; Kamal, M. S.; Shehzad, F.; Al-Harthi, M. A. Graphene/Layered Double Hydroxides Nanocomposites: A Review of Recent Progress in Synthesis and Applications. *Carbon* **2016**, *104*, 241.

(86) Wu, H.; Yi, W.; Chen, Z.; Wang, H.; Du, Q. Janus Graphene Oxide Nanosheets Prepared via Pickering Emulsion Template. *Carbon* **2015**, *93*, 473.

(87) Akbari, M.; Shariaty-Niassar, M.; Matsuura, T.; Ismail, A. F. Janus Graphene Oxide Nanosheet: A Promising Additive for Enhancement of Polymeric Membranes Performance Prepared via Phase Inversion. *J. Colloid Interface Sci.* **2018**, *527*, 10.

(88) Naebe, M.; Wang, J.; Amini, A.; Khayyam, H.; Hameed, N.; Li, L. H.; Chen, Y.; Fox, B. Mechanical Property and Structure of Covalent Functionalised Graphene/Epoxy Nanocomposites. *Sci. Rep.* **2014**, *4*, 1.

(89) Wan, Y. J.; Tang, L. C.; Gong, L. X.; Yan, D.; Li, Y. B.; Wu, L. Bin; Jiang, J. X.; Lai, G. Q. Grafting of Epoxy Chains onto Graphene Oxide for Epoxy Composites with Improved Mechanical and Thermal Properties. *Carbon* **2014**, *69*, 467.

(90) Wu, G.; Cheng, Y.; Wang, Z.; Wang, K.; Feng, A. In Situ Polymerization of Modified Graphene/Polyimide Composite with Improved Mechanical and Thermal Properties. *J. Mater. Sci. Mater. Electron.* **2017**, *28*, 576.

(91) Ha, H. W.; Choudhury, A.; Kamal, T.; Kim, D.-H.; Park, S.-Y. Effect of Chemical Modification of Graphene on Mechanical, Electrical, and Thermal Properties of Polyimide/Graphene Nanocomposites. *ACS Appl. Mater. Interfaces* **2012**, *4*, 4623.

(92) Li, Y.; Pei, X.; Shen, B.; Zhai, W.; Zhang, L.; Zheng, W. Polyimide/Graphene Composite Foam Sheets with Ultrahigh Thermostability for Electromagnetic Interference Shielding. *RSC Adv.* **2015**, *5*, 24342.

(93) Wan, Y. J.; Yang, W. H.; Yu, S. H.; Sun, R.; Wong, C. P.; Liao, W. H. Covalent Polymer Functionalization of Graphene for Improved Dielectric Properties and Thermal Stability of Epoxy Composites. *Compos. Sci. Technol.* **2016**, *122*, 27.

(94) Liao, K. H.; Aoyama, S.; Abdala, A. A.; Macosko, C. Does Graphene Change T g of Nanocomposites? *Macromolecules* **2014**, *47*, 8311.

(95) Wang, S.; Tambraparni, M.; Qiu, J.; Tipton, J.; Dean, D. Thermal Expansion of Graphene Composites. *Macromolecules* **2009**, *42*, 5251.

(96) Tseng, I. H.; Chang, J. C.; Huang, S. L.; Tsai, M. H. Enhanced Thermal Conductivity and Dimensional Stability of Flexible Polyimide Nanocomposite Film by Addition of Functionalized Graphene Oxide. *Polym. Int.* **2013**, *62*, 827.

(97) Bai, L.; He, S.; Fruehwirth, J. W.; Stein, A.; Macosko, C. W.; Cheng, X. Localizing Graphene at the Interface of Cocontinuous Polymer Blends: Morphology, Rheology, and Conductivity of Cocontinuous Conductive Polymer Composites. *J. Rheol.* **2017**, *61*, 575.

(98) Bai, L.; Sharma, R.; Cheng, X.; Macosko, C. W. Kinetic Control of Graphene Localization in Co-Continuous Polymer Blends via Melt Compounding. *Langmuir* **2018**, *34*, 1073.

(99) Verdejo, R.; Bernal, M. M.; Romasanta, L. J.; Lopez-Manchado, M. A. Graphene Filled Polymer Nanocomposites. *J. Mater. Chem.* **2011**, *21*, 3301.

(100) Chen, Z.; Xu, C.; Ma, C.; Ren, W.; Cheng, H. M. Lightweight and Flexible Graphene Foam Composites for High-Performance Electromagnetic Interference Shielding. *Adv. Mater.* **2013**, *25*, 1296.

(101) Shen, B.; Li, Y.; Yi, D.; Zhai, W.; Wei, X.; Zheng, W. Strong Flexible Polymer/Graphene Composite Films with 3D Saw-Tooth Folding for Enhanced and Tunable Electromagnetic Shielding. *Carbon* **2017**, *113*, 55.

(102) Ma, X.; Shen, B.; Zhang, L.; Liu, Y.; Zhai, W.; Zheng, W. Porous Superhydrophobic Polymer/Carbon Composites for Lightweight and Self-Cleaning EMI Shielding Application. *Compos. Sci. Technol.* **2018**, *158*, 86.

(103) Ling, J.; Zhai, W.; Feng, W.; Shen, B.; Zhang, J.; Zheng, W. G. Facile Preparation of Lightweight Microcellular Polyetherimide/Graphene Composite Foams for Electromagnetic Interference Shielding. *ACS Appl. Mater. Interfaces* **2013**, *5*, 2677.

(104) Yan, D. X.; Ren, P. G.; Pang, H.; Fu, Q.; Yang, M. B.; Li, Z. M. Efficient Electromagnetic Interference Shielding of Lightweight Graphene/Polystyrene Composite. *J. Mater. Chem.* **2012**, *22*, 18772.

(105) Eswaraiah, V.; Sankaranarayanan, V.; Ramaprabhu, S. Functionalized Graphene-PVDF Foam Composites for EMI Shielding. *Macromol. Mater. Eng.* **2011**, *296*, 894.

(106) Guo, Y.; Bao, C.; Song, L.; Yuan, B.; Hu, Y. In Situ Polymerization of Graphene, Graphite Oxide, and Functionalized Graphite Oxide into Epoxy Resin and Comparison Study of on-the-Flame Behavior. *Ind. Eng. Chem. Res.* **2011**, *50*, 7772.

(107) Wang, X.; Song, L.; Yang, H.; Lu, H.; Hu, Y. Synergistic Effect of Graphene on Antidripping and Fire Resistance of Intumescent Flame Retardant Poly(Butylene Succinate) Composites. *Ind. Eng. Chem. Res.* **2011**, *50*, 5376.

(108) Graphene, B. F. F.; Feng, Y.; Li, X.; Zhao, X.; Ye, Y.; Zhou, X.; Liu, H.; Liu, C.; Xie, X. Synergetic Improvement in Thermal Conductivity and Flame Retardancy of Epoxy / Silver Nanowires Composites by Incorporating "Branch-like" Flame Retardant-Functionalized Graphene. *ACS Appl. Mater. Interfaces* **2018**, *10*, 21628.

(109) Pethsangave, D. A.; Khose, R. V.; Wadekar, P. H.; Some, S. Deep Eutectic Solvent Functionalized Graphene Composite as an Extremely High Potency Flame Retardant. *ACS Appl. Mater. Interfaces* **2017**, *9*, 35319.

(110) Wang, X.; Xing, W.; Feng, X.; Yu, B.; Lu, H.; Song, L.; Hu, Y. The Effect of Metal Oxide Decorated Graphene Hybrids on the Improved Thermal Stability and the Reduced Smoke Toxicity in Epoxy Resins. *Chem. Eng. J.* **2014**, *250*, 214.

(111) Gu, J.; Liang, C.; Zhao, X.; Gan, B.; Qiu, H.; Guo, Y.; Yang, X.; Zhang, Q.; Wang, D. Y. Highly Thermally Conductive Flame-Retardant Epoxy Nanocomposites with Reduced Ignitability and Excellent Electrical Conductivities. *Compos. Sci. Technol.* **2017**, *139*, 83.

(112) Hegab, H. M.; Elmekawy, A.; Zou, L.; Mulcahy, D.; Saint, C. P.; Ginic-Markovic, M. The Controversial Antibacterial Activity of Graphene-Based Materials. *Carbon* **2016**, *105*, 362.

(113) Shi, L.; Chen, J.; Teng, L.; Wang, L.; Zhu, G.; Liu, S.; Luo, Z.; Shi, X.; Wang, Y.; Ren, L. The Antibacterial Applications of Graphene and Its Derivatives. *Small* **2016**, *12*, 4165.

(114) Liu, S.; Hu, M.; Zeng, T. H.; Wu, R.; Jiang, R.; Wei, J.; Wang, L.; Kong, J.; Chen, Y. Lateral Dimension-Dependent Antibacterial Activity of Graphene Oxide Sheets. *Langmuir* **2012**, *28*, 12364.

(115) Liu, S.; Zeng, T. H.; Hofmann, M.; Burcombe, E.; Wei, J.; Jiang, R.; Kong, J.; Chen, Y. Antibacterial Activity of Graphite, Graphite Oxide, Graphene Oxide, and Reduced Graphene Oxide: Membrane and Oxidative Stress. *ACS Nano* **2011**, *5*, 6971.

(116) Zhang, Z. B.; Wu, J. J.; Su, Y.; Zhou, J.; Gao, Y.; Yu, H. Y.; Gu, J. S. Layer-by-Layer Assembly of Graphene Oxide on Polypropylene Macroporous Membranes via Click Chemistry to Improve Antibacterial and Antifouling Performance. *Appl. Surf. Sci.* **2015**, *332*, 300.

(117) Mazaheri, M.; Akhavan, O.; Simchi, A. Flexible Bactericidal Graphene Oxide-Chitosan Layers for Stem Cell Proliferation. *Appl. Surf. Sci.* **2014**, *301*, 456.

(118) He, L.; Dumée, L. F.; Feng, C.; Velleman, L.; Reis, R.; She, F.; Gao, W.; Kong, L. Promoted Water Transport across Graphene Oxide-Poly(Amide) Thin Film Composite Membranes and Their Antibacterial Activity. *Desalination* **2015**, *365*, 126.

(119) Hegab, H. M.; ElMekawy, A.; Barclay, T. G.; Michelmore, A.; Zou, L.; Saint, C. P.; Ginic-Markovic, M. Fine-Tuning the Surface of Forward Osmosis Membranes via

Grafting Graphene Oxide: Performance Patterns and Biofouling Propensity. *ACS Appl. Mater. Interfaces* **2015**, *7*, 18004.

(120) Deepachitra, R.; Ramnath, V.; Sastry, T. P. Graphene Oxide Incorporated Collagen-Fibrin Biofilm as a Wound Dressing Material. *RSC Adv.* **2014**, *4*, 62717.

(121) Fan, Z.; Liu, B.; Wang, J.; Zhang, S.; Lin, Q.; Gong, P.; Ma, L.; Yang, S. A Novel Wound Dressing Based on Ag/Graphene Polymer Hydrogel: Effectively Kill Bacteria and Accelerate Wound Healing. *Adv. Funct. Mater.* **2014**, *24*, 3933.

(122) Cui, Y.; Kundalwal, S. I.; Kumar, S. Gas Barrier Performance of Graphene/Polymer Nanocomposites. *Carbon* **2016**, *98*, 313.

(123) Yoo, B. M.; Shin, H. J.; Yoon, H. W.; Park, H. B. Graphene and Graphene Oxide and Their Uses in Barrier Polymers. *J. Appl. Polym. Sci.* **2014**, *131*, 1.

(124) Huang, H. D.; Ren, P. G.; Chen, J.; Zhang, W. Q.; Ji, X.; Li, Z. M. High Barrier Graphene Oxide Nanosheet/Poly(Vinyl Alcohol) Nanocomposite Films. *J. Memb. Sci.* **2012**, *409*, 156.

(125) Layek, R. K.; Das, A. K.; Park, M. J.; Kim, N. H.; Lee, J. H. Enhancement of Physical, Mechanical, and Gas Barrier Properties in Noncovalently Functionalized Graphene Oxide/Poly(Vinylidene Fluoride) Composites. *Carbon* **2015**, *81*, 329.

(126) Chen, J. T.; Fu, Y. J.; An, Q. F.; Lo, S. C.; Zhong, Y. Z.; Hu, C. C.; Lee, K. R.; Lai, J. Y. Enhancing Polymer/Graphene Oxide Gas Barrier Film Properties by Introducing New Crystals. *Carbon* **2014**, *75*, 443.

(127) Yan, N.; Buonocore, G.; Lavorgna, M.; Kaciulis, S.; Balijepalli, S. K.; Zhan, Y.; Xia, H.; Ambrosio, L. The Role of Reduced Graphene Oxide on Chemical, Mechanical

and Barrier Properties of Natural Rubber Composites. *Compos. Sci. Technol.* **2014**, *102*, 74.

(128) Yang, Y. H.; Bolling, L.; Priolo, M. A.; Grunlan, J. C. Super Gas Barrier and Selectivity of Graphene Oxide-Polymer Multilayer Thin Films. *Adv. Mater.* **2013**, *25*, 503.

(129) Gerasimov, G. Graphene-Based Gas Sensors. *RSC Detect. Sci.* **2017**, *10*, 133.

(130) Lee, D. C.; Yang, H. N.; Park, S. H.; Kim, W. J. Nafion/Graphene Oxide Composite Membranes for Low Humidifying Polymer Electrolyte Membrane Fuel Cell. *J. Memb. Sci.* **2014**, *452*, 20.

(131) Chang, K. C.; Hsu, M. H.; Lu, H. I.; Lai, M. C.; Liu, P. J.; Hsu, C. H.; Ji, W. F.; Chuang, T. L.; Wei, Y.; Yeh, J. M.; et al. Room-Temperature Cured Hydrophobic Epoxy/Graphene Composites as Corrosion Inhibitor for Cold-Rolled Steel. *Carbon* **2014**, *66*, 144.

(132) Chang, C. H.; Huang, T. C.; Peng, C. W.; Yeh, T. C.; Lu, H. I.; Hung, W. I.; Weng, C. J.; Yang, T. I.; Yeh, J. M. Novel Anticorrosion Coatings Prepared from Polyaniline/Graphene Composites. *Carbon* **2012**, *50*, 5044.

(133) Ganesh, B. M.; Isloor, A. M.; Ismail, A. F. Enhanced Hydrophilicity and Salt Rejection Study of Graphene Oxide-Polysulfone Mixed Matrix Membrane. *Desalination* **2013**, *313*, 199.

(134) Pascault, J. P.; Sautereau, H.; Verdu, J.; Williams, R. J. J. *Thermosetting Polymers*; Marcel Dekker: New York, USA, **2002**.

(135) Wu, X.-F.; Yarin, A. L. Recent Progress in Interfacial Toughening and Damage Self-Healing of Polymer Composites Based on Electrospun and Solution-Blown Nanofibers: An Overview. *J. Appl. Polym. Sci.***2013**, *130*, 2225.

(136) Sharmila, R. J.; Premkumar, S.; Alagar, M. Toughened Polyester Matrices for Advanced Composites. *J. Appl. Polym. Sci.***2007**, *103*, 167.

(137) Builes, D.; Hernandez, H. The Morphology of Nanostructured Unsaturated Polyesters Modified with PEO-B-PPO-B-PEO Triblock Copolymer and Their Optical and Mechanical Properties. *J. Phys. Chem. C* ***2013***, *117*, 3563.

(138) Carothers, W. H.; Arvin, J. A. Studies on Polymerization and Ring Formation. II. poly-esters. *J. Am. Chem. Soc.* ***1929***, *51*, 2560.

(139) Cherian, a. B.; Thachil, E. T. Blends of Unsaturated Polyester Resin with Functional Elastomers. *J. Elastomers Plast.* **2003**, *35*, 367.

(140) Zijian, W.; Linghui, M.; Li, L.; Zaixing, J.; Lixin, X.; Dawei, J.; Yudong, H. Interface Enhancement of Carbon Fiber Reinforced Unsaturated Polyester Composites with Sizing Agent Containing Carbon Nanotubes. *J. Reinf. Plast. Compos.* **2013**, *33*, 242.

(141) Zhou, G.; Movva, S.; Lee, L. J. Preparation and Properties of Nanoparticle and Long-Fiber-Reinforced Unsaturated Polyester Composites. *Polym. Compos.* **2009**, *30*, 861.

(142) Gamstedt, E.; Skrifvars, M.; Jacobsen, T.; Pyrz, R. Synthesis of Unsaturated Polyesters for Improved Interfacial Strength in Carbon Fibre Composites. *Compos. Part A Appl. Sci. Manuf.* **2002**, *33*, 1239.

(143) Thitithanasarn, S.; Yamada, K.; Ishiaku, U. S.; Hamada, H. Jute Fabric Reinforced Engineering Thermoplastic Sandwich Composites. I. The Effect of Molding Time. *J. Appl. Polym. Sci.* **2013**, *127*, 2952.

(144) Corbiere-Nicollier, T. Life Cycle Assessment of Biofibres Replacing Glass Fibres as Reinforcement in Plastics. *Resour., Conserv. Recycl.* **2001**, *33*, 267.

(145) Wambua, P.; Ivens, J.; Verpoest, I. Natural Fibres: Can They Replace Glass in Fibre Reinforced Plastics? *Compos. Sci. Technol.* **2003**, *63*, 1259.

(146) Idicula, M.; Joseph, K.; Thomas, S. Mechanical Performance of Short Banana/Sisal Hybrid Fiber Reinforced Polyester Composites. *J. Reinf. Plast. Compos.* **2009**, *29*, 12.

(147) Idicula, M.; Neelakantan, N. R.; Oommen, Z.; Joseph, K.; Thomas, S. A Study of the Mechanical Properties of Randomly Oriented Short Banana and Sisal Hybrid Fiber Reinforced Polyester Composites. *J. Appl. Polym. Sci.* **2005**, *96*, 1699.

(148) Al-Kaabi, K.; Al-Khanbashi, a.; Hammami, a. Date Palm Fibers as Polymeric Matrix Reinforcement: DPF/polyester Composite Properties. *Polym. Compos.* **2005**, *26*, 604.

(149) Ganan, P.; Mondragon, I. Fique Fiber-Reinforced Polyester Composites: Effects of Fiber Surface Treatments on Mechanical Behavior. *J. Mater. Sci.* **2004**, *9*, 3121.

(150) Huang, Y.; Kinloch, A. J.; Bertsch, R. J.; Siebert, A. R. Particle-Matrix Interfacial Bonding. In Toughened Plastics I*;* Advances in Chemistry 233; American Chemical Society: Washington, DC, **1993**, 189.

(151) Unnikrishnan, K. P.; Thachil, E. T. Toughening of Epoxy Resins. *Des. Monomers Polym.* **2006**, *9*, 129.

(152) Bagheri, R.; Marouf, B. T.; Pearson, R. a. Rubber-Toughened Epoxies: A Critical Review. *Polym. Rev.* **2009**, *49*, 201.

(153) Garg, A.; Mai, Y. Failure Mechanisms in Toughened Epoxy Resins—a Review. *Compos. Sci. Technol.* **1988**, *31*, 179.

(154) Abbate, M.; Martuscelli, E. Maleated Polyisobutylene: A Novel Toughener for Unsaturated Polyester Resins. *J. Appl.Polym. Sci.* **1995**, *58*, 1825.

(155) Abbate, M.; Martuscelli, E. A Novel Reactive Liquid Rubber with Maleimide End Groups for the Toughening of Unsaturated Polyester Resins. *J. Appl. Polym. Sci.* **1996**, *62*, 2107-2119.

(156) Martuscelli, E.; Musto, P. Reactive Rubbers as Toughening Agents for Thermoset Polyester Resins. Molecular Analysis by FTIR and Fracture Behavior of the Resulting Blends. *J. Polym. Sci. Part B Polym. Phys.* **1993**, *31*, 619-632.

(157) Guhanathan, S.; Saroja Devi, M. Synthesis and Application of Multilayered Core Shell Particles for Toughening of Unsaturated Polyester Resin. *J. Appl. Polym. Sci.* **2004**, *94*, 511.

(158) Pham, S.; Burchill, P. J. Toughening of Vinyl Ester Resins with Modified Polybutadienes. *Polymer.* **1995**, *36*, 3279.

(159) Dreerman, E.; Narkis, M. Mechanical Behavior and Structure of Rubber Modified Vinyl Ester Resins. *J. Appl. Polym. Sci.* **1999**, *72*, 647.

(160) Robinette, E. J.; Ziaee, S.; Palmese, G. R. Toughening of Vinyl Ester Resin Using Butadiene-Acrylonitrile Rubber Modifiers. *Polymer.* **2004**, *45*, 6143.

(161) Ahmadi, M.; Moghbeli, M. R.; Shokrieh, M. M. Rubber Modification of Unsaturated Polyester Resin with Core-Shell Rubber Particles: Effect of Shell Composition. *Polym. Eng. Sci.* **2012**, *52*, 1928.

(162) Huang, Y.-J.; Wu, J.-H.; Liang, J.-G.; Hsu, M.-W.; Ma, J.-K. Toughening of Unsaturated Polyester Resins with Core. *J. Appl. Polym. Sci.* **2008**, *107*, 939.

(163) Builes, D.; Hernandez, H. Relationship Between the Morphology of Nanostructured Unsaturated Polyesters Modified with PEO-B-PPO-B-PEO Triblock

Copolymer and Their Optical and Mechanical Properties. *J. Phys. Chem. C* **2013**, *117*, 3563−3571.

(164) Builes, D. H.; Tercjak, A.; Mondragon, I. Nanostructured Unsaturated Polyester Modified with Poly[(ethylene oxide)-*b*-(propylene oxide)-*b*-(ethylene oxide)] Triblock Copolymer. *Polymer* **2012**, *53*, 3669.

(165) Builes, D. H.; Labidi, J.; Eceiza, A.; Mondragon, I.; Tercjak, A. Unsaturated Polyester Nanocomposites Modified with Fibrillated Cellulose and PEO-*b*-PPO-*b*-PEO Block Copolymer. *Compos. Sci. Technol.* **2013**, *89*, 120.

(166) Sinturel, C. Nanostructured Polymers Obtained from Polyethylene- Block -Poly(Ethylene Oxide) Block Copolymer in Unsaturated Polyester. *Macromolecules* **2007**, *40*, 2532.

(167) Builes, D. H.; Hernández-Ortiz, J. P.; Corcuera, M. A.; Mondragon, I.; Tercjak, A. Effect of Poly(ethylene oxide) Homopolymer and Two Different Poly(ethylene oxide-*b*-Poly(propylene Oxide)-*b*-Poly(ethylene Oxide) Triblock Copolymers on Morphological, Optical, and Mechanical Properties of Nanostructured Unsaturated Polyester. *ACS Appl. Mater. Interfaces* **2014**, *6*, 1073.

(168) Chandramohan, a.; Alagar, M. Synthesis and Characterization of 1, 1-Bis (3-Methyl-4-Epoxyphenyl) Cyclohexane-Toughened DGEBA and TGDDM Organo Clay Hybrid Nanocomposites. *High Perform. Polym.* **2011**, *23*, 197.

(169) Evora, V.; Shukla, a. Fabrication, Characterization, and Dynamic Behavior of polyester/TiO_2 Nanocomposites. *Mater. Sci. Eng. A* **2003**, *361*, 358.

(170) Goodarzi, V.; Monemian, S. A.; Maleki, F.; Angaji, M. T. In Situ Radical Copolymerization in Presence of Surface-Modified TiO2 Nanoparticles: Influence of a

Double Modification on Properties of Unsaturated Polyester (UP) Nanocomposites. *J. Macromol. Sci. Part B* **2008**, *47*, 472.

(171) Zhang, M.; Singh, R. P. Mechanical Reinforcement of Unsaturated Polyester by Al_2O_3 Nanoparticles. *Mater. Lett.* **2004**, *58*, 408.

(172) Sue, H.-J.; Meitin, E. I. G.; Pickelman, D. M.; Bott, C. J. Fracture Mechanisms in Rigid Core-Shell Particle Modified High Performance Epoxies. *Colloid Polym. Sci.* **1996**, *274*, 342.

(173) Kim, J.; Robertson, R. Toughening of Thermoset Polymers by Rigid Crystalline Particles. *J. Mater. Sci.* **1992**, *27*, 161.

(174) Tang, L.-C.; Zhang, H.; Sprenger, S.; Ye, L.; Zhang, Z. Fracture Mechanisms of Epoxy-Based Ternary Composites Filled with Rigid-Soft Particles. *Compos. Sci. Technol.* **2012**, *72*, 558.

(175) Toughening, R. P.; Resins, E. Rubbery and Rigid Particle Toughening. *J. Appl. Polym. Sci.* **1994**, *54*, 177.

(176) Tang, L.-C.; Wan, Y.-J.; Yan, D.; Pei, Y.-B.; Zhao, L.; Li, Y.-B.; Wu, L.-B.; Jiang, J.-X.; Lai, G.-Q. The Effect of Graphene Dispersion on the Mechanical Properties of Graphene/epoxy Composites. *Carbon* **2013**, *60*, 16.

(177) Wang, X.; Jin, J.; Song, M. An Investigation of the Mechanism of Graphene Toughening Epoxy. *Carbon* **2013**, *65*, 324.

(178) Chandrasekaran, S.; Seidel, C.; Schulte, K. Preparation and Characterization of Graphite Nano-Platelet (GNP)/epoxy Nano-Composite: Mechanical, Electrical and Thermal Properties. *Eur. Polym. J.* **2013**, *49*, 3878.

(179) Zaman, I.; Phan, T.; Kuan, H.; Meng, Q. Epoxy/graphene Platelets Nanocomposites with Two Levels of Interface Strength. *Polymer.* **2011**, *52*, 1603.

(180) Jiang, T.; Kuila, T.; Kim, N.; Ku, B.; Lee, J. Enhanced Mechanical Properties of Silanized Silica Nanoparticle Attached Graphene Oxide/epoxy Composites. *Compos. Sci.Technol.* **2013**, *79*, 115.

(181) Chandrasekaran, S.; Sato, N.; Tölle, F. Fracture Toughness and Failure Mechanism of Graphene Based Epoxy Composites. *Compos. Sci.Technol.* **2014**, *97*, 90.

(182) Bortz, D. R.; Heras, E. G.; Martin-Gullon, I. Impressive Fatigue Life and Fracture Toughness Improvements in Graphene Oxide/Epoxy Composites. *Macromolecules* **2012**, *45*, 238.

(183) Zaman, I.; Kuan, H.-C.; Meng, Q.; Michelmore, A.; Kawashima, N.; Pitt, T.; Zhang, L.; Gouda, S.; Luong, L.; Ma, J. A Facile Approach to Chemically Modified Graphene and Its Polymer Nanocomposites. *Adv. Funct. Mater.* **2012**, *22*, 2735.

(184) Cho, D.; Hwang, J. H. Elastomeric Coating of Exfoliated Graphite Nanoplatelets with Amine-Terminated Poly(butadiene-*co*-acrylonitrile): Characterization and Its Epoxy Toughening Effect. *Adv. Polym. Technol.* **2013**, *32*, 21366.

(185) Yavari, F.; Rafiee, M. a; Rafiee, J.; Yu, Z.-Z.; Koratkar, N. Dramatic Increase in Fatigue Life in Hierarchical Graphene Composites. *ACS Appl. Mater. Interfaces* **2010**, *2*, 2738.

(186) Li, Y.; Umer, R.; Isakovic, A.; Samad, Y. A.; Zheng, L.; Liao, K. Synergistic Toughening of Epoxy with Carbon Nanotubes and Graphene Oxide for Improved Long-Term Performance. *RSC Adv.* **2013**, *3*, 8849.

(187) Bora, C.; Gogoi, P.; Baglari, S.; Dolui, S. K. Preparation of Polyester Resin/graphene Oxide Nanocomposite with Improved Mechanical Strength. *J. Appl. Polym. Sci.* **2013**, *129*, 3432.

(188) Geim, K.; Novoselov, K. S. The Rise of Graphene. *Nat. Mater.***2007**, *6*, 183.

(189) Huang, Y. J.; Wu, J. H.; Liang, J. G.; Hsu, M. W.; Ma, J. K. Toughening of unsaturated polyester resins with core–shell rubbers, *J. Appl. Polym. Sci.* **2008**, *107*, 939.

(190) Messori, M.; Toselli, M.; Pilati, F.; Tonelli, C. Unsaturated polyester resins modified with poly(ε-caprolactone)–perfluoropolyethers block copolymers. *Polymer.* **2001**, *42*, 09877.

(191) Singh, R. P.; Zhang, M.; Chan, D. Toughening of a brittle thermosetting polymer: effects of reinforcement particle size and volume fraction. *J. Mater. Sci.* **2002**, *37*, 781.

(192) Park, Y. T.; Qian, Y.; Chan, C.; Suh, T.; Nejhad, M. G.; Macosko, C. W.; Stein, A. Epoxy toughening with low graphene loading. *Adv. Funct. Mater.* **2015**, *25*, 575.

(193) Hernandez, Y.; Nicolosi, V.; Lotya, M.; Blighe, F. M.; Sun, Z.; De, S.; McGovern, I. T.; Holland, B.; Byrne, M.; Gun'ko, Y. K.; et al. High yield production of graphene by liquid phase exfoliation of graphite. *Nat. Nanotechnol.* **2008**, *3*, 563.

(194) Lu, J.; Yang, J.; Wang, J.; Lim, A.; Wang, S.; Loh, K. P. One-pot synthesis of fluorescent carbon nanoribbons, nanoparticles, and graphene by the exfoliation of graphite in ionic liquids. *ACS Nano* **2009**, *3*, 2367.

(195) ASTM Standard D790-10, 2010. Standard test methods for flexural properties of unreinforced and reinforced plastics and electrical insulating materials. ASTM International, West Conshokocken, 2010.

(196) ASTM Standard D5045-99, 1999. Standard test methods for plane-strain fracture toughness and strain energy release rate of plastic materials. ASTM International, West Conshokocken, 2010.

(197) Galande, C.; Mohite, A. D.; Naumov, A. V.; Gao, W.; Ci, L.; Ajayan, A.; Gao, H.; Srivastava, A.; Bruce Weisman, R.; Ajayan, P. M. Quasi-molecular fluorescence from graphene oxide. *Sci. Rep.* **2011**, *1*, 1.

(198) Szabó, T.; Berkesi, O.; Dékány, I. DRIFT Study of deuterium-exchanged graphite oxide. *Carbon.* **2005**, *43*, 3186.

(199) Silverstein, R. M.; Bassler, G. C.; Morrill, T. C. Spectrometric identification of organic compounds, 4th ed., John Wiley & Sons: New York, 1981.

(200) Compton, O. C.; Dikin, D. A.; Putz, K. W.; Brinson, L. C.; Nguyen, S. T. Electrically conductive "alkylated" graphene paper via chemical reduction of amine-functionalized graphene oxide paper. *Adv. Mater.* **2010**, *22*, 892.

(201) Jeong, H. K.; Lee, Y. P.; Jin, M. H.; Kim, E. S.; Bae, J. J.; Lee, Y. H. Thermal stability of graphite oxide. *Chem. Phys. Lett.* **2009**, *470*, 255.

(202) Zhang, J.; Deng, S.; Wang, Y.; Ye, L. Role of rigid nanoparticles and CTBN rubber in the toughening of epoxies with different cross-linking densities. *Compos. Part A Appl. Sci. Manuf.* **2016**, *80*, 82.

(203) Quaresimin, M.; Schulte, K.; Zappalorto, M.; Chandrasekaran, S. Toughening mechanisms in polymer nanocomposites: from experiments to modelling. *Compos. Sci. Technol.* **2016**, *123*, 187.

(204) Wetzel, B.; Rosso, P.; Haupert, F.; Friedrich, K. Epoxy nanocomposites - fracture and toughening mechanisms. *Eng. Fract. Mech.* **2006**, *73*, 2375.

(205) Liff, S. M.; Kumar, N.; McKinley, G. H. High-Performance Elastomeric Nanocomposites via Solvent-Exchange Processing. *Nat. Mater.* **2007**, *6*, 76.

(206) Qian, Y.; Lindsay, C. I.; Macosko, C.; Stein, A. Synthesis and Properties of Vermiculite-Reinforced Polyurethane Nanocomposites. *ACS Appl. Mater. Interfaces* **2011**, *3*, 3709.

(207) Kim, H.; Miura, Y.; Macosko, C. W. Graphene/polyurethane Nanocomposites for Improved Gas Barrier and Electrical Conductivity. *Chem. Mater.* **2010**, *22*, 3441.

(208) Song, Y. S.; Youn, J. R. Influence of Dispersion States of Carbon Nanotubes on Physical Properties of Epoxy Nanocomposites. *Carbon* **2005**, *43*, 1378.

(209) Suetsugu Y. State of Dispersion–mechanical Properties Correlation in Small Particle Filled Polymer Composites. *Int. Polym. Proc*. **1990**, *5*, 184.

(210) Hussain M. B.; Oku Y. B.; Nakahira A. B.; Niihara K. B. Effects of Wet Ball-milling on Particle Dispersion and Mechanical Properties of Particulate Epoxy Composites. *Mater. Lett.* **1996**, *26*, 177.

(211) Khare, H. S.; Burris, D. L. A Quantitative Method for Measuring Nanocomposite Dispersion. *Polymer* **2010**, *51* (3), 719.

(212) Si, Y.; Samulski, E. T. Synthesis of Water Soluble Graphene. *Nano Lett.* **2008**, *8*, 1679.

(213) Chua, C. K.; Pumera, M. Covalent Chemistry on Graphene. *Chem. Soc. Rev.* **2013**, *42*, 3222.

(214) Pokharel, P.; Lee, D. S. High Performance Polyurethane Nanocomposite Films Prepared from a Masterbatch of Graphene Oxide in Polyether Polyol. *Chem. Eng. J.* **2014**, *253*, 356

(215) Bao, C.; Song, L.; Xing, W.; Yuan, B.; Wilkie, C. A.; Huang, J.; Guo, Y.; Hu, Y. Preparation of Graphene by Pressurized Oxidation and Multiplex Reduction and Its Polymer Nanocomposites by Masterbatch-Based Melt Blending. *J. Mater. Chem.* **2012**, *22*, 6088.

(216) Bai, L.; He, S.; Fruehwirth, J. W.; Stein, A.; Macosko, C. W.; Cheng, X. Localizing Graphene at the Interface of Co-continuous Polymer Blends: Morphology, Rheology, and Conductivity of Co-continuous Conductive Polymer Composites. *J. Rheol.* **2017**, *61*, 575.

(218) Park, S.; He, S.; Wang, J.; Stein, A.; Macosko, C. W. Graphene-polyethylene Nanocomposites: Effect of Graphene Functionalization. *Polymer*. **2016**, *104*, 1.

(219) Prolongo, S. G.; Moriche, R.; Jiménez-Suárez, A.; Sánchez, M.; Ureña, A. Advantages and Disadvantages of the Addition of Graphene Nanoplatelets to Epoxy Resins. *Eur. Polym. J.* **2014**, *61*, 206.

(220) He, S.; Petkovich, N. D.; Liu, K.; Qian, Y.; Macosko, C. W.; Stein, A. Unsaturated Polyester Resin Toughening with Very Low Loadings of GO Derivatives. *Polymer*. **2017**, *110*, 149.

(221) Li, T.; He, S.; Stein, A.; Francis, L. F.; Bates, F. S. Synergistic Toughening of Epoxy Modified by Graphene and Block Copolymer Micelles. *Macromolecules* **2016**, *49*, 9507.

(222) Rafiee, M. A.; Rafiee, J.; Wang, Z.; Song, H.; Yu, Z. Z.; Koratkar, N. Enhanced Mechanical Properties of Nanocomposites at Low Graphene Content. *ACS Nano* **2009**, *3*, 3884.

(223) Rafiee, M. A.; Rafiee, J.; Srivastava, I.; Wang, Z.; Song, H.; Yu, Z. Z.; Koratkar, N. Fracture and Fatigue in Graphene Nanocomposites. *Small* **2010**, *6*, 179.

(224) Zhang, M.; Yan, H.; Yang, X.; Liu, C. Effect of Functionalized Graphene Oxide with a Hyperbranched Cyclotriphosphazene Polymer on Mechanical and Thermal Properties of Cyanate Ester Composites. *RSC Adv.* **2014**, *4*, 45930.

(225) Ren, F.; Zhu, G.; Ren, P.; Wang, Y.; Cui, X. In Situ Polymerization of Graphene Oxide and Cyanate Ester-Epoxy with Enhanced Mechanical and Thermal Properties. *Appl. Surf. Sci.* **2014**, *316*, 549.

(226) Qian, J. Y.; Pearson, R. A.; Dimonie, V. L.; El-Aasser, M. S. Synthesis and Application of Core-shell Particles as Toughening Agents for Epoxies. *J. Appl. Polym. Sci.* **1995**, *58*, 439.

(227) Liu, T.; Tjiu, W. C.; Tong, Y.; He, C.; Goh, S. S.; Chung, T. S. Morphology and Fracture Behavior of Intercalated Epoxy/clay Nanocomposites. *J. Appl. Polym. Sci.* **2004**, *94*, 1236.

(228) Li, T.; Heinzer, M. J.; Francis, L. F.; Bates, F. S. Engineering Superior Toughness in Commercially Viable Block Copolymer Modified Epoxy Resin. *J. Polym. Sci. Part B Polym. Phys.* **2015**, 189.

(229) Levita, G.; De Petris, S.; Marchetti, A.; Lazzeri, A. Crosslink Density and Fracture Toughness of Epoxy Resins. *J. Mater. Sci.* **1991**, *26*, 2348.

(230) Sprenger, S. Epoxy Resin Composites with Surface-Modified Silicon Dioxide Nanoparticles: A Review. *J. Appl. Polym. Sci.* **2013**, *130*, 1421.

(231) Strong AB. *Fundamentals of Composites Manufacturing: Materials, Methods and Applications.* Society of Manufacturing Engineers; **2008**.

(232) Kargarzadeh, H.; Sheltami, R. M.; Ahmad, I.; Abdullah, I.; Dufresne, A. Cellulose Nanocrystal Reinforced Liquid Natural Rubber Toughened Unsaturated Polyester: Effects of Filler Content and Surface Treatment on Its Morphological, Thermal, Mechanical, and Viscoelastic Properties. *Polym.* **2015**, *71*, 51.

(233) He, S.; Qian, Y.; Liu, K.; Macosko, C. W.; Stein, A. Modified-Graphene-Oxide-Containing Styrene Masterbatches for Thermosets. *Ind. Eng. Chem. Res.* **2017**, 56, 11443.

(234) Seyhan, A. T.; Tanoğlu, M.; Schulte, K. Tensile Mechanical Behavior and Fracture Toughness of MWCNT and DWCNT Modified Vinyl-Ester/polyester Hybrid Nanocomposites Produced by 3-Roll Milling. *Mater. Sci. Eng. A* **2009**, *523*, 85.

(235) Grishchuk, S.; Castella, N.; Apostolov, A. A.; Karger-Kocsis, J. Structure and Properties of Vinyl Ester Resins Modified with Organophilic Synthetic Layered Silicates Bearing Non- and Co-Reactive Intercalants. *J. Compos. Mater.* **2012**, *46*, 941.

(236) Green, D. J.; Nicholson, P. S.; Embury, J. D. Fracture of a Brittle Particulate Composite - Part 2 Theoretical Aspects. *J. Mater. Sci.* **1979**, *14*, 1657.

(237) Faber, K. T.; Evans, A. G. Crack Deflection Processes—I. Theory. *Acta Metallurgica*, **1983**, *31*, 565.

(238) Walls, H. J.; Caines, S. B.; Sanchez, A. M.; Khan, S. A. Yield Stress and Wall Slip Phenomena in Colloidal Silica Gels. *J. Rheol.* **2003**, *47*, 847.

(239) Sun, C. T.; Jin, Z. H. Chapter 6 – Crack Tip Plasticity. In *Fracture Mechanics*; Academic Press: Boston, **2012**; 123.

(240) Yu, A.; Ramesh, P.; Itkis, M. E.; Bekyarova, E.; Haddon, R. C. Graphite Nanoplatelet-Epoxy Composite Thermal Interface Materials. *J. Phys. Chem. C* **2007**, *111*, 7565.

(241) Teng, C. C.; Ma, C. C. M.; Lu, C. H.; Yang, S. Y.; Lee, S. H.; Hsiao, M. C.; Yen, M. Y.; Chiou, K. C.; Lee, T. M. Thermal Conductivity and Structure of Non-Covalent Functionalized Graphene/Epoxy Composites. *Carbon* **2011**, *49*, 5107.

(242) Song, S. H.; Park, K. H.; Kim, B. H.; Choi, Y. W.; Jun, G. H.; Lee, D. J.; Kong, B. S.; Paik, K. W.; Jeon, S. Enhanced Thermal Conductivity of Epoxy-Graphene Composites by Using Non-Oxidized Graphene Flakes with Non-Covalent Functionalization. *Adv. Mater.* **2013**, *25*, 732.

(243) Ma, J.; Meng, Q.; Zaman, I.; Zhu, S.; Michelmore, A.; Kawashima, N.; Wang, C. H.; Kuan, H. C. Development of Polymer Composites Using Modified, High-Structural Integrity Graphene Platelets. *Compos. Sci. Technol.* **2014**, *91*, 82.

(244) He, S.; Qian, Y.; Liu, K.; Macosko, C. W.; Stein, A. Effects of Inorganic Fillers on Toughening of Vinyl Ester Resins by Modified Graphene Oxide. *Ind. Eng. Chem. Res.* **2018**, *57*, 4592.

(245) Nečas, D.; Klapetek, P. Gwyddion: An Open-Source Software for SPM Data Analysis. *Cent. Eur. J. Phys.* **2012**, *10*, 181.

(246) Schindelin, J.; Arganda-Carreras, I.; Frise, E.; Kaynig, V.; Longair, M.; Pietzsch, T.; Preibisch, S.; Rueden, C.; Saalfeld, S.; Schmid, B.; et al. Fiji: An Open-Source Platform for Biological-Image Analysis. *Nat. Methods* **2012**, *9*, 676.

(247) Botas, C.; Pérez-Mas, A. M.; Álvarez, P.; Santamaría, R.; Granda, M.; Blanco, C.; Menéndez, R. Optimization of the Size and Yield of Graphene Oxide Sheets in the Exfoliation Step. *Carbon* **2013**, *63*, 576.

(248) Tsai, L. D.; Hwang, M. R. *Thermoplastic and Thermosetting Polymers and Composites*. Nova Science Publishers. New York, 2011

(249) Chikhi, N.; Fellahi, S; Bakar, M. Modification of Epoxy Resin Using Reactive Liquid (ATBN) Rubber. *Eur. Polym. J.* **2002**, *38*, 251.

(250) Kunz, S. C.; Sayre, J. A.; Assink, R. A. Morphology and Toughness Characterization of Epoxy-Resins Modified with Amine and Carboxyl Terminated Rubbers. *Polymer*. **1982**, *23*, 1897.

(251) Garg, A. C.; Mai, Y. W. Failure Mechanisms in Toughened Epoxy-Resins - A Review. *Compos. Sci. Technol.* **1988**, *31*, 179.

(252) Dadfar, M.; Ghadami, F. Effect of Rubber Modification on Fracture Toughness Properties of Glass Reinforced Hot Cured Epoxy Composites. *Mater. Design.* **2013**, *47*, 16.

(253) Day, R. J.; Lovell, P. A.; Wazzan, A. A. Toughened Carbon/Epoxy Composites Made by Using Core/Shell Particles. *Compos. Sci. Technol.* **2001**, *61*, 41.

(254) Giannakopoulos, G.; Masania, K.; Taylor, A. C. Toughening of Epoxy Using Core-Shell Particles. *J. Mater. Sci.* **2011**, *46*, 327.

(255) Quan, D.; Ivankovic, A. Effect of Core-Shell Rubber (CSR) Nano-Particles on Mechanical Properties and Fracture Toughness of An Epoxy Polymer. *Polymer.* **2015**, *66*, 16.

(256) Ngah, S. A.; Taylor, A. C. Toughening Performance of Glass Fibre Composites with Core-Shell Rubber and Silica Nanoparticle Modified Matrices. *Composites Part A.* **2016**, *80*, 292.

(257) Thompson, Z. J.; Hillmyer, M. A.; Liu, J.; Sue, H. J.; Dettloff, M.; Bates, F. S. Block Copolymer Toughened Epoxy: Role of Cross-Link Density. *Macromolecules.* **2009**, *42*, 2333.

(258) Declet-Perez, C.; Francis, L. F.; Bates, F. S. Deformation Processes in Block Copolymer Toughened Epoxies. *Macromolecules.* **2015**, *48*, 3672.

(259) Pearson, R. A.; Yee, A. F. Toughening Mechanisms in Elastomer-Modified Epoxies .3. The Effect of Cross-Link Density. *J. Mater. Sci.* **1989**, *24*, 2571.

(260) Yee, A. F.; Pearson, R. A. Toughening Mechanisms in Elastomer-Modified Epoxies .1. Mechanical Studies. *J. Mater. Sci.* **1986**, *21*, 2462.

(261) Liang, Y. L.; Pearson, R. A. Toughening Mechanisms in Epoxy-Silica Nanocomposites (ESNs). *Polymer.* **2009**, *50*, 4895.

(262) Sprenger, S. Improving Mechanical Properties of Fiber-Reinforced Composites Based on Epoxy Resins Containing Industrial Surface-Modified Silica Nanoparticles: Review and Outlook. *J. Compos. Mater.* **2015**, *49*, 53.

(263) Dorigato, A.; Pegoretti, A.; Quaresimin, M. Thermo-Mechanical Characterization of Epoxy/Clay Nanocomposites as Matrices for Carbon/Nanoclay/Epoxy Laminates. *Mat. Sci. Eng. A-Struct.* **2011**, *528*, 6324.

(264) Wang, K.; Chen, L.; Wu, J. S.; Toh, M. L.; He, C. B.; Yee, A. F. Epoxy Nanocomposites with Highly Exfoliated Clay: Mechanical Properties and Fracture Mechanisms. *Macromolecules.* **2005**, *38*, 788.

(265) Gojny, F.; Wichmann, M.; Köpke, U.; Fiedler, B.; Schulte, K. Carbon Nanotube-Reinforced Epoxy-Composites: Enhanced Stiffness and Fracture Toughness at Low Nanotube Content. *Compos. Sci. Technol.* **2004**, *64*, 2363.

(266) Kim, H.; Abdala, A. A.; Macosko, C. W. Graphene/Polymer Nanocomposites. *Macromolecules.* **2010**, *43*, 6515.

(267) Yasmin, A.; Abot, J. L.; Daniel, I. M. Processing of Clay/Epoxy Nanocomposites by Shear Mixing. *Scripta. Mater.* **2003**, *49*, 81.

(268) Mahrholz, T.; Stangle, J.; Sinapius, M. Quantitation of The Reinforcement Effect of Silica Nanoparticles in Epoxy Resins Used in Liquid Composite Moulding Processes. *Composites Part A.* **2009**, *40*, 235.

(269) Mallick, P. K. *Fiber-Reinforced Composites: Materials, Manufacturing, and Design.* 3rd ed. CRC Press, Boca Raton, FL, 2008.

(270) Kinloch, A. J.; Mohammed, R. D.; Taylor, A. C.; Sprenger, S.; Egan, D. The Interlaminar Toughness of Carbon-Fibre Reinforced Plastic Composites Using 'Hybrid-Toughened' Matrices. *J. Mater. Sci.* **2006**, *41* 5043.

(271) Yan, C.; Xiao, K. Q.; Ye, L.; Mai, Y. W. Numerical and Experimental Studies on The Fracture Behavior of Rubber-Toughened Epoxy in Bulk Specimen and Laminated Composites. *J. Mater. Sci.* **2002**, *37*, 921.

(272) Tsai, J. L.; Huang, B. H.; Cheng, Y. L. Enhancing Fracture Toughness of Glass/Epoxy Composites by Using Rubber Particles Together with Silica Nanoparticles. *J. Compos. Mater.* **2009**, *43*, 3107.

(273) Zeng, Y.; Liu, H-Y.; Mai, Y-W.; Du X-S. Improving Interlaminar Fracture Toughness of Carbon Fibre/Epoxy Laminates by Incorporation of Nano-Particles. *Composites Part B.* **2012**, *43*, 90.

(274) Hsieh, T. H.; Kinloch, A. J.; Masania, K.; Lee, J. S.; Taylor, A. C.; Sprenger, S. The Toughness of Epoxy Polymers and Fibre Composites Modified with Rubber Microparticles and Silica Nanoparticles. *J. Mater. Sci.* **2010**, *45*, 1193.

(275) Siddiqui, N. A.; Woo, RSC.; Kim, J. K.; Leung, CCK.; Munir, A. Mode I Interlaminar Fracture Behavior and Mechanical Properties of CFRPs With Nanoclay-Filled Epoxy Matrix. *Composites Part A.* **2007**, *38*, 449.

(276) Xu, Y.; Van Hoa, S. Mechanical Properties of Carbon Fiber Reinforced Epoxy/Clay Nanocomposites. *Compos. Sci. Technol.* **2008**, *68*, 854.

(277) Zhang, D.; Ye, L.; Deng, S.; Zhang, J.; Tang, Y.; Chen, Y. CF/EP Composite Laminates with Carbon Black and Copper Chloride for Improved Electrical Conductivity and Interlaminar Fracture Toughness. *Compos. Sci. Technol.* **2012**, *72*, 412.

(278) Wichmann, M. H.; Sumfleth, J.; Gojny, F. H.; Quaresimin, M.; Fiedler, B.; Schulte, K. Glass-Fibre-Reinforced Composites with Enhanced Mechanical and Electrical Properties–Benefits and Limitations of A Nanoparticle Modified Matrix. *Eng. Fract. Mech.* **2006**, *73*, 2346.

(279) Gojny, F. H., Wichmann, M. H.; Fiedler, B.; Schulte, K. Influence of Different Carbon Nanotubes on The Mechanical Properties of Epoxy Matrix Composites–A Comparative Study. *Compos. Sci. Technol.* **2005**, *65*, 2300.

(280) Karapappas, P.; Vavouliotis, A.; Tsotra, P.; Kostopoulos, V.; Paipetis, A. Enhanced Fracture Properties of Carbon Reinforced Composites by The Addition of Multi-Wall Carbon Nanotubes. *J. Compos. Mater.* **2009**, *43*, 977.

(281) Godara, A.; Mezzo, L.; Luizi, F.; Warrier, A.; Lomov, S. V.; van Vuure, A. W. Influence of Carbon Nanotube Reinforcement on The Processing and The Mechanical Behaviour of Carbon Fiber/Epoxy Composites. *Carbon.* **2009**, *47*, 2914.

(282) Kepple, K. L.; Sanborn, G. P.; Lacasse, P. A.; Gruenberg, K. M.; Ready, W. J. Improved Fracture Toughness of Carbon Fiber Composite Functionalized with Multi Walled Carbon Nanotubes. *Carbon.* **2008**, *46*, 2026.

(283) Borowski, E.; Soliman, E.; Kandil, U. F.; Taha, M. R. Interlaminar Fracture Toughness of CFRP Laminates Incorporating Multi-Walled Carbon Nanotubes. *Polymers.* **2015**, *7*, 1020.

(284) Menbari, S.; Ashori, A.; Rahmani, H.; Bahrami, R. Viscoelastic Response and Interlaminar Delamination Resistance of Epoxy/Glass Fiber/Functionalized Graphene Oxide Multi-Scale Composites. *Polym. Test.* **2016**, *54*, 186.

(285) Kostagiannakopoulou, C.; Loutas, T. H.; Sotiriadis, G.; Markou, A.; Kostopoulos, V. On the Interlaminar Fracture Toughness of Carbon Fiber Composites Enhanced with Graphene Nano-species. *Compos. Sci. Technol.* **2015**, *118*, 217.

(286) Ye, Y. P.; Chen, H. B.; Wu, J. S.; Chan, C. M. Interlaminar Properties of Carbon Fiber Composites with Halloysite Nanotube-Toughened Epoxy Matrix. *Compos. Sci. Technol.* **2011**, *71*, 717.

(287) Deng, S. Q.; Zhang, J. N.; Ye, L.; Wu, J. S. Toughening Epoxies With Halloysite Nanotubes. *Polymer.* **2008**, *49*, 5119.

(288) Miller, N. A.; Stirling, C. D. Effects of ATBN Rubber Additions on The Fracture Toughness of Unsaturated Polyester Resin. *Polym. Polym. Compos.* **2001**, *9*, 31.

(289) Compston, P.; Jar, PYB.; Burchill, P. J.; Takahashi, K. The Transfer of Matrix Toughness to Composite Mode I Interlaminar Fracture Toughness in Glass-Fibre/Vinyl Ester Composites. *Appl. Compos. Mater.* **2002**, *9*, 291.

(290) Burchill, P. J.; Kootsookos, A.; Lau, M. Benefits of Toughening A Vinyl Ester Resin Matrix on Structural Materials. *J. Mater. Sci.* **2001**, *36*, 4239.

(291) Kobayashi, S.; Kitagawa, J. Effect of Fine Particle Incorporation into Matrix on Mechanical Properties of Plain Woven Carbon Fiber Reinforced Plastics Fabricated with Vacuum Assisted Resin Transfer Molding. *Composites Part B.* **2016**, *85*, 31.

(292) Klingler, A.; Sorochynska, L.; Wetzel, B. Toughening of Glass Fiber Reinforced Unsaturated Polyester Composites by Core-Shell Particles. *Key Engineering Materials*. **2017**, *742*, 74.

(293) Seyhan, A. T.; Tanoglu, M.; Schulte, K. Mode I and Mode II Fracture Toughness of E-Glass Non-Crimp Fabric/Carbon Nanotube (CNT) Modified Polymer-based Composites. *Eng. Fract. Mech.* **2008**, *75*, 5151.

(294) Sadeghian, R.; Gangireddy, S.; Minaie, B.; Hsiao, K-T. Manufacturing Carbon Nanofibers Toughened Polyester/Glass Fiber Composites Using Vacuum Assisted Resin Transfer Molding for Enhancing the Mode-I Delamination Resistance. *Composites Part A.* **2006**, *37*, 1787.

(295) Yuan, L.; Ma, X. Y.; Liang, G. Z.; Yan, H. X. Fibre Reinforced Organic Rectorite/Unsaturated Polyester Composites. *Compos. Sci. Technol.* **2007**, *67*, 2311.

(296) Compston, P.; Jar, PYB. Comparison of Interlaminar Fracture Toughness in Unidirectional and Woven Roving Marine Composites. *Appl. Compos. Mater.* **1998**, *5*, 189.

(297) Fanteria, D.; Lazzeri, L.; Panettieri, E.; Mariani, U.; Rigamonti, M. Experimental Characterization of The Interlaminar Fracture Toughness of A Woven and A Unidirectional Carbon/Epoxy Composite. *Compos. Sci. Technol.* **2017**, *142*, 20.

(298) Liu, L.; Zhang, J.; Zhao, J.; Liu, F. Mechanical Properties of Graphene Oxides. *Nanoscale*. **2012**, *4*, 5910.

(299) Xu, L. Q.; Lee, L. J. Kinetic Analysis and Mechanical Properties of Nanoclay Reinforced Unsaturated Polyester (UP) Resins Cured at Low Temperatures. *Polym. Eng. Sci.* **2005**, *45*, 496.

(300) Roy, P. K.; Iqbal, N.; Kumar, D.; Rajagopal, C. Rubber Toughening of Unsaturated Polyester with Core-Shell Poly(Siloxane)-Epoxy Microspheres. *Polym. Bull.* **2014**, *71*, 2733.

(301) Auad, M. L.; Frontini, P. M.; Borrajo, J.; Aranguren, M. I. Liquid Rubber Modified Vinyl Ester Resins: Fracture and Mechanical Behavior. *Polymer.* **2001**, *42*, 3723.

(302) Arias, M. L.; Frontini, P. M.; Williams, R. J. J. Analysis of The Damage Zone Around The Crack Tip for Two Rubber-Modified Epoxy Matrices Exhibiting Different Toughenability. *Polymer.* **2003**, *44*, 1537.

(303) Pearson, R. A.; Yee, A. F. Toughening Mechanisms in Elastomer-Modified Epoxies .2. Microscopy Studies. *J. Mater. Sci.* **1986**, *21*, 2475.

(304) Huang, Y.; Kinloch, A. J. The Role of Plastic Void Growth in The Fracture of Rubber-Toughened Epoxy Polymers. *J. Mater. Sci. Lett.* **1992**, *11*, 484.

(305) Yee, A. F.; Li, D. M.; Li, X. W. The Importance of Constraint Relief Caused by Rubber Cavitation in The Toughening Of Epoxy. *J. Mater. Sci.* **1993**, *28*, 6392.

(306) Erden, S.; Sever, K.; Seki, Y.; Sarikanat, M. Enhancement of The Mechanical Properties of Glass/Polyester Composites Via Matrix Modification Glass/Polyester Composite Siloxane Matrix Modification. *Fiber Polym.* **2010**, *11*, 732.

(307) Park, S. J.; Jin, J. S. Effect of Silane Coupling Agent on Mechanical Interfacial Properties of Glass Fiber-Reinforced Unsaturated Polyester Composites. *J. Polym. Sci. Pol. Phys.* **2003**, *41*, 55.

(308) Yeung, P.; Broutman, L. J. The Effect of Glass-Resin Interface Strength on The Impact Strength of Fiber Reinforced Plastics. *Poly. Eng. Sci.* **1978**, *18*, 62.

(309) Drzal, L. T.; Madhukar, M. Fiber Matrix Adhesion and Its Relationship to Composite Mechanical Properties. *J. Mater. Sci.* **1993**, *28*, 569.

(310) Ozdemir, N. G.; Zhang, T.; Aspin, I.; Scarpa, F.; Hadavinia, H.; Song, Y. Toughening of Carbon Fibre Reinforced Polymer Composites with Rubber Nanoparticles for Advanced Industrial Applications. *Express Polym. Lett.* **2016**, *10*, 394.

(311) Kim, J. K.; Baillie, C.; Poh, J.; Mai, Y. W. Fracture Toughness of CFRP with Modified Epoxy-Resin Matrices. *Compos. Sci. Technol.* **1992**, *43*, 283.

(312) Pantano, V.; Compston, P.; Stachurski, Z.; Jar, P-Y. Effect of Matrix Toughness on The Shear Strength of Brittle and Rubber-Modified Glass-Fiber/Vinyl Ester Composites. *J. Mater. Sci. Lett.* **2002**, *21*, 771.

(313) Carveili, V.; Betti, A.; Fujii, T. Fatigue and Izod Impact Performance of Carbon Plain Weave Textile Reinforced Epoxy Modified with Cellulose Microfibrils and Rubber Nanoparticles. *Composites Part A.* **2016**, *84*, 26.

(314) Gaggar, S. K.; Broutman, L. J. Effect of Matrix Ductility and Interface Treatment on Mechanical-Properties of Glass-Fiber Mat Composites. *Polym. Eng. Sci.* **1976**, *16*, 537.

(315) Schrauwen, B.; Peijs, T. Influence of Matrix Ductility and Fibre Architecture on The Repeated Impact Response of Glass-Fibre-Reinforced Laminated Composites. *Appl. Compos. Mater.* **2002**, *9*, 331.

(316) Albertsen, H.; Ivens, J.; Peters, P.; Wevers, M.; Verpoest, I. Interlaminar Fracture Toughness of CFRP Influenced by Fibre Surface Treatment: Part 1. Experimental Results. *Compos. Sci. Technol.* **1995**, *54*, 133.

(317) Friedrich, K.; Walter, R.; Carlsson, L. A.; Smiley, A. J.; Gillespie, J. W. Mechanisms for Rate Effects on Interlaminar Fracture-Toughness of Carbon Epoxy and Carbon PEEK Composites. *J. Mater. Sci.* **1989**, *24*, 3387.

(318) Liu, K.; Macosko, C. W. The Interlaminar Toughening Effects of Nanoparticles – A Review. Submitted. 2018.

(319) Ivens, J.; Albertsen, H.; Wevers, M.; Verpoest, I.; Peters, P. Interlaminar Fracture-Toughness of CFRP Influenced by Fiber Surface-Treatment .2. Modeling of the Interface Effect. *Compos. Sci. Technol.* **1995**, *54*, 147.

(320) Haider, M.; Hubert, P.; Lessard, L. Cure Shrinkage Characterization and Modeling of A Polyester Resin Containing Low Profile Additives. *Composites Part A.* **2007**, *38*, 994.

(321) Nairn, J. A. Energy Release Rate Analysis for Adhesive and Laminate Double Cantilever Beam Specimens Emphasizing the Effect of Residual Stresses. *Int. J. Adhes. Adhes.* **2000**, *20*, 59.

(322) Kim, J-K.; Mai, Y. W. Engineered Interfaces in Fiber Reinforced Composites. 1st ed. Amsterdam, Elsevier Sciences, 1998.

(323) Jordan, W. M.; Bradley, W. L.; Moulton, R. J. Relating Resin Mechanical-Properties to Composite Delamination Fracture-Toughness. *J. Compos. Mater.* **1989**, *23*, 923.

(324) Hu, K.; Kulkarni, D. D.; Choi, I.; Tsukruk, V. V. Graphene-Polymer Nanocomposites for Structural and Functional Applications. *Prog. Polym. Sci.* **2014**, *39*, 1934.

(325) Zhang, W.; Dehghani-Sanij, A. A.; Blackburn, R. S. Carbon Based Conductive Polymer Composites. *J. Mater. Sci.* **2007**, 42, 3408.

(326) Aneli, J. N.; Khananasvili, L. M.; Zaikov, G. E. *Structuring and Conductivity of Polymer Composites*. Nova Science Publishers, New York, 1998.

(327) Li, J.; Ma, P. C.; Chow, W. S.; To, C. K.; Tang, B. Z.; Kim, J. K. Correlations Between Percolation Threshold, Dispersion State and Aspect Ratio of Carbon Nanotube. *Adv. Funct. Mater.* **2007**, *17*, 3207.

(328) Ma, P. C.; Kim, J. K.; Tang, B. Z. Effects of Silane Functionalization on The Properties of Carbon Nanotubes/Epoxy Nanocomposites. *Compos. Sci. Technol.* **2007**, 67, 2965.

(329) Ma, P. C.; Tang, B. Z.; Kim, J. K. Effect of CNT Decoration with Silver Nanoparticles on Electrical Conductivity of CNT-Polymer Composites. *Carbon* **2008**, *46*, 1497.

(330) Bauhofer, W.; Kovacs, J. Z. A Review and Analysis of Electrical Percolation in Carbon Nanotube Polymer Composites. *Compos. Sci. Technol.* **2009**, *69*, 1486.

(331) Biercuk, M. J.; Llaguno, M. C.; Radosavljevic, M.; Hyun, J. K.; Johnson, A. T.; Fischer, J. E. Carbon Nanotube Composites for Thermal Management. *Appl. Phys. Lett.* **2002**, *80*, 2767.

(332) Zhang, L.; Allen, S. D.; Woelfle, C.; Zhang, F. Influence of Polymer Structures on Optical Power Limiting Performance of Single-Walled Carbon Nanotubes. *J. Phys. Chem. C* **2009**, *113*, 13979.

(333) Park, S.; Ruoff, R. S. Chemical Methods for The Production of Graphenes. *Nat. Nanotechnol.* **2009**, 4, 217.

(334) Li, D.; Muller, M. B.; Gilje, S.; Kaner, R. B.; Wallace, G. G. Processable Aqueous Dispersions of Graphene Nanosheets. *Nat. Nanotechnol.* **2008**, *3*, 101.

(335) Geng, Y.; Wang, S. J.; Kim, J. K. Preparation of Graphite Nanoplatelets and Graphene Sheets. *J. Colloid. Interface Sci.* **2009**, *336*, 592.

(336) Vasileiou, A. A.; Kontopoulou, M.; Docoslis, A. A Noncovalent Compatibilization Approach to Improve the Filler Dispersion and Properties of Polyethylene/ Graphene Composites. *ACS Appl. Mater. Interfaces* **2014**, *6*, 1916.

(337) Kim, H.; Kobayashi, S.; AbdurRahim, M. A.; Zhang, M. J.; Khusainova, A.; Hillmyer, M. A.; Abdala, A. A.; Macosko, C. W. Graphene/Polyethylene Nanocomposites: Effect of Polyethylene Functionalization and Blending Methods. *Polymer* **2011**, *52*, 1837.

(338) Zheng, D.; Tang, G.; Zhang, H. B.; Yu, Z. Z.; Yavari, F.; Koratkar, N.; Lim, S. H.; Lee, M. W. In-situ Thermal Reduction of Graphene Oxide for High Electrical

Conductivity and Low Percolation Threshold in Polyamide-6 Nanocomposites. *Compos. Sci. Technol.* **2012**, *72*, 284.

(339) Compton, O. C.; Nguyen, S. T. Graphene Oxide, Highly Reduced Graphene Oxide, and Graphene: Versatile Building Blocks for Carbon-Based Materials. *Small* **2010**, *6*, 711.

(340) Mandelkern, L.; Fatou, J. G.; Denison, R.; Justin, J. A Calorimetric Study of The Fusion of Molecular Weight Fractions of Linear Polyethylene. *J. Polym. Sci. Part B* **1965**, *3*, 803.

(341) Schniepp, H. C.; Li, J. L.; McAllister, M. J.; Sai, H.; Herrera-Alonso, M.; Adamson, D. H.; Prud'homme, R. K.; Car, R.; Saville, D. A.; Aksay, I. A. Functional Single Graphene Sheets Derived from Splitting Graphite Oxide. *J. Phys. Chem. B* **2006**, *110*, 8535.

(342) Liu, G.; Wang, Y.; Xu, C.; Qiu, F.; An, C.; Li, L.; Jiao, L.; Yuan, H. Excellent Catalytic Effects of Highly Crumpled Graphene Nanosheets on Hydrogenation/Dehydrogenation of Magnesium Hydride. *Nanoscale* **2013**, *5*, 1074.

(343) Lim, Y. D.; Lee, D. Y.; Shen, T. Z.; Ra, C. H.; Choi, J. Y.; Yoo, W. J. Si-compatible Cleaning Process for Graphene Using Low-Density Inductively Coupled Plasma. *ACS Nano* **2012**, *6*, 4410.

(344) Ryu, S.; Liu, L.; Berciaud, S.; Yu, Y. J.; Liu, H.; Kim, P.; Flynn, G. W.; Brus, L. E. Atmospheric Oxygen Binding and Hole Doping in Deformed Graphene on A SiO_2 Substrates. *Nano Lett.* **2010**, *10*, 4944.

(345) Ye, S.; Feng, J. A New Insight into The In-situ Thermal Reduction of Graphene Oxide Dispersed in A Polymer Matrix. *J. Polym. Chem.* 2013, *4*, 1765.

(346) Akhavan, O. The Effect of Heat Treatment on Formation of Graphene Thin Films from Graphene Oxide Nanosheets. *Carbon* **2009**, *48,* 509.

(347) Thomassin, J. M.; Trifkovic, M.; Alkarmo, W.; Detrembleur, C.; Jerome, C.; Macosko, C. W. Poly(methyl methacrylate)/Graphene Oxide Nanocomposites by A Precipitation Polymerization Process and Their Dielectric and Rheological Characterization. *Macromolecules* **2014**, *47*, 2149.

(348) Chen, W.; Yan, L. Preparation of Graphene by A Low-Temperature Thermal Reduction at Atmosphere Pressure. *Nanoscale* **2010**, *2,* 559.

(349) Li, H.; Pang, S.; Wu, S.; Feng, X.; Mullen, K.; Bubeck, C. Layer-by-Layer Assembly and UV Photoreduction of Graphene-Polyoxometalate Composite Films for Electronics. *J. Am. Chem. Soc.* **2011**, *133*, 9423.

(350) Williams, G.; Seger, B.; Kamat, P. V. Tio_2-Graphene Nanocomposites: UV-Assisted Photocatalytic Reduction of Graphene Oxide. *ACS Nano* **2008**, *2*, 1487.

(351) Traina, M.; Pegoretti, A. In-Situ Reduction of Graphene Oxide Dispersed in A Polymer Matrix. *J. Nanopart. Res.* **2012**, *14*, 1.